In situ X-ray computed tomography for soft contact mechanics

Vito Acito

Nº. d'ordre NNT: 2023ECDL0054

MÉMOIRE DE THÈSE

PRÉSENTÉ POUR L'OBTENTION DU TITRE DE

DOCTEUR

DE

L'ECOLE CENTRALE DE LYON

SPÉCIALITÉ **GÉNIE MÉCANIQUE**

ECOLE DOCTORALE MEGA
MÉCANIQUE - ÉNERGÉTIQUE - GÉNIE CIVIL - ACOUSTIQUE

PAR

VITO ACITO

IN SITU X-RAY COMPUTED TOMOGRAPHY FOR SOFT CONTACT MECHANICS

Soutenue publiquement le 15 Décembre 2023 devant le jury d'examen composé de :

C. GAUTHIER	Professeur, Université de Strasbourg	Rapporteur
J. RÉTHORÉ	DR CNRS HDR, EC Nantes	Rapporteur
E. BAYART	CR CNRS, ENS Lyon	Examinatrice
E. GOUILLART	Directrice Scientifique, SGR Paris	Examinatrice
C. MINFRAY	Professeure, EC Lyon	Présidente
D. DALMAS	CR CNRS HDR, EC Lyon	Directeur
S. DANCETTE	MCF HDR, INSA Lyon	Co-Directeur (Invité)

"Quando sei curioso e vorresti sapere la risposta alle tue domande, incominci a cercare: una volta sui libri, adesso in rete. Quando sei fortunato, trovi le risposte, ma quando le risposte non ci sono, perché nessuno le conosce, se sei veramente curioso inizi a domandarti se non dovresti essere proprio tu a trovare la risposta. Il fatto che nessuno l'abbia trovata prima non t'intimorisce, in fondo quello è proprio il tuo mestiere: immaginare o fare ciò che nessuno ha mai fatto prima."

"When you are curious and would like to know the answer to your questions, you start searching: once in books, now on the net. When you are lucky, you find the answers, but when the answers are not there, because nobody knows them, if you are really curious you start to wonder if you should not be the one to find the answer. The fact that no one has found it before does not intimidate you, after all, that is your job: to imagine or do what no one has done before."

Giorgio Parisi - In un volo di storni

Contents

Nomenclature of the main variables and abbreviations

Variables

P	Normal Force
Q	Tagential Force
a	Contact Radius
R	Curvature Radius
r	Radius
a	Contact Radius
δ_c	Normal Indentation
δ_s	Shear Displacement
A_A	Apparent Contact Area
A_R	Real Contact Area
μ	Friction Coefficient
E	Young's Modulus
ω_0	Work of Adhesion
K	Bulk Modulus
p	Normal Pressure
p_0	Maximum Normal Pressure
σ	Interface Shear Strength
λ	Tabor Parameter
$\sqrt{J_2}/p_0$	Normalised Mises Parameter
U_i	Displacement Field Component
ε_{ij}	Strain Field Component
σ_{ij}	Stress Field Component

Abbreviations

DMT	Derjaguin-Muller-Toporov
JKR	Johnson-Kendall-Roberts
CM	Cattaneo-Mindlin
XRCT	X-ray Computed Tomography
DIC	Digital Image Correlation
DVC	Digital Volume Correlation

1 Introduction

1.1 General context

Contact events are encountered in each moment in our daily life. Each time that two bodies are in contact and/or that it is needed to separate them or to slide one over the other, the presence of normal and/or tangential forces can be easily felt. We can just cite, for example, the reaction forces generated when we press two bodies in contact, the peeling force when we try to separate an adhesive tape or the force opposite to the direction of movement clearly felt when pushing a body across the ground. This last force is called friction and is a dissipating force which acts when two bodies slide one over each. The separation of two adhesive bodies also results in an energy dissipation because the peeling force is directed contrary to the separation movement.

From an engineering point of view, we have always tried to control friction and dissipating phenomena by modifying crucial parameters like the rheology of contacting bodies, inserting a third body like lubrifiants in between them or playing with the topograhy of the surfaces. The presence of friction could be desired, *e.g.* when we want to guarantee adherence when walking or driving a car, or undesired, *e.g.* when it produces heat and energy dissipation in engine due to contact between the moving parts. Another relevant phenomenon caused by high friction forces and adhesion is wear that, in this case too, could be desired (friction welding, polishing...) or not when the integrity of a surface is essential for the good usage of mechanical part in terms of geometrical tolerances and/or physio-chemical characteristics of the interfaces.

While friction could be easily experienced and measured by simply knowing the evolution of the normal and/or tangential forces, understanding the measurements and the observed phenomena could be very complicated because it involves several interconnected parameters. Recent results, obtained by using modern optical observation and image acquisition analysis, revealed that the contact area evolves and that these changes play a relevant role in understanding the frictional behaviour of an interface. In this sense, we have to define two quantities: an apparent contact area A_A corresponding to the shared overlaying contact zone and the real contact area A_R that is actually smaller than the previous one in most situations. Basically, A_A corresponds to the contact area that could generate if the bodies were perfectly smooth while A_R is due to the fact that, in nature, surfaces are always rough at many different scales and contact happens between a few asperities rather than on the total superposing surface.

The measurement of A_R is, then, of relevant importance for understanding the frictional behaviour of an interface. However, despite a huge number of contact models, accessing this quantity remains, nowadays, a big challenge. Up to now, the vast majority of the experimental measurements are based on optical observations where at least one of the two bodies must be transparent to access the contact interface. Furthermore, in these techniques only the 2D projected area is observable without any information about what happens in the out-of-plane zone. That is why other experimental techniques are needed to have a 3D description of the contact surface and also to overcome the transparency limit.

Following these objectives, X-Ray Computed Tomography (XRCT) is a good candidate to fill all these gaps. As a well-developed non-destructive technique, XRCT is mainly used, nowadays, to characterise a material in a three dimensional way, giving information on all the volume of an object. Despite a few preliminary works on the use of XRCT for contact mechanics, a detailed examinations of the limits and the reliability of XRCT for tribology purposes is still necessary.

Based on simple modeled surfaces submitted to normal and/or tangential loading, the present work aims at answering the numerous questions related to the advantages and disadvantages of XRCT for the evaluation of the real contact area, surface deformation and bulk strain/stress field for two bodies in sheared contact. Thanks to the use of a soft and smooth PDMS specimen in contact with a smooth PMMA plane, the obtained results will be compared with optical observations issued by well-established devices and with already existing theoretical models for which very few experimental validations are available.

1.2 Scientific Context

Starting from the previous general introduction, an overview of the main laws of contact mechanics and experimental techniques related to the objectives of our study will be presented here.

1.2.1 The Amonton-Coulomb friction laws

The pioneering works in the field of friction date back to the experiments of Leonardo Da Vinci (1452-1519) [1] which were formulated successively by Guillaume Amontons (1663-1705) in the well-known Amontons' friction laws, which are:

- The friction force Q_s is proportional to the normal load P (1st Amontons' law);
- The friction force is independent of the apparent contact area for a constant normal load (2nd Amontons' law).

A third law was successively added by Coulomb [2] as:

- The kinetic friction coefficient μ_d (the ratio between the friction force and normal load during full sliding at constant velocity) is much smaller than the static friction coefficient μ_s (defined as the ratio between the maximum tangential force required to start sliding over the normal applied load) and this one is independent of the sliding speed.

To summarise (see Fig. 1.1), the three friction laws just announced explain that the measured tangential force Q of two bodies in contact submitted to an increasing tangential displacement δ_s and a constant normal load P, increases up to the peak Q_s for which we can measure a static friction coefficient μ_s. After this point, the body starts moving and it experiences a constant friction force Q_d that is constant over time and which defines the dynamic friction coefficient μ_d. Here we can notice that there is no need to involve the contact area but, we will see just after, that this one is hidden in the measured friction coefficients implying that the measurement of the real contact area is fundamental.

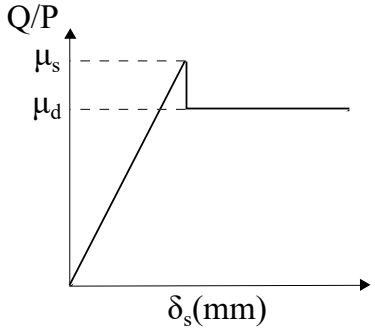

Figure 1.1: Evolution of the tangential force Q as a function of the imposed tangential displacement δ_s for a constant applied normal load P according to Amontons-Coulomb friction laws.

1.2.2 The role of the real contact area A_R

Modern technologies (microscopes, profilometers, interferometers etc...) have shown that surfaces are actually rough on multiple scales ranging from millimeters to fractions of nanometers. The first study about the influence of the topography on contact were performed by Bowden and Tabor [3] in their pioneering work. Figure 1.2 illustrates the transition from A_A to A_R as a function of the resolution of observation. At the lower resolution (a) the contacting bodies seem to share a unique planar contact area. However, if we zoom over, one can notice that contact does not happen everywhere but only between a few asperities characterizing the surface topography (b). Finally, if we zoom sufficiently (c), we could model a single asperity-asperity contact as a simple modeled surface like a sphere-on-sphere contact or a sphere-on-plane one. As a result, the total friction force exerted on the two bodies is basically the sum of all tangential forces developed at each mono-contact asperity when the two bodies are moved one over the other. Then, it is the real contact area A_R, considered as the sum of all the asperities contact area, that controls friction.

$$Q = \sigma A_R \tag{1.1}$$

From an experimental point of view, the observation of A_R is not easy, especially because it should be made *in-situ* and *in-operando*. As a consequence, the vast majority of experiments are based on optical measurements and thus limited to very few materials as one of these should be optically transparent (details about the observations technique will be provided in section 1.2.4).

One interesting experimental work, which allows to see the evolution of A_R, is from Dieterich and Kilgore [5]. In their study, they put into contact two rough and transparent PMMA block

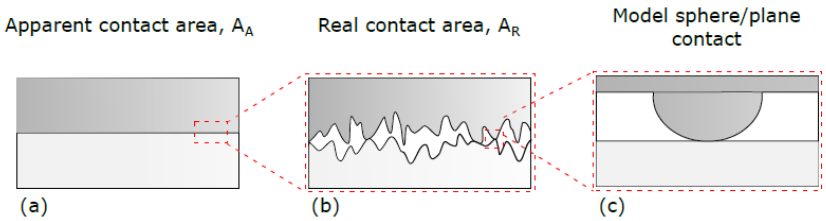

Figure 1.2: The single asperity approach. (a) Apparent contact area A_A. (b) Multi-asperity contact at the origin of A_R. (c) Sphere-on-plane mono-contact pair. Illustration from [4].

under normal load with the aim of observing the real contact area. Thanks to the use of an optical device, they were able to distinguish the contact spots as the zone where the incident monochromatic light was not scattered (the incident light is perpendicular to the contact plane while it takes another angle with non-contact zones) and they obtained the images shown in Fig. 1.3. The first relevant result was to see that A_R (the colored spots) were much smaller than A_A (the black zone) as expected by Bowden and Tabor. Additionally, in these images, two main effects were studied: the normal load applied and the time spent in contact. The effect of an increasing normal pressure was to increase the real contact area and the same effect was obtained by just waiting in contact and allowing the material to relax.

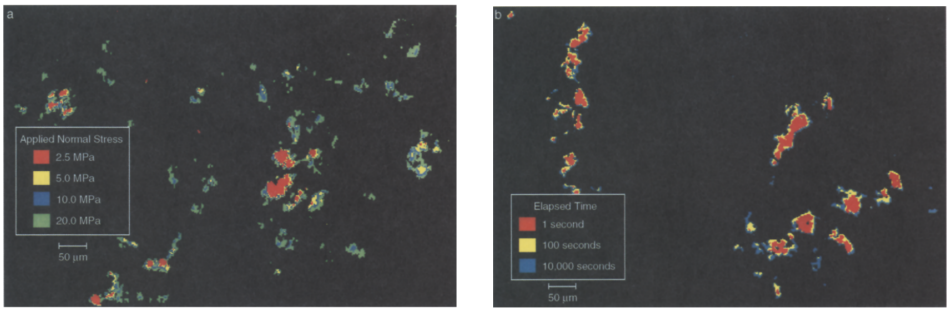

(a) (b)

Figure 1.3: Visualization of the contact area between two rough PMMA blocks. (a) Effect of the normal load. (b) Effect of the relaxation time. Images from [5].

When a rough contact interface is submitted to a shear displacement, the contact area also changes as shown in the work of Sahli *et al.* [6]. They generated a rough PDMS/glass contact and they applied different normal loadings and a shear displacement at constant speed. The evolution of the real contact area versus the measured tangential force is shown in Fig. 1.4 for increasing normal load with data plotted until the presence of full sliding. From this image we can retain two important conclusions. The first one is that the value of the dynamic friction force (the value at the end of each curve) increases with the normal load and then with the initial contact area. Second, the contact area decreases under the application of a shear displacement until full sliding and, at these points, a linear fit underlines how the transition to full sliding is characterised by a shear strength σ so that $Q = \sigma A_R$ in dynamic conditions.

The physical origin of σ at the asperity level is made of two contributions:

- **adhesion**: it appears between the asperities with short-range interactions like Van der Waals forces;

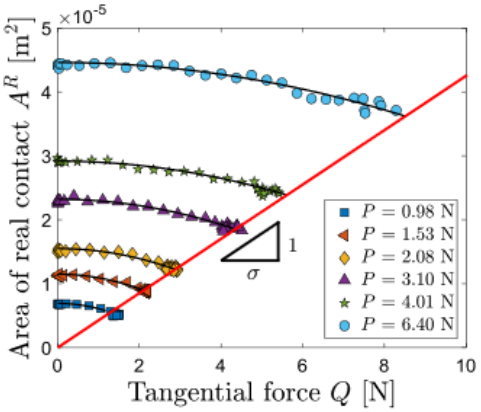

Figure 1.4: A_R versus Q for a PDMS/glass multicontact shear experiment under the application of an increasing normal load P. The linear fit characterising σ passes from the points where full sliding initiates. $R_q = 26$ µm and $v = 0.1$ mm/s. Image from [6].

- **deformation**: it is linked to the deformation of each asperity. With the application of tangential force, it generates an opposite dissipating force.

To sum up, the real contact area depends on several quantities playing interconnected roles. We can list the main influencing parameters as:

- the surface topography: dependence on the distribution of the asperities;
- the normal load: as shown in Fig. 1.3a, A_R increases with the applied normal pressure;
- the time spent in contact: materials can be more or less visco-elastic or visco-plastic so that the material properties can change over time and affect directly the contact area. This is especially important in our study involving soft polymers;
- the application of a tangential force: experimental observations have shown that there is proportionality between the dynamic friction force Q_d and A_R so that we can define an interface shear strength σ [7, 8, 9].

As a conclusion, the proportionality between the friction force and the normal load described by the Amonton-Coulomb laws can be explained after these observations. The friction force is proportional to the real contact area A_R by a constant σ and, at the same time A_R is proportional to the normal load P. Consequently, the coefficients of friction μ_s and μ_d hide all the physical quantities that we have introduced up to here such as the surface topography, the mechanical properties of the materials, the ageing of the contact (especially for visco-elastic materials) etc.

1.2.3 Monocontact models

Passing from the macro to the micro scale, we have observed how a multi contact interface can be modeled by the sum of the interaction of each single asperity. Furthermore each asperity contact, at a given scale, can be approximated by a sphere-on-sphere or sphere-on-plane contact. Then, the modelling of these mono-contact pairs is the basis of all theoretical models developed in contact mechanics and will be detailed in this section.

Adhesionless normal contact - Hertz's theory

The first and the most used normal contact model is the theoretical work of Hertz [10] who considered the adhesionless and frictionless normal contact of two quadratic elastic bodies (having radii of curvature of R_1 and R_2, elastic moduli of E_1 and E_2 and Poisson's ratios of ν_1 and ν_2). The model was able to predict the radius of a circular contact a obtained under the application of a normal force P as [11]:

$$a = \left(\frac{3RP}{4E^*}\right)^{1/3} \tag{1.2}$$

and the corresponding contact pressure distribution as:

$$p(r) = p_0\left(1 - \left(\frac{r}{a}\right)^2\right)^{1/2}, \quad p_0 = \frac{3P}{2\pi a^2} = \frac{2E^* a}{\pi R} \tag{1.3}$$

where $\frac{1}{R} = \frac{1}{R_1} + \frac{1}{R_2}$, $\frac{1}{E^*} = \frac{1-\nu_1^2}{E_1} + \frac{1-\nu_2^2}{E_2}$ and p_0 represents the maximum normal stress at the contact center. The representation in Fig. 1.5 corresponds to a rigid sphere indenting a deformable half-space so that $E_1 >> E_2$ and $R_1 << R_2$ (in the case of a plane $R = \infty$). In terms of normal pressure distribution and contact dimensions, the problem of the rigid sphere over a deformable half-space is equivalent to the one of a deformable sphere over a rigid plane.

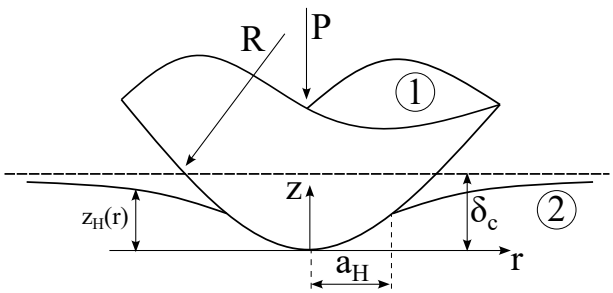

Figure 1.5: Illustration of an adhesionless normal contact of a rigid sphere indenting a deformable half-space. The half-space is deforming according to the Hertz's theoretical prediction. P is the normal load, R is the radius of curvature of the spherical indenter, δ_c is the corresponding normal indentation, a_H is the obtained contact radius and $z_H(r)$ is the vertical position of the deformed external surface.

The laws of Hertz are only valid under the following conditions:

- The materials are isotropic;
- Strains are small and a linear elastic law is applicable ($a << R$);
- Surfaces are continuous and non-conforming;
- The contact is considered as adhesionless and frictionless;
- Bodies are considered as two half-spaces.

According to the objectives of the present study, it is also interesting to provide the equation of the vertical displacement $z_H(r)$ (assuming that the direction of the normal load P is also vertical) corresponding to the position of the deformed external surface of the body 2 with

respect to the origin indicated in Fig. 1.5. This quantity is defined piecewise depending on the position of the radial point, inside or outside the contact area.

If $r \leq a$ it is defined as [12]:

$$z_H(r) = \delta_c - \frac{\pi p_0}{4E^* a}\left(2a^2 - r^2\right) \tag{1.4}$$

that is basically the rigid sphere external shape, otherwise, if $r > a$, it becomes [13]:

$$z_H(r) = \delta_c - \frac{a^2}{\pi R}\left[\left(2 - \frac{r^2}{a^2}\right) arcsin\left(\frac{a}{r}\right) + \frac{\sqrt{r^2 - a^2}}{a}\right] \tag{1.5}$$

Adhesive contact models

Depending on the chemical composition of the external surfaces and of the deformability of the contact bodies, the "simple" Hertz's contact model cannot describe properly a contact involving adhesion. The main contributions in the extension of the Hertz's theory are found in the works of Johnson, Kendall and Roberts (JKR) [14] and of Derjaguin, Muller and Toporov (DMT) [15]. The main difference between their theories concerns the range of influence of the adhesive forces. While the first model considers that attractive interactions act only at very small gaps, the second one assumes these additional forces act outside the contact area. One of the main results is that the shape of the deformed surfaces is different from the Hertz's one and provides a stress singularity on the contact edge for the JKR model while, in the DMT one, the shape is the same as the Hertz's case. In both cases, anyway, bodies are considered as perfectly smooth and linear elastic.

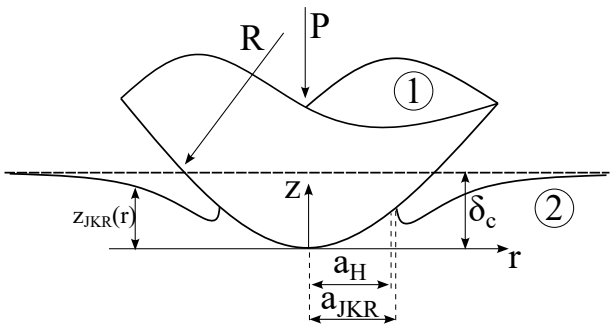

Figure 1.6: Illustration of the JKR adhesive normal contact of a rigid sphere indenting a deformable half-space. Differently from the Hertz's and DMT's case, the deformed surface rebond near the contact edge.

The relation between the contact radius and the normal force becomes for the JKR and DMT models, respectively:

$$a_{JKR} = \left[\frac{3R}{4E^*}\left(P + 3w_0\pi R + \sqrt{6\omega_0\pi RP + \left(3\omega_0\pi R\right)^2}\right)\right]^{1/3} \tag{1.6}$$

$$a_{DMT} = \left[\frac{3R}{4E^*}\left(P + 2\omega_0\pi R\right)\right]^{1/3} \tag{1.7}$$

where ω_0 is work of adhesion that measures the work needed, per unit area of the interface, to separate the surfaces.
One of the most important effects of adhesion is that the contact radius keeps a finite value even for a vanishing load and a contact is still present even for negative loads down to an instability value called *pull-off force*. As introduced before, the shape of the deformed surface ($z_{JKR}(r)$) for the JKR case changes from the Hertz-DMT case due to the re-bonding of the surface near the contact edge caused by the adhesive interactions in the contact zone (see Fig. 1.6).

After the introduction of these two models, the question remains about their validity and fields of application. Indeed, these are only two extreme cases of an adhesive contact while a huge variety of intermediate situations could appear depending on the elastic properties of the materials in contact and on the range of the attractive force involved. Tabor [16] introduced then a new parameter λ to distinguish the different cases. This parameter is given by [17]:

$$\lambda = \frac{\sigma_0}{\left(\frac{\omega_0 E^{*2}}{\pi R}\right)^{1/3}} \tag{1.8}$$

where σ_0 measures the amplitude of the attractive interaction stresses.
As a result, the JKR theory applies when λ is large, *i.e.* when compliant and adhesive materials are in contact. Conversely, DMT equations applies for small values of λ, when stiff and weakly adhesive materials are involved.

A complete and detailed modelling of what happens for different values of the Tabor parameters is provided in the studies of Maugis [18]. One of the main results of this study is presented in Fig. 1.7 where the evolution of the normalised contact radius is plotted against the normalised normal indentation. The plot illustrates the differences between the two extreme theories and what happens in intermediate cases. For vanishing values of λ the problem is led to the Hertz-DMT case where the shape of the deformed half-space is the same leading to the same contact radius, reducing to zero for a vanishing indentation. As soon as the Tabor parameter increases, there is a bigger influence of the adhesive interactions in the contact zone which changes the shape of the deformed skin and the size of the contact radius that keeps a finite value even for $\delta_c = 0$. Another relevant phenomenon is related to what happens during unloading, *i.e.* starting from a finite value of a and decreasing the indentation from right to left in the graph. The contact area remains positive even for negative values of the indentation up to an instability point (where the tangent to the curve is vertical) and the contact radius goes rapidly to 0 and contact is lost.

Fig. 1.8 illustrates the behaviour of the normalised air gap $\bar{u_g}$ (the gap between a rigid indenter with a parabolic shape and an elastic half-space deformed to the effect of the indentation) as a function of the normalised radius r. One can observe how the curvature of these curves is continuous for the Hertz-DMT case while it starts to be discontinuous for increasing λ underlining the presence of the typical re-bonding of the deformed skin caused by the effect of the adhesive force in the contact area and easily visible in Fig. 1.6. The equations for this gap are provided distinguishing two different zones depending if the radial position is in the cohesive zone (the zone where the adhesive, attractive, stresses are present) or not. The extent of this zone is measured by the parameter c. Details about the computation of these profiles are provided in Appendix 6. By means of this model, the JKR profile $z_{JKR}(r)$ will be determined using high values of λ (10 for instance) while the Hertz-DMT one $z_H(r)$ will rather be extracted with $\lambda = 0$.

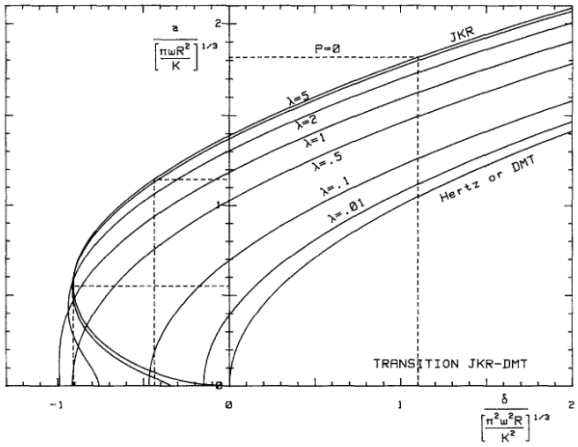

Figure 1.7: Normalised contact radius a plotted versus the normalised indentation δ_c for different values of the parameter λ. Plot from [18].

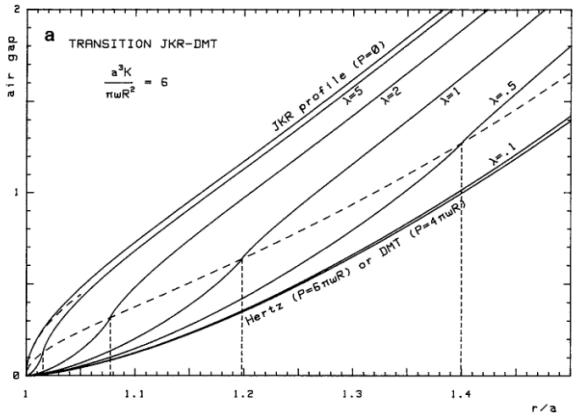

Figure 1.8: Profiles of the air gap $\bar{u_g}$ for different values of λ and for $A^3 = 6$. Plot from [18]. For the definition of A and the computation of the air gap, see the Appendix 6.

The effect of tangential forces - the Cattaneo-Mindlin model

In the previous section, the case of a purely normal load applied to a rigid sphere on a smooth elastic half-space was introduced. We have observed how, both in the adhesive and non-adhesive cases, how a perfectly circular contact area is obtained. Now, the effect of a tangential force, parallel to the contact plane, is presented. Fig. 1.9b, from the work of Barquins [19], shows the superposition of two successive images capturing the contact area of a smooth rigid sphere on a smooth rubber surface under the application of a shearing force before steady sliding. As soon as the sphere start sliding, the contact area decreases in size and loses its circularity and isotropy. The loss of symmetry is especially marked by a shrinkage at the trailing edge caused by peeling due to the existence of tensile stresses (a crack tip propagating in mode I, opening mode). In their work, an artificial scratch created on the rubber surface enabled to measure the displacement field on a line perpendicular to the sliding direction and passing from the contact center. The presence of a superimposed horizontal line in the contact center underlines the existence of stick zone, while partial slip occurs in the annular region adjacent to the contact edge, as already found in the works of Cattaneo-Mindlin (CM) in the non-adhesive contact type [20, 21].

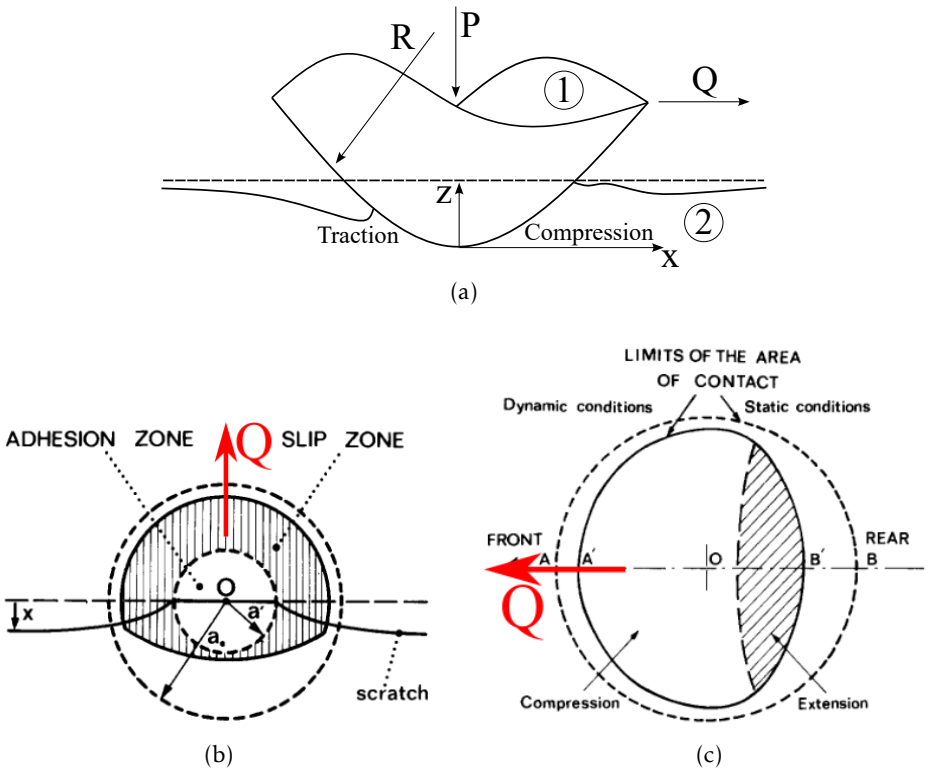

Figure 1.9: (a) Lateral view. Illustration of the contact problem of a smooth rigid sphere sliding on a smooth elastic half-space. (b) Top view. Superimposed views of the smooth sphere-on-plane contact area under purely normal load and in the first preliminary phase of friction. (c) Top view. Evolution of the contact area during full sliding. Images (b) and (c) from [19].

It is important to notice that the stick zone keeps concentric to the initial contact circle and still remains circular. We define the stick radius as b and its evolution is provided by the CM's model assuming that 1) both surfaces are smooth, 2) the pressure distribution normal to the contact plane is unchanged after shearing and expressed by the Hertz contact model (this is

reasonable in the case of elastomer/glass contact as the elastomer is incompressible and very soft if compared to the glass) and 3) Amontons-Coulomb's friction law applies locally at any position in the contact. In other words slip occurs wherever the shear stress $\sigma_{xz} = \mu\sigma_{zz}$ with μ being the macroscopic friction coefficient (in the CM problem the static and dynamic friction coefficients are assumed to be equal). The evolution of the adhesive zone can thus by expressed by the equation

$$b = a_H\left(1 - \frac{Q}{\mu P}\right)^{1/3} \tag{1.9}$$

where P is the applied normal load, Q the applied tangential force and a_H is the Hertzian contact radius for the given normal load.

The work of CM also provides the equations for the shear stress in the contact area which are given by [22]:

$$\sigma_{xz}(r) = \frac{3\mu P}{2\pi a_H^3}\left(\left(a_H^2 - r^2\right)^{1/2} - \left(b^2 - r^2\right)^{1/2}\right), \quad 0 \le r \le b,$$
$$\sigma_{xz}(r) = \frac{3\mu P}{2\pi a_H^3}\left(\left(a_H^2 - r^2\right)^{1/2}\right), \quad b < r \le a_H,$$
$$\sigma_{xz}(r) = 0, \quad r > a_H$$

The evolution of the normalised shear stress σ_{xz}/p_0 (p_0 is the maximum normal pressure in the Hertz contact problem.) as a function of the normalised radius r/a for increasing an increasing shear force Q is plotted in Fig. 1.10 for a problem similar to the one that will be treated in this study in terms of material properties ($E = 1.5$MPa, $R = 9.42$mm, $P = 1$N and $\mu = 2$). One can observe that the shear stress field along the shear direction is characterised essentially by two zone: a slip zone at the periphery of the contact where the stress shape is simply μp (p being the Hertz pressure at a given point in the contact as shown with equation 1.3) and an adhesive zone composed of a quadratic shape. As soon as Q is increased, the size of the adhesive zone decreases down to a point where full sliding occurs and the shear stress is simply μp everywhere.

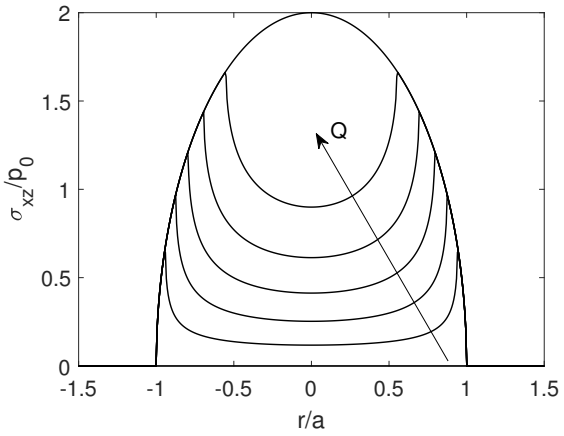

Figure 1.10: Evolution of the shear stress σ_{xz}, along the contact diameter, according to the CM model for $E = 1.5$ MPa, $\nu = 0.5$, $P = 1$N and $\mu = 2$.

The effect of tangential forces - the Savkoor model

Another study investigating the effect of a tangential load on a contact interface, in the presence of adhesion, was made by Savkoor in his thesis [23]. The work still considers, in the analysis, the use of two ideally smooth elastic bodies with a spherical shape and distinguishes essentially the effect of a tangential load Q in two different and consecutive phenomena that are shown in Figure 1.11. When $Q < Q_0$, through an energy-balance analysis, it is shown how the contact area shrinks in size in a stable manner under the effect of peeling. As soon as Q exceeds Q_0, instead, this peeling is unstable but it cannot continue indefinitely. In fact, it is unlikely that the contact peeling can continue up to the complete receding of the contact area when a normal load is still applied. Hence, peeling terminates when the contact radius equals the Hertzian value in the absence of adhesion. For further increases of the tangential load $Q > Q_C$, the phenomenon of slip occurs in the contact area to release high stresses as in the Cattaneo-Mindlin model.

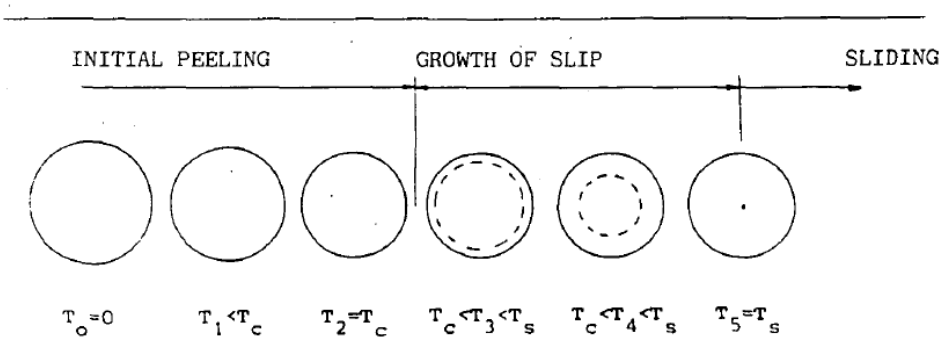

Figure 1.11: The effect of the tangential load on a circular contact area according to the model of Savkoor [23]. The contact is firstly characterised by peeling up to the Hertzian contact radius while it is followed by slip invading the contact area. In this picture the term Q for tangential force is replaced by T. Image from [23].

The problem, in this part, is considered as a phenomenon of shear fracture with the use of mode II (K_{II}) and mode III (K_{III}) stress intensity factors. When they attain a critical value, it denotes the starting of slip with a mechanism of crack propagation. Savkoor also remarks that, after the initial peeling, the contact area remains constant in the subsequent phase of invading slip, as in the CM model. In the analysis, he makes the simplification that there is no distinction between the radial (K_{II}) and tangential (K_{III}) components of the Stress Intensity Factor (SIF) with respect to the axis of application of the tangential force and that only K_{II} is sufficient to treat the problem. This SIF is constant during the slip process so that the effect of Q is only to let the slip zone growing. Treating the slip problem as a shear fracture one defines the main difference with the CM model: the Savkoor investigation does not consider the influence of the normal pressure and the shear stress, in the slip zone, is simply characterised by a constant residual shear stress σ_d. However, in agreement with the CM model, the stick zone is still assumed to be circular of a radius b and that this stick zone keeps concentric with the contact boundary. Finally, in this study, the assumption that normal and tangential problems are uncoupled is also made. This last one is valid when:

- bodies are made of the same material (as in the CM model);
- bodies are incompressible ($\nu_1 = \nu_2 = 0.5$) but with different elastic moduli;

- one of the two bodies is very rigid with respect to the other.

According to the experimental framework of the present study, we can expect that we respect the third hypothesis and that this model can apply to our measurements.

The determination of shear stress and the value of b inside the contact is made possible by dividing the problem into two sub-problems: that for the locked region ($r \leq b$) and that for the slip region ($b < r \leq a$). In the first sub-problem it is considered the shift of a rigid disk where no slip is allowed so that:

$$\sigma_{xz}(r) = Q_1 \frac{(b^2 - r^2)^{-1/2}}{2\pi b} \quad if \quad r < b \tag{1.10}$$

and that $\sigma_{xz}(r) = 0$ for $r > b$. The displacement in the direction of shear is then defined as

$$\delta_1 = \frac{Q_1 \Lambda}{8b} \tag{1.11}$$

with $\Lambda = (2-\nu_1)/G_1 + (2-\nu_2)/G_2$. This traction is axially symmetric in magnitude and parallel to the force Q_1.
In the second sub-problem, instead, it is necessary to find a stress distribution where the stress is constant in the slip region and that also gives rise to an uniform displacement in the shear direction inside the locked region. The author found that this type of distribution should be of type

$$\sigma_{xz}(r) = \frac{\sigma_d}{\pi} arccos\left(\frac{2b^2 - a^2 - r^2}{a^2 - r^2}\right) \quad for \quad 0 \leq r \leq b \tag{1.12}$$

while $\sigma_{xz}(r) = \sigma_d$ for $b < r \leq a$ and $\sigma_{xz}(r) = 0$ outside the contact area. In this second sub-problem, the force component associated to this stress is

$$Q_2 = 2a^2 \sigma_d \left[arccos\left(\frac{b}{a}\right) + \left(\frac{b}{a}\right)\left(1 - \frac{b^2}{a^2}\right)^{1/2} \right] \tag{1.13}$$

while the rigid displacement of the disk is

$$\delta_2 = \frac{\Lambda \sigma_d}{2} \left(a_0^2 - b^2\right)^{1/2} \tag{1.14}$$

The determination of the size of the locked region is obtained assuming that the stress intensity factor at the boundary between the adhesion and slip regions assumes its critical value so that

$$Q = Q_1 + Q_2 = 2\sqrt{2}\pi K_{IIC} b^{3/2} + 2a^2 \sigma_d \left[arccos\left(\frac{b}{a}\right) + \left(\frac{b}{a}\right)\left(1 - \frac{b^2}{a^2}\right)^{1/2} \right] \tag{1.15}$$

while

$$\delta_s = \delta_1 + \delta_2 = \frac{\pi \Lambda}{2\sqrt{2}} K_{IIC} b^{1/2} + \frac{\Lambda \sigma_d}{2} \left(a_0^2 - b^2\right)^{1/2}. \tag{1.16}$$

This last two equations, together with the relation between kinetic friction force during total slip and shear stress (defined as the Tresca's slip criterion):

$$Q_d = \pi a^2 \sigma_d \tag{1.17}$$

allow to determine the amount of the stick zone with respect to the slip zone knowing the values of Q_d, δ_s and a. The typical profiles of shear stress determined with these equations is shown in Figure 1.12 where it can be noted the plateau in the slip zone assuming the constant value σ_d and the decreasing shear stress in the slip zone limited by the radius b.

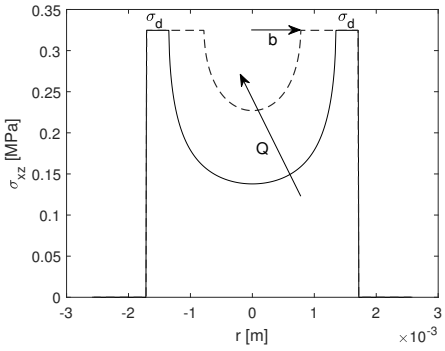

Figure 1.12: Profile of the shear stress according to the Savkoor's model. The profile is characterised by a constant shear stress σ_d in the slip zone followed by a decreasing shear stress in the stick zone limited by b.

The shear stress beneath a contact under normal and tangential loading

Up to now, we have only analysed what happens in the contact area but from a bi-dimensional point of view, *i.e.* restricted to the contact plane. However, this analysis should be more likely done with a three-dimensional observation in order to properly understand the mechanisms found at the surface. The main pioneering work in the modelling of the contact stress field beneath a sliding spherical contact was made by Hamilton in 1983 [24] who provided the explicit equations for the entire stress field under a sliding contact with the following assumptions:

- both the rigid sphere and the elastic half-space have smooth surfaces;
- the contact pressure at the surface obeys to the Hertz distribution;
- the presence of shearing does not affect neither the radius of the circle of contact nor the contact pressure;
- equations are provided during macroscopic sliding, for $Q = \mu P$.

First, based on the equations provided by Hamilton it is interesting to focus on the evolution of the stress parallel to the sliding direction at the surface. Fig. 1.13 shows the normalised component σ_x over the maximum normal pressure p_0 along the normalised x-coordinate x/a. When the coefficient of friction is set to 0, *i.e.* the case where there is no tangential force, the maximum tensile stress is at the contact periphery (vertical gray line). This significant tensile stress is what causes the well known ring-crack in brittle materials that starts from the contact edge. The effect of friction is to add a compressing stress to the front edge and, complementary, to intensify the tensile stress at the back edge.

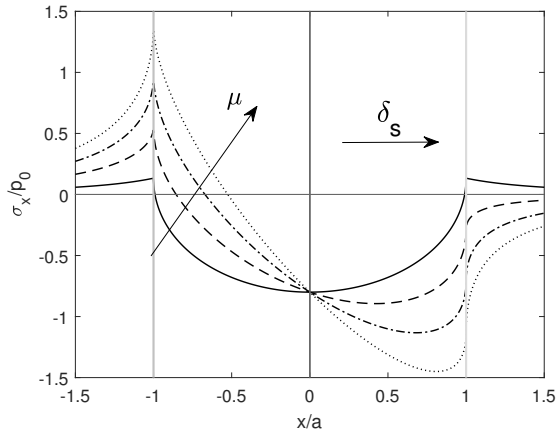

Figure 1.13: Distribution of the stress σ_x (along the sliding direction) for various friction coefficients μ (0,0.25,0.5,0.75). Plot according to the equations provided in [24] with a Poisson coefficient $\nu = 0.3$. p_0 is the maximum normal pressure in the Hertz contact problem. The vertical gray lines underline the limits of the contact area. The horizontal arrow indicates the direction of shear.

Second, in order to understand the evolution of the shear stress at the surface, we should rather observe what happens below the surface. With J_2 as the second invariant of the deviatoric stress tensor and $\sigma_{eq} = \sqrt{3J_2}$ the equivalent von Mises stress, Hamilton introduced a convenient representation of the normalised deviatoric stress as $\sqrt{J_2}/p_0$ where p_0 is the maximum normal pressure at surface. Then $\sqrt{J_2}/p_0$ writes:

$$\frac{\sqrt{J_2}}{p_0} = \frac{\sqrt{\frac{1}{6}\left[(\sigma_{xx}-\sigma_{yy})^2+(\sigma_{yy}-\sigma_{zz})^2+(\sigma_{zz}-\sigma_{xx})^2\right]+\sigma_{xy}^2+\sigma_{xz}^2+\sigma_{yz}^2}}{p_0} \tag{1.18}$$

We will refer to $\sqrt{J_2}/p_0$ as the "normalised Mises parameter" in the following. Figure 1.14 shows a contour map of this parameter on the central plane $y = 0$ for a coefficient of friction $\mu = 0$ (a) and $\mu = 0.25$ (b) with a Poisson coefficient $\nu = 0.3$. The first remark is that yielding (essentially caused by the shear components of the stress tensor) starts below the surface, even for purely normal load (Figure 1.14a, at a depth corresponding to 0.48 times the contact radius. Then, the effect of friction is to increase the maximum value of J_2 resulting in yielding at lower loads. Furthermore, this tangential force (see Figure 1.14b) has the effect of shifting this original maximum along the shearing direction (x) and to move it slightly closer to the surface. Another important remark is the apparition of a new zone where the yield parameter start to be high. This last one develops at $x = -a$. Together with what has been shown before ($x = -a$ is also the point where there is the maximum tensile stress), this point ($x = -a, y = 0, z = 0$) becomes the most likely location for failure. More generally, the effect of a tangential force is to shift the highest values of the Von Mises Yield stress closer to the surface.

Summary of monocontact models

A summary of the contact models detailed above is provided in Table 1.1, highlighting the available quantities to be compared to potential experimental measurements, from the deformed surface profile to the bulk stress field in the deforming material. Bearing in mind that they were all developed within the framework of a linear elastic material behavior subjected to small deformation, their application to the case of soft contact mechanics, with compliant

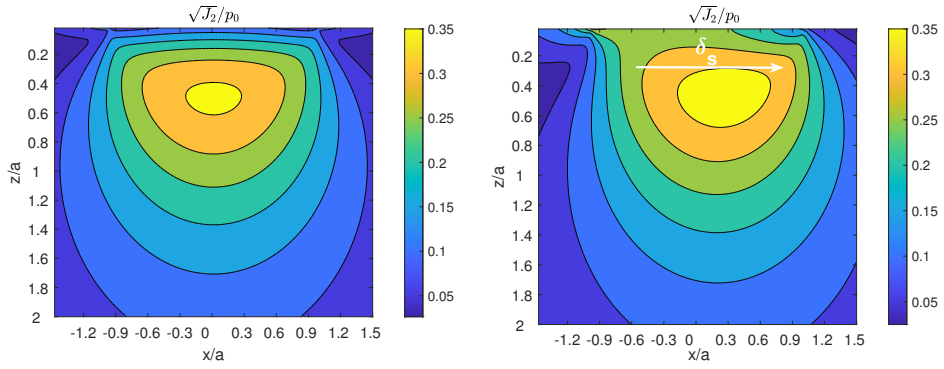

Figure 1.14: Lines of $\sqrt{J_2}/p_0$ for (a) a pure normal contact load ($\mu = 0$) and (b) a tangential load ($\mu = 0.25$) applied along the direction x. The plots are obtained from the equations of Hamilton [24] for a Poisson coefficient $\nu = 0.3$. p_0 is the maximum normal pressure in the Hertz contact problem.

materials exhibiting a viscous and hyperelastic behavior and experiencing finite strains, will have to be discussed carefully.

	Surface Profile	**Surface Stress**		**Bulk Stress**	
	Normal	*Normal*	*Shear*	*Normal*	*Shear*
Without Adhesion	Hertz [10]	Hertz [10]	Cattaneo [20]-Mindlin [21]	Hamilton [24]	Hamilton [24]
With Adhesion	JKR [14], DMT [15], Maugis [18]	JKR [14], DMT [15]	Savkoor [23]		

Table 1.1: Summary of the introduced contact mechanics theoretical models.

1.2.4 Optical observation of A_R and Strain Field

We have shown before how the measurement of the real contact area A_R could be important to understand the adhesive and shear-resistance properties of a contact interface. However, while there are many numerical and/or analytical contact models in the literature (see the works of Vakis *et al.* [25] and Müser *et al.* [26] for a review), the experimental analysis of A_R is still challenging. The vast majority of these measurements have been made through optic-based setups allowing a contrast between the contact area and the rest of the interface [6, 5, 27, 28, 29, 22, 30, 31, 7].

A typical setup used in literature to capture the real contact area during a tribological test is shown in Fig. 1.15 from Lengiewicz *et al.*. The contact area between a smooth PDMS sphere (silicone material) and a smooth glass plate is captured by a camera and is visible because the incident light passes through the planar contact while the out-of-contact zone reflects it.

Due to a black layer at the specimen base, which absorbs the light, the contact area appears as black in the images while the non-contact points (the PDMS surface outside the contact or the dispersed particles) appears as brighter zones. The contact images inserted in the figure refers to the initial stage (d_0 in Figure 1.15b) where no shear is applied (left side) and to the point where the peak of the tangential force is reached (d_s, right side). At the beginning, the contact is perfectly circular according to the geometry and to the isotropic characteristic of the specimen. After shearing, the image shows a shrinkage of the contact with a loss of circularity caused a different reduction at the leading and trailing edges of the contact boundary. Beyond these two representative extreme conditions during the shear test, the complete evolution of the contact area A and the friction force Q are shown in Figure 1.15b. As soon as the glass substrate starts moving, the contact area reduces and the friction force increases up to a peak (here indicated by the vertical line at d_s) indicating the end of the transient regime and the beginning of full sliding. At this stage the contact area gets to a minimum and stabilizes at this level even for higher displacements. The oscillations on the contact area observed on the curve are a sign of the reattachment folds, observed in dynamic conditions, at the trailing edge of the contact [19].

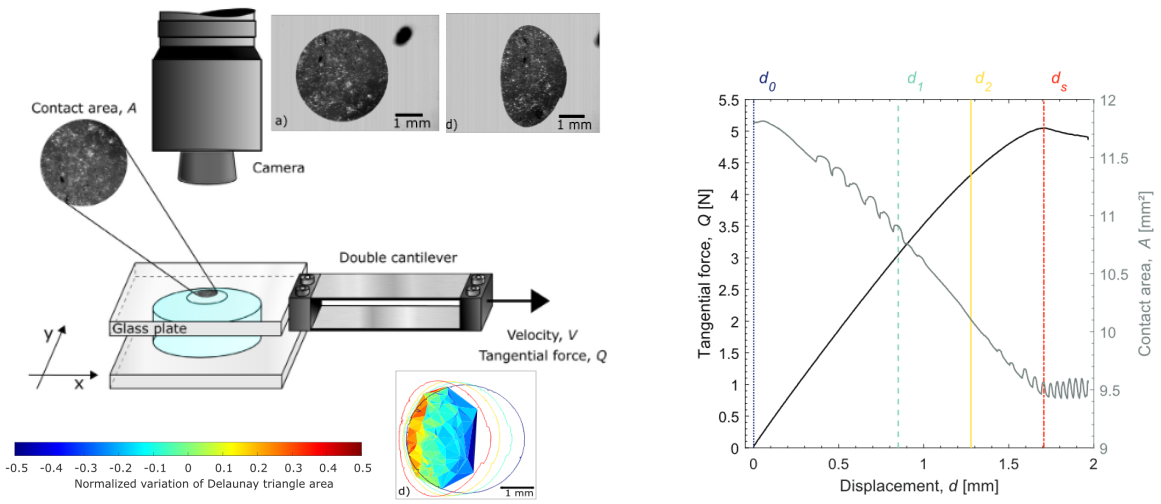

(a) (b)

Figure 1.15: (a) Opto-mechanical device used in the work of Lengiewicz *et al.* [7] for the experimental observation of a contact between a smooth PDMS sphere and a smooth glass plane during a shear experiment. The camera allows to capture images at high resolution and high frequency. The dispersion of particles in a thin film close to the contact permits to have a texture at high contrast used to measure the in-plane strain field (ε_{xx}) in the contact zone by means of particle tracking. The image contains two contact images corresponding to the displacements d_0 and d_s in Figure 1.15b together with the relative measured strain field. (b) Evolution of the tangential force Q (solid black curve on the left axis) and of the contact area A (solid grey curve on the right axis) versus the imposed tangential displacement on the glass substrate. The curve are obtained for a normal load P =1.85 N and for a displacement velocity of v =0.1 mm/s. Images from [7].

The use of dispersed particles near the contact plane allowed to measure the strain field using a tracking procedure where the particle positions where used as nodes for a Delaunay triangulation. The use of these particles was useful to characterise three fundamental mechanisms at the base of the contact deformation: the lifting and laying movement of the PDMS

from and to the PMMA plane and the in-plane strain field. The particles disappeared and appeared during the experiments, which was used to measure, respectively, the amount of lifting and laying area. The measurement of the in-plane strain field (ε_{xx}), conversely, was carried out following the particles always present in the images along the experiment. The change in the area of each mesh element of the triangulation allows indeed to measure the local strain. The strain image shown here refers to the point where the tangential force reach Q_s, *i.e.* the peak value between the incipient sliding regime and full sliding (see Fig. 1.1). At this point, an heterogeneous slip-induced in-plane deformation field is fully developed underlining a large compression zone on the trailing side (cold colors) and a smaller dilation zone on the leading edge (warm colors). The authors found the obtained results in agreement with the field measurement provided, even for a measurement along a central line in the contact, in the work of Barquins [19].

Another relevant experimental investigation aiming at measuring the evolution of the contact area during incipient sliding and the corresponding shear stress related to these mechanisms is found in the work of Chateauminois, Fretigny and Olanier [28]. Differently from the experiment introduced before, the authors performed a torsional friction experiment with a rigid glass sphere in contact with a soft PDMS substrate (the inverse system compared to the experiment presented in the last paragraph) rotating around its symmetry axis to reduce the viscous effects. The specimen was marked, on a layer at a few micro-meters below the surface, by a square network of cylindrical holes obtained by micro-lithography. The obtained typical image of the contact is given in Fig. 1.16a where the the markers and the circular contact area is easily identifiable. The position of the markers was recorded at each step to measure a local displacement field through particle tracking.

The shear stress distribution, derived from the measured displacement field, is shown in Fig. 1.16b at various twist angles during the stiction process, *i.e.* the transition phase between rest and steady-state sliding. At the first angle (a), *i.e.* for low shear, the in-plane shear stress increases monotonically from the contact center to the contact edge until it vanishes rapidly to zero a this position (the contact radius is indicated by the large vertical dotted line). While the imposed angle is increased, *i.e.* increasing shear, the shear stress continues to increase but up to a decreasing radius corresponding to the limit of the adhesive zone. Consequently, a slip zone, that increasingly invades the contact, is characterised by a constant shear stress. The increasing extension of this plateau evidences the invasion of a slip zone through the adhesive zone until the entire contact area enter in a full sliding regime. Differently from the shear stress shape shown in Fig. 1.10, the shear stress in the slip zone does not appear with a bell-shape in the slip zone (due to the proportionality between shear stress and normal pressure for the Hertzian contact type) but a constant value which is more in agreement with the prediction of Savkoor [23].

Finally, the above mentioned experimental devices have some advantages and limitations that we can list below. Regarding the advantages of optical observation of a contact, we can say that:

- it allows an *in situ* and *in operando* observation of the contact;
- the contact area measurement can be done dynamically thanks to high-speed cameras. This can be very useful to see for example visco-elastic effects and to collect more data points during an experiment;

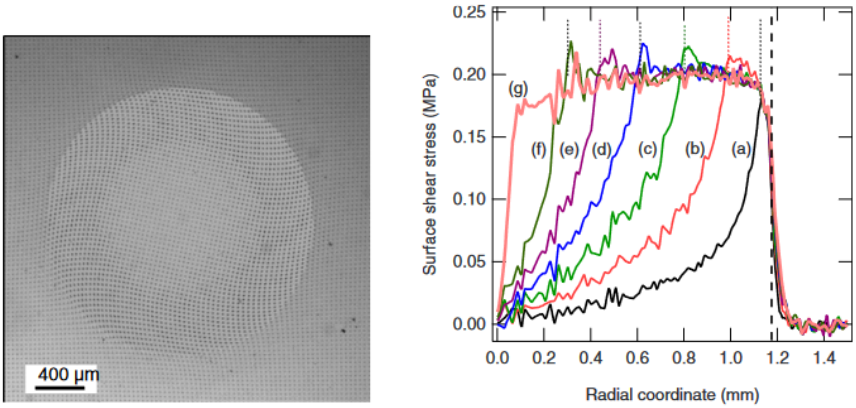

(a) (b)

Figure 1.16: (a) Image of the contact between a rigid glass sphere and a smooth elastic PDMS planar substrate during incipient sliding. (b) Ortoradial surface shear stress profiles derived from the measured displacement field during different stages (from right to left the applied twist angle is increasing). The large black dotted line underline the limit of the contact area. Images from [28].

- the contact images can be very detailed with the use of high-resolution cameras;
- tests can be both very rapid and very slow so that a vast range of displacement speed can be tested on a tribological experiment.

Concerning the limits, we can conversely assert that:

- the measurement of the contact area is bi-dimensional and requires that at least one of the two bodies in contact is optically transparent (limiting the number of materials that can be analysed);
- in the first experiment the measurement of in-plane strain field is possible only inside the contact area, no information is available outside of it;
- the second experiment allows to measures the shear stress even close the contact edge but the presence of holes on the contact surface could also affect the mechanical properties of the interface.

1.2.5 Beyond the limits of optical transparency: X-ray Computed Tomography

Principles of the technique

X-ray Computed Tomography (XRCT in the following) is an experimental technique allowing to image an object and its internal details in three dimensions (3D). In the past years, this technique has seen a growing interest thanks to its non-destructive way to analyse the internal structure of materials down to length scales of a few tens of nanometers. It is therefore well suited to examine samples that cannot be sectioned and to perform *in situ* tests with a 3D observations inside a material under an external loading.

A CT scanner is composed, basically, of three components: the X-ray source, the X-ray detector and the sample stage as shown in Fig. 1.17. In the case of a small specimen (for example in the field of materials research) the object rotates about a rotation axis while the X-ray source and the detector are kept fixed in the lab frame. The X-ray source can be an X-ray tube or a synchrotron storage ring. In both cases, X-rays are obtained by accelerating electrons. Because synchrotron facilities are more expensive and less accessible, X-ray tubes are the main source for laboratory CT. These tubes are characterised by a polychromatic cone beam and the X-ray energy is controlled by the electron accelerating voltage. Due to the solid angle created by the cone, the magnification is controlled by moving the sample at different positions between the source and the detector. Thus, the limit in term of resolution depends on the size of the specimen.

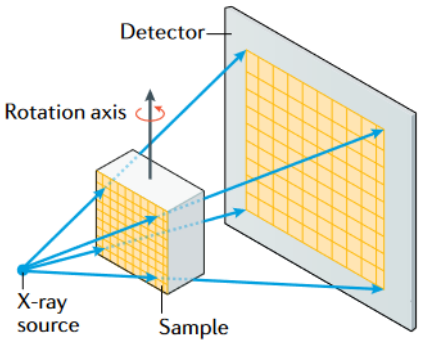

Figure 1.17: Layout of a laboratory X-ray tomograph. The device is composed by a X-ray source (conical beam), the analysed sample installed on a rotation axis and a detector. Image from [32].

Once the object is correctly positioned to adjust magnification and the voltage is correctly set to adapt the image contrast to the analysed materials, a CT scan can start. Image 1.18 illustrates the process of radiographs acquisitions and image reconstruction (for simplicity, the procedure is illustrated with a parallel X-ray beam rather corresponding to synchrotron X-ray sources). During the acquisition process the sample is rotated about the rotation axis while subsequent radiographs are acquired. When a sample is illuminated by the X-ray beam, a contrast image is reproduced on the detector as a function of the attenuation of the beam after its propagation through the sample. Basically, the intensity of the beam when it hits the detector is determined by the line integral of the attenuation encountered on its path through the specimen. Considering n materials in the object, the transmitted intensity I decreases exponentially with respect to the original intensity I_0, according to the Beer-Lambert's law:

$$I = I_0 \exp\left(-\sum_{i=1}^{n} \beta_i x_i\right) \tag{1.19}$$

with β_i being the linear attenuation coefficient and x_i the path length of the material i through the sample. In addition to a sufficient spacial resolution, the materials require different atomic number to clearly detect one from the others. According to equation 1.19, the detector measures an attenuation profile for each row of pixels and for each rotation angle. For a given row in the image, we obtain then a sinogram showing how the attenuation varies as a function of the orientation θ. In order to obtain the reconstructed 3D image, the back-projection algorithm can be used; the code projects back the line profiles in the sinogram along the angle θ at which

is was recorded and adds these projections to the already projected paths. Finally, what we observe in a slice of a 3D reconstructed volume is a map of $\beta(x, y, z)$. With this technique, the gray-level is different from 0 even where there is no mass and this introduces blurring in the image. Filtered back-projection avoid this problem by adding a filter during the projections (a ramp filter). While in parallel beam each row of pixels can be reconstructed separately, in cone beams the problems is more complicated as the absorption of each (x, y, z) point in the sample brings a contribution in the absorption profile for several rows on the detector. To account for the contribution of these different rows in each voxel, different algorithms can be adopted like the Katsevich algorithm [33]. The quality of the reconstructed image depends also on the number of projections collected, *i.e.* the angular step for each radiograph. A general rule is that the number of projections should be nearly πq where q is the diameter of the object in pixels. That requires usually a high number of radiographs and, giving that each radiographs requires a given waiting time for the stabilisation of the signal on the detector, a complete scan can requires minutes or even hours. During this period, we should ensure that the body is not moving or relaxing to avoid blurring. This means that one big limit of this technique is that dynamic analysis can not be easily achieved with standard laboratory X-ray sources.

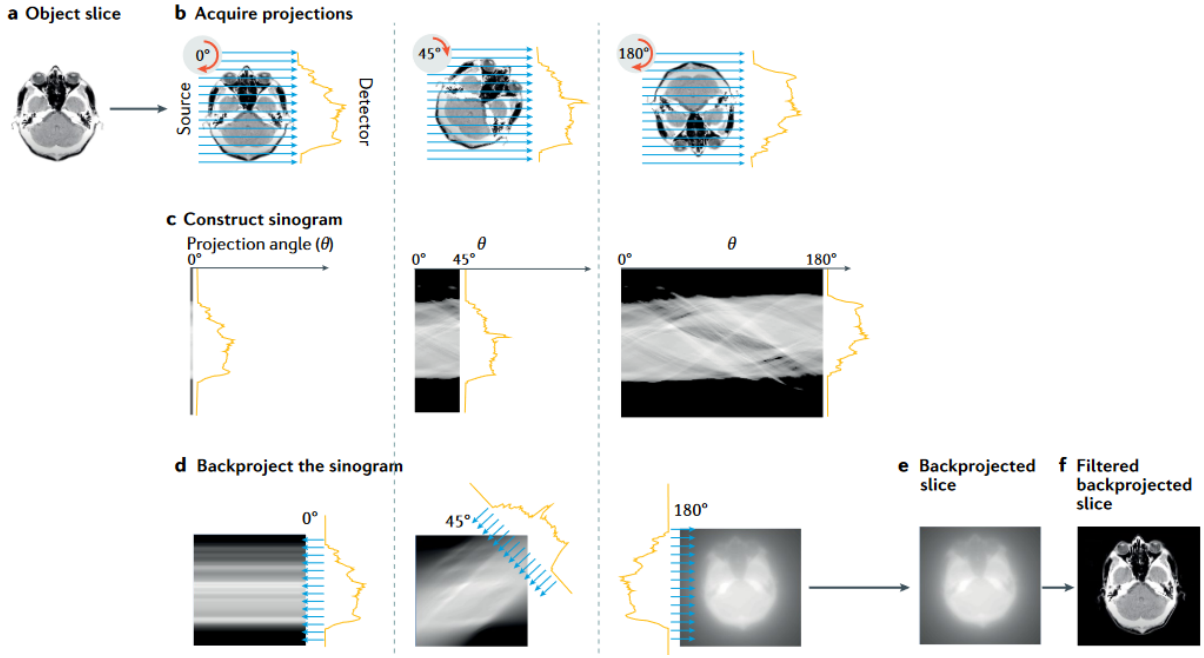

Figure 1.18: (a) Original object slice. (b) Acquisition of projections at different orientations. (c) Sinogram as a function of the rotation angle. (d) Process of back-projection alghoritm. (e) Backprojected image. (f) Backprojected image after application of the filter. Image from [32].

Depending on the settings of the X-ray beam or the material and/or geometrical properties of the object, image artefacts can appear in the tomogram and affect the results. It is worth to mention the main ones and explain their origin:

- Beam hardening (Fig. 1.19a). It results in a change in contrast from the center to the edges of materials having an high atomic number. It is observed for scans performed with polychromatic beams as softer radiation are absorbed more in the center rather than in the edges. This phenomenon can be minimized by using filters reducing the low energy X-rays;

- Limited projection artefacts (Fig. 1.19b). It arises when the number of radiographs is not sufficient and appears as straight lines starting from the object's boundary;
- Partial volume effect. It is found at the interface between two materials as the finite size of the interfacial voxel can take an intermediate gray-level value between that of each material on the two sides of the boundary. It makes the edge detection more difficult;
- Streaking artefacts (Fig. 1.19c). It is due to high-density objects that cause photon starvation.

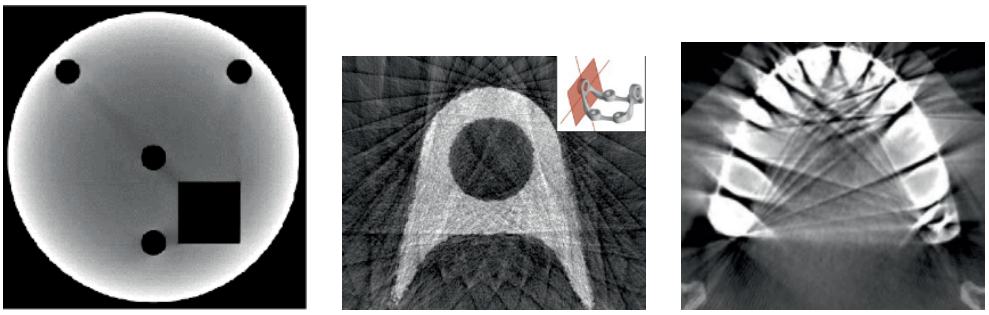

(a) (b) (c)

Figure 1.19: Examples of common XRCT artifacts. (a) Beam hardening artifact. (b) Limited projection artifact. (c) Streak artifact. Images from [32].

In Situ experiments with X-ray Computed Tomography

Nowadays XRCT is not only used to analyse the materials in a non-destructive way (*e.g.* seeing precipitates, cracks, phases etc.) but also to carry out *in situ* mechanical tests such as fatigue, tensile, compression or bending tests (allowing to see the nucleation and propagation of cracks or defects in the materials), which can be performed under (low or high) temperature. All of them require a dedicated experimental set-up installed on the rotating stage of the tomograph so that a scan can be performed during the test without removing the specimen from the testing device and thus keeping the applied load.

In the work of Buffiere *et al.* [34] we can find a review of some existing *in situ* devices for XRCT. For simplicity, we will focus on one of these examples. Fig. 1.20a shows a fatigue tensile test for XRCT. Generally these types of mechanical machines are composed of a load cell in the upper part and a motorized stage to apply the load in the lower one (in the present case the alternating load is generated by an elliptical rotating cam transmitting the load through a cantilever). The two parts of the machine are connected by means of a PMMA cylindrical tube. The latter avoids important X-ray attenuation but is limited in terms of maximum transmitted force (for high-force applications steel or composite tubes are used). The presence of this tube limit, for a conical beam, the image resolution because it sets a minimum distance at which the machine can be placed near the X-ray source. After a given number of cycles, obtained reconstructed images can be segmented to distinguish the different phases inside the material and detect the presence of crack growing during the test. Fig. 1.20b shows an example of segmentation and rendering of a crack after a given amount of loading cycles. In this way cracks can be measured in 3D, giving access to many geometrical characteristics like surface extension, growing direction etc. Clearly, due to the fact that the body must not evolve during

a scan, experiments should be developed step-by-step: after each step (such as an increment of loading, number of cycles or temperature) the experiment is stopped while a scan is recorded. This also limits the type of materials that can be used in order to avoid significant relaxation during the scan and the corresponding image blurring.

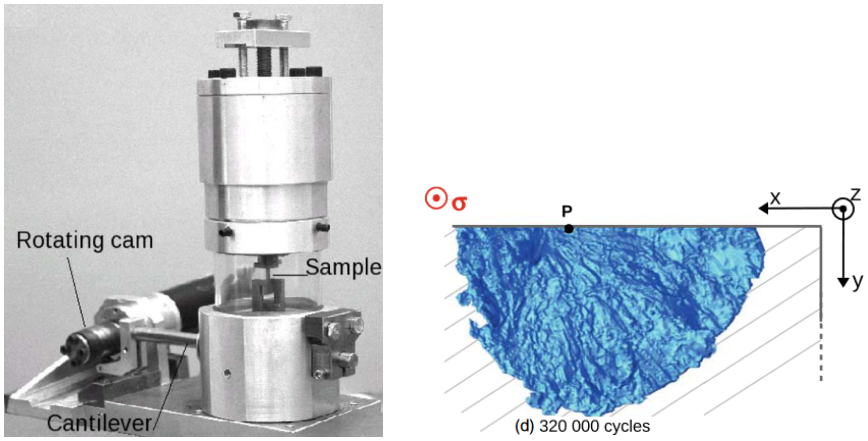

(a) (b)

Figure 1.20: (a) Photo of a cyclic tension/tension device. Loading is applied through a cantilever and an elliptical rotating cam. The closed shape of the device is characterised by a PMMA tube that transmits the load between the top and the bottom of the machine avoiding any X-ray beam screening. (b) 3D rendering of a crack growing during a fatigue test inside a cast aluminium alloy. Images from [34].

Thanks to the adoption of an *in situ* test, if some markers are positioned inside the materials or if a natural pattern is observable inside the bulk, post-processing techniques can be applied to measure the internal displacement field in the 3D reconstructed object. It is usually needed to ensure that the markers can be easily detected in the acquired images and that they do not move too much between consecutive images. In the case of 3D tomography volumes, Particle Tracking or Digital Volume Correlation (DVC) can be used. In the framework of this study only the second one will be presented to point out the main logic of the measurement technique.

Image correlation: the transition from Digital Image Correlation (DIC) to Digital Volume Correlation (DVC)

Starting from a sequence of images taken on an object characterised by a visible natural or artificial pattern, the Digital Image Correlation or DIC is a technique that allows to measure the displacement field between two subsequent images. Applied to mechanical problems, it allows to find the displacement field that matches the deformed state to the reference one. One of the first attempt consisted in dividing the image in small subsets and to find the same subset in the deformed image [35]. This is the so-called *local method*. Let us consider a schematic representation as in Fig. 1.21 showing how a considered subset (bounded by the edges of one element in the chosen square mesh) is deformed under the application of a mechanical loading. In this example the objective is to follow the displacement of the central point $P(x_0, y_0)$. The choice of a square pattern is considered to have a wider variation in gray levels inside a given subset: this would more easily guarantee the distinction of this subset in the deformed image rather than considering a single pixel. Evaluating the displacement of point P consists in finding the position of the element surrounding the point in the deformed image. To evaluate

the subset displacement, a cross-correlation criterion or sum-squared difference correlation could be adopted. Then, the new position P' is determined searching for the position of the peak in the distribution of the correlation coefficient in the subset. One of the limits of this method relies in the fact that only one displacement vector is determined for each subset and that the access to the full displacement field can be obtained by interpolating all the solutions between the subsets. If the body movement is characterised by a simple rigid body motion, then only the information about the central point P would be sufficient. However, this is not usually the case and a local strain can be estimated by looking on how the observed zone is deforming between the first and the second image. Assuming that the neighbours of point P in the present subset should be found also in the target subset, the position of point Q can be determined using the shape functions or displacement mapping functions.

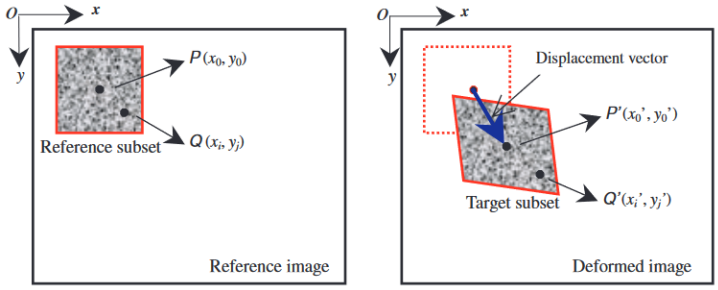

Figure 1.21: Illustration of the deformation of an image subset and the corresponding measured local displacement. Image from [36].

The necessity of having access to the local strain field and to have a better full field displacement measurement has brought, later, to the *global method* which uses the whole image and a geometrical mesh as in Finite Element Methods (FEM) [37]. This method is illustrated and compared to the *local method* in Figure 1.22. This new method uses the whole image to measure the displacement field at the nodes of the finite element mesh, which can be interpolated anywhere in the elements with the appropriate shape functions. Consequently, here the elements are all connected together (which was not the case with the use of subsets). The solution of the displacement at each node is also influenced by the neighbouring elements and the final measurement results are more accurate. When using shape functions the displacement field $u(x)$ can be described as

$$u(x) = \sum N_i(x) u_i \tag{1.20}$$

where u_i is the node value and N_i stands for the element shape function.

The correlation criterion can be described as follows. Having two consecutive images characterised by two gray levels, respectively of $f(x)$ and $g(x)$, with the second image representing the deformed body under the application of displacement field $u(x)$, the DIC numerically finds $u(x)$. The relationship, called equation of the optical flow, between the two gray-levels can be defined as

$$f(x) = g(x + u(x)) \tag{1.21}$$

and the least square method is used to find the displacement field that minimises the residual on the studied domain Ω given by

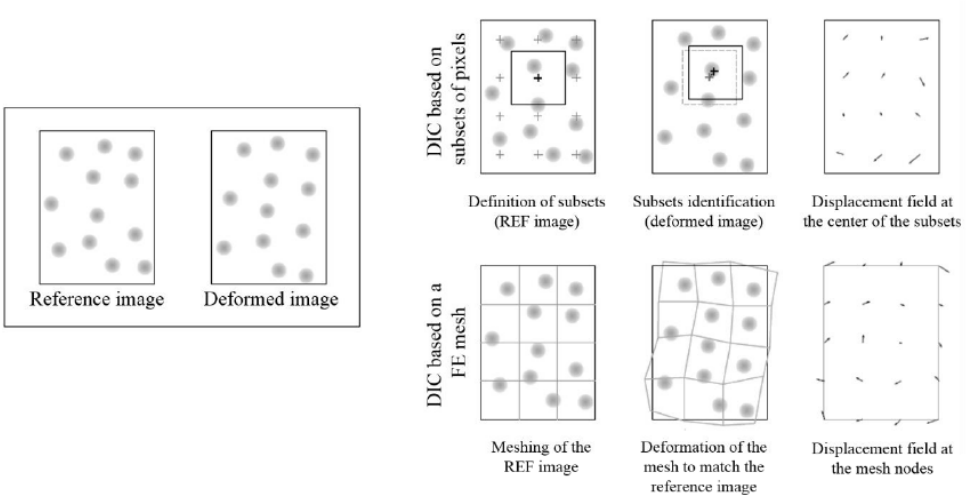

Figure 1.22: Schematic representation of two different approaches for Digital Image Correlation: the *local method* based on subset divisions and the *global method* which uses finite element meshing with the implementation of shape functions. Image from [38].

$$\Phi^2(u) = \frac{1}{2}\int_\Omega [f(x) - g(x + u(x))]^2 \, d\Omega \tag{1.22}$$

The solution of this problem is commonly obtained with a Newton-Raphson algorithm. If du is a small variation of u, the Taylor expansion up the first order gives:

$$g(x + u + du) = g(x + u) + du \cdot \nabla g(x + u) \tag{1.23}$$

The equation for the residual to minimize becomes:

$$\Phi^2(u) = \frac{1}{2}\int_\Omega [f(x) - g(x + u) - du \cdot \nabla g(x + u)]^2 \, d\Omega \tag{1.24}$$

In this formulation, the equation of the optical flow is in simplest way, as considering that no external noise is introduced between the two images and that a material point keeps the same luminescence (or gray-level) during its displacement. More recently, the method has been also applied to 3D images produced by XRCT and becomes the Digital Volume Correlation (DVC) technique [39, 40]. In the case of a DVC, the correlation techniques requires 3D images to present a three-dimensional pattern that can be obtained, for example, with second phase particles such as precipitates or artificially added powder particles. An example about the capabilities of DVC is depicted in Fig. 1.23 where a representation of the displacement and strain field is shown, in 3D, for a sample loaded in three point bending.
DVC starts with a 3D rendered image and the choice of a Region Of Interest (ROI) corresponding to the zone where the displacement values are searched. As for 2D images, a 3D mesh must be built and overlaid to the ROI to divide the volume in a given amount of sub-regions (typically cubic elements) where the nodes will be the displacement measurement points. Accordingly, the relative movement of these nodes for a given cell, will provide the measurement of the local strain that, differently from the displacement field, will be measured at the cell level and will be characterised by the 6 components of the symmetric strain tensor. Once the observation mesh is ready, the computation can start under the constraints that small displacements and deformations appear in between one image and the next one. For example, if the

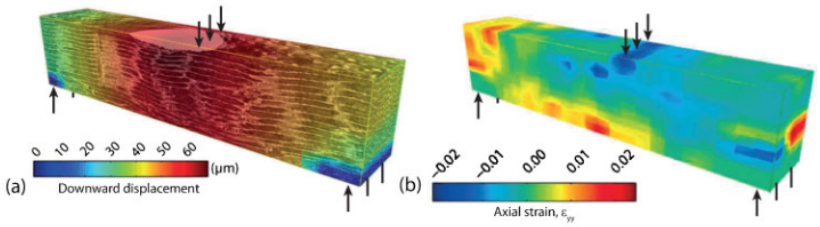

Figure 1.23: Vertical displacement field and corresponding 3D axial strain field for a Scots pine sample loaded in three point bending. Image from [41].

digital image contains discontinuities or abrupt changes in the average gray-level (for example in the presence of cracks or holes) the correlation may fail or provide an inaccurate displacement field that will be propagated in the following steps. For this reason, the ROI should be searched on an internal zone where the average gray-level keeps constant during all steps and where we expect not to see opening cracks or holes. Consequently, this requires an attentive ROI drawing and a pre-processing of the images in order to adjust contrast and avoid huge fluctuations of the gray-level between each step. Generally, in order to obtain a good image or volume correlation, the following aspects should be carefully considered [36]:

- *speckle pattern*: this is the most important aspect. A good speckle pattern is easily related to a good image correlation. A dense dispersion of markers allows to identify more easily the position of the deformed subset. Then, the mesh element could be smaller and will provide a more detailed evaluation of the sample deformation;
- *image noise*: this is related to the fluctuations of the gray-level between one image and the next. The standard deviation of the gray-level distribution should be reduced by means of image processing;
- *element size*: the size of the mesh element should be large enough so that there is a sufficient number of identification markers that will simplify the correlation and reduce the computation of residual. Conversely, the element size should be as small as possible because a smaller element can be easily approximated by a first-order or second-order shape function while a big one may lead to larger errors in the evaluation of its deformation;
- *image contrast*: this should be increased by image processing and/or by the choice of good markers with a sufficient contrast with respect to the bulk. This can be obtained with second phase particles with a different atomic number compared to the matrix for tomography volumes.

The access to the displacement field can open to different mechanical measurements and material properties like Young's modulus, Poisson's ratio, stress intensity factor, residual stress and thermal expansion. This measurement can also be very useful to compare the results with FEM simulations in order to validate models and experiments and to have a more general look at the deformation mechanism of a loaded object.

In the case of high strains inside the observed portion of the body, there could be a risk to incur in a fail of the correlation. This can happens, for example, when dealing with materials having low elastic modulus (like polymers) that can undergo large deformations. Hild *et al.* [42] tried to adopt a multiscale approach to overcome the difficulties of image correlation of

high-compressed mineral-wool samples. With this method the full displacement field is estimated on a coarse resolution first and then, progressively, on higher resolutions. While this technique enabled to reach convergence on high-deformed samples, it is not possible to correlate images with deformations higher than 20 % between two images. For very high strains, in fact, some incremental methods have been developed [43, 44] where the deformed image at a given step n is used as a reference image for the step $n + 1$. Figure 1.24 illustrates this DVC methodology for a compressed sample. Between the first and the second step a conventional DVC is adopted while, from the second to the last the reference image is updated with the measured displacement field from the previous step and used as a reference for the successive step. This method, which allows to avoid high deformations between two consecutive steps, hides a problem: the process of updating the reference image will introduce and accumulate the error of measurement between each step. In fact, the displacement at the step n is the sum of the displacement measured for each previous step. This problem is sometimes avoided adopting a so-called "preconditioned" scheme, where the updating of the reference image is used only when a serious decorrelation is present. This is possible with the use of a tracker (or seed point) and a threshold value defined by the user over which, the tracker displacement is too high to define a status where the incremental correlation is started. In this way it is possible to minimize the number of updating steps and the accumulation of errors.

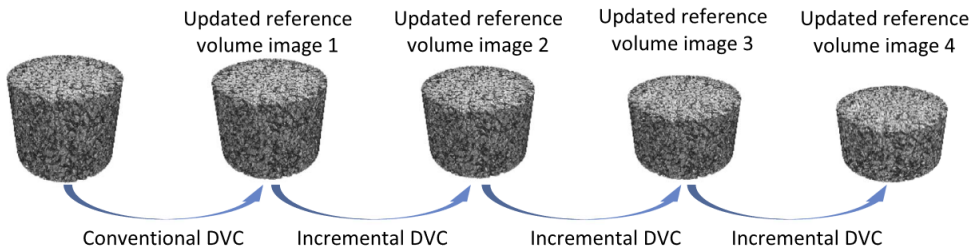

Figure 1.24: Schematic illustration of the incremental method for the image correlation of highly deformed samples undergoing high displacement and strains. Image from [44].

To conclude, DVC gives access to the 3D displacement field in the bulk of the deforming material, compared to the 2D field provided by DIC on 2D images at the surface of the sample. Consequently, all components of the 3D strain field can be computed. It is therefore a promising technique to fully take advantage of 3D tomography images in the framework of *in situ* experiments.

1.2.6 The use of XRCT for contact mechanics and surface analysis

Despite the huge use of XRCT for material science, only a few studies were found in literature where this experimental technique is implemented for contact analysis.

First, in the works of Zhang *et al.* [45, 46], they used XRCT to analyse aluminium or polycarbonate contact pairs between patterned (anisotropic and isotropic) surfaces manufactured by turning, knurling and milling. Their experiments consisted in imaging a planar-rough contact under pure normal load applied through a specially designed compressing device installed into a tomograph. After the application of each load and image acquisition, the real contact area and surface separation were measured with a voxel edge size of 2 μm. Thanks to the use of FEM calculations based on the same surface topographies, they found a very good agreement

between the obtained measurements of A_R and the results obtained from numerical simulations. The method used to detect the surface coordinates (and hence the surface separations) is based on stereolithography, a computed-aided design model used to describe the external surfaces of objects. An example of the obtained result is shown in Fig. 1.25a. In this image, the triangulation of the upper surface is underlined with red lines while that of the lower surface with blue lines. Due to the fact that the same material is in contact, it is not possible to distinguish the boundary between the two materials in the contact zone (see section view A in the image). Caused by this difficulty the contact area is found in the following way. First, they defined a grid of nodes in the $(x, y, 0)$ plane (normal to the direction of the applied load). Second, for each coordinate in this plane, the z coordinate is increased progressively and if the nodes, during this movement, does not hit any nodes of the upper or lower surface, it means that this node is in the contact region. In this way, they obtained a detailed description of the error evaluation of the surface gaps and an high-quality surface reconstruction and contact visualisation. However, a contact area measurement obtained like that could hide a possible error. Indeed, especially for rough-rough contact, the contact plane can take any orientation and a projection can underestimate the contact area. Furthermore, the study does not point out a way to determine the contact boundaries for materials having different densities and, then, different contrast. In other words, the detection of the contact boundary for different materials may be more complicated and may require more considerations on the segmentation algorithms and on the partial volume effect. The latter could indeed indeed tend to blur the contact boundary because of interfacial voxels taking intermediate gray values between those of the two materials.

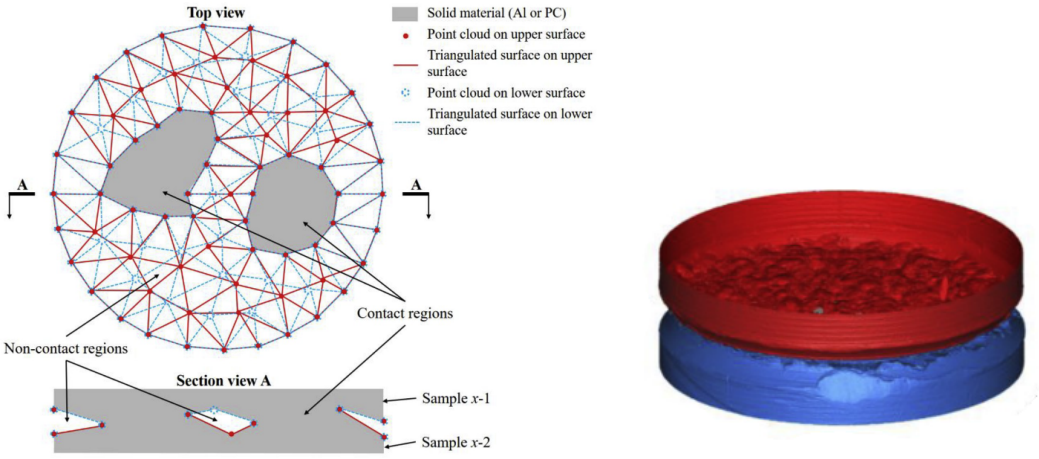

(a) (b)

Figure 1.25: (a) Sketch of the stereolithograpy model used in the work of Zhang *et al.* for the determination of the contact separation and area. (b) 3D representation of the contact between two rough surface obtained by stereolithography. Images from [46].

Another relevant study in that field is found in Kriston *et al.* [47] with, in this case, a contact between different materials. Figure 1.26 shows examples of the contact pairs used in that work: a rough rubber specimen in contact with sandpaper, a planar plastic body and snow. This image represents a slice of the 3D reconstructed volume from tomography. A compressing machine was used to keep the bodies in contact at constant normal load during the scan. The image resolution ranged between 2.05 and 28 µm/pixel. The image segmentation was implemented by applying the Otsu method [48] for each of the three/four materials in the image:

materials are thresholded separately and finally joined in a single final segmented volume. The determination of the contact area is defined as the number of voxels where two different segmented zones show connectivity; in other words, where the euclidean distance between two different materials is 0. The article then analyses in details the effects of the scanning parameters and image filtering on the quality of the image (signal-to-noise ratio) and the average gray-level of the materials in contact. As important remarks they observed that:

- a full rotation scan results in improved contrast and homogeneisation of the phases;
- an optimisation acceleration voltage for the X-ray beam should be found for each contact pair but A_R shows little variation with a voltage changing from its optimum;
- when filtering the image with a median or a patch-based method two changing results can be obtained. The first sets the pixel value as the median of the surrounding pixels. This filter improves the signal-to-noise ratio (but boundaries become less sharp) and could create artifacts such as fake contact points that increases the contact area. The second filter, instead, searches for similar types of pixels in a given area and preserves phase boundary contrast.

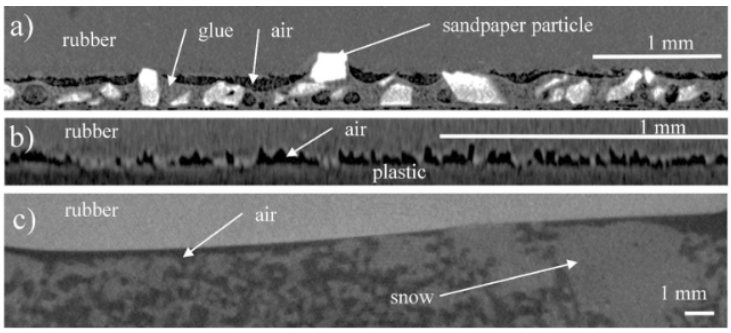

Figure 1.26: Example of contact pairs in the work of Kriston *et al.*, slices of 3D tomograms. (a) rubber-sandpaper. (b) rubber-plastic. (c) rubber-snow. Image from [47].

The last work, from Aleksejev *et al.* [49], presents a study rather focused on wear. In their experiment, two worn aluminium alloy samples (see Fig. 1.26) were put into contact at imposed normal load while a rotation was applied to allow circular sliding between the bodies. After a period of rotation on the mechanical device, a plastic clamping tube was slid over the sample to keep the samples in intimate contact, maintain the load and install the sample inside the tomograph. Indeed, differently from the previous examples, the mechanical device is not installed inside the tomograph but outside it. In this case the image resolution is of $2.47\ \mu\mathrm{m}$/voxel. To obtain the measurement of A_R, the volumes were segmented into a metallic and an air region and, similarly to Zhang *et al.* the contact area was determined as the zones where there was continuity between materials in the direction z (that of the symmetry axis) and no air gap was found. Again, this shows one of the limits of XRCT: the area of contact is not easy to measure for contact between the same material and, hence, having the same gray-level. In this case, only the described methods are possible with a probably smaller detected contact area caused by the fact that the effective edges of the contact zones are not determined.

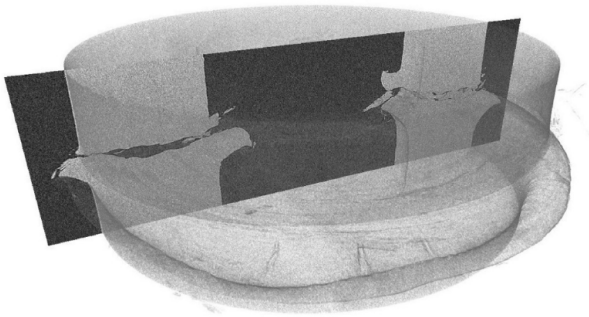

Figure 1.27: Radial cross-section of the aluminium worn sample used in Aleksejev *et al.*. Image from [49].

1.2.7 Motivation of the study and chapters introduction

We have seen, in this introduction, that a critical quantity that controls the mechanical response of a sheared contact interface is the real contact area A_R, usually much smaller than the apparent contact area A_A. Starting from the real contact topography, each micro-contact can be brought to an equivalent sphere-on-plane contact for which theoretical models have been already developed in the last decades. Knowing the body shape and the material properties, the equations provided are able to quantify the area of contact, the surface deformation and the internal stress in the presence (or not) of adhesive forces. A lot of experimental works have seen an important development in the last few years based on the optical observations of the contact zone. Even though they provide a reliable estimation of the contact area and the surface displacement field in dynamic situations, two non-negligible limits are inherent to these experiments: (i) the fact that at least one of the two bodies in contact should be optically transparent and (ii) that only the 2D projected area of contact is available. Consequently, the number of materials that can be analysed is limited and the out-of-plane mechanical fields are unavailable. However, 3D observation of the deformation of the bodies in contact is expected to provide valuable additional information on the mechanisms of contact as observed in 2D.

In this study we aim at overcoming these limits by taking advantage of a 3D non-destructive technique: X-ray Computed Tomography. We have seen how this promising technique allows to access to a lot of information in 3D both inside and on the external surface of the body. Furthermore, the use of dispersed markers can also provide a measurement of the displacement field with sub-voxel resolution. Up to now, only a few studies have tried to use XRCT for contact mechanics analysis. In all of them, the analysis were carried out on already complex surfaces without a preliminary analysis on the limits and the precision of XRCT in determining the contact area and the surface deformation.

The present thesis focuses on the *in situ* contact measurements during normal and/or tangential loading on a model system composed of a smooth PDMS sphere in contact with a rigid and smooth PMMA plane. The choice of these materials and geometries derived from the following requirements:

- at least one of the body in contact must be optically transparent in order to reproduce the same experiment on an optical device and to benchmark the measurement with a well-developed and tested experimental device;

- the choice of a smooth contact must allow us to compare the obtained results with already existing theoretical models for which there are still no observations in 3D and in the bulk of the deformed body;
- the use of a soft material must ensure large contact areas with respect to the image resolution in order to increase the quality of the contact area extraction and to minimize image artefacts that can affect the measurement.
- the choice of PMMA and PDMS must favor high contrast in the XRCT images and also with air to be able to clearly distinguish the two solids in contact.

After this first introductory part, the chapter 2 will consist of a general presentation of the material used and on the sample preparation followed by the description of the optical and the XRCT tribology devices, with details about a newly developed test for *in situ* shearing experiments under tomography. This second chapter will end with a general overview of the data analysis involving image processing, surface displacement measurement and Digital Volume Correlation for the evaluation of the 3D internal displacement, strain and stress fields. The manuscript will then diverge into two chapters with a similar layout but a different focus: chapter 3 is about normal loading experiments while chapter 4 is about shear loading ones. In both cases all the quantities such as A_R, surface deformation and stress fields will be provided with comparison with already existing theoretical models.

2 Experimental Methods

In the previous chapter, we showed the importance to characterise the real contact area A_R and the surface/bulk deformation to understand, in a more general overview, the mechanisms behind the evolution of the friction and normal forces in a contact interface. In order to overcome the limits of optical transparency and the 2D observation of the contact, *in-situ* experiments on a mechanical device installed in a X-ray tomograph are carried out using a model contact system composed of a smooth spherical PDMS sample in contact with a rigid and smooth PMMA plane.

Thus, this chapter introduces in detail (i) the mechanical device used with XRCT for normal loading and an adaptation for the application of a shear displacement, (ii) the sample preparation according to the geometrical limits of XRCT, (iii) the optical device for the characterisation of the mechanical properties of the samples and the comparison with XRCT measurements, (iv) the post-processing techniques that allowed us to access the contact area like image processing, segmentation, surface fitting etc. and, finally, (v) how we implemented an already developed code for Digital Volume Correlation to our special case in order to measure the bulk displacement and strain field.

2.1 *In situ* loading devices

The two machines used in this work to deform the contact samples are described in this section. They were developed to fit on the rotating stage of the V-TomeX tomograph available at the Mateis laboratory. The details of the tomograph itself and of the acquisition parameters will be provided in section 2.4.1.

2.1.1 Normal load experiments

The experimental device used for normal loading experiments is shown in Fig. 2.1 and Fig. 2.2. This machine, commonly used in the lab to perform *in situ* tensile or compression test in the tomographs, has been only slightly adapted to insert the contact samples and perform the contact experiments under normal loading. It is composed of a moving linear stage installed at the base. Thanks to a sloped ramp of 18° the horizontal movement of the motor is transformed into a vertical movement used to carry out tensile or compression experiments on the investigated specimens. The sample is connected to the motor through a vertical steel rod with a circular thread used for easy installation of the specimens. On the upper side, a 200 N

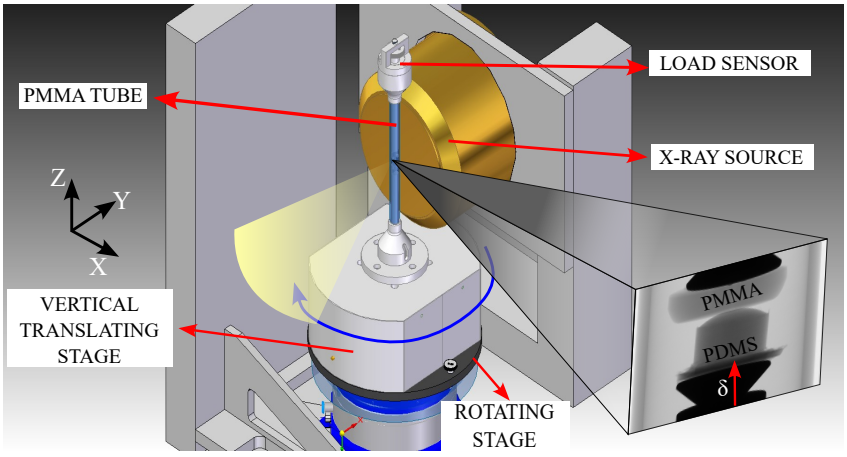

Figure 2.1: Schematic representation of the experimental device installed in the tomograph. The two bodies in contact are installed inside the device where a vertical displacement can be imposed through a motorized stage (not visible here). The X-ray source generates an X-ray beam to which the two materials are exposed. While the exposure is kept on, the entire devices rotates by means of a rotating stage. During the 360° rotation a detector collects a series of radiographs (one of them is shown in the lower right corner) at different angles. In the shown configuration the PMMA is fixed and connected to the load sensor, while the PDMS is connected to the vertical translating motor.

load sensor (U9B, HBM) with a sensitivity of $8\ \mathrm{mN}$ is installed on the top of the PMMA tube and connected to another steel rod also equipped with a circular thread for installation.

The PMMA tube (external diameter $30\ \mathrm{mm}$ and internal diameter of $26\ \mathrm{mm}$) enclosing the two rods connects the upper and lower parts of the system and allows the transmission of the forces to the installed samples while avoiding too much X-ray absorption. The base of the machine with the motorized stage is installed first on a 4-axes stage allowing a displacement of the machine in the three directions of space in the tomograph and also allowing the rotation of the whole system about the vertical axis for the acquisition of the radiographs at different angles. The entire system is controlled using an home-made Labview® program that also records the values of the forces (normal and/or tangential) and of the vertical displacement.

2.1.2 Shear Experiments

The experimental configuration described just before did not allow to apply a shear displacement to the contact interface. For this reason, a mechanical adaptation has been designed to be installed onto the upper part of the PMMA tube keeping the remaining part of the device unchanged. The 3D assembly of the shearing device, together with a picture of its installation into the tomograph, is shown in Fig. 2.3. The device is composed of a linear translating stage (M-UMR8.25, Newport™) that is shifted along its working axis with a micrometer head (BM17.25, Newport™) with an accuracy of $10\ \mu\mathrm{m}$. Between the translating stage and the steel rod supporting the upper specimen, a 3-axis load sensor (K3D40-50N, ME MeßSysteme GmbH) is used to measure the normal and shear loading during the experiments with an accuracy of $2\ \mathrm{mN}$. Thanks to the use of two goniometers (M-Gon65-L(U), Newport™) we are able to horizontally align the translating stage (the alignment is made by looking to the radiographs for two orientations of the machine at 0° and 90°).

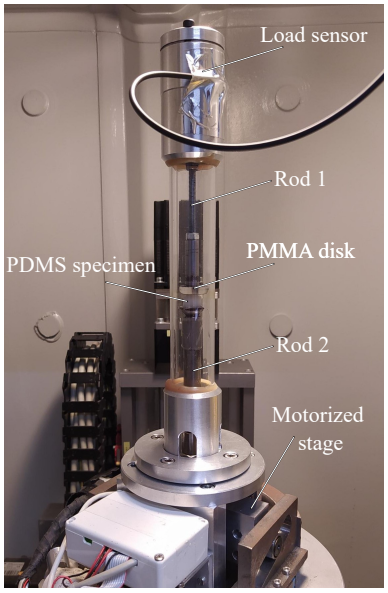

Figure 2.2: Picture of the experimental setup used for normal load experiments. The PDMS sample is connected to a moving stage through the lower rod while the PMMA is linked to the load sensor by means of the upper rod. The whole device is enclosed into a PMMA tube for the transmission of the forces.

2.2 Samples

2.2.1 Design of the sample shape

Fig. 2.4a shows a picture of the typical sample used in this study. To reproduce sphere-on-plane experiments, we started from the shape of an already used specimen in a previous study [7] (see Fig. 2.4b) and we adapted this sample to comply with our objectives and to the geometrical limits of the used experimental device. The PDMS specimen is characterised by a cylindrical base (diameter of $12\ \mathrm{mm}$) surmounted by a spherical cup (radius of curvature $R = 9.42\ \mathrm{mm}$).
The total height of the specimen can be adjusted and in this example is shown in the case of an height of $9\ \mathrm{mm}$. To avoid boundary effects coming from the base of the PDMS sample, some works [50] had underlined that the thickness of the bulk beside the contact zone should be nearly 10 times the contact radius a. In our experiment, we expect a to be of the order of $1\ \mathrm{mm}$, leading to a bulk thickness of nearly $1\ \mathrm{cm}$. However, differently from the work of Lengiewicz *et al.* [7], in the present case the specimen must be installed in the PMMA tube of the compressing machine having an internal diameter of $26\ \mathrm{mm}$. This clearly limits the size of the surrounding part from the curved zone with respect to the example in Fig. 2.4b. In order to guarantee a sufficient clearance of our sample from the tube walls (especially in the case of shearing experiments), we decided to crop our sample to the diameter of the glass lens used for the moulding which is $12\ \mathrm{mm}$.
Because the smooth spherical surface is obtained by moulding the PDMS over a smooth concave glasse lens and, based on previously done experiments, the choice of a radius of curvature of $R = 9.42\ \mathrm{mm}$ (among the commercially available lenses) allowed to obtain a contact radius sufficiently big for our image resolution (in the order of 1-2 mm) applying small normal forces in the (1-2 N). This contact radius together with the size of the radius of curvature consented also to respect the assumption, used in the theoretical models, for which a should be much

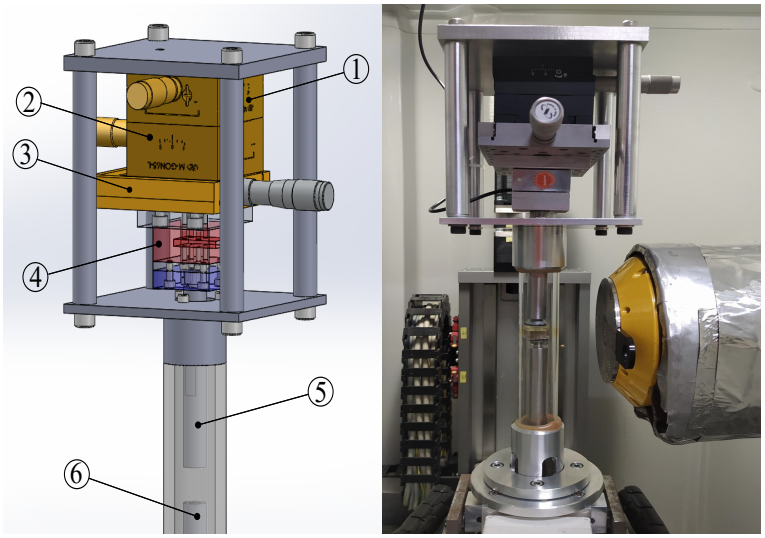

(a) (b)

Figure 2.3: (a) Assembly of the designed shear device: (1) Goniometer M-GON65-U (Newport™), (2) Goniometer M-GON65-L (Newport™), (3) Linear translating stage M-UMR8.25 (Newport™) with a micrometric head (BM17.25, Newport™), (4) 3-axis load sensor K3D40-50N (ME MeßSysteme GmbH), (5) upper rod for PMMA holding, (6) lower rod for PDMS holding. (b) Picture of the device installed into the tomograph.

smaller than R.

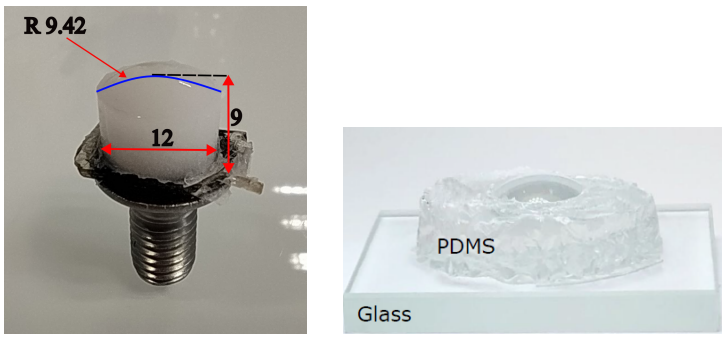

(a) (b)

Figure 2.4: Pictures of: (a) typical sample used in the present study and (b) sample used in the work of Lengiewicz *et al.* [7].

In order to measure the displacement field with DVC, and in the absence of a natural 3D pattern in the PDMS, some particles are also dispersed in the bulk to have good contrast with the matrix. To avoid that these dispersed particles are present into the contact and to ensure a smooth contact, an external PDMS film is embedded on the surface of the sample.

In the present study, two types of specimen are used, characterised by two different heights. The first one has an height of 9 mm that will be indicated, in the next, as **A**. The second is 6 mm tall and will be labelled with **B**. In the next section we detail the preparation procedure of the sample.

2.2.2 Sample preparation

Glass lens cleaning

Before the molding process, the glass lenses ($9.42\ \mathrm{mm}$ radius of curvature, model 45-014, Edmund Optics ®) are firstly cleaned in an ultrasonic bath with three different baths (each step lasts 15 minutes): 1) soapy water (∼5% of Decon 90 in water), 2) ethanol, 3) distilled water. Between each bath, the lens is rinsed with distilled water to avoid contamination. This careful cleaning is made to ensure a clean glass lens, removing also the probable presence of PDMS from precedent reticulations. The choice of this type of glass lens is made to obtain a smooth PDMS surface after molding, as the glass roughness is several order of magnitude lower than the typical size of the curvature radius.

PDMS preparation

The PDMS material used for our sample is a Sylgard 184 silicone (®™Dow Corning) that is largely used for tribological experiments due to its low Young's modulus, large toughness, good chemical resistance and, of course, its optical transparency [51] that allows to easily access the contact zone with optical devices. Despite its large use in contact mechanics experiments for its transparency, the use of dispersed particles, in the present study, erases this characteristics but we decide to adopt this material for its low modulus, its interesting adhesive properties and for the facility of the moulding process. Sylgard 184 is provided as a two-part liquid component kit composed of a pre-polymer base and a curing agent that can be mixed with different ratios to get a target Young's modulus. We adopt two different mass ratios (base/curing): 20:1 and 10:1 to test the effect of different Young's moduli and surface adhesion energy during our tests. In the following we will add the suffix -**20** or -**10** to refer to the first or the second ratio respectively (*e.g.* A-20 indicates a specimen with a $9\ \mathrm{mm}$ height and characterised by a mixture ratio of 20:1).

First, to prepare the PDMS, the curing and the base are mixed with a rotating spatula at 1000 RPM for 10 minutes. Then, part of the mixture is collected apart for the film preparation while the resting part is mixed with hollow micrometric glass beads (K15, 3M™) previously filtered to an external diameter between $80\ \mu\mathrm{m}$ and $100\ \mu\mathrm{m}$ with a volume fraction of 7.16 %. This type of markers is chosen because it suits very well with the conditions for a good particle tracking for the measurement of displacement. Due to their size, their perfect sphericity and good contrast in the tomogram (we see essentially the air inside the spheres) they are the perfect candidate for an easy identification and labelling of each marker.
Another type of particles composed of silver coated aluminium powder (eConduct Aluminium 202000, Eckart) that is mixed in a volume fraction of 3 % is also tested. This last ones show a better dispersion and creates also a better pattern for the image correlation. To distinguish the two types of specimen with different particles, a third suffix will be added; respectively -**G** for the glass particles and -**A** for the aluminium. Once the particles are added, the compound is then mixed again at 500 RPM for 10 minutes to ensure a an homogeneous distribution. Before the moulding, the mixture is put into a desiccator under vacuum to remove air bubbles that were previously introduced with the mixing.

Figure 2.5 illustrates the sample preparation. Once the material and the lenses are ready, the sample preparation starts with the creation of a PDMS external protective film that avoids the dispersed particles in the bulk to be found at the contact interface. The curved lens (previously

cleaned) is positioned at the base of the sample and a small drop of pure PDMS (without dispersed particles) is put onto the glass surface. Then, the mould is installed inside a spin coater (model SPIN 150, APT GmbH) and rotated at 3000 RPM/s for 30 seconds with an acceleration of 300 RPM/s^2 to allow an homogeneous spread of the PDMS on the glass. Fig. 2.6 illustrates the obtained external film evidenced by two red lines on a slice of a tomogram of a specimen A-10-A. The thickness of this film is estimated to be around $40\ \mu\mathrm{m}$. The mould is positioned inside an oven (Prolabo, Astel) for 10 minutes at $80\ ^\circ\mathrm{C}$ for complete reticulation. Successively, the PDMS mixture is deposited onto the PDMS film to fill the mould and a small piece of microscopy glass is put at the top of the mould to guarantee a planar basis for the sample after reticulation. In this way, the PDMS sample is reticulated directly on the glass base to ensure good adhesion strength during the shear experiment.

The PDMS sample inside the mould and closed with the glass plate is finally placed in a oven for 90 minutes at $80\ ^\circ\mathrm{C}$ to reach complete cross-linking of the PDMS [51]. Choosing such an high temperature and short time allows to obtain an homogeneous dispersion of particles in the bulk. Indeed, as the density of the particles is different from that of the PDMS liquid ($\rho_{PDMS} = 1.03\ \mathrm{g/cm^3}$, $\rho_{K15} = 0.15\ \mathrm{g/cm^3}$, $\rho_{Al} = 3.17\ \mathrm{g/cm^3}$), they may move, while the PDMS remains liquid, respectively upward (far from the glass lens) due to Archimede's thrust for the glass particles and downward due to gravity for the aluminium ones. A rapid cross-linking time has the effect of reducing these effects. To improve even more the homogenisation, the sample is also rotated alternatively upside-down during the reticulation process.

With the aim of applying the tracking procedure present in the thesis of De Souza [4], in some of the samples, we also dispersed some particles in the external film before the application of the spin coating. The presence of such particles aims at allowing to compare the displacement field at the surface measured both with XRCT and optics. These particles are pearlescent pigments based on artificial mica (Symic B001, Eckart) put in the PDMS used for the external film with a weight ratio of 4% and mixed at 500 RPM for 5 minutes with the mixer. If the samples contains this type of particles in the film, we will notice it by the suffix -X. It is important to remark that, for these types of samples, two external films are created to avoid particles in the contact interface: the first one is made of pure PDMS and the second, full of mica particles, is created above the other and with the same procedure. For clarity for the reader, Figure 2.7 summarizes the nomenclature of the PDMS specimens investigated in the present work.

After complete cross-linking of the PDMS, the mould with the sample is kept at room temperature to ensure cooling and it is then de-moulded and glued on a M8 countersunk screw with a cyano-acrylate glue that ensures good adhesion in the range of the acting forces. Thanks to this screw, the specimen is installed into the threaded rod of the *in situ* loading machine. Note that a small piece of black paper is introduced between the glass base of the specimen and the screw to have an absorbing layer necessary for optical experiments (the light passes through the contact area while is reflected on non-contact zones) and guarantee a good contrast between the contact area and the surface (see section 2.3). The resulting PDMS samples show an apparent Young's modulus of $E \simeq 0.7\ \mathrm{MPa}$ or $E \simeq 1.55\ \mathrm{MPa}$ respectively for the mixing ratios of 20:1 and 10:1. Details about the Young's modulus measurement are provided in section 2.3.3. Some examples of the specimens are shown in Fig. 2.8 with different heights and particles.

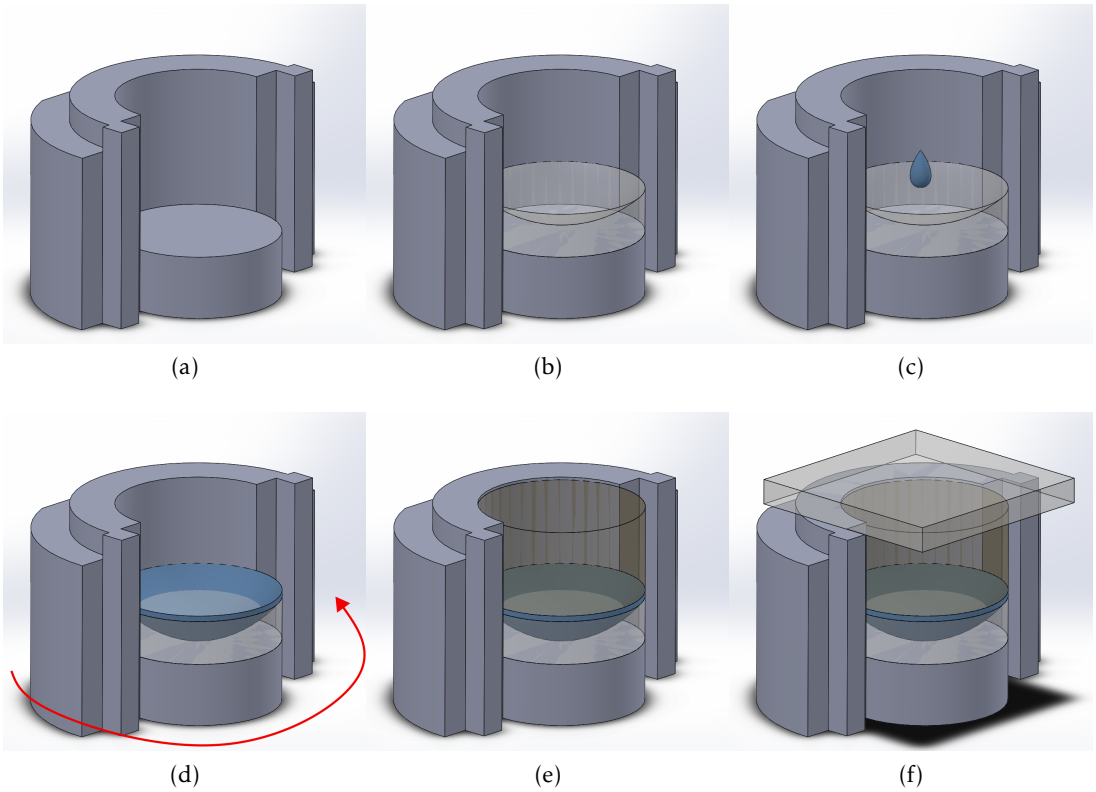

Figure 2.5: Sample preparation. (a) 3D printed mould. (b) A glass lens is positioned at the base of the mould. (c) A drop of pure PDMS is deposited in the lens. (d) The mould is installed into a Spin-Coater to spread the PDMS glass onto the glass surface and then is reticulated at 80 °C. (e) The liquid PDMS mixture filled with particles is then added to fill the mould. (f) A glass miscrope glass plane is added at the top of the surface to obtain a base for the sample after full reticulation.

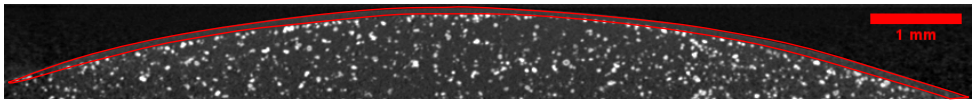

Figure 2.6: Evidence of the external film (red contour) made of pure PDMS empty of particles. The image refers to the specimen A-10-A on a tomography scan cropped along the $X-Z$ central plane.

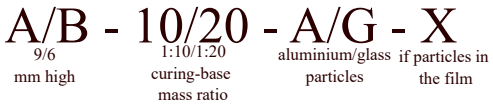

Figure 2.7: Nomenclature of the PDMS specimens

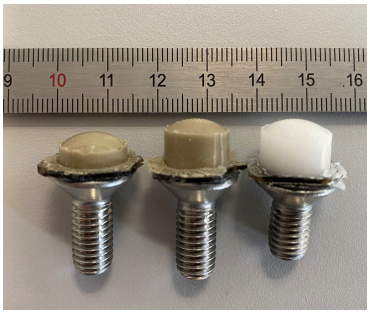

Figure 2.8: Picture of some of the used samples. From left to right a 6 mm high 10:1 PDMS filled with aluminium particles (B-10-A), a 9 mm high 10:1 PDMS filled with aluminium particles (A-10-A) and a 9 mm high 20:1 PDMS filled with glass particles (A-20-G).

2.2.3 Tensile properties of the elaborated PDMS specimens

The characterisation of the obtained PDMS used for the samples of this study is made using an uniaxial tensile machine. 2 mm-thick PDMS sheets are elaborated to cut the tensile samples, with the same compositions and reticulation procedure as described above for the contact samples. Figure 2.9 shows a picture taken during one of these tensile tests in the case of a PDMS filled with aluminium particles and characterised by a curing-base mixing ratio of 1:10. The shape of the samples complies with *ISO527-2-5A* and the uniform gage section is characterised by a width of 4 mm, a thickness of 2 mm and a length of 20 mm. Experiments were conducted with a loading speed of 6 mm/s.

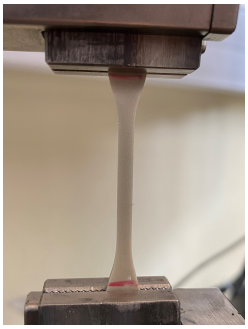

Figure 2.9: Picture of the sample used for the tensile tests (here the PDMS with aluminium particles and a curing-base mixing ratio of 1:10.

Figure 2.10 plots the evolution of the true stress versus the true strain for the three types of PDMS used: the PDMS filled with glass particles having two curing-base ratios of 1:10 and 1:20 and the PDMS filled with aluminium particles with a curing-base ratio of 1:10. The samples are pulled up to failure. The strongest sample is the one filled with aluminium while the weakest is the one filled with glass particles with the 1:20 ratio. The graph on the right of Fig. 2.10 shows a zoom on the initial part of the tensile curve. Here, it is possible to determine the initial (small-strain) elastic modulus of the materials before the subsequent non-linear (hyperelastic) evolution under large deformation. The obtained results for the initial elastic moduli are provided in Table 2.1. Note that these moduli are systematically smaller than the ones obtained with the fit based on contact mechanics law, as will be detailed in section 2.3.3 (Fig. 2.21).

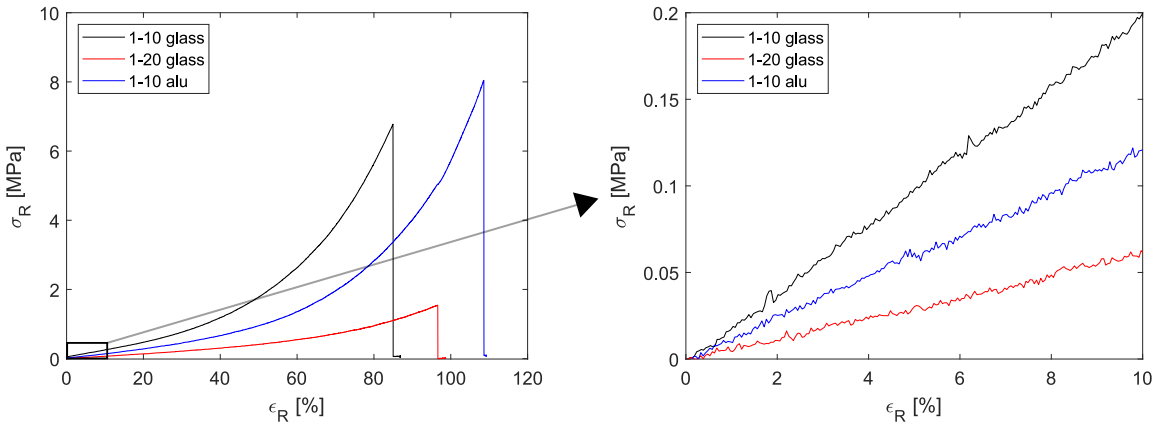

Figure 2.10: Stress strain curves during a unidirectional tensile test applied on the PDMS filled with glass particles having two curing-base ratios of 1:10 and 1:20 and the PDMS filled with aluminium particles with a curing-base ratio of 1:10. Tests are carried out up to failure. The panel on the right represent a magnification over the first part of the graph, at small strain. The loading speed is 6 mm/s.

	$E(MPa)$
1-10 glass	1.989 ± 0.005
1-20 glass	0.613 ± 0.003
1-10 aluminium	1.205 ± 0.004

Table 2.1: Fitted elastic Young's modulus for the three PDMS mixture used.

Previous studies ([7]) showed how, due to high strains reached during shear experiments, hyper-elastic phenomena should not be neglected when analysing the shear response of an elastomer. Furthermore, the evaluation of the best constitutive model describing our PDMS samples will be useful to translate the strain measurements obtained by digital image (or volume) correlation into the corresponding stress field in the materials.

Three candidate hyperelastic models are considered to fit the tensile behavior of the investigated PDMS materials: Neo-Hooke [52], Mooney-Rivlin [53, 54] and Arruda-Boyce [55] models. The tensile curves are fitted in Figure 2.11 with these three models for the different PDMS samples. The tensile behavior is expressed here in terms of the nominal stress σ_N as a function of the tensile stretch λ. The latter is defined as $\lambda = l/l_0 = 1 + \varepsilon_N$ where l is the actual length of the specimen, l_0 is the initial length and ε_N is the nominal strain.

Hyper-elastic materials are usually described in terms of a strain energy potential $U(\varepsilon)$ indicating the strain energy stored per unit volume in the initial configuration. The Arruda-Boyce model has been developed based on statistical mechanics of a material represented by a cubic volume element composed of eight chains across the diagonal directions. The Neo-Hooke model is based on the statistical thermodynamics of cross-linked chains, but does not predicts the increase in the elastic modulus at very high strains. For this reason it is useful only for strains less than 20 %. To overcome this limit and to better describe biaxial states, the Neo-Hooke model has been subsequently extended with the Mooney-Rivlin model. For simplicity, we do not report here the formulation of $U(\varepsilon)$ for the three models.

After fitting, we note in Figure 2.11 that the best model describing the behaviour of the stretched PDMS samples corresponds to the Arruda-Boyce model. Note that, in those fits, the Neo-Hooke and Mooney-Rivlin curves are superimposed. The values of the fitting parameters useful to describe the materials (especially in a FEM simulation) are reported in Table 2.2 where we remark that the parameters C_{01} characterising the difference between the Mooney-Rivlin and the Neo-Hooke models is almost zero. As the Poisson's coefficient is not possible to fit with a simple uniaxial tensile test without dedicated equipment for transverse strain measurement, we assumed that:

$$\nu = \frac{3K_0/\mu_0 - 2}{6K_0/\mu_0 + 2} = 0.495 \tag{2.1}$$

where $K_0/\mu_0 = 100$ with K_0 and μ_0 are, respectively, the initial bulk and shear moduli. The adoption of this Poisson's coefficient will be explained in more details in section 3.3.3 with the digital volume correlation results of the contact specimens under compression. The fitting of the experimental tensile data with the hyperelastic models allows to compute μ_0 from which it is possible to compute K_0 for a given ν. Then the parameter D has been determined with $D = 2/K_0$.

Because we deal with filled elastomers, it is important to analyse the effect of a cyclic loading on the stress-strain curve as Mullins effect [56] may arise. Mullin effect is an instantaneous softening happening when load increases again after reaching a maximum. Figure 2.12 shows the response of the three materials analysed under cyclic loading. Even after the first load, no appreciable hysteresis was noticed for the three samples. The same behaviour was obtained for further loading too. Thus, we conclude that the effect of the added particles does not influence the mechanical behaviour under cyclic loading.

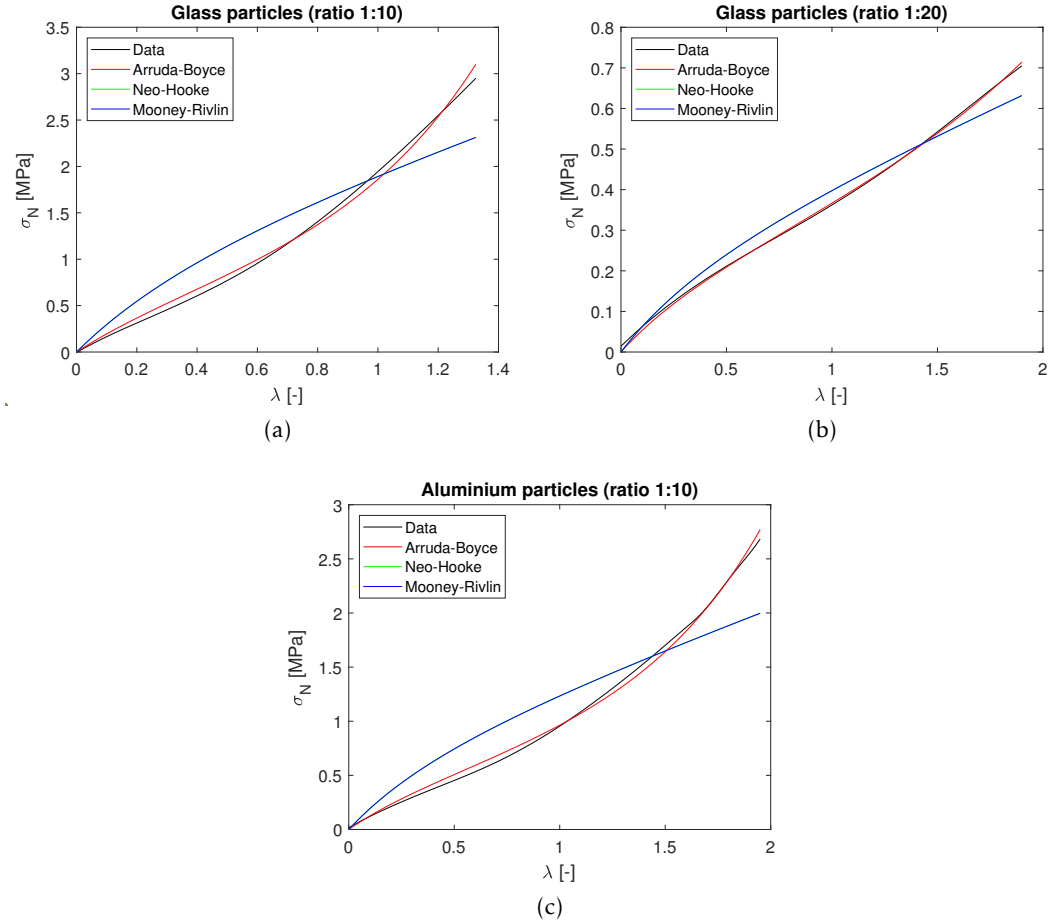

Figure 2.11: Fit of the tensile tests with the Arruda-Boyce, Neo-Hooke and Mooney-Rivlin models for the PDMS (a) filled with glass particles with a curing-base ratio of 1:10, (b) filled with glass particles with a curing-base ratio of 1:20 and (c) filled with aluminium particles with a curing-base ratio of 1:10.

Arruda - Boyce	μ (MPa)	λ_m (-)	D (MPa^{-1})
1-10 glass	0.490 ± 0.012	1.503 ± 0.015	0.0281 ± 0.0003
1-20 glass	0.176 ± 0.001	2.597 ± 0.016	0.1032 ± 0.0006
1-10 aluminium	0.375 ± 0.005	1.917 ± 0.011	0.0437 ± 0.0003
Neo-Hooke	C_{10} (MPa)		D (MPa^{-1})
1-10 glass	0.540 ± 0.090		0.0185 ± 0.0005
1-20 glass	0.114 ± 0.001		0.0880 ± 0.0008
1-10 aluminium	0.352 ± 0.009		0.02838 ± 0.0007
Mooney-Rivlin	C_{10} (MPa)	C_{01} (MPa)	D (MPa^{-1})
1-10 glass	0.540 ± 0.090	~ 0	0.0185 ± 0.0089
1-20 glass	0.114 ± 0.005	~ 0	0.0880 ± 0.0123
1-10 aluminium	0.352 ± 0.041	~ 0 0	0.02838 ± 0.0107

Table 2.2: Fitting parameters for the three models in Fig. 2.11.

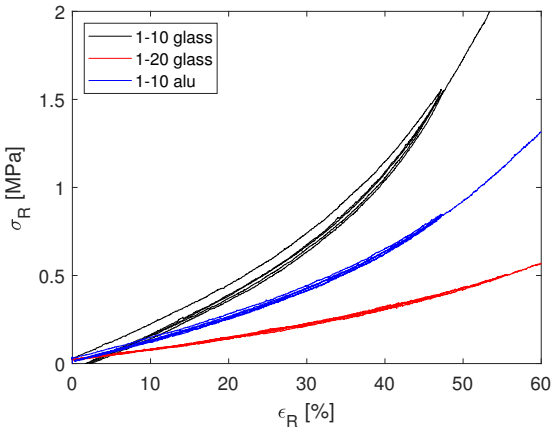

Figure 2.12: Stress strain curves during a uni-axial and cyclic (three cycles) tensile test applied on the PDMS filled with glass particles having two curing-base ratios of 1:10 and 1:20 and the PDMS filled with aluminium particles with a curing-base ratio of 1:10. The loading and unloading speed is 6 mm/s.

2.2.4 Analysis of the glass particle dispersion

As the use of empty glass spheres embedded in our PDMS sample is devoted to perform particle tracking, it is important to check that the dispersion of the particles is sufficiently homogeneous with large enough inter-distance. To do so, we observed inside the bulk of a specimen A-10-G using one of the tomogram obtained through tomography before any loading. Figure 2.13 (a) shows a slice of such tomogram. To extract the relative position of each particles, we use the following procedure. First, a small part of the bulk is cropped and segmented. Then, using an open source plugin in the Fiji software (Mateis/labelling3D) each particle is labelled and their respective diameter and centroid position is recorded. We find an average diameter of 57 µm, obviously smaller than the filter grid holes (80 µm) used for particle filtering during sample preparation. 10% of the particles have a size bigger than 80 µm. An explanation of this may be linked to the saturation of the filter caused by the biggest particles so that the smaller particles are not correctly removed. However, we validate our protocol as this particle size is sufficient to allow for their identification inside the 3D images.

From the centroid position of each particle in 3D, the distance between each particle can be estimated as $L = \sqrt{(x_{gi} - x_{gi})^2 + (y_{gj} - y_{gj})^2) + (z_{gj} - z_{gj})^2)}$. By fixing and implementing in MATLAB a touching criterion where particles are considered in contact when the distance L is smaller or equal to the sum of the radii $(R_i + R_j)$ of the two considered particles, we find that the vast majority of particles are not in contact (only 15% of the particles are touching). Thus they may be easily identified and tracked. Furthermore, with the particles being distant from each other, we have assumed that the PDMS bulk could still be considered as isotropic.

2.2.5 The PMMA plane

In our sphere-on-plane contact, the planar body is a 5 mm-thick PMMA (Polymethyl methacrylate) disk glued on a M8 countersunk screw for easy installation in the loading machine (see Fig. 2.14). The use of this material is guided by the fact that, to reproduce the same experiment on an optical device, we have the necessity to keep at least one material as optically transparent. Unlike other experiments in literature, we use this material instead of glass because of

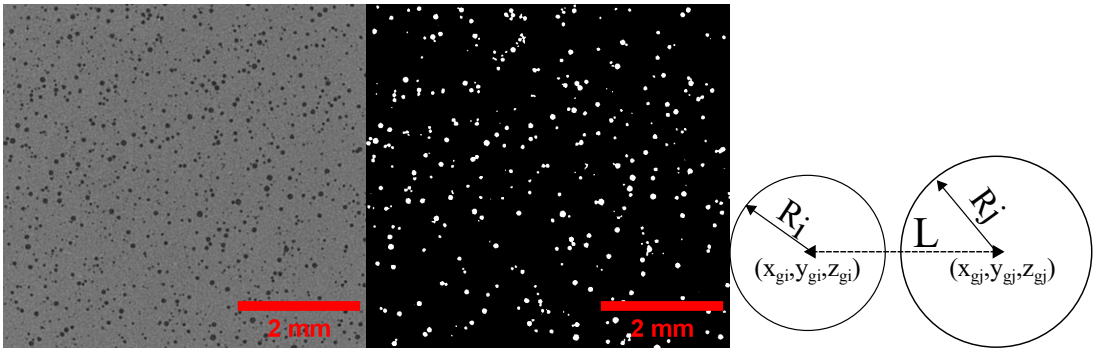

Figure 2.13: Verification of the glass sphere dispersion on the sample A-10-G. (a) Crop of a tomogram inside the bulk of the specimen. (b) Segmentation and labelling of each particle. (c) Illustration of the touching criterion for two spheres.

its higher contrast with respect to PDMS in tomography images. Furthermore, it enables an easy machining with laser cutting and micro-milling, essential in the present study to fit the tomography limits.

The diameter of the disk is of $20\ \mathrm{mm}$. The choice of this shape and dimension is due again to the size of the PMMA tube in the *in situ* loading machine (see section 2.1.1). The cylindrical shape is chosen to avoid image artefacts in the tomogram due to the presence of sharp edges. Furthermore, the upper circular edge is also rounded to reduce these artefacts (details will be provided in section 3.1.1). To follow the PMMA displacement two holes are created by micro-milling with a $1\ \mathrm{mm}$ large drilling tool rotated at 5000 RPM with a feeding speed of $2\ \mathrm{mm/min}$. The holes are stopped at $0.3\ \mathrm{mm}$ from the surface to both have access to these holes in the Region Of Interest (ROI) of the tomogram and to ensure that the heating created by the milling does not deform the external surface.

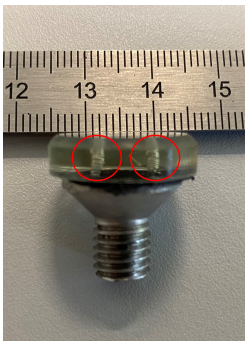

Figure 2.14: Picture of the PMMA plane. The holes obtained with micro-milling, and used as trackers, are visible inside the body.

2.3 The optical observation of the contact

2.3.1 The opto-mechanical devices

With the objective to validate the tomography results with similar experiments using optical observation of the contact, two different opto-mechanical devices are used. We will call them, for simplicity, *optic-1* and *optic-2*. They both allow to load and shear a contact between two solids and to perform *in-situ* observation of the real contact area, if one at least of the material is transparent. We detail here these two devices as they were used with different aims and during different periods of the study. For example, the normal loading experiment was conducted on the device *optic-2* because it allowed an easy automation of the displacement and enables to launch automatically long experiments with an high number of indentation steps (the high number of steps is necessary to increase the precision of the fit used to characterise the material properties).

Figure 2.15 presents a schematic view and a photo of the first device (*optic-1*). The PDMS sample is installed into a sample holder connected to the optical table through: (i) two goniometers (M-GON65-U and -L, Newport) rotating along the X and Y axes (they are used essentially for adjusting the alignment of the PDMS surface) and (ii) four load cells (LSB200, Futek) measuring the normal load P with a resolution of 1 mN. The PMMA plane is installed onto the upper sample holder connected to the motorized stage through a double cantilever. This last one is made of two identical steel arms, with low vertical stiffness, and it is used to ensure that the PMMA plane is not changing its orientation during normal and/or tangential loading. The stiffness of the cantilever is very weak in the direction Z (the direction normal to the contact) to minimize its influence on the applied normal force. Conversely, the double cantilever is rigid in the X and Y directions, so that the displacement of the motorized stage is transmitted quasi perfectly to the PMMA. The translation system is composed of a motorized X-stage where the motion is provided by a linear motor (LTA-HL, Newport) with a controller (SMC100CC, Newport). The motor can move with a maximum range of 25 mm, a resolution of 50 nm, a maximum speed of 1 mm/s and a pulling force of 100 N. The measurement of the tangential force Q is obtained through a piezoelectric force sensor (Type 9217 A, Kistler) positioned between the rigid end of the cantilever and a goniometer allowing the rotation of the cantilever itself. The cell is connected to an amplifier (Type 5018A, Kistler, long measuring mode, 100 Hz low pass filter) with a range between -500 and 500 N and a resolution of 1 mN. Finally, the observation of the contact area is possible thanks to the use of a LED panel and a CCD camera (2M360 MCL, Flare, 8bits, 2048x1088 square pixels, 340 fps maximum) connected to a zoom objective lens (7000 type C, Navitar) and controlled by a commercially available software (Hiris,R&D vision). The camera, force acquisition and the motor movement are controlled by an home-made LabVIEW™ (National Instruments Corporation) program.

Fig. 2.16 shows a schematic view of the device *optic-2*. We can sum up the most important parts of this second device as follows [57]:

- The guiding columns (2). Associated to a motor, they allow the vertical displacement of the upper base;
- The 6-axis force cell (4). It is installed between the upper base and the upper sample holder. The detailed description of the sensor is provided in [58]. The load cell measures three forces and three couples in a range between 0.005 N and 10 N with a measurement noise of 1 mN. Ref : Piezojena Tritor 320;

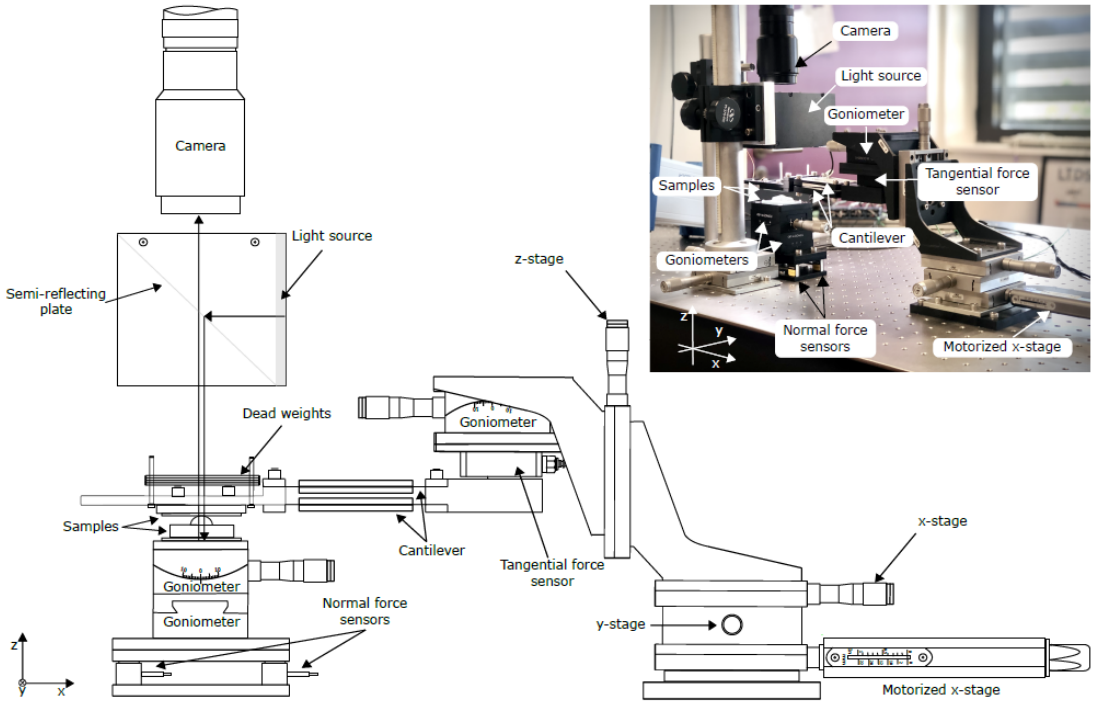

Figure 2.15: Schematic view of the optical tribometer, called *optic-1*, used to benchmark the tomography measurements. The PDMS sample is installed onto the lower sample holder that is connected to the fixed optical table through two goniometers and 4 load cells measuring the normal load P. The PMMA plane is installed onto the upper holder that, through a double cantilever, is moved according to the movement imposed to a translating stage controlled by a linear motor. The presence of a piezoelectric load sensor provides the measurement of the tangential force Q. The access to the contact area is possible thanks to the presence of a LED illuminating the contact interface and a CCD camera recording the images during the experiments. Image from [4].

- The piezo-electric actuator (8). It allows a very precise control of the displacement on the Z axis. In displacement controlled experiments, it enables a positioning with a precision of 100 nm and a range of 320 µm. In force controlled experiments, it ensures the imposed force with a precision of 3 mN in a range from 10 mNand 5 N;
- The 6-axis interferometric displacement sensor (10). It allows a very precise measurement (resolution of 1 nm provided by the designer) of all relative displacements (three displacements and three rotations) between the two sample holders;
- The goniometer (7). It can impose a rotation on the lower sample holder with a precision of $0.001°$ in the range $[-10, 10]$ along the X and Y axes. Ref: OWIS, TPM 150-20-20-243;
- The high resolution camera (12). The detector is composed of 3008x4012 pixels with the highest image resolution of 1 µm/pixel at the contact interface. An external light creates an homogeneous lighting on the contact interface.
- The lateral translating stage in the $X - Y$ plane (9) which allows to obtain shear experiments. It is composed of two linear motors on the two axes X and Y. They allows a positioning error of 1 µm over a displacement range of 100 µm. The displacements speeds can change between 1 µm/s and 100 mm/s. Ref: Allio AI-LM-10000-XY.

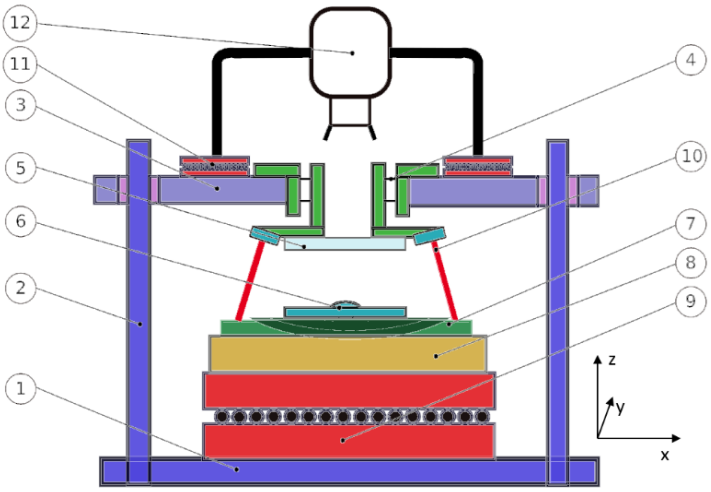

Figure 2.16: Schematic view of the optical tribometer, called *optic-2* , used to benchmark the tomography measurements and to characterise the PDMS samples. (1) lower base, (2) guiding columns, (3) upper base, (4) 6-axis load cell, (5) upper sample holder, (6) lower sample holder, (7) goniometer, (8) piezo-electric actuator, (9) moving stages in the plane XY, (10) 6-axis interferometric displacement sensor, (11) moving stages of the camera in the plane XY, (12) High-resolution camera. Image from [57].

2.3.2 Observation of the contact area

The observation of the contact area is based on an interplay between absorbed and reflected light at the contact interface as illustrated in Fig. 2.17. The PMMA plane is installed on the upper sample holder while the PDMS is on the lower one. An incident light reaches the PDMS surface through the transparent PMMA. Two phenomena happen at the PMMA-PDMS interface: as the refractive index of PMMA and PDMS is very close, the light passes through the

interface with little reflection and diffusion and reaches the black absorbing layer at the bottom of PDMS. The black layer absorbs the incident light and prevents any reflection back to the camera. As the refractive index of air and PDMS outside of the contact area are different, the light is partially reflected, which is sufficient to generate a contrast with the contact area. As a result, the contact area appears darker than the out-of-contact zone.

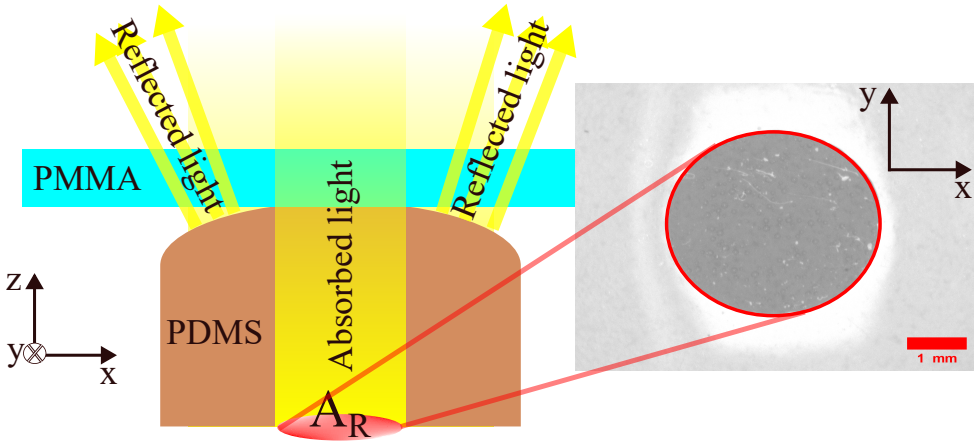

Figure 2.17: Schematic view of the contact observation through optics. The PMMA is installed on the upper sample holder while the PMDS in installed downside. An incident light illuminates the PDMS sample through the transparent PMMA. The contact area being plane and the refractive index of PDMS and PMMA being similar, the incident light passes through the interface and reaches the black layer at the bottom of the PDMS sample, where it is absorbed; the contact points are black. Conversely, on non-planar zones (out-of-contact) the light is reflected and non-contact points appears brighter in the picture. The picture on the right shows the typical image of the contact in the case of the sample A-20-G installed in the device *optic-2*.

2.3.3 Experimental procedure for optical experiments

We detail here two types of experiments performed between a PDMS sphere and a PMMA plane. The first one is a normal loading test used to characterise the material properties of the PDMS (Young's modulus and work of adhesion). The second is a classical shear test that will be use to validate the results obtained with the mechanical device installed inside the tomograph.

Normal indentation tests

The normal indentation tests is obtained by simply imposing to the PDMS a vertical displacement along the direction Z up to a maximum indentation depth of 200 μm (loading phase) and then by bringing back the specimen to its initial position (unloading phase). The vertical displacement is imposed thanks to the piezoelectric actuator, step-by-step. Each step of 2 μm is then followed by a dwell time of 60 seconds to account for visco-elastic relaxation that could appear during imposed displacement experiments.

During the experiment, the force in all three directions and images of the contact interface are recorded simultaneously. The force values are taken all along the experiment at a frequency of 10 Hz and the saved value is the average of the collected point during each step. The images, instead, are saved at the end of each step. An example of the evolution of the contact area during this type of test is shown in Fig. 2.18 for the specimen A-20-G.

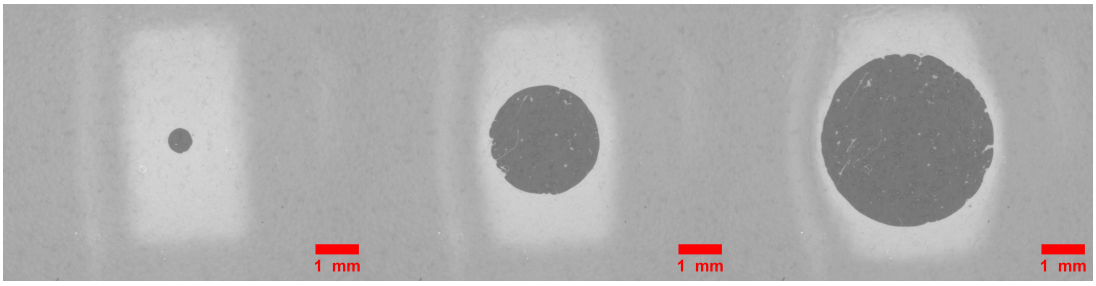

(a) (b) (c)

Figure 2.18: Pictures of the contact interface during a normal indentation step at three different steps of 0, 100 and 200 μm for the specimen A-20-G installed into the device *optic-2*.

Shear tests

The objectives of those tests is to provide both the evolution of the real contact area (size and morphology) and of the tangential force during the shearing of a sphere-on-plane PDMS on PMMA contact for different normal contact loads. In this section, the complete procedure of these shear-induced experiments is presented.

Once the PDMS and PMMA samples are installed onto the corresponding holders, the cantilever is moved vertically by means of a linear moving stage. The movement is kept up to the the point where PMMA snaps into contact under the effect of adhesion. In practice, this corresponds to the first observation of a contact dot on the live images of the contact and to a small variation in the measured normal force. Then, the normal force P is applied by putting dead weights in a special case placed on the PMMA holder. As the magnification of the camera is adapted for each sample, a ruler is placed near the contact zone to calibrate the conversion from pixels to meters.

After having set the parameters of the experiment (displacement, velocity, frame-rate), the recording of the normal and tangential forces starts at a frequency of 2 kHz while a square trigger signal is sent to the camera for image acquisition to control the image acquisition rate. Before starting to shear the interface, the contact is opened by gently raising the PMMA holder using a thread tied to the free end of the cantilever, the tangential force Q is set to 0 and the contact is consequently created by moving the PMMA back into its initial position. This procedure allows to remove a potential initial tangential force that could be generated during the contact creation.
Subsequently, a waiting time of one minute is applied before the shear movement to take the visco-elastic relaxation into account so that the experiment could start from an equilibrium state. Then, the motor (and thus the PMMA plane) starts to move at constant imposed velocity v up to a maximum tangential displacement d. At the end, a second waiting time of 10 seconds is also set to capture potential visco-elastic relaxation after the application of the shear displacement. Images are recorded at a frequency of 50 Hz during the displacement step and 10 Hz during the two waiting steps. Fig. 2.19 illustrates, as an example, some images acquired during a shear test for a specimen A-10-A-X with particles in the external film used for particle tracking in a previous study. The three images show the evolution of the contact area. It starts as circular and then looses its circularity by the application of the shear load.

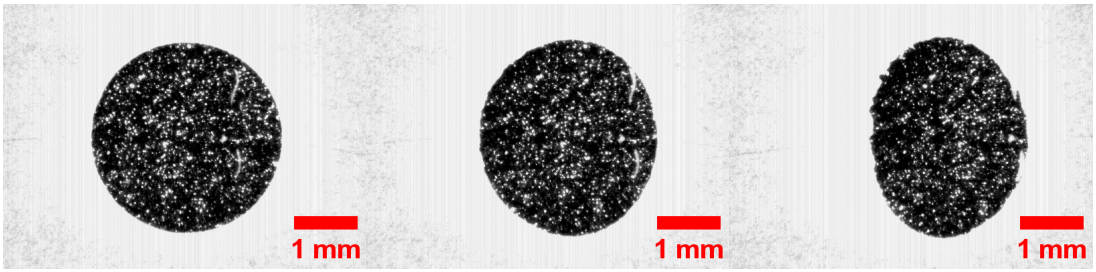

(a) (b) (c)

Figure 2.19: Pictures of the contact interface during a shear test at a constant velocity of $0.1\ \mathrm{mm/s}$ at: (a) the beginning of the experiment (no shear), (b) during shear and before full sliding, (c) during full sliding. Images are shown for the specimen A-10-A-X installed into the device *optic-1*.

Contact Area Measurement

For all optical experiments, the contact area has to be identified and measured. As images are characterised by only two regions, they are segmented using the Otsu's method [48]. This method sets one pixel to white or black depending if its gray-level (from 0 to 255 as we deal with *8-bit* images) is, respectively, above or below a threshold that can be either evaluated automatically (as a function of the average gray-level of the overall image) or imposed manually by the user. When the PDMS is filled with particles, while the light passes through the sample, it can be reflected by some of these particles. Thus, small brighter dots appears in the contact zone (the particle outside the real contact are not visible) as seen in the contact image in Figure 2.17. As we prepared an external film of pure PDMS, we expect these particles which lay below the contact surface, will not affect the contact area. The dots corresponding to the particles are considered as contact points by filling the contact region with the MATLAB® function *imfill*. The result of the image segmentation performed on the images of Fig. 2.19 is shown in Fig. 2.20.

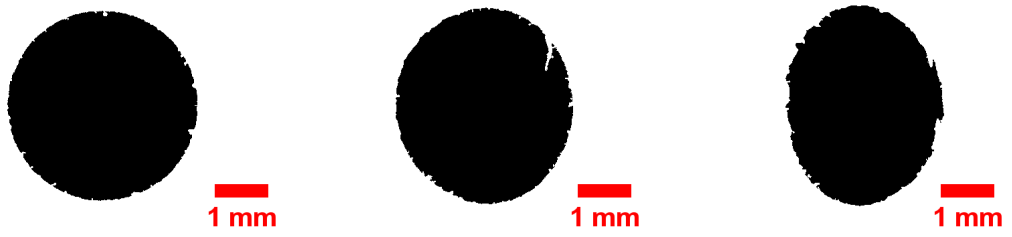

(a) (b) (c)

Figure 2.20: Binarized contact area images with the application of the Otsu's method. Pictures refers to the ones in Fig. 2.19.

After image segmentation, by using the MATLAB® function *regionprops*, the real contact area A_R is measured and corresponds to the number of pixels inside the contact boundary. Finally, the contact area is converted from pixel to square meters.

Determination of the material properties using contact models

From the P(A) curves (normal load as a function of the contact area), it is now possible to extract the value of E and ω_0 by using the classical contact models (see Chapter 1).

As firstly proposed by Chaudhury *et al.* for the JKR model [59], the measurement of the material properties such as the Young's modulus E and the work of adhesion ω_0 passes through the normalisation of the normal load P ($P/\sqrt{6\pi a^3}$) and the contact radius a ($a^{3/2}/\sqrt{6\pi}R$). In this way the data are linearized and the material characteristics of the contact (E, ω_0) are determined, respectively, with the slope of and the intercept of the fitted linear curve on the normalised data. The normalisation of the experimental data in this sense is presented in Fig. 2.21 for an indentation test on the device *optic-2* with a sample A-20-G in contact with a PMMA plane. The results are shown during loading with blue crosses and during unloading with red crosses. We can remark how, at low loads, this normalisation is not able to capture the deviation from the linear fit. For this reason, we decided to fit the (P, a) data with the Maugis-Dugdale model [18] to try to account for this cut-off.

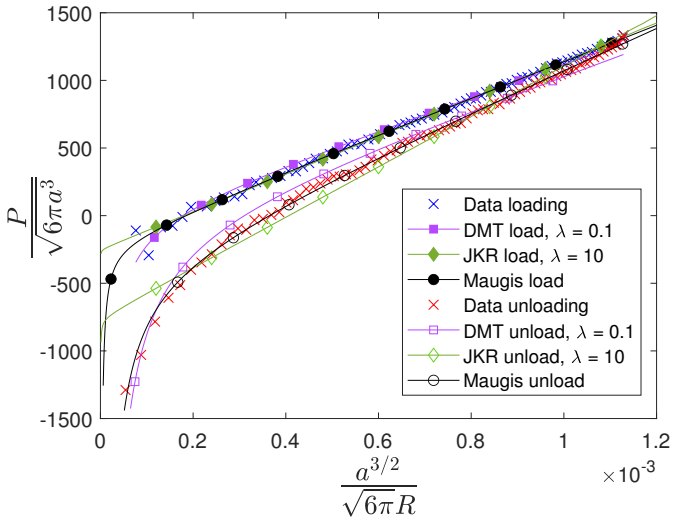

Figure 2.21: Evolution of the normalised normal load versus the normalised contact radius during loading (blue crosses) and unloading (red crosses) for an indentation test carried out on the sample A-20-G. The superposed lines represent the fits with the three adhesive contact models (JKR in green, DMT in purple and Maugis-Dugdale in black) both during loading (solid markers) and unloading (open markers).

Indeed, we use the Maugis-Dugdale equations by imposing the values of the parameter λ for the DMT and JKR models (respectively of 0.1 and 10) while this last one is an additional parameter for the Maugis-Dugdale fit. The results of this fitting are shown in Fig. 2.21 (with the normalised representation of Chaudhury *et al.* [59]). The values of the materials properties and of the λ parameter are reported in table 2.3 with the error bars representing a 95% confidence interval. All three models are able to capture the affine evolution at large normal loads and the adhesion hysteresis (the difference between loading and unloading) attributed to the presence of chemical heterogeneity [60], visco-elasticity [61] and roughness [62]. Nevertheless, the three models underline some differences at low loads: only the DMT and Maugis-Dugdale models seem to capture the lower cut-off properly (i.e. the deviation from a straight line). Discussion

about these differences at low load is nevertheless out of the objective of the present study.

A-20-G	$E(MPa)$	$\omega_0(J/m^2)$	λ
Maugis load	0.750 ± 0.016	0.059 ± 0.008	1.22 ± 0.51
Maugis unload	0.840 ± 0.014	0.305 ± 0.007	0.71 ± 0.06
DMT load	0.671 ± 0.009	0.095 ± 0.010	0.1
DMT unload	0.675 ± 0.016	0.292 ± 0.018	0.1
JKR load	0.779 ± 0.010	0.045 ± 0.004	10
JKR unload	1.043 ± 0.046	0.309 ± 0.038	10
A-10-A	$E(MPa)$	$\omega_0(J/m^2)$	λ
Maugis load	1.687 ± 0.022	0.096 ± 0.015	9.37 ± 0.30
Maugis unload	1.623 ± 0.011	0.118 ± 0.009	7.72 ± 0.15
DMT load	1.528 ± 0.021	0.187 ± 0.0443	0.1
DMT unload	1.459 ± 0.016	0.239 ± 0.045	0.1
JKR load	1.450 ± 0.019	0.004 ± 0.001	10
JKR unload	1.376 ± 0.014	0.005 ± 0.001	10
B-10-A	$E(MPa)$	$\omega_0(J/m^2)$	λ
Maugis load	1.551 ± 0.009	0 ± 0	0.01 ± 0
Maugis unload	1.576 ± 0.012	0.028 ± 0.006	4.05 ± 0.24
DMT load	1.559 ± 0.010	0.01 ± 0	0.1
DMT unload	1.521 ± 0.008	0.119 ± 0.025	0.1
JKR load	1.581 ± 0.018	0.010 ± 0.001	10
JKR unload	1.519 ± 0.004	0.014 ± 0.001	10

Table 2.3: Values of Young's modulus E, work of adhesion ω_0 and Tabor parameter λ resulting from fits based on Maugis' contact model [18] of the evolution of the normalized contact load versus the normalized contact area during the compression of the sample A-20-G against a rigid PMMA plane. DMT and JKR fits are obtained by imposing, respectively, a value of 0.1 and 10 for λ in the Maugis-Dugdale equations.

2.4 Observation of the contact area with X-ray Computed Tomography

After having introduced how the contact area is measured through the optical devices, we move to the description of the procedure developed to reach the same goal by X-ray Computed Tomography. We then distinguish again two different stages of the experiment: the normal load one and the shear load one.

2.4.1 Experimental procedure

Preparation of the tomograph and of the mechanical device

The tomograph used in this study is a V-TomeX (GE Phoenix X-ray GmbH) with a 2520 V detector from Varian (Pixel matrix 1920x1536 with pixel pitch of 127 μm^2). First, the detector is calibrated to the imposed parameters of the X-ray source (here a voltage of 80 kV and a

current of 280 mA). In this way the *mean free ray* (the energy hitting the detector when an X-ray does not cross any absorbing material on its path) could be determined and it is useful to adjust the contrast on the radiographs as a function of the X-ray beam energy.

When the tomograph is ready, the PMMA plane is aligned horizontally using, as a reference, the central horizontal axis of the tomograph detector and by looking at radiographs with a resolution of 4 µm/pixel . Then, the point of first contact is searched. Contrary to optical experiments, we do not have any direct observations of the contact area. The point of first contact is thus obtained only by the live measurement of the normal force P when the PDMS is pushed against the PMMA. This is done by varying the normal indentation up to a position where the lowest change in the normal force is observed. The smallest indentation resulting in the smallest change in the normal force is of 10 µm. Having this uncertainty in the detection of the first contact point, we move away the PDMS of 30 µm to ensure that the first recorded image is obtained in a non-contact situation. Finally, the effective distance from the PDMS apex to the PMMA plane is confirmed afterward with the reconstructed 3D images.

Before starting a complete experiment, the mechanical device is positioned as close as possible to the X-ray source to maximize the image resolution. Because of the external diameter of the PMMA tube, the distance from the source is limited. The best resolution obtained in the present configuration is of 4 µm/voxel. The resulting field of view close to the contact zone is of 6.8x6.8x2.8 mm^3. Thus, all our measurements are in a condition of local tomography, *i.e.* when the object is larger than the region of interest of the detector.

Normal/shear tests procedure

The compression and shear tests are carried out step-by-step under controlled displacement in two consecutive parts: a compression/indentation part and a shear keeping the final normal indentation reached at the end of the compression part. For the sample B-10-A, Figure 2.22 shows the evolution of the normal and tangential forces during a complete compression and shearing test. During the compression part, the PDMS is moved vertically with steps of 40 µm (we call the normal indentation δ_c) up to a maximum value of 280 µm. The choice of this value is a compromise between two factors. The first one is the time duration of 20 minutes required for each scan that limits the total number of steps that could be taken in a typical work day. The number of steps is, in fact, due to the final indentation needed to reach the corresponding target normal force of nearly 1 N . This is chosen with the aim of comparing our results with the available optical experiments at this normal force and to reach a sufficient contact size for the resolution of the 3D experiments. Additionally, the choice of this incremental step is done to limit the maximum displacement, between two consecutive scans, of the markers inserted in the PDMS and avoid decorrelation problems that may arise for high displacements.

At the end of the compression part, during the shear part, the upper horizontal stage is moved with steps of 150 µm (we call the shear displacement δ_s) while the final normal indentation is kept constant. As before, this step is mainly due to ensure to get to full sliding conditions in a reasonable time (the number of necessary steps to get to full sliding is found with a preliminary shear test without image acquisition). Furthermore, we cannot apply an higher displacement in the full-sliding regime because XRCT is not relevant for dynamic experiments. We can then observe an increasing tangential force while the normal force keeps constant. At the last two steps the rapid decreasing of the tangential force expresses the transition to full sliding and, at this stage, the experiment is stopped. Indeed, the PDMS recovers

the position of the previous step during the stationary (full sliding) regime so that there is no point in applying an higher tangential force in such quasi-static testing conditions.

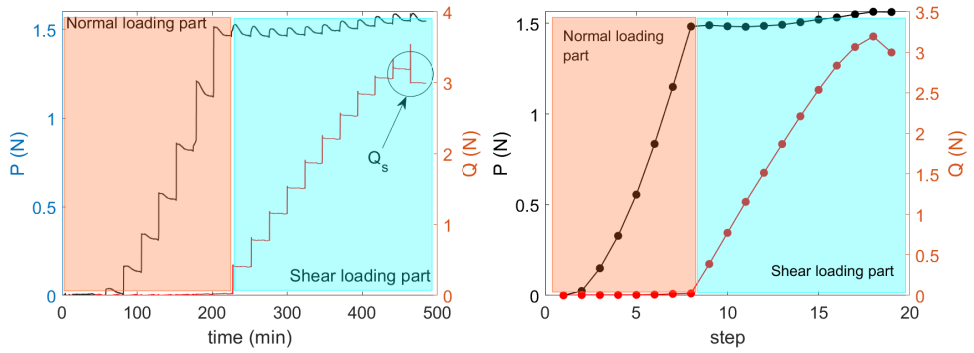

Figure 2.22: (a) Normal (P) and shear (Q) loads during a compressing and shearing experiments as a function of time for Sample B-10-A. The sample is firstly compressed step-by-step up to a target displacement. Then, this indentations is kept constant while a step-by-step shear displacement is imposed. The point Q_s identifies the point where the static friction peak is observed. For each step, a 3D scan is recorded. (b) Average normal and shear loads as a function of the loading steps.

Correction of the shear displacement

Before starting the experiment, some radiographs of the operating system are recorded to capture the global movements of the mechanical devices (the two rods for instance) that are not visible during the 3D image acquisition made in a condition of local tomography. By putting the device sufficiently far from the X-ray source, and with a resolution of 11 µm/pixel, we are able to fully observe, at the same time, both the PDMS and PMMA samples. Figure 2.23 shows an example of the obtained radiographs for a compressing and shear experiment performed on a sample B-10-A. The first image (Figure 2.23 (left)) is obtained when the PDMS is at the its initial position (set as reference). Then, a vertical displacement of δ_c =280 µm is applied to the PDMS sample through the motorized stage (in the lower part of the device) (Figure 2.23 (center)). While this indentation is kept constant, the PMMA is moved horizontally up to a shear displacement δ_s =1500 µm thanks to the horizontal stage (present on the upper part of the device) (Figure 2.23 (right)).

Several radiographs are taken at different shear displacements steps to look at the response of the system in terms of stiffness. It is then possible to track the position of the PMMA and of the PDMS glass base (as indicated in Figure 2.23) to understand how they are moving under the effect of the imposed displacement. The PDMS/PMMA displacement is obtained following the position of the edge of each screw in the images. In Figure 2.24, the displacement measured on the PMMA and on the PDMS are plotted versus the imposed displacement for the specimen B-10-A. Ideally, the PMMA should move of the same amount as the imposed displacement. In our case, the PMMA displacement is $\sim 25\%$ lower compared to the imposed one. However, contrary to what is expected, the PDMS sample is not fixed. It exhibits an unexpected displacement of about $\sim 6\%$ of the imposed displacement during shearing which, in our opinion is not only due to the bending of the lower rod. Taking into account, the material property and the dimensions

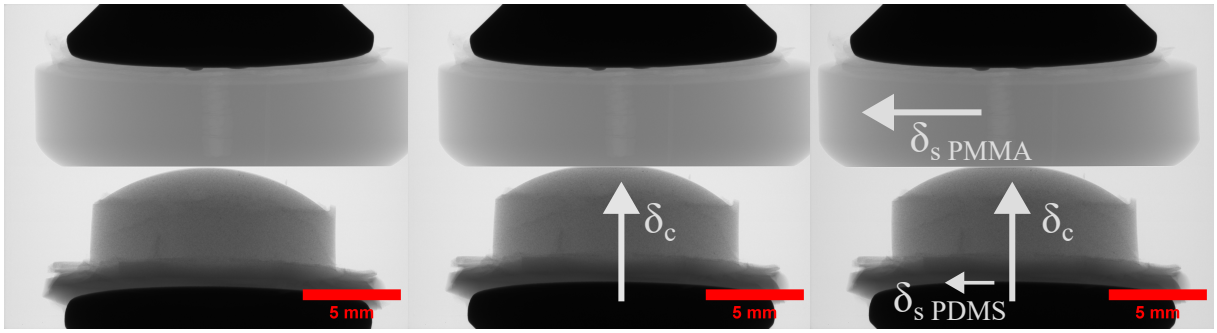

Figure 2.23: Radiographs of a compressing and shear experiment at a resolution of 11 µm/pixel. From left to right the PDMS is moved vertically by $\delta_c = 280\mu m$ and then the PMMA is moved horizontally by $\delta_s = 1500\mu m$ while keeping the normal indentation constant. The radiographs are taken with the experimental device oriented so that the shear plane is parallel to the tomograph detector. The PDMS observed here is of type B-10-A.

of the rods, we have estimated that the maximum displacement at the top of the rod due to bending is only of the order of 2 µm when the shear force reaches its maximum value; far less than the 90 µm which are measured. We thus suspect that these displacements results from a more complex behaviour of the entire device that is not possible to characterise.

During each experiment, to account for the real displacement of the PMMA, we evaluate it for each reconstructed 3D volume. To do this, we measure the relative position of a small hole introduced into the PMMA close to the surface and visible in all reconstructed volumes. Unfortunately, with the resolution of the 3D volumes, the real position of the PDMS is not accessible. Thus, we assume it to be always 6% of the imposed displacement. As a consequence, in the rest of this manuscript, all displacements will correspond to the corrected ones both for the PMMA and for the PDMS samples. It is also important to notice that the behaviour of the PMMA and PDMS displacement changes when reaching full sliding. When the contact area enters into a regime where there is no more stick zone, the friction force reduces and the two samples are not adhering anymore. As a consequence, the PMMA experiences a smaller resistance and moves faster (the slope of the curve increases), while the PDMS sample moves back for the same reason. Together with the phenomena observed on the tangential force, this confirms when the interface passes to a full sliding regime.

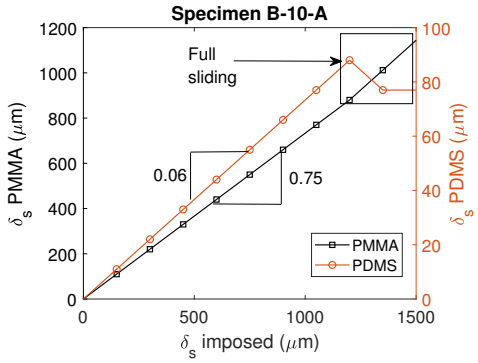

Figure 2.24: Measurement of the PMMA and PDMS displacement as a function of the imposed displacement on the translating horizontal stage for the specimen B-10-A. The upper right box underline when the system passes to full sliding conditions.

Image acquisition

After the application of each normal/shearing displacement, both the PDMS and PMMA are kept fixed to perform image acquisition. The image acquisition is launched after a waiting time of 5 minutes that was determined from a complementary test made on the device *optic-1*. In this test, we measured the evolution of the contact area as function of the time for different fixed normal loads (see Figure 2.25). For each tested normal loads, a plateau is reached after less than 1 minute. Thus to ensure that our sample is in an equilibrium state during image acquisition and to minimize image blurring, we have chosen a very conservative waiting time of 5 minutes. In any case, after the application of each indentation or shear displacement, the evolution of the normal/tangential force is checked and scan are launched only if the forces reaches a stable value.

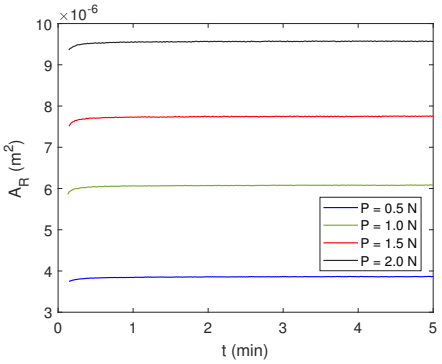

Figure 2.25: Evolution of the contact area for the specimen B-10-A as a function of time for different normal loads. Data are obtained on the device *optic-1*.

For each 3D image, 900 radiographs are recorded with an exposure time of 999 ms (each radiograph is the average of 3 images obtained with an exposure of 333 ms for each image) during the 360° rotation of the mechanical device about its vertical axis. This rotation is not continuous but obtained step-by-step by increasing the angle of rotation every 999 ms to allow the acquisition of the three radiograph. The use of these three averaged images at each angular step ensures a reduction of the noise but brings the total acquisition time to 20 minutes. The time required for each step is clearly visible in Figure 2.22a where each normal or shear force increment is followed by a plateau during which all displacements are kept constant. Ideally, the force should also be constant under constant displacement but it is not always the case, especially for the normal force. We connect the small increase of force present at the beginning of the plateau to the rotation of the machine required for the image acquisition; the consequent rotation of the sensor cable can justify this small and periodic increase happening with the rotation of the device. Furthermore, the small decrease observed for the tangential force could be due to a relaxation of the PDMS. However, it does not perturb our acquisition as no changes are appreciated between the last and the first radiograph, *i.e.* any movement of the PDMS surface is smaller than the typical size of the voxel. The forces associated to each 3D volume and used for further theoretical comparisons are the average values during each step (these are shown in Fig. 2.22b).

After all the radiographs are recorded, the 3D volumes are obtained with the filtered back-projection algorithm [63] available in the commercial software provided with the tomograph. The final 16-bit gray level volumes are then converted to 8-bit for further image visualization

and processing. Figure 2.26 shows three images taken along the central $X-Z$ plane of three reconstructed volumes, respectively (from top to bottom): (i) at the initial position with no contact, (ii) at the application of a normal indentation of 280 µm and (iii) at the application of shear displacement of 1650 µm keeping the same normal indentation. The images show clearly the upper part of the PDMS sample with, in white, the markers that are dispersed inside, the shape of the external PDMS skin (underlined by the green curve), the PMMA plane (dark gray upper part of the image) and the air. From the first to the second image, the apparition of a plateau highlights the deformation of the PDMS sample and the apparition of a contact zone of radius a. By comparing both images, one can clearly capture the deformation of the PDMS sample due to the contact with the PMMA plane and have an estimation of the real contact radius a. Looking at the the two last images, instead, under the shear displacement, the deformation of the PDMS skin is clearly visible. Indeed, the green line looses its symmetry and the contact zone shifts to the right following the PMMA displacement as underlined by the movement of the central dashed red line.

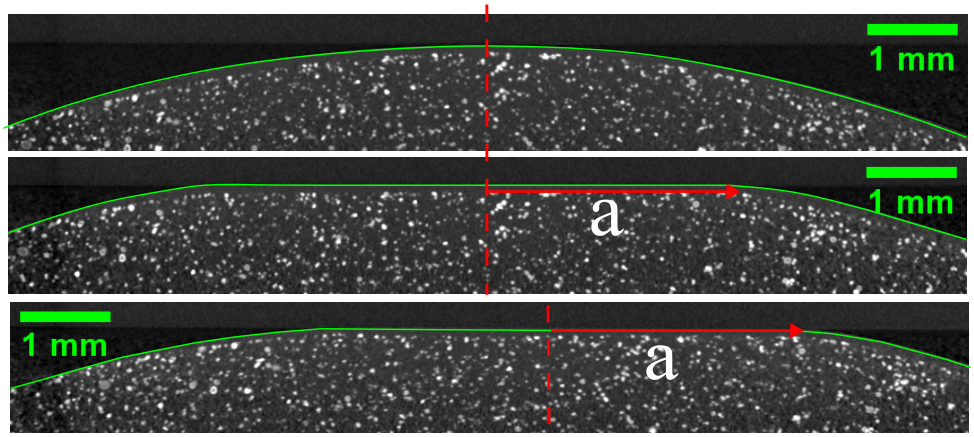

Figure 2.26: Slices of the reconstructed volumes on the central $X-Z$ plane after the application of a compression displacement of $\delta_c = 280$ µm (second image) and of a shear displacement $\delta_s = 1650$ µm (third image) keeping the normal displacement constant. The red arrow indicates the apparition of a contact area of radius a. The vertical red dashed lines underlines how the contact zone shifts according to the shear displacement. Specimen B-10-A.

2.4.2 Data Analysis

In order to extract the maximum of the information from the 3D images, it is necessary to identify each material (*i.e.* the PMMA, the PDMS and the Air) so that the contours of the PDMS and the PMMA could be easily recognized for further analysis. Knowing the coordinates of each material's border will allow us to measure the contact area, to follow the PDMS skin deformation and also to create an adapted ROI (Region Of Interest) for the upcoming DVC measurement. In the following sections we details the algorithm used for the image segmentation, the contact area measurement, the surface displacement field measurement and the Digital Volume Correlation procedure for the evaluation of the 3D displacement field in the bulk.

Image segmentation

The process of image segmentation consists of labelling each voxel in a 3D image, *i.e.* link one of the three materials involved (PDMS, air, PMMA) to each voxel. Differently from the 2D

optical images, the obtained volumes from tomography are rather characterised by 3 ranges of gray-levels corresponding to the three materials. It means that a simple binary Otsu filter cannot be used anymore and other segmentation algorithm should be looked for in the literature. Among the different ones found, we choose to use the Random Walker Segmentation method [64] and use the python *scikit-image* package [65] to implement it. The algorithm starts from a set of labelled markers for each phase and an anisotropic diffusion equation is solved, where the diffusion coefficients are a function of the local gradient in gray-level. The technique corresponds in a certain way to the expansion of a liquid spreading from an initial set of labeled voxels. Each voxel reached by the liquid front takes the value of the voxel from which the diffusion started. This diffusion is facilitated when neighbouring voxels have similar gray values, while it is penalized by high gradients. In the end, each voxel is labelled with the value of the labelled voxel that has the highest probability to reach it during the diffusion process. The python code requires also a penalty coefficient β for this diffusion and we found empirically that a value of $\beta = 10^4$ showed the best compromise in terms of segmentation accuracy near the contact border and computation time.

Figure 2.27 illustrates how the algorithm is implemented on a reconstructed volume of a specimen A-20-G in contact with the PMMA. Before starting the segmentation, the images are filtered using a Gaussian Filter with a size of 2x2x2 voxels to smooth the image and reduce the gray-level fluctuations. In the first step the image is analysed in terms of average gray-level. To do so, a profile along a chosen x-coordinate crossing PMMA, air and PDMS (see the dashed blue vertical line) is extracted and the corresponding gray-level evolution is shown (see red curve on Figure 2.27 (a)). The objective of this analysis is to determine the average gray-level in each material and to use these values for the choice of the labelling markers. Consequently, the markers for a given phase correspond to all the voxels of the original volume having a gray-level equal to the average grey-level plus or minus a tolerance of 10 % (see the narrow colored bands superposed to the red profile in the first image). The obtained markers for each phase are then shown in the Figure 2.27 (b) with three different grey level. Finally, the Random Walker algorithm is launched to produce the segmented volume presented in the last image where each voxels has a unique label corresponding to air (black), PMMA (white) and PDMS (grey).

We should mention that this method is only possible with the PDMS specimens filled of glass particles; while the use of aluminium particles allows a good pattern for the digital volume correlation, they also saturate the image making the Random Walker segmentation less effective. All the results concerning the deformed PDMS surface or the contact area measurements will be then referred to this type of specimen while the aluminium filled specimens will be rather used for bulk displacement measurements using DVC.

Contact area measurement - surface reconstruction

Starting from the labelled volume, surface extraction techniques allow to identify the boundaries between the two phases or materials in the labelled volume. In our case, these correspond to air-PMMA, air-PDMS and PMMA-PDMS interfaces. The contact area thus corresponds to the PDMS-PMMA one. To do so, a procedure based on a multi-material extension of the marching cubes algorithm [66, 67] is implemented. This method is available, for example, in the commercially Avizo software (ThermoFisher Scientific). Basically, the algorithm creates a surface mesh of the materials boundaries using triangular elements having, as a characteristic length, the voxel edge. An example of the obtained mesh reconstruction is shown in Fig. 2.28 for a

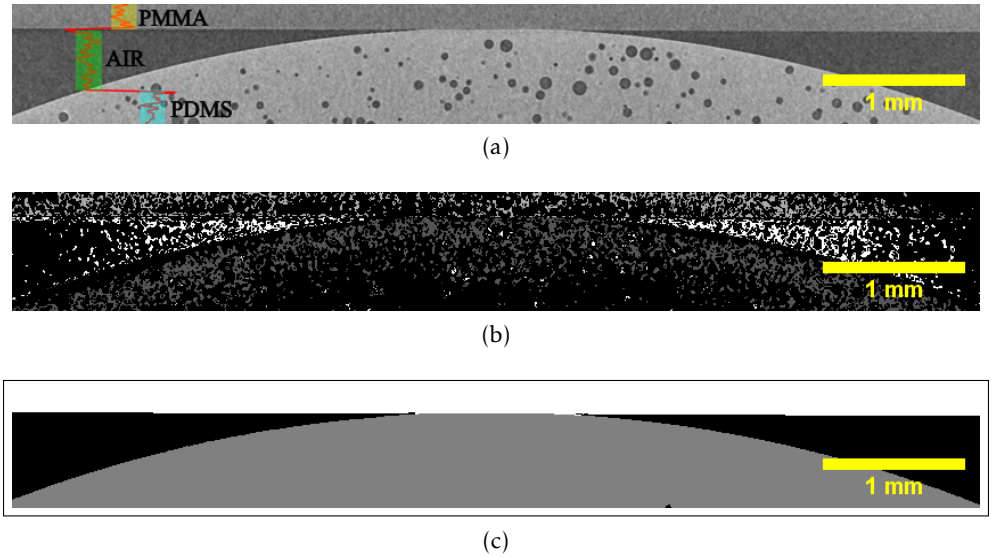

Figure 2.27: Illustration of the segmentation process. (a) Original volume together with a representation of the grey-level G in red taken along the dashed blue line crossing all three phases (PMMA in grey, air in dark grey and PDMS in light grey). (b) Positioning of markers for the different materials, corresponding to voxels with a grey level equal to the average value in each phase - extracted from the red profile in the image (a) - plus or minus a tolerance of 10 % (colored bands: yellow for PMMA, Green for air and blue for PDMS). (c) Labelled volume obtained with the Random Walker Segmentation algorithm with air in black, PMMA in white and PDMS in grey.

specimen A-10-G indented of $80\ \mu\mathrm{m}$. The image on left shows a transparent view of the mesh underlying the apparition of the contact area while the one on the right indicates the typical size of the mesh used for the surface description. The contact area A_R (the interface PDMS-PMMA) correponds thus to the sum of the area of each triangle in the contact patch. During the reconstruction the mesh is also simplified to reduce the number of elements and deal with a lighter dataset. This simplifications, made with a characteristic length of the triangles set to 4-times the voxel size, does not affect the computed contact area as this element size remains sufficiently fine to preserve the morphology of the surfaces.

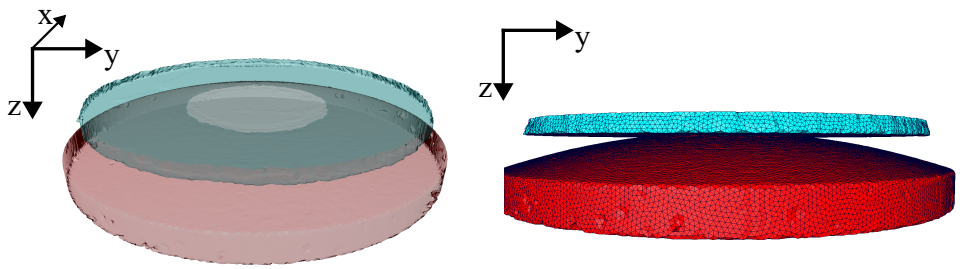

Figure 2.28: Reconstruction of the material's surfaces with the Marching Cubes algorithm for a specimen A-10-G indented at $\delta_c = 80\ \mu\mathrm{m}$.

Contact area measurement - "Z-projection"

When passing from the glass particles to the aluminium ones, the Random Walker Segmentation is no longer well suited. In fact, due to their high absorption with respect to the PDMS bulk, these particles appear very bright compared to the PDMS and the PMMA. The result is that the contrast between the two materials in contact is very low and the automated segmentation introduced before gives unsatisfactory results and reconstructions. Another technique is then needed to capture the evolution of the contact area during the experiment. We propose to use the Tool "Z Project" implemented in the software Fiji. An illustration of this method is shown in Fig. 2.29 for a sample B-10-A. The tool scan the 3D volume on a zone having a width chosen by the user (here underlined by the yellow rectangle). When scanning from top to bottom along the Z axis, the minimum gray-value is searched along the path for each $X-Y$ pair. The value for each pixel in the obtained image (see the image in the lower left corner) corresponds to this minimum gray-level found on the path. When the scanning line crosses all the three materials (see green arrow) the minimum gray-value found is the one of the air while, if the line crosses the contact zone (see yellow arrow) the minimum gray-value is the one of the PDMS. The results, as shown in the images below for $\delta_c = 280\mu m$ and $\delta_s = 1650\mu m$ (keeping the same normal indentation), is a 2D image where one can clearly see the contrast between PDMS and air, *i.e.* the contact area. In this way, we get rid of the aluminium particles and we just see the contrast between the contacting materials. The image shows, for a simple normal indentation, a circular contact area as expected from the models for smooth sphere/plane contacts and also the typical shrinkage and dilation of the contact boundary under the effects of a shear load. Despite the simplicity of this method, two problems are hidden here. The first one is that we observe, in this way, only a 2D projection of the contact area as in optics. The second is that the contact border is not clearly defined and is surrounded by noise, which we associate to image artefacts arising during the acquisition of the radiographs in the scans (see section 3.1.1).

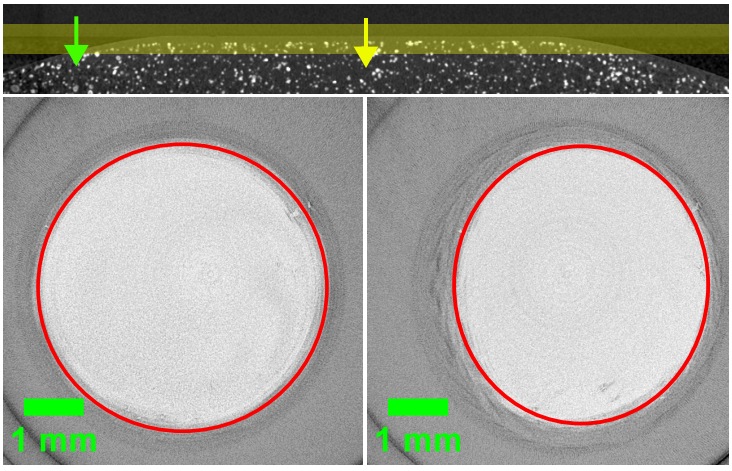

Figure 2.29: "Z-projection" method for contact area estimation on a sample of type B-10-A indented of $\delta_c = 280\mu m$ (upper and lower left image) and $\delta_c = 280\mu m$/ $\delta_s = 1650\mu m$ (lower right image).

Extraction of the PDMS profile

As introduced in the previous chapter, the study of the evolution of the external deformation of the contact bodies is of relevant interest to understand the evolution of the contact area

and the potential adhesive effects. Differently from the optical observation of a contact, this information is accessible with tomography measurements with the additional feature of having this information in three dimensions.

Figure 2.30 shows the contour of the PDMS surface for a sample A-20-G indented of $\delta_c = 32\mu m$ in a section along the central $X - Z$ plane 2.30a and in 3D 2.30b. The edge of the deformed PDMS is obtained after the image segmentation with the Random Walker algorithm and eliminating the PMMA phase. Thanks to a Matlab® code the coordinate Z of each point of the edge is searched for each (X, Y) coordinate in order to obtain a map as shown in Fig. 2.31a. Fig. 2.31b, instead, shows the profile of the edge taken along the horizontal black line overlaid on the colormap on the left. The profile is a little noisy with a step-like behaviour in relation with the typical size of the voxel.

(a)

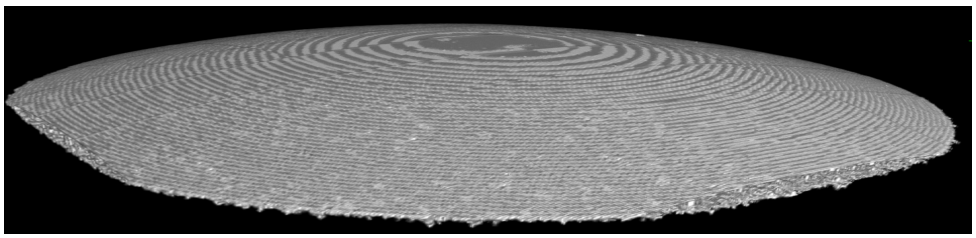

(b)

Figure 2.30: (a) 2D edge of the segmented PDMS on the central $X-Z$ plane. (b) 3D observation of the segmented PDMS edge. Specimen A-20-G at an indentation $\delta_c = 32$ µm.

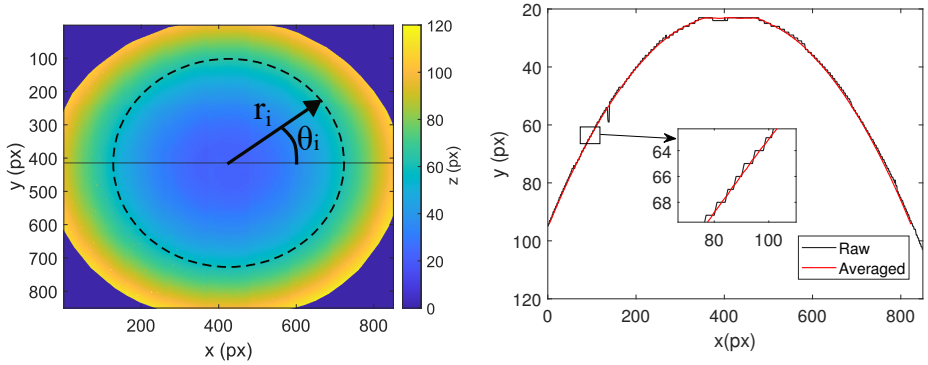

(a) (b)

Figure 2.31: (a) Colored map of the Z-coordinates of the PDMS for according to the edges shown in Fig. 2.30. (b) 2D edges along the central horizontal black line in the image on the left. The plot underlines the difference before and after the smoothing algorithm.

In order to reduce this noise and to smooth the edge, a circular average is adopted. First, the center of the sphere is searched fitting the Z coordinates with a spherical function. Then,

starting from the center and for a given radius r_i, the angle θ_i is incremented gradually to find the corresponding Z-value at the corresponding extremity of the vector $\vec{r_i}$. All values of Z measured along the path underlined by the dashed circle in Fig. 2.31a are averaged for a given radius r_i. The procedure continues by increasing incrementally the radius up to the maximum value r_{max}. The number of steps for the radius and for the angle are both obtained dividing the maximum values (r_{max} and 2π) into 1000 steps. This results into more spaced averaging points at the extremity of the volume (far from the center) and a finer average close to the contact zone. The results of this smoothing is visible in Fig. 2.31b for a profile corresponding to the central horizontal black line on the colored map. Clearly, this method only applies for axisymmetric profiles.

Digital Volume Correlation applied to contact experiments

Before performing Digital Volume Correlation to measure the displacement field in our experiments, some pre-processing of 3D images is necessary as illustrated in Figure 2.32. First, starting from the original image, the PMMA is removed (we remind that the DVC will only be performed in a ROI entirely positioned in the PDMS) and a corresponding mask is created with values between 0 (for voxels outside the PDMS) and 1 (for voxels inside the PDMS). Second, to remove the image background and to exalt the particle pattern, a Gaussian Blurring Filter is applied on both the original image removed of the PMMA and on the mask with a kernel size of 30x30x30 voxels (typical 3D images used for DVC have a size of 850x850x350 voxels). This filter, which is typically used to reduce image noise and details in an image, is a convolution of the image with a Gaussian function with a kernel size decided by the user. For each pixel in the image, the values inside a square kernel surrounding the input pixel are used to determine a Gaussian distribution of gray-values. Then, the value in the pixel in the output image is the one at the center of the Gaussian distribution determined before. In other words, the values of each pixel's value in the output image are the weighted averages of each pixel's neighborhood where the weight is determined with a Gaussian distribution as a function of the distance of the pixel with respect to the center of the Gaussian function. The main results of this filter is to reduce the image's high-frequencies; a Gaussian Blurring filter acts then as a low-pass filter. The objective of applying this filter on the mask too is to remove the high-frequencies values outside the PDMS bulk that can affect the correlation at the PDMS boundary.

Figure 2.33 shows the profiles of gray-values taken along the colored straight lines in Fig. 2.32 to underline the effects of the different operations on the images. The profile of the original image is shown in red where lots of peaks are visible, essentially due to the presence of the dispersed particles. After the application of the Gaussian Blurring, the profile is smooth and contains only the low frequencies of the precedent profile (the profile for the blurred mask is not shown for simplicity). The profile of the blurred original image divided by the blurred mask is shown in blue and shows an almost straight line passing through the average values of the red one. Finally, to obtain the final image, the original image is divided by the blurred image of itself to obtain the purple curve. With this division, the low frequencies are removed or, in other words, the background noise is removed exalting only the peaks corresponding to the particles which will simplify the correlation between two successive images. The final image shows a visible improvement with an higher contrast between particles and matrix.

The DVC code used in this study is a python code (pyFEDIC module) created by Joël Lachambre (CNRS). The procedure is based on the division of an observed Region Of Interest (ROI) into several connected elements forming a mesh. Some examples of the used mesh for the

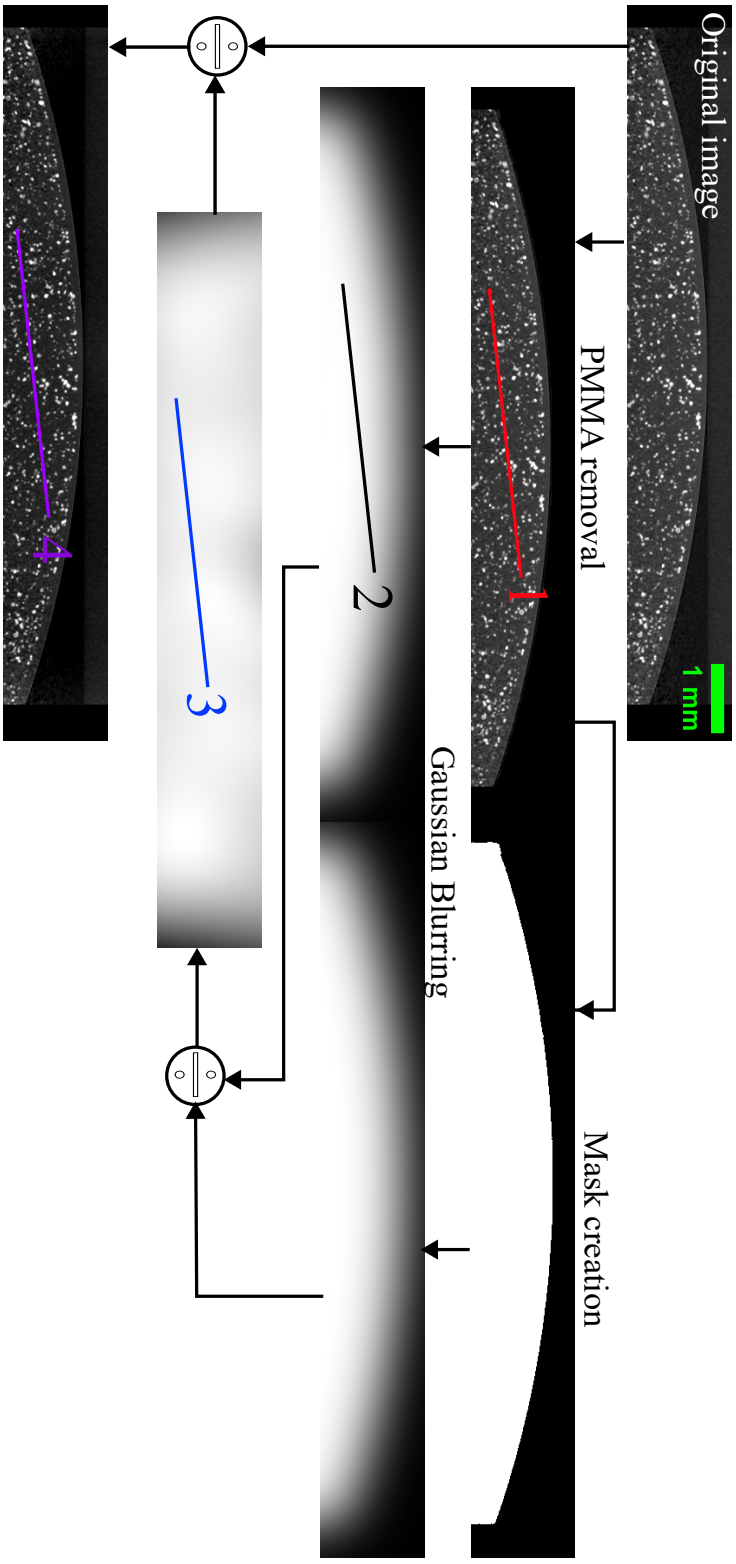

Figure 2.32: Illustration of the process used for the preparation of the 3D images before the Digital Volume Correlation computation.

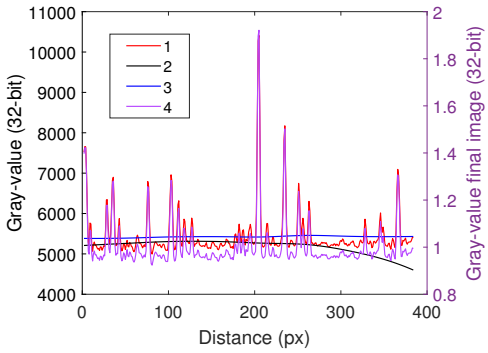

Figure 2.33: Profiles of gray-value for the images in Fig. 2.32. These correspond to the colored lines on the figures using the same colors.

DVC are shown in Fig. 2.34 both for the samples filled of glass and aluminium particles. The shape of the mesh follows the one of the PDMS having the same radius of curvature. To obtain that, an initial cylindrical mesh is used and the positions of the nodes are adapted to follow the shape of a mask corresponding to the PDMS sample using an interpolation method. The external diameter of the cylinder and its height are chosen to exclude a given region from the boundaries of the image in order to avoid movement of external material (with respect to the initial configuration) entering into the ROI and to ensure the convergence of the computation.

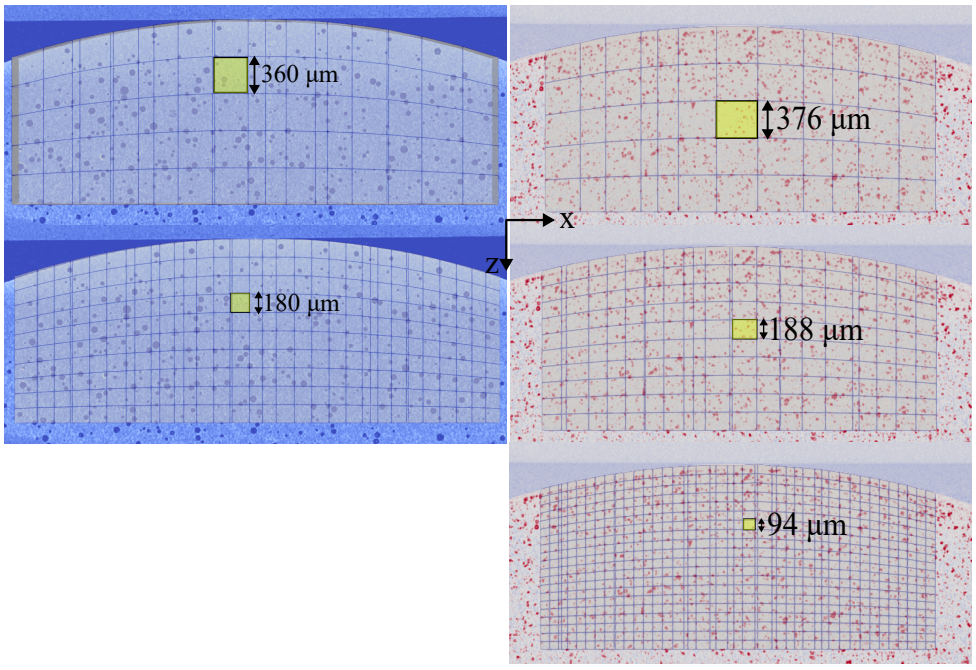

Figure 2.34: Examples of the meshes used for the DVC in the case of the PDMS filled with glass particles (left) and aluminium particles (right). For all images, the resolution is 8 µm/voxel.

Then, to prevent the presence of local minima, a multi-scale solution [37] is used by refining the mesh between each step of the correlation. This methods consists of making smaller and smaller images by aggregating the pixels by a scale factor of 2 between each step. It means that, for an image of $L \times M \times N$ voxels (scale 1), we create an image of $\frac{N}{2} \times \frac{M}{2} \times \frac{N}{2}$ at the scale 2 and an image of $\frac{N}{4} \times \frac{M}{4} \times \frac{N}{4}$ at the scale 3. To keep the same element size in voxels and the same pattern inside one element, the mesh is coarsened by the same ratio as the volumes at scale 1

to scale 3. In this way the coarsest mesh is used for the most aggregated image, while the finest mesh for the original image. Finally, with this method, the solution obtained at the scale 3 is used as a solution for the scale 2 and so on up to the scale 1.
By looking at Figure 2.34, one can see how the mesh is refined up to the original image. We started, in both cases, from a mesh made of 5 layers in the direction Z which is refined with 10 and 20 layers to the finest case. Unfortunately, one problem occurred for the PDMS filled of glass particles because of the particle size and dispersion. In fact, for this type of pattern an element mesh smaller than nearly $180\ \mu\mathrm{m}$ is not applicable at the original scale because several elements contain no particles, leading thus to a bad correlation accuracy and an high correlation residual. Furthermore, a mesh having this element size is too coarse to capture the evolution of external skin of the deformed PDMS and results into an approximate displacement measurement, as the nodes are too far away from each other. As a matter of fact, the glass particles were originally inserted for particle tracking rather than for DVC. However, as visible in the image, the use of aluminium particles allows to refine the mesh size by a factor of 2. As a consequence, a more detailed measurement of the displacement field is obtained, leading to a better evaluation of the PDMS surface deformation during the application of normal and shear loads.
Furthermore, in order to deal with the high deformations especially encountered during shear experiments, the incremental DVC method is used, where the reference image is updated at each step with the displacement field measured during the previous step. In the following chapters only the results obtained with aluminium particles and using the incremental method will be shown for field measurements.

Interpolation of the DVC data

The 3D DVC displacement field is measured at the nodes of the finite element mesh. As the number of nodes is finite, the plots of the displacement or strain field can be step-like. In order to smooth the data, a linear interpolation is performed (see Figure 2.35). Figure 2.35a shows the position of the mesh nodes from a top-view with black circles while the interpolating grid, obtained with a mesh of 500x500 points, is shown in red. Figure 2.35b shows a zoom which allows to distinguish the red and black points relative position. The two horizontal lines in Figure 2.35a (in white) and in Figure 2.35b (in black) depict the average element size. Linear interpolation of the DVC nodal data on the dense grid (in red) enables for example to obtain a smooth representation of the vertical surface displacement U_z as illustrated in Figure 2.35c along the central $X-Z$ plane of the specimen during the compression test. Figure 2.35c shows at the same time that the interpolation does not interfere with the DVC nodal measurement (black points).

DVC residual and uncertainty

Beyond the measurement of the 3D displacement field by DVC, the correlation residual also provides interesting insight about the quality of correlation. It is defined as

$$R = |f(x,y,z) - g((x,y,z) + U(x,y,z)| \tag{2.2}$$

which is basically the absolute value of the difference between the reference image and the deformed image corrected by the calculated displacement $U(x,y,z)$. This quantity, in fact, contains several information such as the potential apparition of noise between the two images or the change in contrast. While it is sometimes useful for the detection of porosity or cracks, in the present study, it is rather useful for identifying areas where the displacement field has been

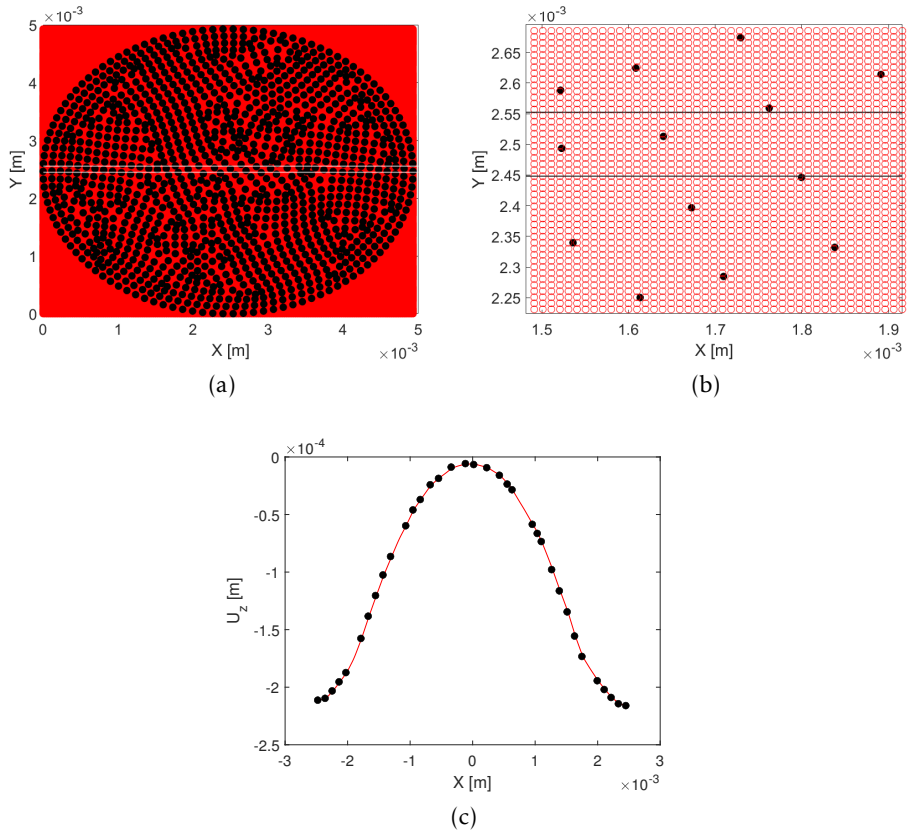

Figure 2.35: Interpolation of nodal data on a denser grid to smooth the representation of the measured fields. (a) Coordinates of the mesh nodes at surface. (b) Zoom on the coordinates of the mesh nodes (black circles) with representation of the interpolating points of the grid (red circles). (c) Profile of the vertical displacement field during a compression test along the contact diameter: raw data (black circles) and interpolation result (red line). The two horizontal white lines in (a) or the two horizontal dark lines in (b) represent the average element size.

measured with better precision. Figure 2.36 shows the residual during a normal indentation test under the application of δ_c =280 µm on the central $X-Z$ plane. Data is represented as the percentage of the overall gray-scale of the *8-bit* image (values ranging from 0 to 255). Despite the fact that it is accumulated due to the use of the incremental algorithm, the residual shows a maximum value of the order of 3 %. Considering that the perfect correlation with a residual of 0 cannot be obtained, such low residual is acceptable and indicates that the DVC calculation works properly with our images and the applied incremental algorithm. It is worth to underline, however, that the maximum residual is reached close to the PDMS surface and below the contact area. This can come from two mains reasons: first, the image noise is higher at the PDMS surface than in the bulk and, second, the surface is the part of the specimen exhibiting the highest gradients in displacement and strains, which complicates the correlation at each step of loading.

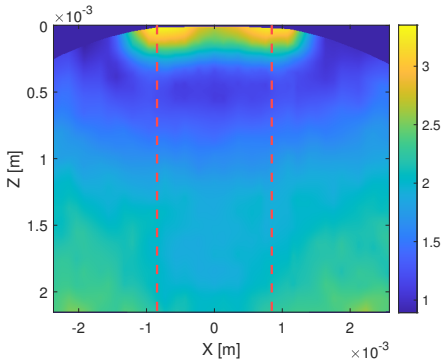

Figure 2.36: Residual of correlation during a compression test (δ_c =280 µm) on the central $X-Z$ plane. The unit of the residual is the percentage of the global gray-level scale that ranges, in this case of a *8-bit* image, between 0 and 255.

To compute the uncertainty of the field measurement we conduct a simple rigid body motion experiment. We move the specimen on the Z axis by 0.5 voxels according to the image resolution. This allows to characterise both the quality of the image acquisition (contrast, stability of the specimen) and of the precision of the DVC algorithm. The standard deviation σ_i of the displacement is computed for the three components in space and the uncertainty becomes [68]:

$$uncertainty = \sqrt{\frac{\sigma_x^2 + \sigma_y^2 + \sigma_z^2}{3}} \tag{2.3}$$

The evolution of this uncertainty is plotted in Figure 2.37 for different sizes of the finite element mesh used for the DVC procedure. In the present study, with an average element size of 12 voxels in the mesh, the uncertainty is of the order of 0.086 voxels (see red cross in the figure). As a conclusion, we can confirm that the measurement of the displacement field by DVC is determined with a sub-voxel resolution. It can be also remarked how this uncertainty decreases with the size of the element that can suggest to adopt coarser meshes to reduce the error. However, this reduction is not linear and shows a plateau at high element sizes. Because the improvement in uncertainty is less important at high element sizes and because we need a fine mesh to better reproduce the deformation of the body close to the contact area, the element size of 12 voxels is identified as a good compromise.

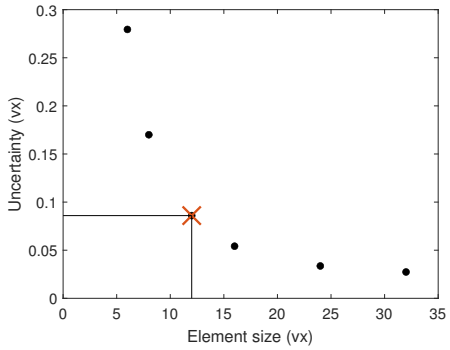

Figure 2.37: Uncertainty of DVC computed according to equation 2.3 for an experiment where a simple rigid body motion is applied to the specimen.

2.5 Conclusions on experimental methods

Up to now, we have seen how the experiments are obtained and what type of data is available for the analysis. To summarize, after one series of experiments we have, for each loading step:

- the measurement of the normal P and tangential Q forces;
- a 3D reconstructed volume;
- a 3D segmented volume where each material (PDMS, PMMA and air) has been identified;
- the values of the normal δ_c and shear δ_s displacements;
- the 3D displacement field in the bulk obtained through DVC.

In the next two chapters, respectively dedicated to normal loading and to shear loading, these quantities will be used to present results and discussions. We will look at the evolution of the contact area trying to benchmark the measurements with the optical experiments. In addition, the access to the surface and bulk displacement fields will allow us to compare the measurements with existing theoretical contact models and to demonstrate how such 3D measurement procedure is able to provide new and important insights on the soft contact mechanics of a model sphere-on-plane sample subjected to compression and shear.

3 Normal indentation experiments

After having introduced the details of the experimental methods and the post-processing algorithms, which allow to extract the contact area and the displacement field in 3D from an XRCT experiment, we show here the main results concerning the normal loading experiments. The two images on the left of Figure 3.1 show our PMDS sample before and after an indentation δ_c along the central $X-Z$ plane of the reconstructed volume. On the right, the resulting measured displacement field is plotted, obtained by Digital Volume Correlation. In this chapter, we start from the analysis of the contact area, showing how is possible to measure it without the limits of optical transparency. We also take advantage of the simple model sphere-on-plane system used in this work to go deeper into the limits and the uncertainties related to the measurement of the contact area. We then present results that were not available with simple 2D optical experiments up to now: the 3D measurement of the superficial and bulk displacement field of a sphere-on-plane mono-contact. Finally, adopting FEM simulations solely based on the experimentally measured 3D displacement field, we show the evolution of the stress field during indentation. By comparing the results with existing theoretical contact models, we underline their limits and emphasize the necessity of new theoretical models which could accurately describe our three-dimensional measurements.

3.1 Analysis of the contact area

Figure 3.2 shows an example of the contact area patch extracted, after the Marching Cubes algorithm on the segmented volume, on the specimen A-20-G indented of $152\ \mu\mathrm{m}$ (see section 2.4.2). In the present case, the shape of the real contact area A_R reduces to a circular area as expected for a smooth sphere-on-plane contact between isotropic materials, according to contact mechanics equations [69]. Starting from this mesh, the value of the contact area is measured as the sum of the area of each element in the mesh (in the following, the values of A_R refers to this sum). The superposition of the red circles highlights the limits of the presented procedure. Indeed, if we consider a smooth isotropic soft sphere in contact with a smooth rigid plane, the models predict a perfectly circular and smooth contact area. In our case, the global shape is isotropic but the external boundary is not perfectly smooth and exhibits some irregularities leading to a rough contact boundary. The aim of the two red circles is thus to underline and quantify the effects of this roughness on the contact area measurement: they connect respectively the peaks and valleys of these irregularities at the contact boundary. Then, the areas of these two circles are used to define an upper and a lower bound of the 3D measurement of A_R, *i.e.* the error-bars related to the measured contact area.

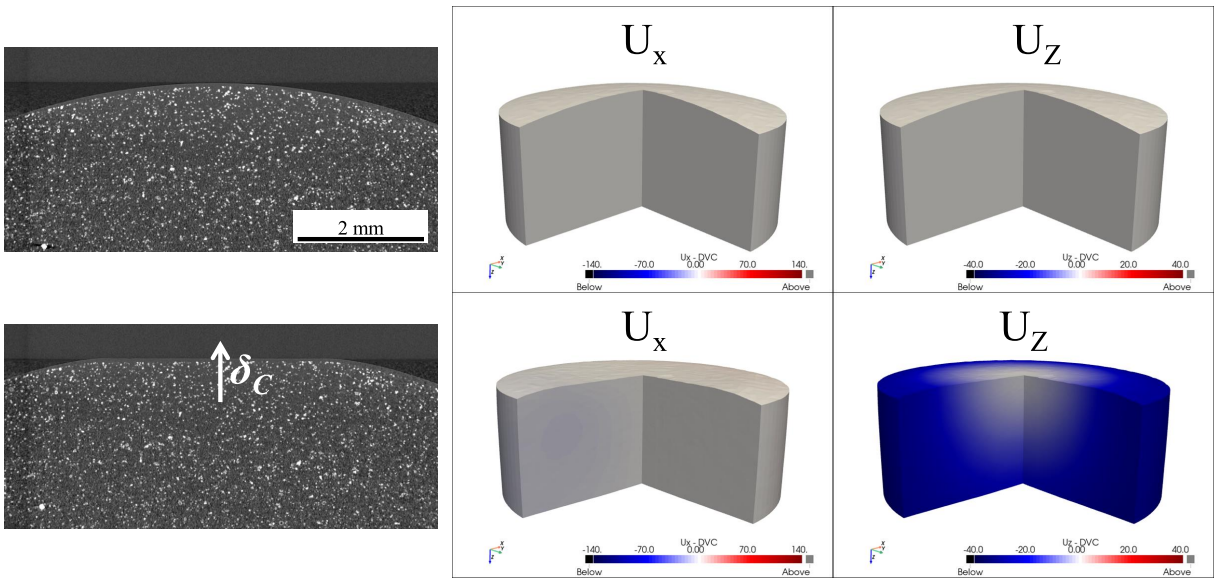

Figure 3.1: First row: slice of the reconstructed volumes on the central $X-Z$ plane (left) and measured displacement field (right) before application of the normal indentation. Second row: slice of the reconstructed volumes on the central $X-Z$ plane (left) after the application of a compressive displacement ($\delta_c = 280$ μm) together with the measured displacement field on the right. Specimen B-10-A.

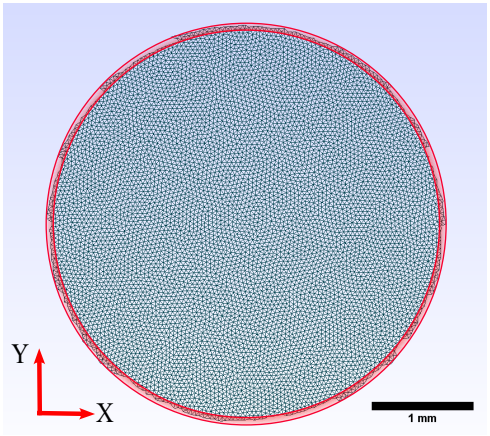

Figure 3.2: Contact surface mesh extracted from the surface reconstruction obtained with the Marching Cubes algorithm. The connection of the peak and valleys of the contact boundary defines an internal and an external circle (in red). The areas of these circles are used to determine the error-bars in the contact area measurement.

We connected the origin of this irregular boundary of the contact zone to the presence of image artefacts, whose origin will be presented in the following section together with some tests carried out to reduce them.

3.1.1 Image artefacts

Fig. 3.3 shows the typical artefacts in our reconstructed images from tomography; it contains some slices of the 3D volume taken along an $X - Y$ plane starting from the PMMA plane (Fig. 3.3 (a)) and going down throughout the PDMS (Fig. 3.3 (b-f)). The images underline the presence of some streaks starting from the boundary of the contact circle. They become more and more visible when approaching the contact plane. In our opinion, these streaks are due to the fact that the contact surface is contained in a plane parallel to the propagation of the X-rays.

To clarify this effect, we first should remind that the geometrical configuration of our experiments promoted the presence of the so-called "phase contrast" [70]. Indeed, this phenomenon is usually weak on laboratory tomographs but, in the present case, it becomes very important because of the long propagation distance of the X-rays on each side of a dissimilar interface. To be more precise, the intensity of this phase contrast could have lead to the saturation of the detector at some particular angles during the rotation of the loading machine and could have cause these well-known "streak artifact" [71]. Unfortunately, the tomograph's reconstruction algorithm only considers the attenuation of the X-rays and not the phase shift. As a consequence, this phase contrast can disturb the subsequent segmentation procedure. Furthermore, the presence of a planar surface (the PMMA surface here) could be difficult to capture in a discrete referential such as a grid of voxels. If, for example, the plane is slightly misaligned with the reference plane defined by this grid, the planar surface could appear with regular steps of 1 voxel height following the tilting of the plane.

Several solutions were attempted to solve or simply reduce this problem and Figure 3.4 illustrates their effects on the streak lines for the case of a specimen A-10-G indented of 200 μm. Figure 3.4(a) shows the artefacts in the initial configuration: the PMMA is a disk with sharp edges and the contact plane is aligned with the horizontal central axis of the detector (the X-rays are parallel to the the contact plane). To reduce the detector saturation due to the presence of this fixed plane, we tried to shift the rotation axis in the $X - Y$ plane (Fig. 3.4(b)) so that the PDMS does not rotate about its symmetry axis and is not in the same position in all radiographs. Unfortunately, this solution did not solved or reduced the problem. We then tried to increase the voltage of the X-ray beam (Fig. 3.4(c)). Apparently, this reduced the artefacts but also reduced the grayscale contrast between the PDMS and the PMMA which is a key parameter to further perform high quality segmentations. Another test consisted in increasing the number of radiographs which, according to literature [32], seemed to be a solution to reduce this kind of artefacts. Unfortunately, increasing the number of radiographs from 900 to 1500 did not solve the problem neither (see Fig. 3.4(d)). Furthermore, the number of radiographs could not be increased indefinitely to prevent long scanning time that may for instance favor visco-elastic relaxations of the PDMS. Figures 3.4(e-f) show, instead, a test passing from a PMMA disk with sharp edges to one with rounded edges in order to avoid the peak effects linked to the presence of a protruding angle. This solution seemed to slightly reduce the problem without reducing the image contrast. Finally, we tried to shift the entire compressing machine upward in order to avoid that the contact plane be aligned with the horizontal central axis of the detector. This solution found to be the best in terms of reduction of the artefacts but

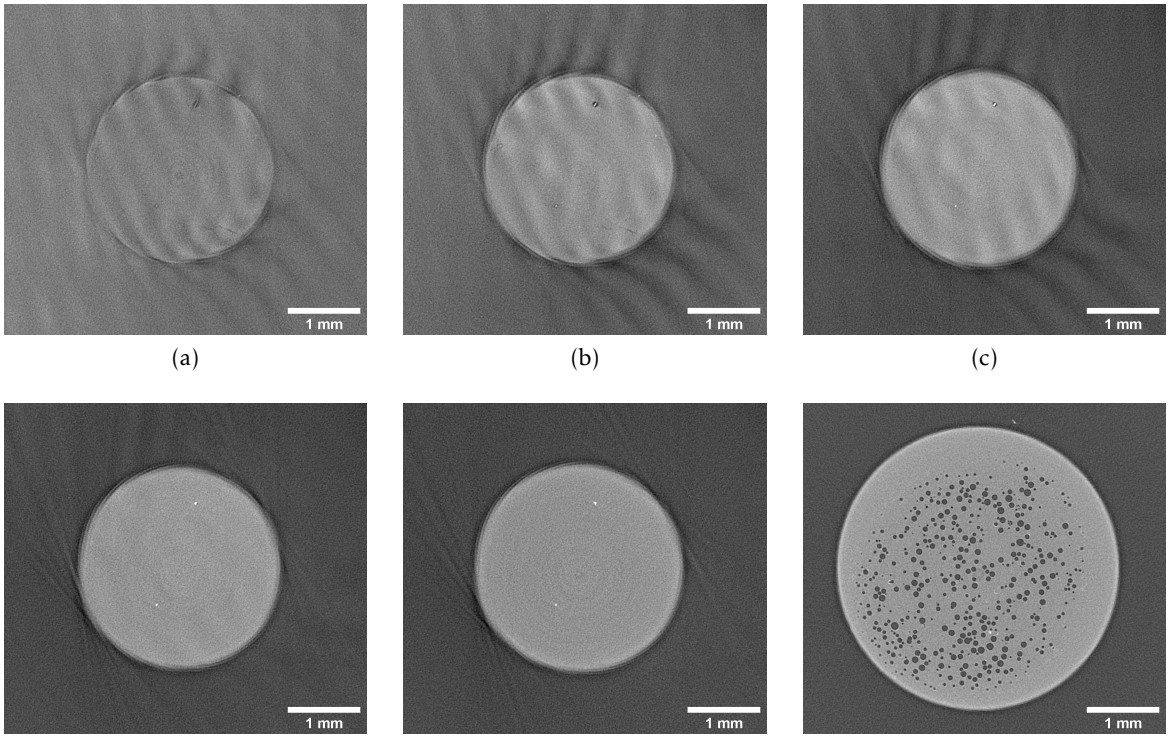

(a) (b) (c)

(d) (e) (f)

Figure 3.3: Artefacts near the contact zone seen on horizontal slices extracted from the 3D volume. The images are taken at different distances moving downwards from the PMMA plane. From (a) to (f) they are $4\ \mu\mathrm{m}$, $8\ \mu\mathrm{m}$, $12\ \mu\mathrm{m}$, $16\ \mu\mathrm{m}$, $20\ \mu\mathrm{m}$ and $220\ \mu\mathrm{m}$. The images correspond to a specimen A-20-G indented of $\delta_c = 152\mu\mathrm{m}$.

it blurred PMMA voxels near the contact zone which again might strongly reduce the quality of the segmentation. To conclude, we were not able to completely remove the streak artefacts. Nevertheless, by adopting the solution based on the use of a rounded PMMA disk we, at least, reduced their effects to a minimum, with as few modifications as possible on the other parameters that can influence the segmentation. Nevertheless, we took into account the presence of these types of artefacts and their consequences on the accuracy of the image segmentation during the analysis of our contact interfaces.

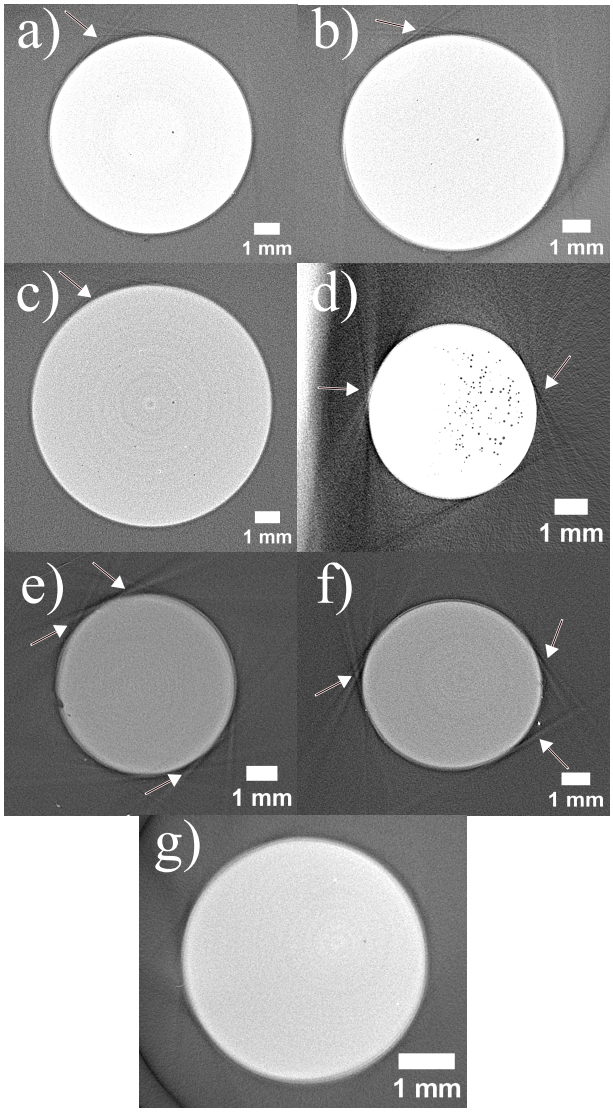

Figure 3.4: Different strategies for reducing the image artefacts near the contact zone. (a) Original image for a scan obtained from 900 radiographs and X-rays voltage an current of $80\ \mathrm{kV}$ and $280\ \mathrm{mA}$. (b) Shift of the rotation axis. (c) Increasing of the Voltage from 80 to 140 kV. (d) Increasing of the number of radiographs from 900 to 1500 per volume scanned. (e-f) Change of the PMMA to one with rounded edges (from e to f). (g) Vertical shift of the compressing machine in the Z-direction (in image (a), the PMMA plane is aligned with the horizontal axis of the detector). The white arrows indicate the position of the artefacts. The contrast of each image has been adapted for each case to exalt the visualisation of the artefacts. All images refer to a specimen A-10-G indented of $200\ \mu\mathrm{m}$.

3.1.2 Evolution of the contact area

The evolution of the contact area is plotted during loading and unloading in Figure 3.5 as a function of the normal indentation δ_c (left) and the normal load P (right) for both the specimens A-20-G and A-10-G which, essentially, only differs in terms of their elastic Young's modulus (they are respectively E ∼0.7 MPa and E ∼2.7 MPa). The behaviour of A_R exhibits an hysteresis between loading and unloading as we already showed for optical measurements (see Fig. 2.21) and as it is predicted in literature [60, 61, 62]. Furthermore, as expected due to its higher Young's modulus, the curves A_R are always smaller for specimen A-10-G for each indentation or force. According to the predictions of the Hertz's contact theory, the relation between A_R and δ_c is linear and the one between A_R and P shows a a power-law behaviour with an exponent of approximately $1/3$. However, as opposed to Hertz's theory, the intercept on the vertical axis is not zero and the value of such intercept is usually attributed to the effect of adhesion [59]. Nevertheless, the intercepts are unexpectedly high in Figure 3.5 with respect to optical experiments.

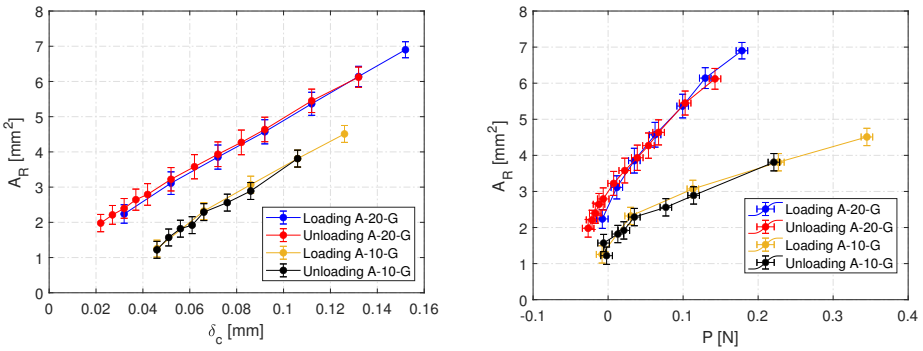

(a) (b)

Figure 3.5: Measured contact area from XRCT. (a) Contact area as a function of the normal imposed indentation δ_c during loading and unloading for the specimens A-20-G and A-10-G. (b) Contact area as a function of the normal measured force P during loading and unloading for the specimens A-20-G and A-10-G.

The evolution of the contact area versus the normal indentation δ_c is compared with the optical measurement in Figure 3.6 during loading for a specimen A-20-G with data obtained from XRCT (blue curves) and optics (purple curve). The different blue curves refer to results obtained with increasing image resolutions: (i) 8 µm/voxel (blue circles), (ii) 4 µm/voxel (blue triangles) and (iii) 4 µm/voxel with a theoretical correction (blue diamonds). While both measurements from the two devices show an affine behaviour as expected by the theoretical models, an offset between the curves is noticeable for the different image resolutions. Discussions about the effect of the reconstruction method and the image resolution will be discussed hereafter together with the theoretical correction in order to understand the origin of these differences.

3.1.3 Effect of the surface reconstruction on the contact area measurement

To ensure that the Marching Cubes algorithm and the corresponding discretization of the contact area by finite elements did not affect the measurement of A_R, we applied the full analysis (reconstruction and computation of the contact area) to an artificial 3D labeled volume

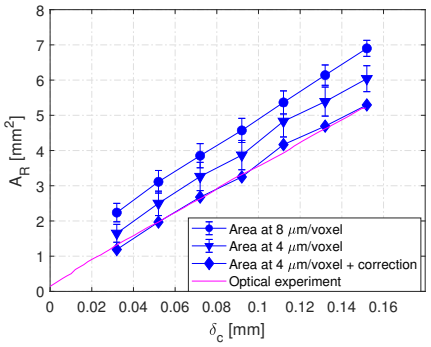

Figure 3.6: Contact area as a function of the normal indentation for different image resolution of the tomograms (4 µm and 8 µm voxel size) compared with the the optical measurement. The figure contains also the corrected curve obtained removing the area of the annulus where the air gap around the contact area is smaller than 4 µm (more details are provided in Figure 3.9). Specimen A-20-G.

made of a sphere (radius of 400 voxels) in contact with a plane intersecting the sphere at 50 voxels from the tip of the sphere. An example of this type of artificial volume is shown in Fig. 3.7 in the top left part. Based only on geometrical considerations (a sphere cut by a plane), and neglecting any mechanical law, this type of sphere-on-plane contact provides a theoretical contact area $A_{th} = 1.178 \cdot 10^5$ pixels. This labeled volume (voxels take the values of 0, 1, 2 for the air, PDMS and PMMA respectively) was used as input for the successive Marching Cubes surface reconstructions using the same procedure as for the real images from XRCT (see section 2.4.2). The result is shown in the same figure in the bottom left part where the finite elements characterising the two bodies (sphere and plane) are clearly visible. Then, the contact area is extracted from this mesh (elements shared between the two bodies) and is shown in the right part of the figure. As expected for such theoretical interface, the contact area is perfectly circular with no roughness on the boundary. The sum of the elements' areas in the contact patch gave the same contact area independently if the mesh was simplified with elements having a edge length of 4 voxels or 8 voxels and we found $A_{4vx} = A_{8vx} = 1.186 \cdot 10^5$ pixels. This result confirmed that the size of the mesh did not affect the contact area measurement. Furthermore, computing the relative error between theoretic and computed values as $(A_{4vx} - A_{th})/A_{th}$, we found a relative error of 0.7% on the estimation of the contact area with this method. Therefore, such small error due to the surface discretization did not explain the differences between XRCT and optical measurements in Figure 3.6. We focused then on the effect of the image resolution during the acquisition of the scans.

3.1.4 Effect of the image resolution on the contact area measurement

To understand the effect of the image resolution on A_R measurements, Figure 3.8 shows how increasing the voxel size results in a blurring phenomenon near the contact edge, which complicates its precise detection. This figure presents the results of the segmentation on a theoretical Hertzian profile ($R = 9.42$ mm, $\delta_c = 152$ µm) after the discretization with a grid of voxels of 4 µm, 8 µm and 16 µm. In our opinion, the origin of the differences between XRCT and optical measurements is connected to the so-called "partial volume effect" and its consequences on segmentation based on the Random Walker algorithm or any other segmentation algorithm.

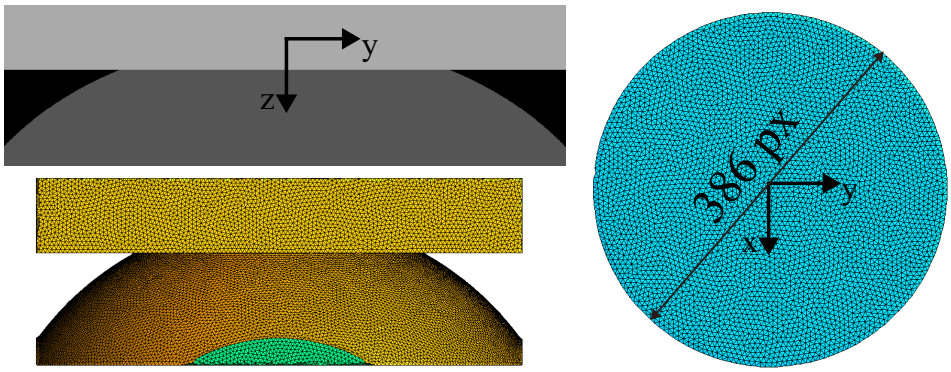

Figure 3.7: Marching Cubes surface reconstruction applied to an artificial sphere cut by a plane to capture the error introduced by this method. The image contains the 3D volume built artificially with three different labels for the sphere, the plane and the air (top left), the obtained mesh with the Marching Cubes algorithm (bottom left) and the contact area patch with its dimension (right).

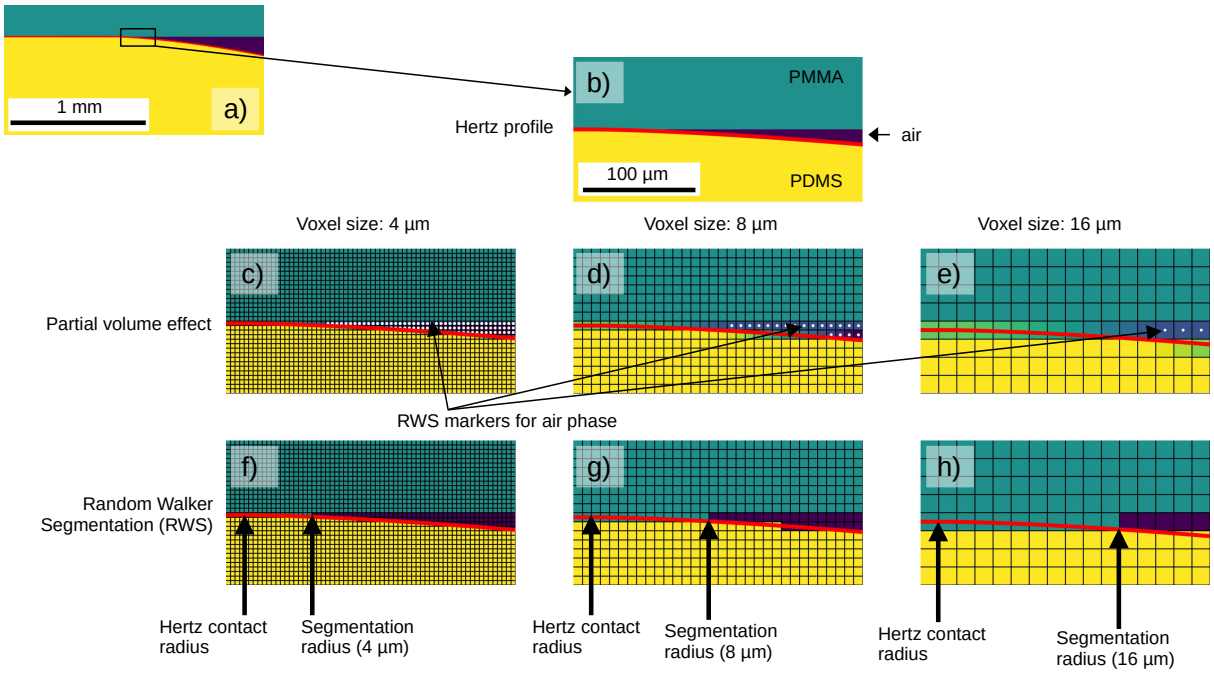

Figure 3.8: Evolution of the contact edge position as a function of the image resolution. (a)-(b) Theoretical Hertz profile of a deformed sphere (R=9.42 mm, δ_c =152 µm) (c)-(e) Partial volume effect at increasing voxel size, from 4 µm to 16 µm. The blurring of gray levels near the contact zone (pixels are averaged between green, PMMA, and yellow, PDMS) tends to move the last air marker (white points) far from the contact edge when the voxel size is increasing. (f)-(h) Random Walker segmentation result. The contact radius tends to be overestimated as the PDMS and PMMA phases diffuse abnormally in the blurred region where air markers are absent. The contact region shown in panels (c) to (h) is the same as that in (b).

Indeed, the partial volume effect is linked to the discreteness of the pixels in the images and tends to blur the gray-level in the regions where there are strong gradients (such as at the contact interface where the X-ray attenuation changes sharply from one voxel to the next in the neighboring materials). In the present case (see fig 3.8b), the border of the contact area is defined by a triple line joining air, PDMS and PMMA and is surrounded by a thin layer of air between PDMS and PMMA. In that region, the partial volume blurring can thus result in a strong overestimation of the contact area if the voxel size (i.e. the overall grid discretization of the image) is not sufficiently fine. Figures 3.8(c-e) show how this blurring is significant when the contact opening is smaller than the voxel size, especially close to the contact boundary where a precise determination of the contact edge is necessary to capture an accurate value of the real contact area. As a result, the positioning of the air markers near the contact tip for the Random Walker segmentation is not easy and they are often positioned far from the real contact edge. This causes an error in the position of the contact edge after segmentation because the PMMA can diffuse more easily towards the PDMS. This error increases dramatically when the voxel size increases (see Fig. 3.8(f-h)). In the present example this additional error on contact radius can be of the order of 10 times the voxel size. The main conclusion is that the measurement of A_R is only accurate at very high image resolutions. Note that any other segmentation procedure (we tested the Watershed [72] and the Statistical Region Merging [73] algorithms for example, on top of standard multilevel thresholding) may also suffer from such partial volume effect near the contact edge. In the present work, the Random Walker algorithm is identified as the most efficient to perform the segmentation operation at a given resolution. On Figure 3.6, by comparing measurement with two voxels sizes (4 µmand 8 µm), we show how the image resolution can strongly affect the measurement of A_R.

Forced by the size of the loading machine and the presence of a conic X-ray beam, our voxel size was limited to 4 µm. We propose then an alternative method to compare our measurements to the optical ones based on theoretical considerations. Figure 3.9 shows the theoretical shape of a deformed sphere on a rigid plane according to the Hertz contact model at two indentations of 32 µm and 152 µm. The contact area corresponds to the plateau at $Z = 0$ while the air gap is located under the curve. Depending on the image resolution, we can assume that the apparent position of the contact edge (the one that can be detected by the image segmentation) corresponds to the position of this theoretical profile at a coordinate Z equal to the voxel size (see the vertical dashed lines crossing the profiles at an altitude of 4 µm and 8 µm from the contact surface).

We can then define an apparent contact radius $\hat{a}$ (the length of the arrows at $Z = 4$µm and $Z = 8$µm for example) that includes an additional contribution δ_r to the theoretical contact radius a_H. As this offset depends on the normal indentation δ_c, we obtain:

$$\Delta_r(\delta_c) = \hat{a}(\delta_c) - a_H(\delta_c). \tag{3.1}$$

The additional contribution to the contact area A_{add} can be then evaluated with respect to the theoretical Hertzian contact area A_H as :

$$A(\delta_c) = \pi\big(a_H(\delta_c) + \delta_c r(\delta_c)\big)^2 = A_H(\delta_c) + \pi\big(2 \cdot \delta_c r(\delta_c) \cdot a_H(\delta_c) + \delta_c r^2\big) = A_H(\delta_c) + A_{add} \tag{3.2}$$

By making the assumption that A_R is close enough to the Hertzian contact area, the value of A_{add} can be subtracted for each indentation from the experimental 3D segmented results. This subtraction is shown in Figure 3.6 (blue diamonds) where now the data are linear, the intercept is close to 0 and in very good agreement with the optical observations. Figure 3.9b also displays

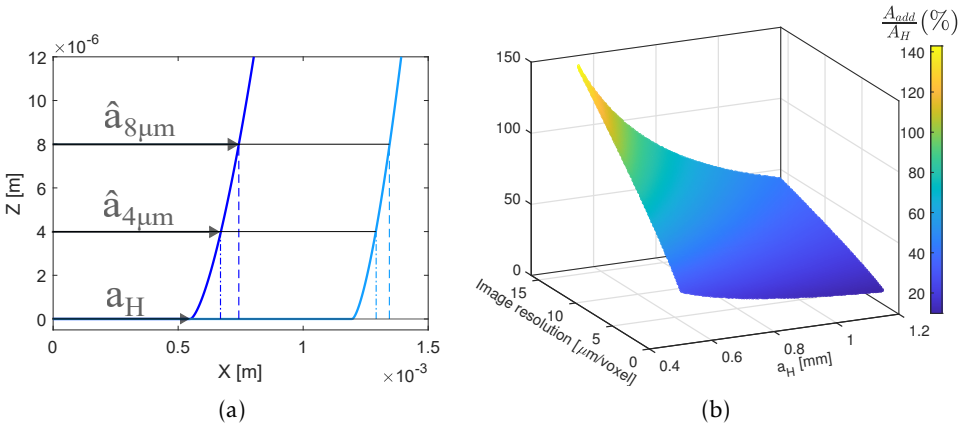

(a) (b)

Figure 3.9: Correction of the experimental measurement based on the Hertz's theory: (a) Deformation of the surface of a sphere (R=9.42 mm) according to Hertz's displacement field, for a normal indentation of 32 µm (red dark blue) and 152 µm (light blue). $\hat{a}_{4\mu m}$ and $\hat{a}_{8\mu m}$ indicates the smallest contact radii detectable with each resolution. (b) Evolution of the relative area error A_{add}/A_H (as calculated using Eq. 3.2), as a function of both the Hertz contact radius and the image resolution (the typical offset from the contact surface).

how A_{add} evolves as a function of the contact radius and the image resolution. This error can rapidly grow to high values when the image resolution decreases (see the growing speed for a given Hertzian radius a_H). Conversely, this relative error is less important and is decreasing when increasing the contact radius for a given image resolution. These considerations too, underline, again, how the measurement of A_R requires the finest possible spatial resolution.

3.2 Surface displacement field

Another important information that we can extract from the image segmentation is the shape of the deformed PDMS specimen during the experiment. This is an outstanding measurement that is not available with classical 2D optical observations and would help understanding important contact mechanisms related to the evolution of the contact area. Figure 3.10 shows, both during loading and unloading, how the PDMS (a specimen A-20-G) is deforming near the contact zone along the central $X-Z$ plane passing through the center of the specimen. These profiles are obtained as introduced in the previous chapter (see section 2.4.2) and correspond to the smooth versions of the original profiles coming from image segmentation as shown in Figure 2.31b. The plots show clearly how the PDMS deforms when a movement in the Z direction is imposed to the vertical translating stage (the PMMA plane is represented here by the horizontal line at $Z=0$). Furthermore, the plot on the right indicates also how the PDMS retrieves its initial position during unloading.

Starting from these profiles, it is possible to extract the surface displacement field by subtracting the original non-deformed shape of the PDMS hemisphere from the deformed ones. The results of this operation is visible in Fig. 3.11 for the three indentations steps indicated before during loading ($\delta_c = 72$, 112 and 152 µm) and unloading ($\delta_c = 132$, 72 and 37 µm). The plots of the obtained profiles are surrounded by colored bands which width corresponds to twice the size of a voxel (here 4 µm) to underline that the real profiles are presumably positioned inside these bands within an error of one voxel on both sides. This uncertainty is related

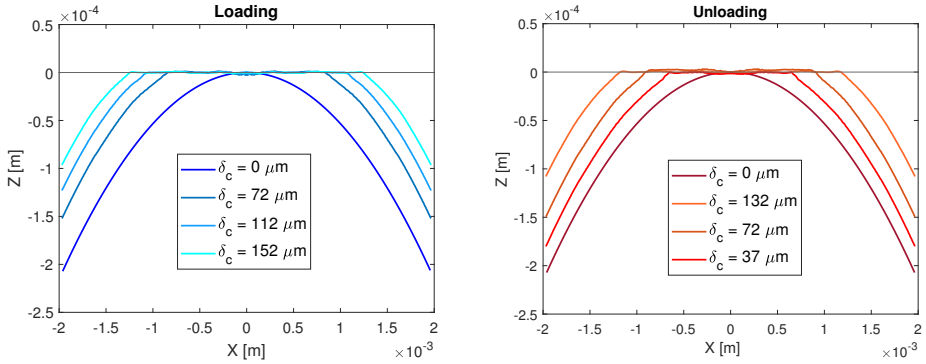

(a) (b)

Figure 3.10: Shape of the deformed PDMS surface as a function of the normal indentation during (a) loading and (b) unloading. Only 3 indentation steps are represented to simplify the visualisation, together with the non-deformed case (δ_c=0). The profiles correspond to the radially-averaged position of the PDMS surface around the contact center (this is possible because the profiles are symmetric with respect to 0). Specimen A-20-G.

to the factors discussed above such as the image blurring and the accuracy of segmentation.

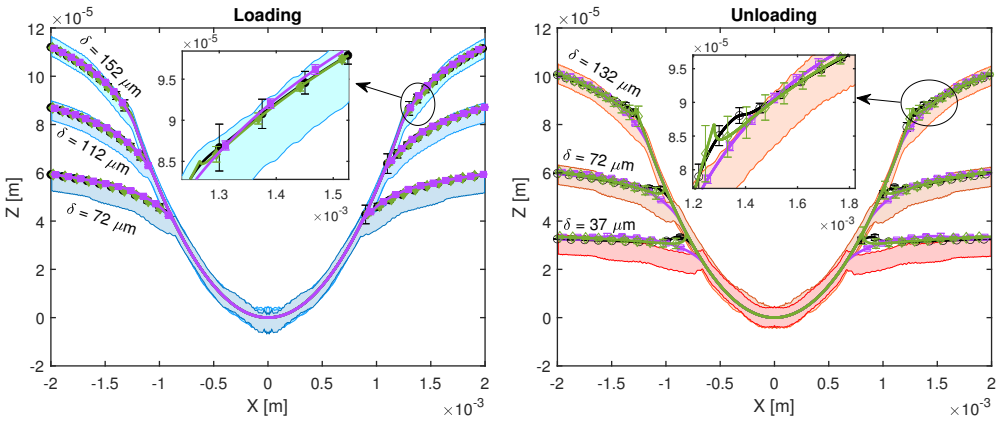

(a) (b)

Figure 3.11: Surface displacement field for the three indentations shown in Figure 3.10 during loading (a) and unloading (b). The colored bands correspond to the XRCT experimental results where the bandwidth two times the voxel size (4 μm). Solid lines are the theoretical profiles calculated with the Maugis-Dugdale (black), JKR (green) and DMT (purple) models. The necessary model parameters are the ones provided in Tab. 2.3. The symbols and colors are the same as in Fig. 2.21. Error bars: see text.

First, we remark how the profile during unloading is above the one during loading for an identical indentation of 72 μm, indicating the presence of an adhesive force delaying the recovery of the PDMS surface to its original shape and causing an hysteresis with probably the same physical origin as the one observed for the contact area evolution (see Fig. 3.5). Second, these figures are also provided in order to compare the experimental measurements with the theoretical displacement profiles evaluated by the three contact models introduced in section 2.3.3: JKR (green lines), DMT (purple lines) and Maugis-Dugdale (black lines). The shape

of these theoretical profiles are obtained according to equations (7.3) and (7.6) of the work of Maugis [74] and by using the material properties provided in table 2.3. The error-bars are related to the uncertainty of the fit parameters and were accounted for in the computation of the profiles through a Monte Carlo method (details in Appendix 6). Basically, we performed 10000 Gaussian draws with the same mean value and standard deviation as in table 2.3 for the three parameters E, ω_0 and λ. From these 10000 profiles we evaluated the mean position and its standard deviation. In the present case, the error-bars corresponds to three times this standard deviation.

The comparison between the experimental results and the models indicates that the agreement between the experimental results and the models predictions is good, especially at large indentation. Nevertheless, some deviations are observed at low indentations, especially during unloading. We link these discrepancies to unavoidable inaccuracies in determining the material properties of PDMS. Indeed, the XRCT and optical devices present different stiffnesses, which can affect the effective indentation applied on PDMS. More importantly, the temperature difference between the two experiments could have affected the mechanical and adhesive properties of the PDMS. As a conclusion, the fit parameters used to calculate the theoretical profiles may not be completely representative of the real experimental conditions during XRCT. If we focus on the slight dissimilarities of the three theoretical profiles, we can notice that these profiles are very similar during loading while some differences are more remarkable during unloading, especially near the contact edge. The JKR profile, for example, exhibits the expected neck near the contact edge caused by short-ranged adhesion forces [17]. In order to see these particularities characterising each of the models, we should have had a better image resolution to reduce the band width of our error-bars and capture these slight details. However, our measurement allowed to capture the global behaviour of the displacement field at the surface, even though an higher resolution is required to capture with accuracy both the contact area and the local surface deformation near the contact edge.

3.3 3D surface and bulk field measurements with DVC

One of the advantages of XRCT is that we do not have only access to surface measurements but also to information inside the bulk. The use of dispersed particles in the PDMS, together with the Digital Volume Correlation procedure, allows to follow the three-dimensional displacement and strain fields inside of the specimens and *in-situ* during the tests. Unfortunately, it was not possible to conduct unloading experiments with the aluminium particles dispersed into the PDMS sample. Indeed, results related to the 3D displacement field will only be shown for the loading and shear cases. Starting from these measurements, we were also able to calculate the 3D stress field by means of FEM simulations with different constitutive models. We present here the main results concerning these measurements, together with some discussion and comparison with theoretical models. For clarity, the values of the imposed indentation δ_c during the normal load experiment are the following:

$$\delta_c = [0, 16, 56, 95, 135, 174, 215, 252]\mu m \tag{3.3}$$

Unless specified otherwise, the Z direction is positive towards the PDMS sample base.

3.3.1 Displacement field

Evolution of the ROI

The evolution of the external boundary of the mesh during a compression test in the deformed configuration is plot in Figure 3.12. From this simple observation, we can clearly assert that DVC is capturing the deformation of the PDMS surface on the PMMA plane (here at $Z = 0$), with the apparition of a growing plateau (indicating the contact area) at increasing indentation. Furthermore, these profiles are also showing a dilation of the specimen in the direction X (see inset) due essentially to the incompressibility of the elastomer. The base of the PDMS is deforming too and not just moving in a rigid manner as expected for the base of the sample. This is due the fact that we are observing a subset of the whole PDMS sample in the vicinity of the contact region in local tomography condition.

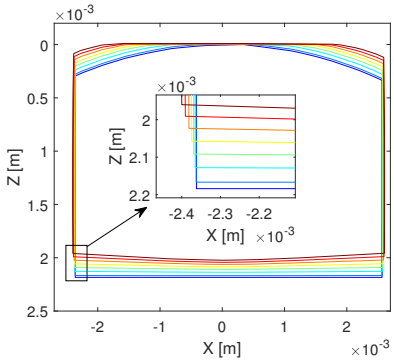

Figure 3.12: Evolution of the ROI used for the DVC along the central $X - Z$ plane during the compression test (deformed configuration). From blue to red the profiles represent all the compression steps according to eq. 3.3. Specimen B-10-A.

Evaluation of the contact area with U_z at surface

Figure 3.13a shows, in 3D, the vertical displacement U_z of the surface at three indentation steps (16 , 135 and 252 μm). The displacement is here presented according to the used reference system: points moving towards the PDMS measures negative displacements. In this 3D representation, the points are positioned on the vertical axis according to their measured vertical displacement in order to easily observe the real movement of the surface inside and outside the contact. For an easier observation, Figure 3.13b presents the evolution of U_z at the surface of the specimen in a cross section along the central $X - Z$ plane. The deformed profile, then, is showed in Figure 3.13c and is obtained, for each step, by adding to the Z coordinate of the non-deformed shape of the PDMS the measured displacement at the same radial position. The evolution of the PDMS shape obtained is similar to the one presented in Figure 3.10 but, in this case, these are obtained with the DVC displacement and not with image segmentation.

The evolution of the profiles in Fig. 3.13b underlines how the displacement is zero at the center (the PDMS can not move due to the presence of the contact with the PMMA) and it is negative elsewhere (*i.e.* moving towards the PMMA plane). Each profile is marked also by a central part with a parabolical shape and two external zones marked by a change of concavity. The points laying on the parabola identify the zone of contact while, far from the center, the presence of the PMMA is less experienced and points are free to move according to rigid body motion. In other words, far from the center, the profiles tends to a plateau. The amount

of points laying on the parabola increases with the normal indentation, indicating how the contact area increases.

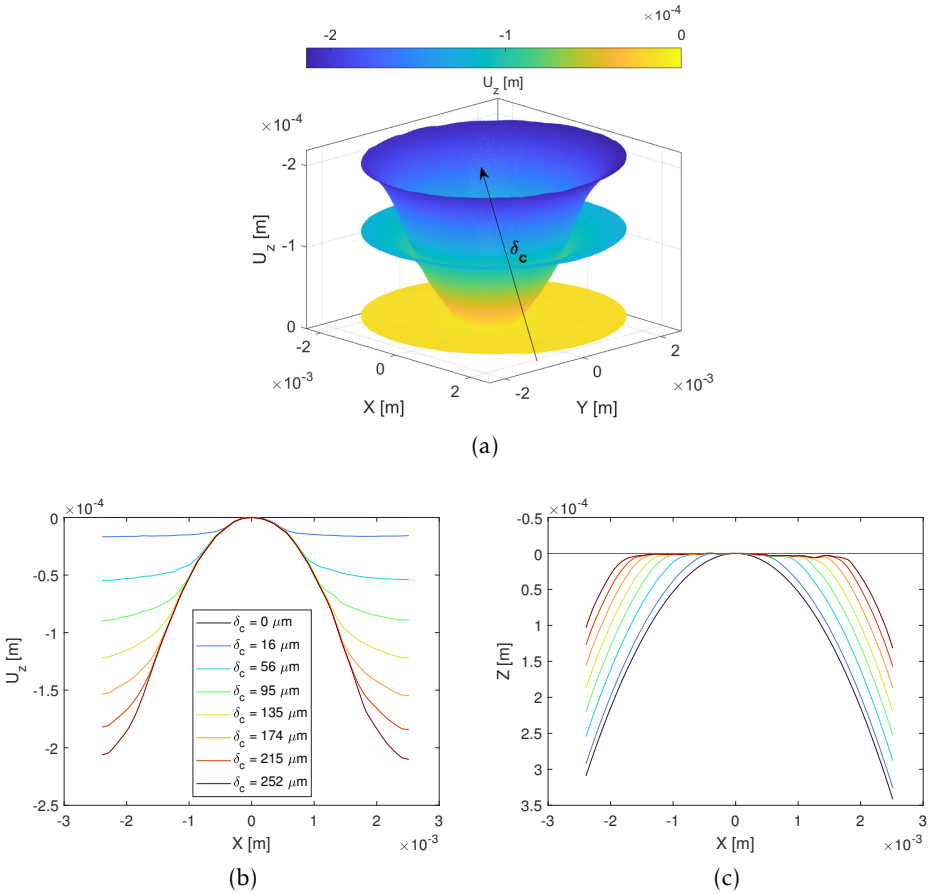

Figure 3.13: (a) Three-dimensional representation on the surface displacement field (component U_z) for three indentation steps of 16 , 135 and 252 µm. (b) Two-dimensional displacement profile of U_z along the central $X - Z$ plane during all the indentation steps. (c) Evolution of the specimen's deformed shape obtained summing the displacement profiles in the plot (b) to the original shape of the specimen. Specimen B-10-A.

As the plateau observed in Fig. 3.13c is strongly linked to contact zone, we propose an alternative method to evaluate the contact area only based on the measurement of the displacement field and its values at the surface of the PDMS sample. Because the transition from the plateau to the non-contact zones is smooth and, due to the difficulties of evaluating the extension of the plateau with a simple threshold on the vertical coordinates, we believe that the extraction of the gradient $(\partial Z/\partial X)$ of the profiles in Fig. 3.13c can exalt the presence of the contact edge. On Figure 3.14a, the contact area can be easily observed as a plateau in the gradient (points share the same vertical coordinate), the dimension of which gives an evaluation of the contact area. The position of the contact edge (see colored points in the figure) thus corresponds to the first point bigger than a threshold indicated by the horizontal dashed line. From these position, it is now possible to evaluate the contact radius. With a profile centered at the axis of symmetry of the sphere, the contact radius can be determined by observing only one side of the gradient profile (positive or negative). Finally, the evolution of the contact radius as a function of the normal load P, for two different samples A-10-A and B-10-A, is plot in Figure 3.14b and com-

pared with the benchmark measurement obtained with the device *optic-2* at the same normal indentations as the tomography experiments. The contact radius is obtained assuming that the area is circular (this hypothesis if confirmed by experimental evidences) and computed as $\sqrt{(A_R/\pi)}$. Error-bars for the contact radii measurement are obtained varying the tolerance of $0.1 \cdot 10^{-7}$ m but are too small to be visible.
The evolution of the contact radius in this way seems to capture very well the evolution of the contact radius of the benchmark experiment for both samples. This new method proves to be reliable for the determination of the contact area and may be applied to different types of interfaces. It only requires the measurement of the displacement field at the surface of the specimen but does not requires any image segmentation and surface reconstruction. Despite the fact that it was done, for simplicity, in 2D, the method can be extended in 3D finding the real shape of the contact area and without making any prior assumption. However, extending it to a the entire surface and not only on one profile would add other difficulties concerning the computation of the gradient and the definition of a unique threshold over the whole surface. Furthermore, we show here that the measurement, contrary to those of Figure 3.6, is not affected by the image resolution and by the image partial volume effects that requires additional considerations to capture the optical experiment.

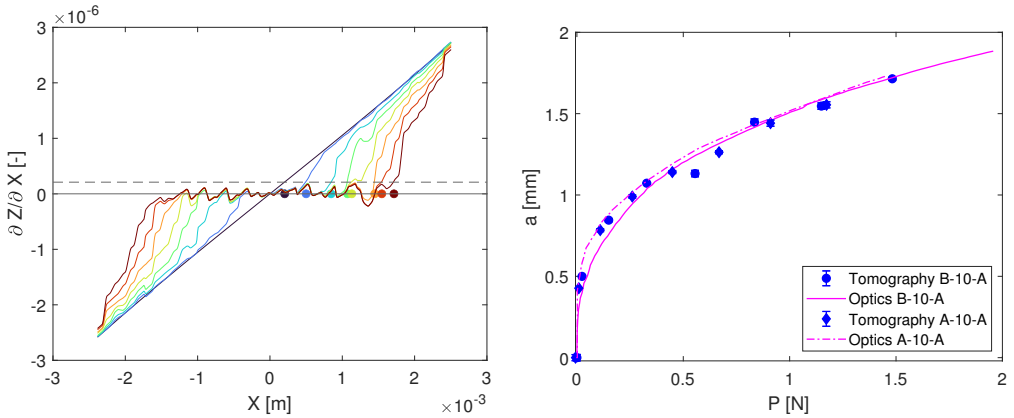

(a) (b)

Figure 3.14: (a) Gradient of plot in Fig. 3.13c, the horizontal dashed line indicates the tolerances adopted for the determination of the contact radii. (b) Evolution of the contact radius at equilibrium versus the measured normal load at imposed displacement for the specimens A-10-A and B-10-A (experiments obtained on the device *optic-2*) compared to the contact radii obtained with surface displacement considerations. Between the two specimens only the height is changing (the heights for specimens A and B are respectively 9 and 6 mm).

Bulk displacement field

The DVC measurement is not limited to the surface characterisation of the PDMS surface but also provides the deformation and the strains inside the bulk. Figure 3.15, for example, shows a vector plot of the evolution of the global displacement field on the central $X - Z$ plane for the same experiment of Figure 3.14. By zooming on two internal points chosen symmetrically with respect to the central vertical axis (see images on the right), we can capture the local movement of the PDMS. The colored arrows (same color code as in Figure 3.13b) indicate where the chosen point was at the beginning of the test (base of the arrows) and where it is at the end of each step (tip of the arrows). Globally, the vertical component Z of the arrows is increasing at each step, according to the global movement of the material as imposed by the

mechanical stage. Additionally, the absolute value of the X component increases towards the exterior of the sample. Accounting for the axisymmetry of the specimen, the behaviour in the direction X corresponds to the radial behaviour of the displacement field.

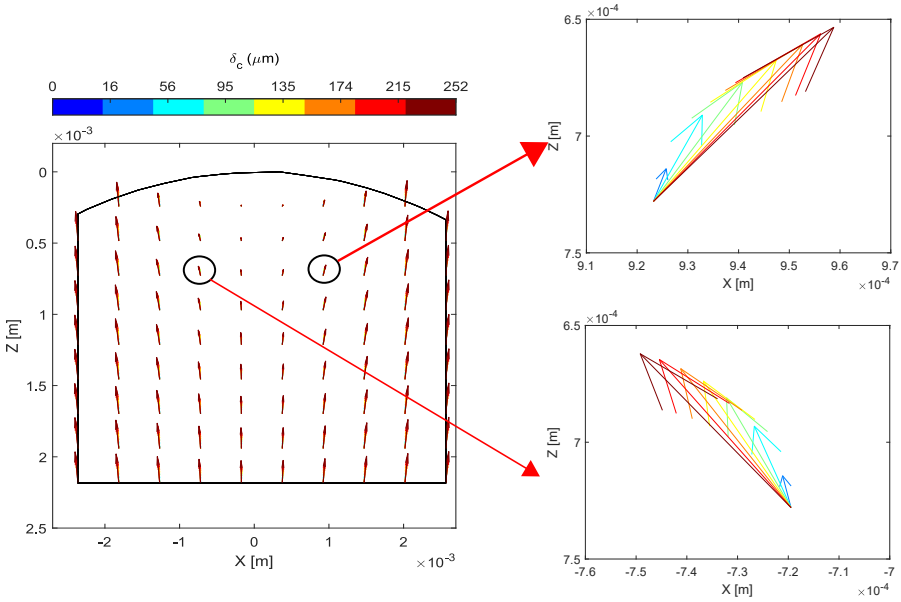

Figure 3.15: Vector field along the central $X - Z$ plane for all the indentation steps (the color code is the same as Fig. 3.13b) and on two arbitrarily chosen points to show the symmetry of the displacement field. The scale of the arrows is of 1:1 meaning that the arrow's tip indicates the position of the observed point at the end of each indentation step. The black contour is the original ROI shape. The measurements refer to the specimen B-10-A.

To better quantify these displacements inside the PDMS bulk, Figure 3.16 and 3.17 show respectively the contour map of the vertical displacement U_z and the lateral displacement U_x both normalised by the imposed indentation δ_c at two indentations steps. For the two figures figures, the shape of the ROI is deformed according to the measured displacement and normalised by the contact radius measured as in Figure 3.14b. The position of the contact boundary is indicated by two vertical red dashed lines at ± 1 and the plots are produced with the same scale to follow the evolution of the same contour lines.

On Figure 3.16, the position of the contour lines is globally the same between the two indentation steps (see for example the highest and lowest point of the contour line at -80 %). This means that the vertical displacement component scales with the normal indentation δ_c and thus with the contact radius a. Secondly, the normalisation allows to capture that the displacement at the contact boundary is always close to 60 % of the imposed displacement while higher values are only reached outside the contact zone. Globally, we could define a parabola starting from the contact edge and assert that the displacement inside this parabola is less than the 60 % of the external indentation. Unfortunately, the size of our observation zone is not large enough to see where the 100 % of the imposed displacement is reached. But we can at least say that almost 90 % is obtained at a distance of two times the contact area.

In Figure 3.17, the lateral displacement field shows the same antisymmetry as the one qualitatively underlined by the arrows in Figure 3.15. The contour lines highlight the presence of

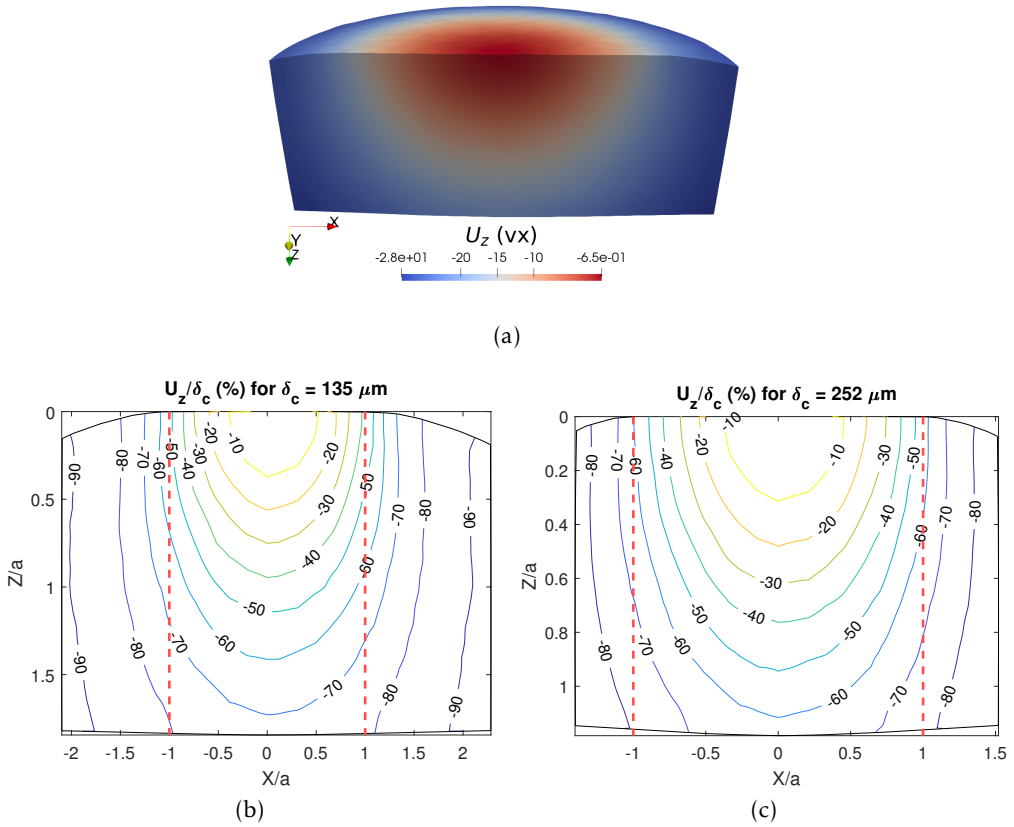

Figure 3.16: (a) 3D observation of the vertical displacement field U_z in voxels in the deformed configuration at normal indentation of 252 µm. (b-c) Contour plot of the displacement U_z normalised by the imposed displacement δ_c on the central $X-Z$ plane for the specimens B-10-A at two indentations of: (a) 135 µm and (b) 252 µm. The vertical red dashed lines indicates the position of the contact boundary.

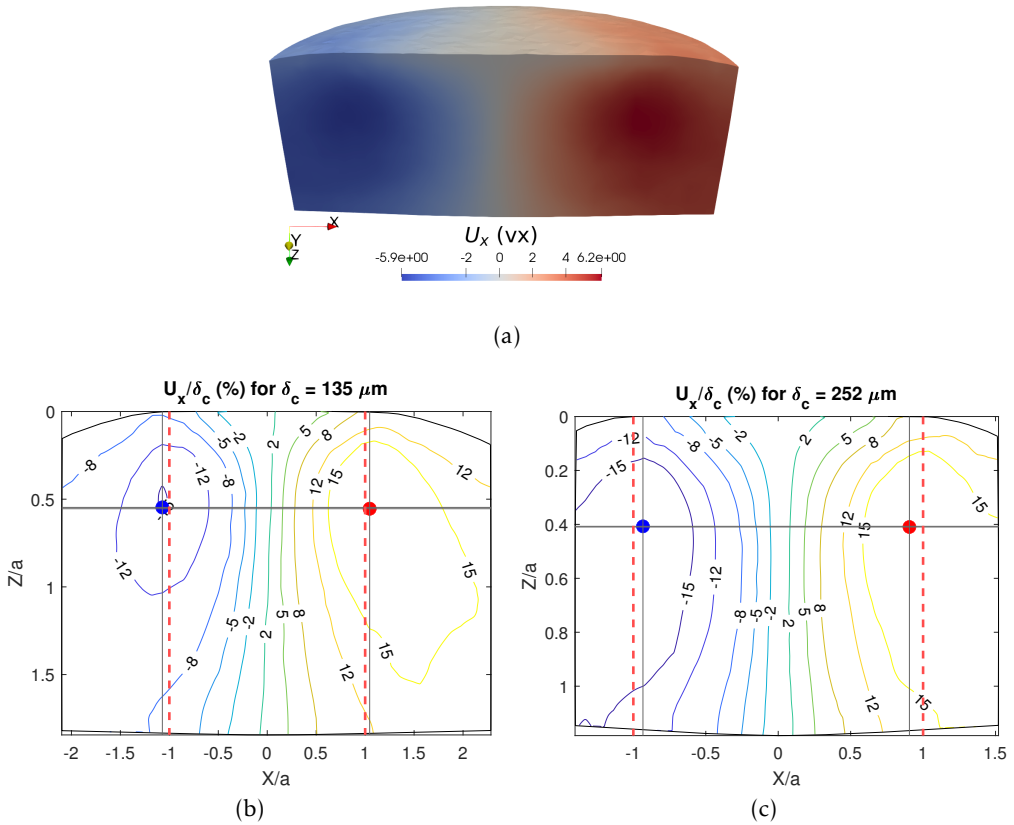

Figure 3.17: (a) 3D observation of the lateral displacement field U_x in voxels in the deformed configuration at normal indentation of 252 µm. (b-c) Contour plot of the displacement U_x normalised by the imposed displacement δ_c on the central $X - Z$ plane for the specimens B-10-A at two indentations of: (a) 135 µm and (b) 252 µm. The red and blue points stand, respectively, for the maximum and minimum values of the lateral displacement. The vertical red dashed lines indicates the position of the contact boundary.

two extremes inside the bulk and below the contact edges. The positions of these minima and maxima can be followed inside the bulk in Figure 6.3 of Appendix 6, which contains the plots for all the indentation steps, and their average values are presented in Table 3.1. The maxima and minima are below the contact edge at a lateral position of $x/a = \pm 1$ and at a depth of approximately 0.5 times the contact radius for all the indentations. This underlines how the position of the maxima and minima also scales with the contact radius. This allows to better understand the global movement of the bulk under the effect of a normal indentation. As soon as the normal displacement increases, the material is compressed towards the PMMA plane and also moves laterally due to incompressibility. This phenomenon is especially true below the contact area, where the vertical movement is obstructed by the presence of the PMMA plane. Outside the region below the contact area, the points are more free to move vertically, they are not forced to move horizontally and the X component of the displacement starts to decrease causing the presence of this maximum (or minimum) at the level of the contact edge.

	Min	Max
x/a	-0.81 ± 0.20	0.99 ± 0.08
z/a	0.43 ± 0.06	0.50 ± 0.09

Table 3.1: Average values of the coordinates of the maxima and the minima of U_x calculated from all the indentation steps as shown in Fig. 6.3 in Appendix 6.

In order to realize how the specimen reacts under the effect of an imposed normal displacement, we would like to plot the evolution of the vertical displacement on the central axis of symmetry of the specimen. So, first, we have to identify this axis which corresponds to the vertical axis passing through the apex of the undeformed sphere, *i.e.* the first point of contact under normal load. As our coordinate system is aligned on the PMMA, we know that the central axis will be vertical and the only unknown is thus the apex of the sphere which will define its exact position. Figure 3.18 shows how the position of this apex was found. We fit (black surface in panel (a), black curve in panel (b)) the position the PDMS surface before contact with an ellipsoid shape equation. The result of this fit is more appreciable in the 2D plot on panel (b) showing the step-like behaviour of the original surface (due essentially to the voxel discretization) and the obtained fit in black. The position of the center of the ellipsoid now can be used as the position of the central symmetry axis of the specimen.

Figure 3.19 presents the evolution the displacement U_z as a function of the coordinate Z along the central axis of symmetry. The values of the displacement U_z are normalised by the imposed displacement δ_c while the coordinates Z are normalised by the measured contact radius at each step. The first observation is that the behaviour of the displacement into the bulk is not linear and monotonic, showing a rapid growth just below the contact zone and a stabilization far from the contact. While the behaviour is similar, for all the steps, up to nearly 0.25 times the contact radius, a growing difference starts from this point as we go down into the bulk. This trend indicates that the points far from the contact feels more and more the presence of the moving rigid glass plate under the PDMS. At a given distance from the contact plane (at a value of 1 for instance), an higher indentation results in an higher proportion of the imposed displacement reached. In other words, the region of influence of the moving base is getting closer and closer to the contact plane. Theoretically, these curves should attain the values of 1 at an height equal to the specimen height (*i.e.* at the base of the specimen, where the

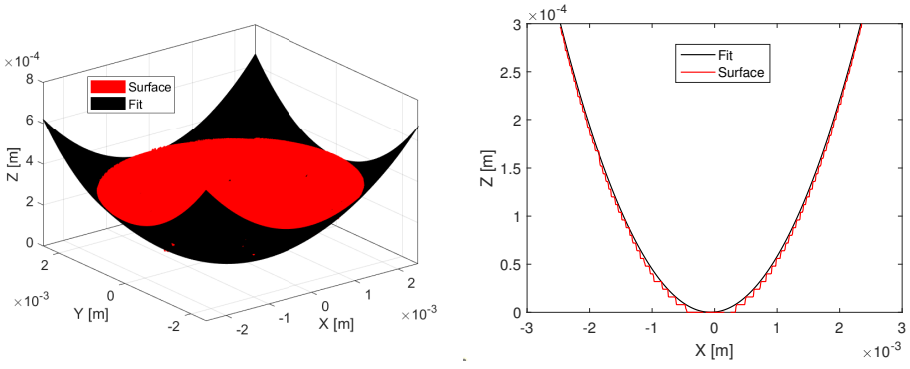

(a) (b)

Figure 3.18: Three-dimensional surface fit with a paraboloid of the PDMS surface not in contact for the determination of the apex coordinate and the relative position of the central symmetry axis of the specimen. (a) 3D representation of the fit. (b) 2D representation o f the fit results on the central $X - Z$ plane. Specimen B-10-A.

displacement is imposed). However, due to our local measurement, the complete stabilization of these curves is not observable.

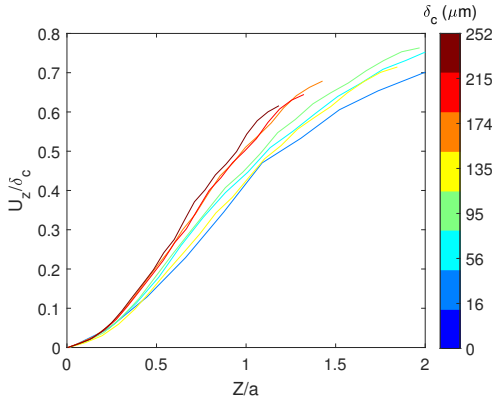

Figure 3.19: Evolution of the displacement U_z normalised by the imposed displacement δ_c as a function of the coordinate Z normalised by the contact radius a along the central symmetry axis. The colors correspond to the indentation steps (same color code as in Fig. 3.13b) increasing from bottom to top. The experimental data are related to the specimen B-10-A.

3.3.2 Strain field

Access to the displacement field measured at mesh nodes during DVC is the basis for element-level strain measurement, which can be calculated in its simplest form using small strain theory (provided that the material does not indeed deform too much). The strain tensor is this case is defined as:

$$\overline{\overline{\varepsilon}} = \frac{1}{2}\left(\nabla\overline{U} + \nabla\overline{U}^T\right) \tag{3.4}$$

where $\overline{U}$ is the local displacement vector.

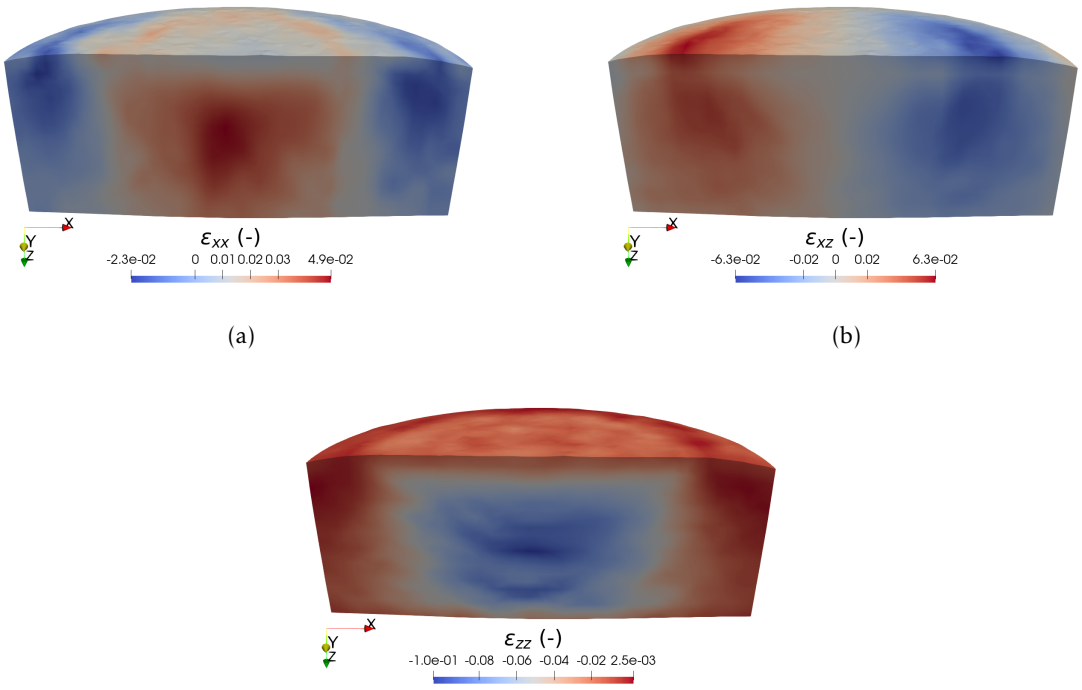

Figure 3.20: 3D observation of the components of strain ε_{xx}, ε_{xz} and ε_{zz} in the deformed configuration for a normal indentation of 252 µm. Specimen B-10-A.

Figure 3.20 shows a 3D view of the components of strain ε_{xx}, ε_{xz} and ε_{zz} in the deformed configuration for a normal indentation of 252 µm and Figure 3.21 presents the corresponding contour maps in the central $X-Z$ plane at two consecutive indentation steps. As for the plots for the displacement field, the ROI is deformed according to the measured displacement field and coordinates are normalised by the contact radius a so that the vertical dashed red lines indicate the contact edges.

In Figure 3.21 (a and b), we observe that the material is in a dilation state (positive values of ε_{xx}) below the contact area while it is in a compressive one (negative values) outside of it. The position of the maxima and minima (on the left and on the right) are visible during all the steps in Figure 6.4 in Appendix 6 while the average values are summarized in table 3.2. The maximum dilation value is reached in the center of the contact area ($X/a = 0$) at a depth that changes as a function of the indentation: it gets closer to the contact plane as indentation increases. The minima are instead outside the contact zone at nearly 1.25 times the contact radius while their depth is not changing considerably and remains between 0.2 and 0.3 times the contact radii.

In Figure 3.21 (c and d), the component ε_{xz} shows an anti-symmetric behavior with positive shear on the left and negative shear on the right, with a neutral line aligned with the center of contact. Differently from the xx component, the maxima and minima (see Fig. 6.5 in Appendix 6 for all steps) are found at the contact edge and at the surface of the specimen. This maximum shear decreases vertically along the contact edge and its relaxed far from the contact plane. This remark, together with what we have observed in Fig. 3.17 where the lateral displacement increases from the contact center to the contact edge, could indicate that the increase in the contact area is not only due to vertical laying (main contribution) but can also be accentuated by the contact dilation. The maximum shear stress found at the surface originates in adhesion effect at the interface between PDMS and PMMA that prevents the lateral movement induced by incompressibility . Points that already are in contact can not move laterally, the shear strain is enhanced at the contact boundary where there is a sudden transition between fixed points (within the contact zone) and points free to move (outside the contact). As a consequence, the presence of an important strain at the contact edge is an indication of the adherence of the PDMS over the PMMA plane: if the contact was frictionless, nothing would have opposed the lateral expansion and the edges would not have been sheared.

Finally, in Figure 3.21 (e and f), in the central $X-Z$ plane, the component ε_{zz} is everywhere in a compressive state with a maximum value reached below the contact zone and at the center of the contact. This is in accordance with the fact that, at a given depth Z, the minimum of the vertical displacement field is measured below the contact center (see Fig. 3.16). In other words, with an increasing indentation, points are more and more compressed below the contact area as they not free to move upward. The depth of the maximum (see Fig. 6.6 in Appendix 6) is also stable around an average value of 0.6 times the contact radius.

The position of highest vertical compression (ε_{zz}) is the same as the maximum of the component ε_{xx} and predicts that this point can be one of the most stressed and should be monitored during the compression of a sphere over a plane. We should also consider the contact edges, where the maximum shear is reached. However, in order to properly consider where, in a sphere-plane contact, plasticity can start (in the case of a metal sample for instance) and then where failures can start, we should rather try to compute the normalised Mises parameter and

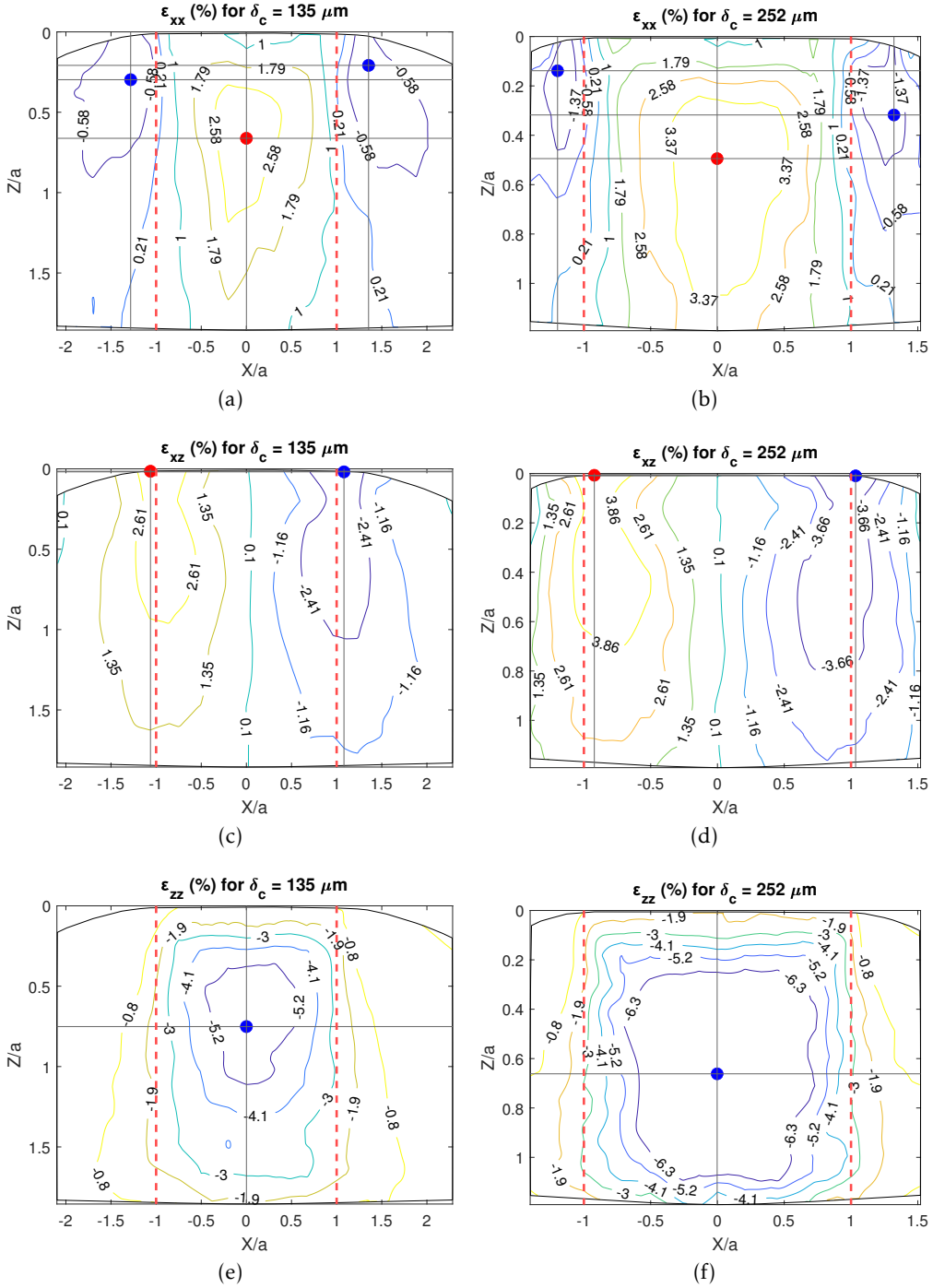

Figure 3.21: Contour plots of the strain field (in %) on the central $X - Z$ plane obtained with the DVC measurement for the specimen B-10-A at two different indentation steps of 135 µm and 252 µm. The plots represent the components ε_{xx} (a-b), ε_{xz} (c-d), ε_{zz} (e-f). The red and blue points stand, respectively, for the maximum and minimum values of the strain the relative plot. The vertical red dashed lines indicates the contact boundary.

find its maximum inside the bulk. We then introduce in the following how we estimate the stress field from the measured displacement and strain fields.

ε_{xx}	Min - L	Min - R	Max
x/a	-1.16 ± 0.09	1.3 ± 0.12	0.04 ± 0.09
z/a	0.25 ± 0.11	0.30 ± 0.10	0.60 ± 0.07
ε_{xz}	Min	Max	
x/a	1.00 ± 0.07	-0.87 ± 0.19	
z/a	0.02 ± 0.01	0.02 ± 0.01	
ε_{zz}	Min		
x/a	0.000 ± 0.001		
z/a	0.65 ± 0.08		

Table 3.2: Average values of the coordinates of the maxima and the minima of ε as calculated from all the steps shown in figures 6.4, 6.5 and 6.6 in Appendix 6.

3.3.3 Stress field

The computation of the stress field in the bulk of the PDMS specimen uses FEM simulation based on the same ROI mesh used for the DVC computation. FEM is performed in this work in the Abaqus-Standard environment. The method is illustrated in Fig. 3.22 where the displacement at the nodes on the surface of the mesh (the ones on the upper, lower and lateral surfaces) was extracted and imposed as the boundary conditions of the finite element simulation. The simulation was performed with two different constitutive models: the linear elastic isotropic one (E =1.55 MPa obtained from the fit shown in Fig. 2.21, $\nu = 0.495$) and an hyper-elastic Arruda-Boyce model [55] that showed to best fit the tensile behavior of our PDMS sample (see section 2.2.3). However, the initial Young's modulus E_0 identified from the tensile test samples was slightly lower than the one obtained from the contact samples (respectively E =1.21 MPa and E =1.55 MPa). The parameters describing the Arruda-Boyce model were therefore adjusted in order to present the same initial Young's modulus as the one used for the linear elastic contact sample simulations. In other words, the Arruda-Boyce fit of section 2.2.3 was stiffened to exhibit E_0 =1.55 MPa at small strains. The corresponding Arruda-Boyce parameters in the FEM code characterising the PDMS material are $\mu = 0.375$ MPa, $\lambda_m = 1.917$ and $D = 0.039$ MPa^{-1}.

When simulating an incompressible elastomer, the choice of proper Poisson's coefficient should be done very carefully. Indeed, in the case of a linear elastic isotropic model the stress components take the following form of (we present here only two of them, shear σ_{xz} and normal σ_{zz}):

$$\sigma_{xz} = \frac{E}{2(1+\nu)}\varepsilon_{xz} = G\varepsilon_{xz} \tag{3.5}$$

$$\sigma_{zz} = \frac{E}{(1+\nu)(1-2\nu)}\Big[\nu\varepsilon_{xx} + \nu\varepsilon_{yy} + (1-\nu)\varepsilon_{zz}\Big] \tag{3.6}$$

Assuming ideal incompressibility of the PDMS ($\nu = 0.5$), the diagonal components of the stress tensor diverge in such linear elastic isotropic model if the lateral strains are constrained. Thus,

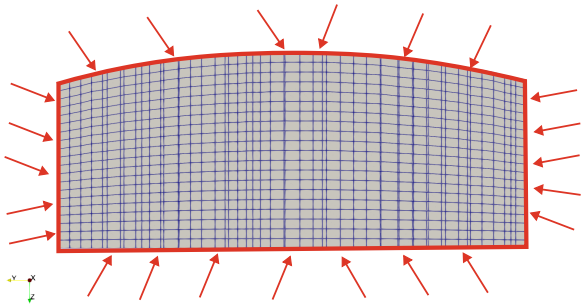

Figure 3.22: Illustration of the DVC-driven FEM simulation. The red contours underlines the surfaces over which the measured DVC displacement was applied as a boundary condition into the simulation.

in a simulation, we could not impose a Poisson's coefficient of 0.5 but a value as close as possible to it in order to avoid singularities in the stress computation. The determination of the best coefficient is presented in Figure 3.23. Imposing a linear elastic isotropic law and the measured displacement from DVC only on the upper and lower surfaces of the mesh, we were able to compute the lateral displacement at nodes. The resulting displacement at nodes on the lateral surface was compared to the one measured by DVC and the root mean square error of prediction (RMSEP) of the difference between these two values was used to find the best ν. As a confirmation of the incompressibility of the sample, the minimum of such RMSEP was obtained for ν close to 0.5. We found that $\nu = 0.495$ was a good compromise to guarantee both a good representation of the mechanical behaviour of our sample and to limit singularities in the stress field. As a conclusion, all linear elastic simulations were performed with a Poisson's coefficient of $\nu = 0.495$, corresponding to a ratio of the initial bulk modulus K_0 to the initial shear modulus μ_0 of 100. Accordingly, the D parameter in simulations with the Arruda-Boyce hyper-elastic behavior was set to enforce $K_0/\mu_0 = 100$.

Abaqus *C3D8RH* elements were used in the finite element simulations. This type of element (8-node linear brick, reduced integration with hourglass control, hybrid with constant pressure) is typically used when simulating the behavior of nearly incompressible materials such as elastomers. Additionally, the large strain formulation was adopted (Abaqus command *NLGEOM = YES*) when simulating the test with an hyper-elastic law.

Figure 3.24 and Figure 3.25 show, respectively, the countour plots of the components σ_{xz} and σ_{zz} in the central $X - Z$ plane. In each plot, the results obtained from simulations (dashed contours) are compared with the predictions of the Hamilton's equations [24] (continuous contours). According to the hypothesis of the this model, simulations were carried out using a linear elastic constitutive law. Plots (a) and (b) contains, respectively, the results for the specimen B-10-A indented of 135 µm and 252 µm. Contrary to previous figures where the ROI was deformed according to the displacement field, here we represent the results in the original reference system in accordance with the Hamilton's equations derived. Regarding the shear component of the stress σ_{xz}, we can confirm that the FEM results for the shear component of the stress σ_{xz} are very well captured quantitatively by the model's prediction for both indentation steps. Conversely, for the component σ_{zz} the agreement is qualitatively good but some quantitative differences are observed especially at low δ_c. We linked this to the limits of our simulations obtained with Poisson's coefficient close to 0.5; a situation that affects more the diagonal components of the stress tensor (the hydrostatic part of the tensor) than the off-diagonal

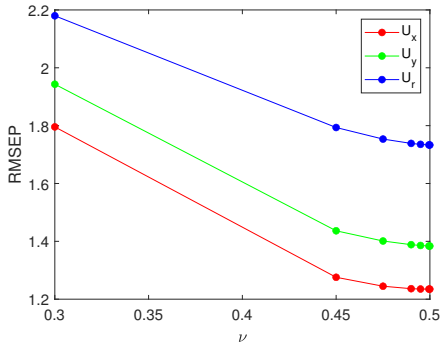

Figure 3.23: Standard deviation of the difference between the the displacements U_{DVC} and U_{FEM} on the lateral surface of the ROI mesh versus the Poisson's Coefficient adopted in the simulation. The plot represents this difference for the three components U_x, U_y and U_r (the radial displacement). The simulations were carried out using a linear elastic isotropic behaviour with an elastic Young's modulus of $E = 1.55$ MPa. The measured displacement field used for the simulation is the one obtained for the specimen B-10-A at a normal indentation of 252 µm.

ones (the deviatoric part).

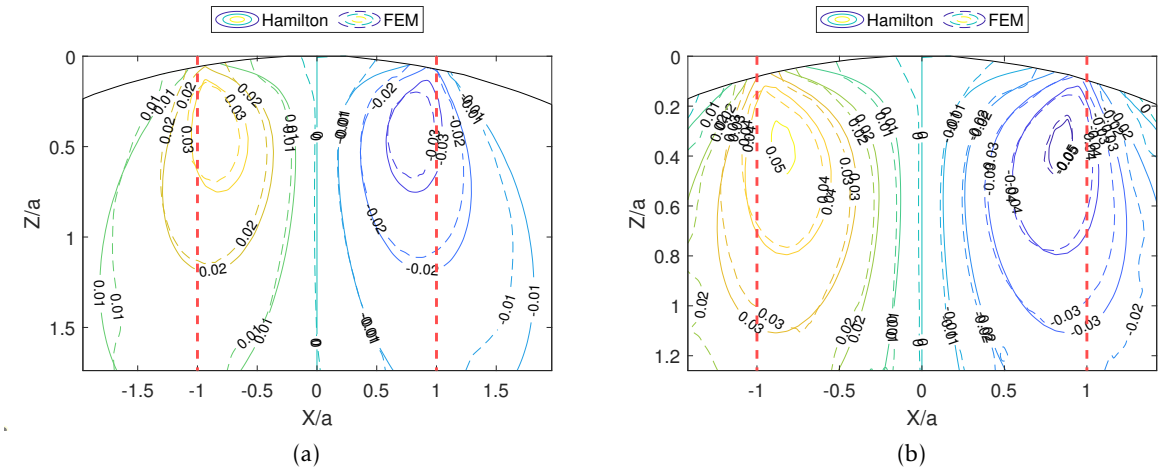

Figure 3.24: Contour plots of the stress component σ_{xz} (in MPa) on the central $X - Z$ plane obtained with DVC-driven FEM simulations (dashed lines) compared to the predictions of the Hamilton's model [24] (continuous lines). The plots represents the data for the specimen B-10-A indented of (a) 135 µm and (b) 252 µm in the case of a linear elastic isotropic constitutive model. The vertical red dashed lines indicates the position of the contact boundary.

The normalised Mises parameter defined with equation 1.18 is finally plotted in Figure 3.26 for simulations adopting a linear elastic behaviour at two indentations of (a) 135 µm and (b) 252 µm. The value of p_0 is derived from Hertz's model with the measured values of the force P and of the Young's Modulus E (see equation 1.3). Similarly, the contact radius a is computed according to the Hertz's model in agreement with the hypothesis of the Hamilton's model. The black and magenta markers represent the positions of the maxima respectively for the Hamilton's model and the FEM simulation.

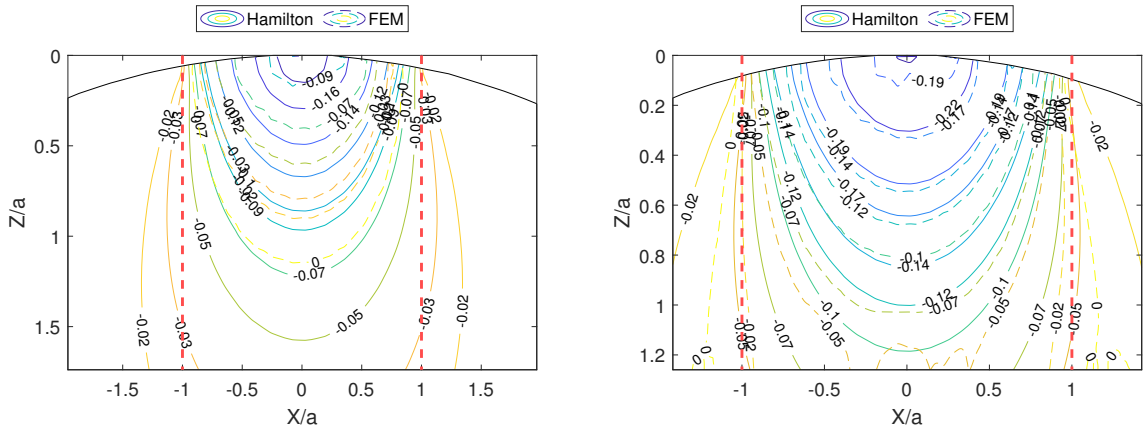

Figure 3.25: Contour plots of the stress component σ_{zz} (in MPa) on the central $X - Z$ plane obtained with DVC-driven FEM simulations (dashed lines) compared to the predictions of the Hamilton's model [24] (continuous lines). The plots represents the data for the specimen B-10-A indented of (a) 135 µm and (b) 252 µm in the case of a linear elastic isotropic constitutive model. The vertical red dashed lines indicates the position of the contact boundary.

The normalised Mises parameter reaches a maximum below the contact center and in the bulk of the sample. From this maximum, concentric isolines are visibile with an important gradient between this point and the contact surface. The contour lines from the FEM simulation and the Hamilton's equations are in very good quantitative agreement for the first indentation step. For increasing indentations, slight discrepancies appear. The general concordance of the simulations and the models can be explained by the fact that the normalised Mises parameter is based on the deviatoric part of the stress tensor, where the potential discrepancies of the hydrostatic part (related to the actual incompressibility of the material) are subtracted. The differences at increasing δ_c can be related to the fact that the real behaviour of our sample can not be properly described by a linear elastic model at higher indentations.

Driven by the observation that the mechanisms of a sheared elastomers are better described by an hyper-elastic constitutive model [7], it is interesting to compare the the stress distributions predicted by the linear elastic model and by the hyper-elastic one (using the Arruda-Boyce model). Figure 3.27 compares the distribution of the σ_{xz} stress component with the two models, for two different indentations of (a) 135 µm and (b) 252 µm. The red markers indicate the position of the maxima (the circle is for linear elasticity while the diamond is for Arruda-Boyce) while the blue ones are for the minima. The isolines of the two models match rather well at the two indentation steps.

Similarly to Figure 3.27, Figure 3.28 displays the contour plot of the σ_{zz} stress component. In this case too, the two constitutive laws provide globally a similar stress distribution. Nevertheless, quantitative difference in the position of the isolines starts to appear at high normal indentation, when the hyper-elastic tensile behavior behavior starts to deviate from the linear elastic one after several percents of deformation.

The difference between the two constitutive laws is more appreciable in the distribution of the normalised Mises parameter (see Figure 3.29) at the same indentation levels of 135 µm and

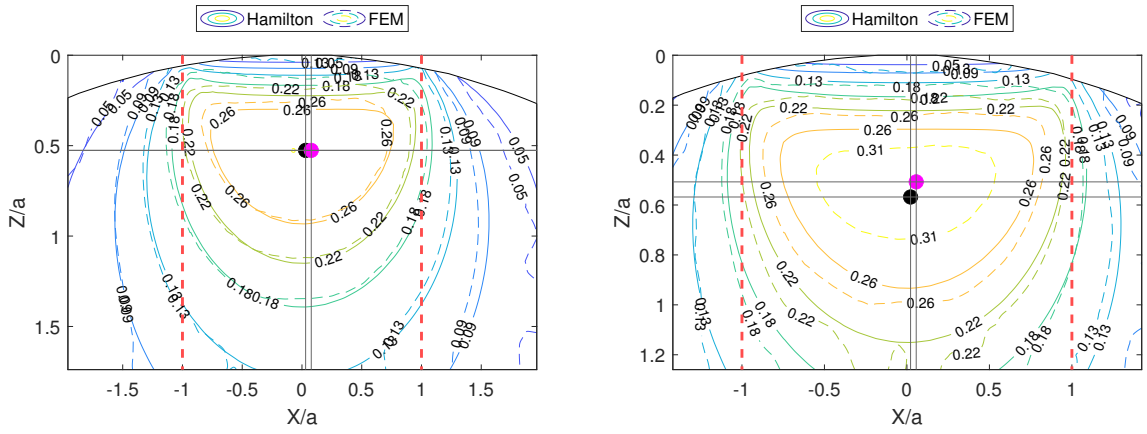

Figure 3.26: Contour plots of the normalised Mises parameter $\sqrt{J_2}/p_0$ on the central $X-Z$ plane obtained with DVC-driven FEM simulations (dashed lines) compared to the predictions of the Hamilton's model [24] (continuous lines). The plots represent the values for the specimen B-10-A indented of (a) 135 µm and (b) 252 µm in the case of a linear elastic isotropic constitutive model. The vertical red dashed lines indicates the position of the contact boundary. The black marker points out the position of the maximum for the Hamilton's model while the magenta one stands for the FEM simulation.

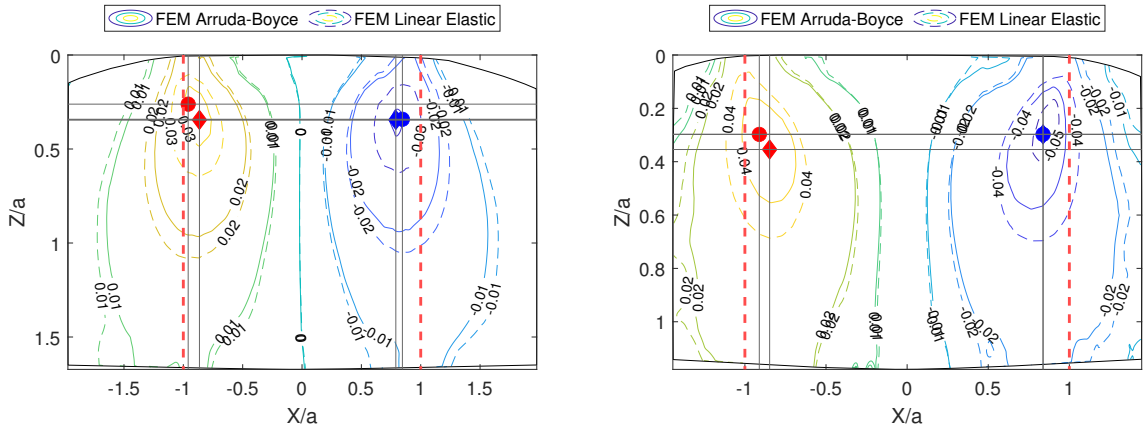

Figure 3.27: Contour plots of the stress component σ_{xz} (in MPa) on the central $X-Z$ plane obtained with DVC-driven FEM simulations with a linear elastic model (dashed lines) compared to those obtained with an hyper-elastic Arruda-Boyce model (continuous lines). The plots represents the data for the specimen B-10-A indented of (a) 135 µm and (b) 252 µm. The vertical red dashed lines indicates the position of the contact boundary. Colored markers represent the position of the maxima (red) and minima (blue) of the shear stress σ_{xz} for the linear elastic model (circle) and the hyper-elastic Arruda-Boyce model (diamond).

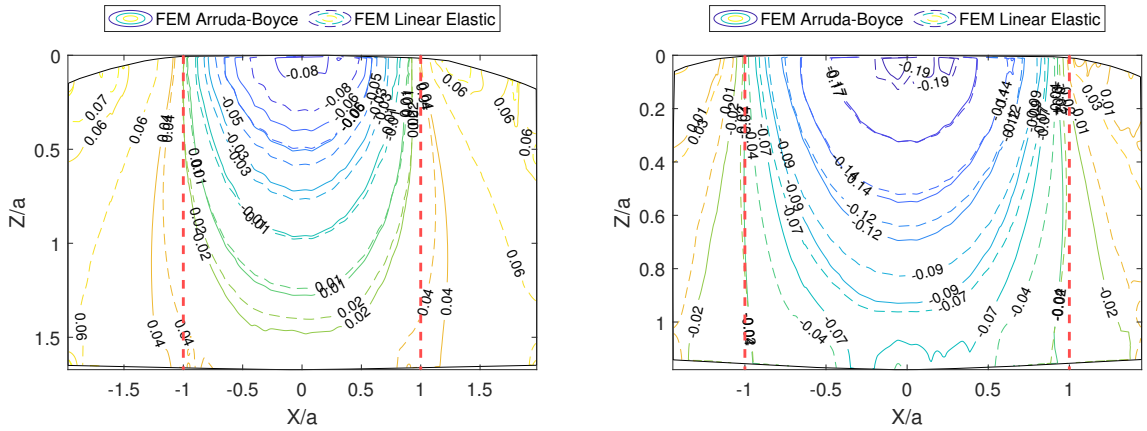

Figure 3.28: Contour plots of the stress component σ_{zz} (in MPa) on the central $X-Z$ plane obtained with DVC-driven FEM simulations with a linear elastic model (dashed lines) compared to those obtained with an hyper-elastic Arruda-Boyce model (continuous lines). The plots represents the data for the specimen B-10-A indented of (a) 135 µm and (b) 252 µm. The vertical red dashed lines indicates the position of the contact boundary.

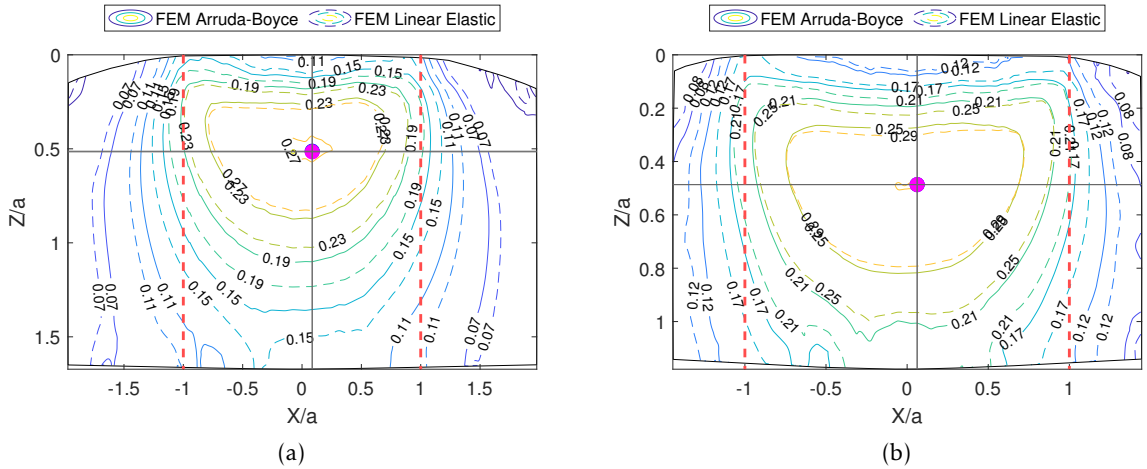

Figure 3.29: Contour plots of the normalised Mises parameter on the central $X-Z$ plane obtained with DVC-driven FEM simulations with a linear elastic model (dashed lines) compared to those obtained with an hyper-elastic Arruda-Boyce model (continuous lines). The plots represents the values for the specimen B-10-A indented of (a) 135 µm and (b) 252 µm. The vertical red dashed lines indicates the position of the contact boundary. The magenta marker points out the position of the maximum for the FEM simulation with a linear elastic model (the corresponding marker for the hyper-elastic model is not visible because it is placed in the same position).

252 µm. While the global shape of the isolines is preserved, quantitatively the Arruda-Boyce shows always a lower value at any given position. It is worth to note that the maximum of the normalised Mises parameter is in the exact same position for the two models (the marker for the Arruda-Boyce model is thus not visible on the plot). However, the normalised values at this maximum position are different: 0.27 for Arruda-Boyce and 0.31 for linear elasticity when δ_c =135 µm, 0.29 for Arruda-Boyce and 0.32 for linear elasticity when δ_c =135 µm. This conforms again with the more compliant behaviour of the non-linear Arruda-Boyce model at moderate strain (*i.e.* a few tens of percents, Figure 2.11), compared to the linear elastic behaviour of the material with a Young's modulus fixed at the initial value E_0 =1.55 MPaat small strain.

Thus, the DVC-driven FEM simulations carried out here tend to indicate that the overall shape of the stress distribution mainly depends on the geometrical and external (loading) parameters of the contact system, while the local extrema depend indeed on the actual constitutive model used. In the context of another class of materials such as metals, where plasticity might occur and influence the course of damage development for example, it is likely that such events become experimentally easier to detect (even *post-mortem*) and allow to provide indirect justification or evidence for the use of one constitutive model rather than another.

As final comments, the 3D coupled experimental and numerical procedure developed here, coupling Digital Volume Correlation and DVC-driven finite element simulation, provides for the first time three-dimensional access to the mechanical fields in the bulk in the deforming contact specimen, focusing in this chapter on the behavior of the sphere-on-plane system under normal loading. While this is a major achievement in itself, several questions remain open regarding the underlying physics of the soft contact mechanism and the choice of proper assumptions to interpret, discuss and compare the obtained results with other experimental works or models:

- The stress fields presented here are obtained indirectly by DVC-driven FEM simulation. This implies several modeling assumptions, regarding for example the small-strain or finite strain formulation of the problem, the linear elastic or hyper-elastic constitutive behavior of the PDMS material. Beyond common sense choices and assumptions adopted in this work (*e.g.* the behavior of PDMS is *a priori* rather hyper-elastic than linear elastic), it is difficult to clearly assert at this point when one assumption (or the other) is obviously leading to improper results;
- As a matter of fact, in the absence of previous experimental full-field results in the bulk of deforming contact samples, the only point of comparison available to date is with existing models. Hamilton's analytical model assuming a linear elastic behavior, there is a need for its extension to hyper-elastic materials, but it is still unclear whether or not this is basically unavoidable to properly assess the mechanical fields in our contact system;
- Beyond analytical models, several numerical contact models exist in the literature for soft contact systems [25, 75, 7, 12]. However, proper account of the adhesion effects is still debated in such numerical models of contact. In this context, the present procedure of DVC-driven FEM simulation in the deforming material presents the advantage of inherently rendering the potential hidden effects of adhesion, without having to implement it explicitly in the numerical model;
- Another question raised is the time-sensitivity of the material. The present experimental 3D procedure is quasi-static in nature and characterizes the equilibrium (or relaxed) state

of the contact system. Further work is needed to assess whether or not the transient relaxation of the system significantly impact the observed (and simulated) 3D strain and stress fields at the end of each XRCT scan. Here again, analytical extensions of Hamilton's model to visco-elastic materials are still missing, even if semi-analytical methods were recently developed [76, 77, 78].

3.4 Conclusions on normal load experiments

We showed, in the first section of this chapter, how the extraction of the contact area based on image segmentation and surface reconstruction is a reliable method to capture the evolution of A_R, as a function of the normal indentation and of the normal load in the investigated sphere-on-plane system. The main advantage of this method is that it is also valid for non-transparent materials, opening the way to real contact area measurements in more realistic systems. Regardless of the global circular shape of the contact area, some irregularities were observed and connected to the presence of image artefacts. A method to reduce them was proposed, even if their complete suppression was not possible. Despite the expected linear behaviour in the relationship between A_R and δ_c, an significant offset was found with respect to the benchmark optical measurements. Its origin was linked to the method of extraction of the contact zone and the resolution of the images. Indeed, because of the "partial volume effect", we showed that, in order to perform accurate measurement of the real contact area, the resolution of the 3D scans should be set to the finest level possible, according to the geometrical limits of the mechanical device. Otherwise, we proposed a *a posteriori* correction that enables to evaluate a better value for the contact area.

The information related to the simple 3D image segmentation is not limited to the extraction of the contact area. Indeed, the measurement of the three-dimensional superficial displacement field can be easily obtained. As an outstanding quantity not available before with classical 2D optical experiments, the evolution of the 3D displacement field at the sample surface allows to understand the corresponding response in terms of contact area. We demonstrated in the second section how this can be obtained by subtracting the original non-deformed shape of the PDMS sample from the deformed one. As expected in the presence of adhesion for this type of problem, the 3D method developed here even proved to be able to capture the hysteresis between loading and unloading. These experimental profiles were also compared with theoretical predictions showing a good agreement between measurement and models. However, the resolution of the present experiment did not allow to clearly discriminate between the different potential adhesive contact model (JKR, DMT or Maugis-Dugdale) to describe the behaviour of such sphere-on-plane contact system, especially in the vicinity of the contact edge. Indeed, it is only in this very restricted area that the predictions of the different models differ. As a consequence, a better resolution, using for example Synchrotron facilities, is expected to help capturing the differences between these theoretical models. Another complementary perspective consists in relying on a different procedure to compute the surface displacement field, e.g. using the sub-voxel accuracy of digital image (or volume) correlation, when it is applicable.

One of the main advantages of XRCT is indeed that we do not only have access to the physical quantities at the contact interface, but also potentially in 3D, in the interior of the materials. Thanks to the insertion of dispersed particles in the bulk of the samples and to the use of Digital Volume Correlation, we were able to measure the local 3D displacement and strain

fields. We started focusing on the measured field at the PDMS surface and we demonstrated how the contact radius could be estimated from the values of the displacement field, with the advantages of a better resolution compared to segmentation methods while limiting the impacts of local image artefacts and partial volume effect. In terms of displacement field inside the bulk, we noticed how the behaviour of the vertical component U_z scaled with the contact radius a and then with the imposed indentation δ_c and how it did not increase linearly from the surface into the bulk. We also showed the influence of the moving substrate under the PDMS as it get closer and closer to the contact interface at increasing indentation. Finally, we showed how the component U_x exhibits a maximum and a minimum related to the lateral movement of the PDMS caused by the high normal deformation reached beside the contact area. These observations were also confirmed by the presence of maxima and minima in the components of the strain tensor.

Thanks to the use of Finite Element simulations based on the DVC mesh and using a linear elastic or an hyper-elastic Arruda-Boyce behaviour, we accessed experimentally, for the first time, to the stress components inside the bulk of a soft material in contact with a rigid flat plate. We were able to compare our results with the prediction based on Hamilton's equations, which is basically the unique explicit model available for the description of the stress beneath a circular contact area. The shear components of the stress showed a very good quantitative agreement with the Hamilton's model. The comparison for the vertical component σ_{zz} was not so good mainly because of the limits in our simulations associated with incompressible materials. This shows the need to develop new models adapted to incompressible materials capable of providing the equations of the displacement (or deformation) field in order to be able to directly compare their predictions to the measurements issued by DVC, without having to resort to FEM simulation. The comparison between the experimental evaluation of normalised Mises parameter, assuming an hyper-elastic behaviour of PDMS, and the prediction based on Hamilton's model (or the corresponding linear elastic assumption in the FEM model) showed how a linear elastic model overestimates the level of stress in the bulk of an elastomer. Consequently, there is also the necessity of developing further models including non linear elasticity. In any case, we demonstrated how the maximum of J_2 is reached always in the same position, independently of the constitutive laws and only derived by geometrical and loading considerations. To conclude, we have shown how, in the absence of theoretical models directly expressed in terms of displacement/strain field, we are able to compare experimental results and models through DVC-based Finite Element Simulations. The main advantage of these simulations are, especially, to both test different constitutive laws and to avoid any assumption on the numerical contact models as the simulations are based on real measurements coming from *in situ* experiments.

4 Shear experiments

While the last chapter focused on the analysis of the contact area and the internal (and external) deformation of a smooth sphere-on-plane contact under pure normal load, here we perform the same type of analysis for sheared contacts up to the transition to macroscopic sliding. Using the device presented in the section 2.1.2, the specimens A-10-A and B-10-A were subjected to shear after the preliminary compressive steps under normal load described in the previous chapter. The tangential displacement was then applied to the PMMA plane, in a similar quasi-static step-by-step procedure. This allows to follow and analyse the effects of shearing on the evolution of the displacement and strain fields in the deforming PDMS material. The results in terms of reconstructed volumes and DVC measurements can be seen in Fig. 4.1 for two steps (the crop in the images are taken along the central $X - Z$ plane of the sample): the first one represents the end of the compression part while the second corresponds to the same volume after the application of a shear displacement keeping the same normal indentation. The objectives of this chapter are thus to analyse both surface phenomena and 3D measurements from DVC calculation during the shearing of our model sphere-on-plane contact system, up to the onset of sliding.

Unlike in the normal load chapter, we do not perform image segmentation and contact area measurement for a sheared contact as the use of aluminium particles led to an high saturation of the image, which complicated the segmentation process. Conversely, the presence of such particles allowed to carry out well-detailed DVC measurements that brought lots of information about the external and internal displacement field and the related strain and stress measurements. Here, we first perform a rapid comparison between optical and tomography results of a similar shearing experiment. Second, we present the analysis of the surface displacement field. Third, a complete discussion on the effects of shear on the 3D bulk displacement field is done with a focus on the effects of the size of the specimens and on the contributions of the global bending of the samples. To conclude, we analyse the deformation and stress states focusing on the position of the most loaded zones and on the comparison of the stress field with the predictions of Hamilton's model.

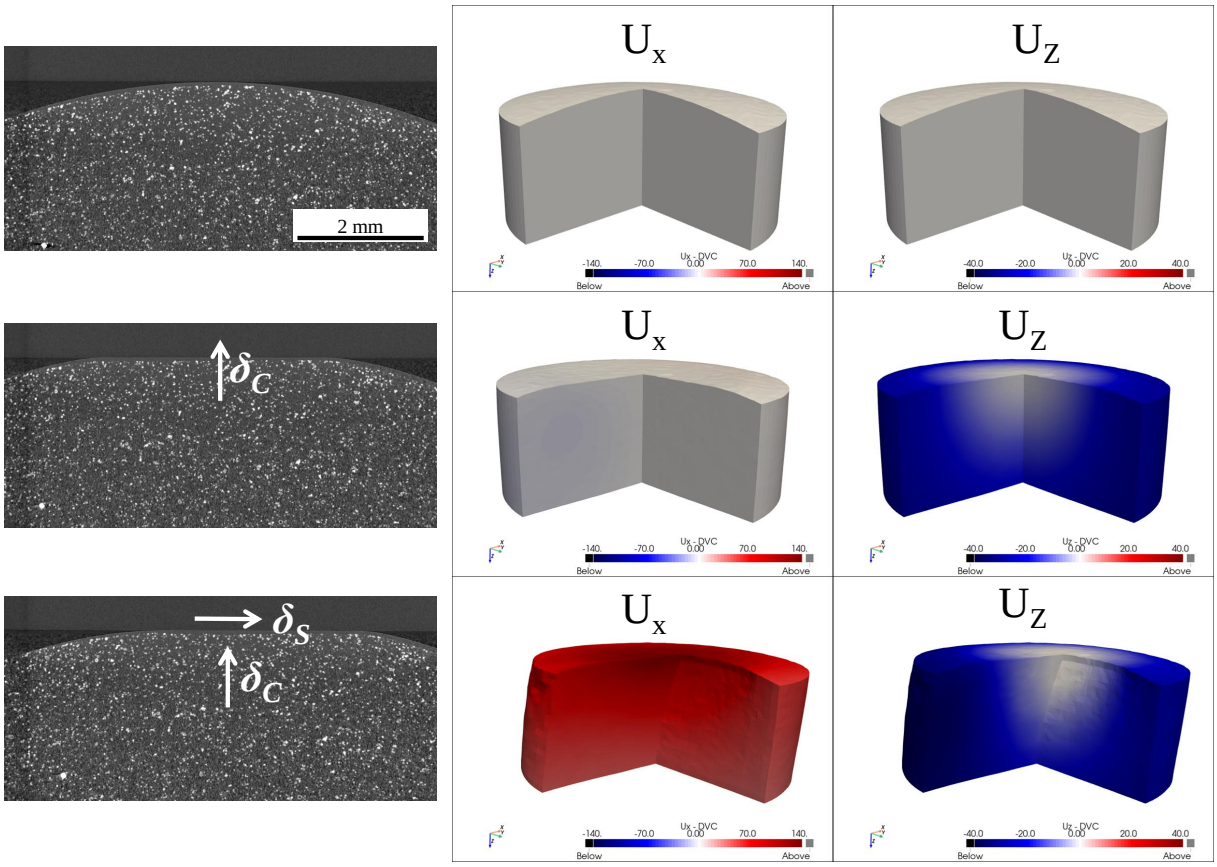

Figure 4.1: Left: slices of the reconstructed volumes on the central $X - Z$ plane after the application of: a compressing displacement ($\delta_c = 280$ μm) and a shear displacement ($\delta_s = 1650$ μm). Right: measured displacement field through DVC. Specimen B-10-A.

4.1 Comparison between tomography and optics during a shear experiment

As a first verification of our XRCT tests, we checked whether or not the measured physical quantities (e.g. the displacement field obtained by DVC) were in agreement with the externally imposed conditions (the imposed displacement on the PMMA). To do so, we firstly quantified the real tangential displacement applied on the specimen during the XRCT test following the fabricated hole inside the PMMA disk. Secondly, assuming that contact points which are in perfect adhesion with the PMMA undergo the maximum tangential displacement, we searched for the maximum of U_x measured at surface with DVC. Figure 4.2 shows how this maximum ($\delta_s PDMS$) compares with the imposed displacement on the PMMA δ_s. In a situation of perfect adhesion, the contact area and the PMMA should move of the same amount and should follow the oriented green line at $45°$ inserted in the figure. The results, both for specimens B-10-A and A-10-A, depict a very good agreement and follow the green line, meaning that the DVC measurement properly captures the surface lateral displacement. Furthermore, this analysis also highlights the transition from partial slip to full sliding. When no more points are in full adhesion, the PMMA continues moving while the surface of the PDMS remains in the same position as we can see in the plot for the last two points, where the PDMS displacement is constant. The tests were stopped there because further displacements would have only brought the specimen to similar states. Upon all the volumes that were reconstructed, we choose in the following analysis to only focus on four of them (underlined by the black crosses in Fig. 4.2) to illustrate the transition from full adhesion to full sliding.

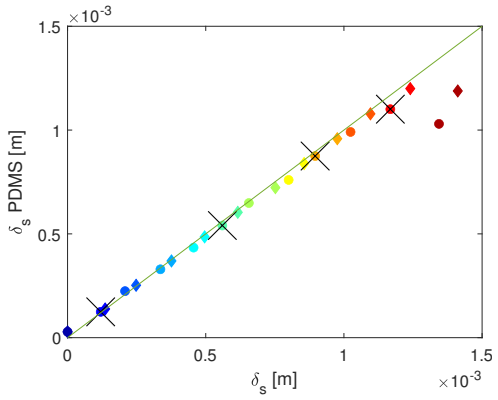

Figure 4.2: Measured tangential displacement of the PDMS surface $\delta_s PDMS$ (through DVC) versus the measured tangential displacement of the PMMA disk δ_s for the two specimens B-10-A and A-10-A. The oriented green line is a line at $45°$ to quantify how two measurements are in agreement. The circles represent the data for the specimen B-10-A while the diamonds are for the specimen A-10-A. The black crosses indicates the steps that will be considered for the analysis in the next sections.

Our XRCT measurements were compared to an equivalent optical test obtained under the same mechanical displacement conditions. This was perfomed on the device *optics-2* to quantify the evolution of the real contact area A_R and of the tangential force Q. These two parameters are compared to the ones measured during tomography experiments in Figure 4.3. Data where obtained applying a step-by-step shear displacement whith a dwell time of 5 minutes between each step to reach equilibrium and to reproduce the same experimental procedure

as in tomography. The blue segments indicates the data during the application of the shear displacement while the empty circles are for the (Q, δ_s) values during the dwell time.

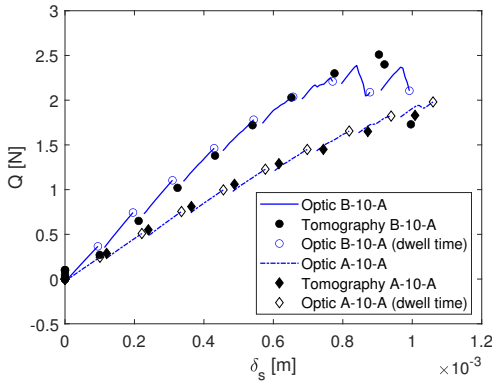

Figure 4.3: Comparison between the measured tangential force Q from the tomography device and the optical one in the case of the same applied shear displacement δ_s for the two specimens A-10-A and B-10-A in conditions of equilibrium and step-by-step loading.

During optics experiments, (continuous blue lines) the $Q - \delta_s$ curve globally exhibit an expected behaviour similar to the one observed during experiments performed with continuous sliding (see Fig. 1.15b). For each single step, the tangential force increases almost linearly with the displacement starting from the previous value. When the full sliding condition is reached (last two steps), the tangential force exhibits the typical stick-slip like behaviour. The data from tomography, represented as black filled scatter points because we only considered the equilibrium values for the volumes, show a very good agreement with the measurement obtained with the optical device during the dwell time (empty circles) which validates the design of our new shearing device for tomography and the associated experimental conditions. In the case of the tomography measurements, the transition to full sliding corresponds to a stabilisation of the tangential force (last two points for both specimens) over the application of two consecutive lateral displacements. In Figure 4.3, the tangential force Q is always higher for the smaller specimen (B-10-A) at a given displacement. Indeed, the smaller one is stiffer in terms of bending and thus reacts with an higher force as it can be expected.

4.2 DVC measurements under the application of a shear displacement

In this section, by analysing the surface displacement field from DVC calculation, we investigate the evolution of the specimen skin, especially in the absence of a good image segmentation. Then, we present the observations of the phenomena inside the bulk by successively considering the displacement field, the strain field and, the stress field. This last field is computed with FEM simulations based on the DVC displacement measurements, as in the previous chapter.

4.2.1 Surface displacement

Evolution of the Region of Interest

As the PDMS is moving vertically during the normal loading experiments, keeping the PMMA plane fixed, the reference system in the previous chapter was the PMMA plane. To

obtain consistent results in the case of a shear experiment, we also express all DVC results during shear in the fixed reference system of the PMMA. Differently from the previous chapter where the PDMS moved vertically, here the moving part of the set-up is the PMMA plane. Thus, we represent the data as if the PMMA was fixed and the PDMS was moving horizontally. To do so, the displacement measured at the nodes of the ROI mesh used for the DVC were corrected of the amount of PMMA displacement δ_s (see Figure 4.2). The results of this procedure is illustrated in Figure 4.4 which represents the evolution of the ROI in the central $X-Z$ plane deformed with the measured displacement. Reminding that the PMMA (not represented in the plot) moves from left to right, the correction of the lateral displacement with the PMMA movement makes the PDMS move from right to left. **Unless specified differently, in the following of this chapter, all the displacement plots will adopt this convention and will be represented in the fixed reference of the PMMA, so that the PDMS moves below the fixed PMMA plane**. The colors adopted in all plots in the upcoming figures, from blue to red, indicate the increasing shear displacement. Moreover, all profile curves in the following are plotted in the central $X-Z$ symmetry plane of the sample, unless specified otherwise.

On Figure 4.4, the first blue curve represents the contour of the ROI mesh in the PDMS sample at the end of the normal loading step. Subsequently, the application of the lateral displacement, makes the PDMS top surface move towards the PMMA plane on the left (leading edge) while it recedes from PMMA on the right (trailing edge). Assuming that the central plateau corresponds to the contact area, these two combined macroscopic movements make the contact area move to the left. In analogy with the works of Lengiewicz *et al.* [7], we can then connect these phenomena to those of contact laying and lifting respectively on the leading and trailing edges; these mechanisms were found to be partially responsible for the change of the contact shape under the application of shear load.

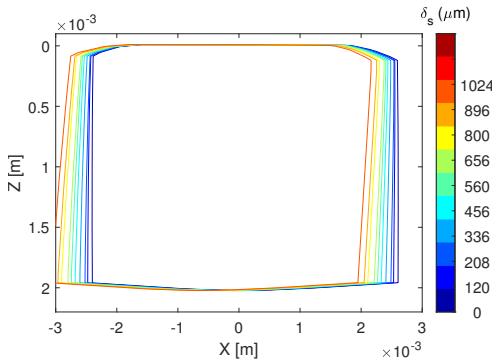

Figure 4.4: Evolution of the ROI mesh on the central $X-Z$ plane deformed according to the displacement measured at nodes and corrected for the PMMA displacement to observe results in the fixed reference system of the PMMA. Data refers to the specimen B-10-A.

Vertical displacement: observation of Lifting and Laying effects

A better illustration of the laying and lifting mechanisms happening at the boundary of the real contact zone during a shear experiment can be performed by following the evolution of the vertical tangential displacement U_z at the top surface (see Figure 4.5). In both cases, the central zone, where all curves are superimposed, corresponds to the real contact area where the vertical displacement is blocked by the rigid PMMA plane. Conversely, in the external zones, the displacement evolves with two different trends. In agreement with what we have

observed in Figure 4.4, the left part of the profile shows an increasing negative displacement (upward movement) while the right part is characterised by the inverse behaviour (downward movement). As the the positive Z direction is through the PDMS bulk, an increasing negative displacement indicates that the material is moving towards the PMMA plane and, assuming that it contributes to increase the contact area, corresponds to a laying mechanism at the leading edge. At the trailing edge, a lifting mechanism is occurring as the PDMS is moving away from the PMMA plane. Even though the lateral displacement is in the same order of magnitude for the two specimens (see Fig. 4.2), the longer specimen exhibits an higher vertical displacement variation that may be linked to an higher bending of this specimen.

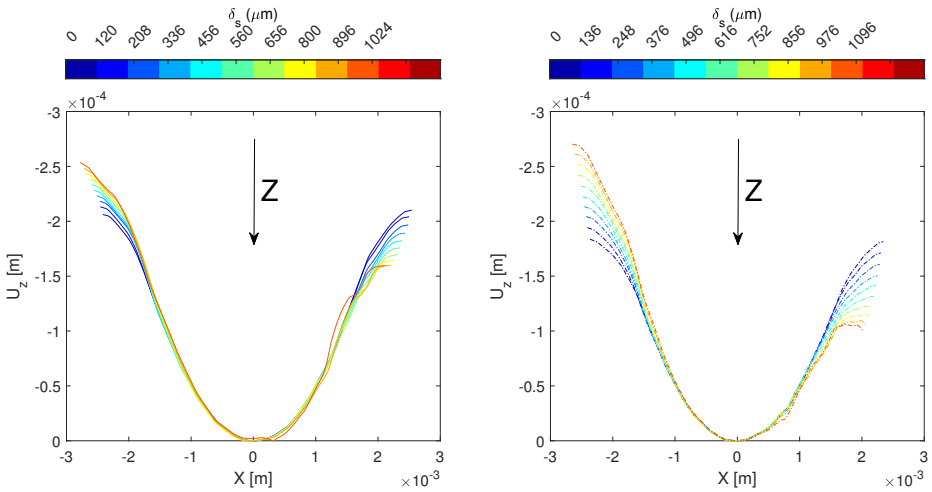

Figure 4.5: Evolution of the vertical displacement component U_z in the fixed reference system of the PMMA at increasing shear displacement δ_s for the specimens (a) B-10-A with an height of 6 mm and (b) A-10-A with an height of 9 mm.

Lateral displacement: an indication of stick and slip zones

Figure 4.6 presents, for the specimen B-10-A, the evolution of the lateral displacement component U_x along the direction of shear. For an easier observation of the presented phenomena, in this plot the displacement field is in the reference system of the fixed PDMS (the PMMA plane moves over the PDMS sample). The typical profile of this component is characterised by a plateau in the center followed by a decrease on each side (this plateau is evidenced by the presence of the horizontal dashed lines indicating the imposed shear displacement). This trend could be the evidence of the presence of a stick part in the center of the contact area and of an external partial slip zone (the accurate delimitation of which requiring an accurate detection of the contact boundary). As the points in a condition of slip are free to move inside the contact, their displacement is much lower than the one imposed and, more importantly, lower than the one visible in the plateau. The profiles are plotted here up to the volume at the onset of full sliding and where no more plateau is observed (there is no more stick zone and all the contact area is invaded by the slip part). The little difference observed between the imposed displacement and the measured one in the plateau can be explained by the fact that, with our procedure, the displacement is measured a few micrometers below the surface of the PDMS sample. Indeed, the measured values may be underestimated.

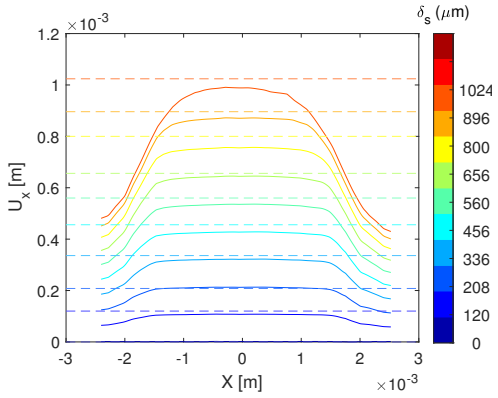

Figure 4.6: Evolution of the lateral displacement U_x at the surface of the PDMS and along the direction of the applied displacement during a shear experiment. Data are for the specimen B-10-A and are in the reference system of the fixed PMMA plane. The horizontal dashed lines represent the imposed lateral displacement.

Consequently, the displacement component U_x can be used to estimate the evolution of the slip and the stick zones inside the real contact area as a function of the shear displacement. So, this evolution of the real contact area has to be determined. As accessing the contact area through image segmentation is not possible, we estimate it with the *z-projection* method introduced in the section 2.4.2. The evolution of the shape of the resulting real contact zone is plotted in Figure 4.7 for increasing shear displacement. In the plot, the contact area reduces together with a change in morphology and a loss of symmetry, both synonyms of lifting (area decrease on the right) and laying (area increase on the left) effect as evidenced in [7]. We only remind that these measurements will be considered as qualitative because the evaluation methods does not account for all the problems related to image artefacts and partial volumes effects.

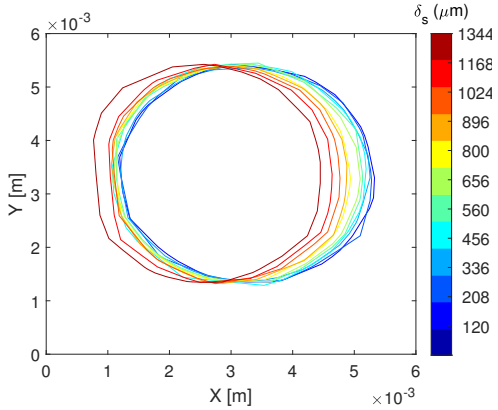

Figure 4.7: Evolution of the contact area boundary under the effect of shear. Data are obtained with the *z-projection* method. Data refers to the specimen B-10-A.

In a rigorous manner, the stick zone should be evaluated by finding the points at the surface where U_x is equal to the imposed displacement δ_s. However, due to the smooth transition between the plateau and the external zones in the curves of Fig. 4.6, the transition between stick and slip zones (the limit of the plateau) is not well defined and hard to compute with precision .

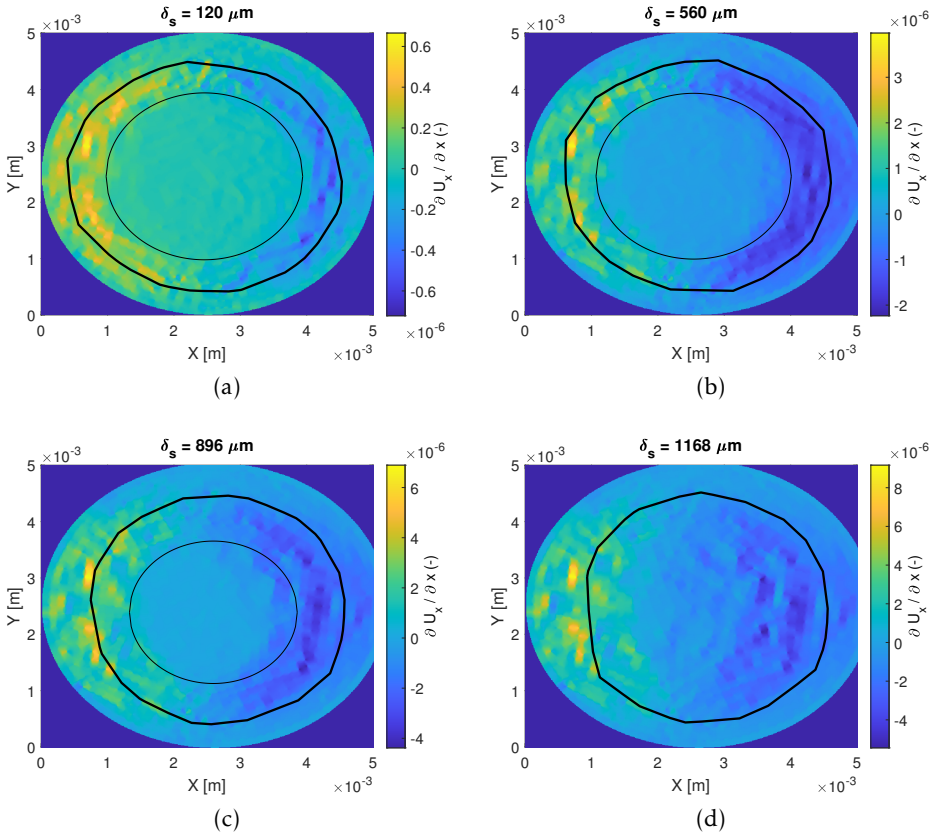

Figure 4.8: Lateral gradient $\partial U_x/\partial x$ on the surface of the PDMS specimen during a shear test. The external black closed curve represents the contact area while the internal one represents the stick zone in the contact area. Data refers to the specimen B-10-A.

To enhance the transition from the stick to the slip zone, we propose to compute the lateral gradient $\partial U_x/\partial x$ of the displacement map of U_x on the entire upper surface of the PDMS (see Figure 4.8) for the 4 steps considered in this analysis. The boundary of the contact area is represented by the external closed bold black line. The inner black circle corresponds to the limit of the stick zone and its position is determined by analysing the radial position of the shear stress maxima (its evaluation method will described and discussed more precisely in the next section). In the central zone of the real contact area, on can clearly see a plateau where the value of the gradient is constant and close to zero. The size of this plateau reduces as the shear displacement increases and it disappears for the highest value of δ_s where full sliding is expected. Thus, we believe that this plateau is representative of the position and morphology of the stick zone inside the contact area. As a natural consequence, the partial slip zone corresponds to the zone between the stick zone and the contact boundary (in between the two black circles). This slip zone is filled by the yellow and blue points indicating a change in the lateral displacement field. The evolution of the stick zone is qualitatively in agreement with what has been observed in previous studies [4].

To confirm that our method to characterize the evolution of the stick zone during a shear test is similar to the results obtained with a more classical test performed on a opto-mechanical device, we performed an optical experiment (with the tribometer *optic-1*) on a PDMS sample having the same geometry as the sample B-10-A, without any particles in the bulk, but having dispersed talc particles inside the external interfacial film. Then, by using a particle tracking method, proposed and validated in the work of De Souza [4], it is possible to evaluate the evolution of the internal lateral displacement field at the surface of the PDMS. The Figure 4.9 presents, in addition to the evolution of the shear force as a function of δ_s, the evolution of this surface field for three δ_s before and after the onset of sliding (similarly to the situation shown in Figure 4.8). In this kind of representations, the stick zone corresponds to the inner isoline, the one corresponding to the lower displacement (see [4] for more details). Despite the fact that this experiments cannot be quantitatively compared to our XRCT experiment (normal and tangential forces are not the same in the optical experiment), we qualitatively observe in both cases that (i) the stick zone is progressively invaded by a slip region, (ii) this stick zone is not concentric with the contact boundary as predicted by the model of Cattaneo-Mindlin but is shifted towards the leading edge of the contact zone and (iii) totally disappears at the onset of full sliding (highest value of δ_s). Note that the precision of our new (that of DVC) method is not sufficient to observe the position of the last sliding point, which is not centered in the contact zone. At the onset of sliding, the dynamics of all physical phenomena increases, it is less stable and requires an higher acquisition rate to be captured (which is by construction contradictory with our 3D step-by-step shearing experiments). Nevertheless, the new method proposed here to capture the evolution of the stick zone inside a sheared interface is very promising and may provide access to this information for types of contact that are not compatible with the optical method.

4.2.2 Surface shear stress

Observation of stick and slip zones

Figure 4.10 plots the evolution, for the increasing shear displacement, of the shear stress component σ_{xz} (at equilibrium) at the PDMS surface. The profiles are extracted along the surface diameter for a FEM simulation (based on the experimental displacement field) obtained with the Arruda-Boyce constitutive law. The colored circles underline the position of the left and right maxima of these profiles. The diamond markers represent the radial position of the

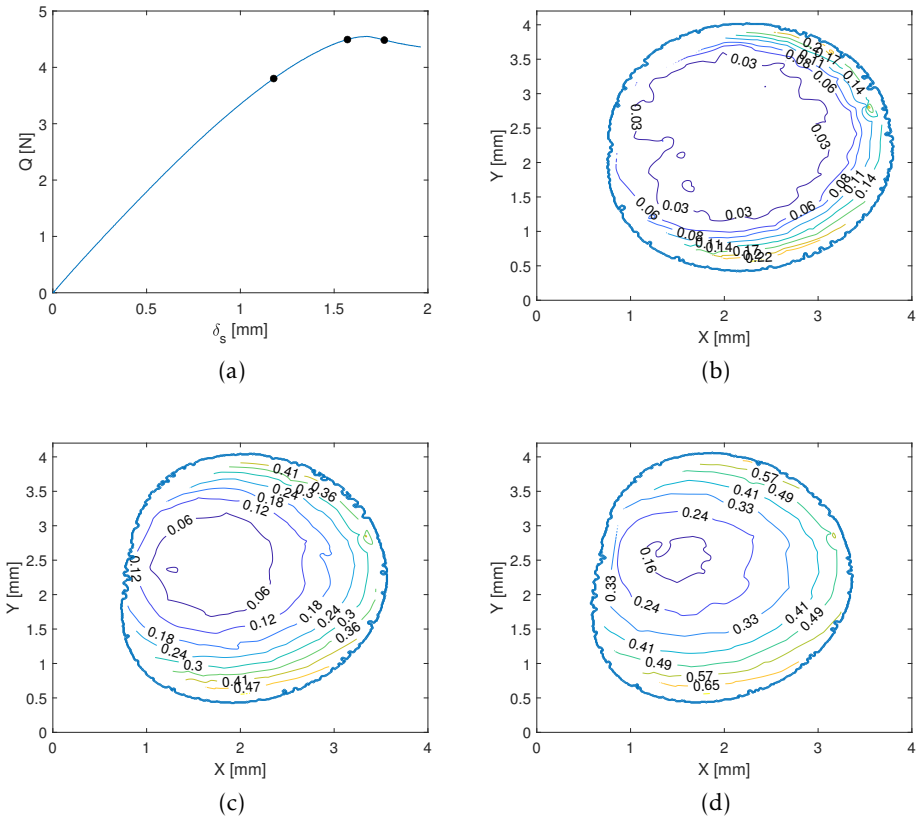

Figure 4.9: Lateral displacement field inside the contact area during a shear experiment on the device *optic-1*. (a) Evolution of the tangential force Q as a function of the lateral displacement (the sliding speed is of 0.1 mm/s and a normal load P of 1.1 N). The three black circles indicate the force and displacement related to the plots (b-d). (b-d) Isolines of the lateral displacement U_x in millimeters inside the contact area at increasing displacement (from b to d). Data refers to an experiment obtained on a sample having the same geometry of the B-10-A without bulk particles and provided with talc particles in the external interfacial film to measure the displacement by tracking.

contact edge as in Figure 4.7. First, these profiles follow, qualitatively, the expected shape of the shear stress in the contact area according to the theoretical prediction of the CM model (see Fig. 1.10). The profiles are divided into three zones: two external ones in which the stress is increasing similarly to the normal pressure profile which, theoretically [20, 21], should exhibit a bell-shape profile and an internal one presenting a quadratic behaviour with a minimum at the contact center. In agreement with the CM model prediction for the shear stress, we expect the external zones (between the diamonds and the circles) to correspond to the external invading slip zones while the central part is expected to represent the stick part of the contact area. We chose to represent these profiles along the direction normal to the sliding direction in order to have fixed contact boundary and to better appreciate the growth of the slip zone. The extension of the slip zone can be observed by looking at the black segments connecting the boundary of the contact (square symbols) and the stress peaks (circle symbols) illustrating the progressive transition to full sliding at large δ_s. The size of the slipping part is almost constant at low δ_s while, for the last 4 phases of the shear experiment, it rapidly increases and invades completely the contact area. From this analysis, it is now possible to extract the 3D boundary of the sticking zone which corresponds to the closed curve passing through the radial position of the shear stress maxima. Those curves were plotted in Fig. 4.8 and they correspond to the inner black curves. As the position of these curves seems to well capture the boundary of the plateau previously observed in this figure, this confirms the validity of the new method, based on the calculation of the lateral gradient $\partial U_x/\partial x$, to determine the evolution of the stick zone. Thus, this preliminary and quite simple calculation is a good candidate to determine the state of an interface, regarding sticking or sliding, without further data processing (such as FEM simulation in the present case).

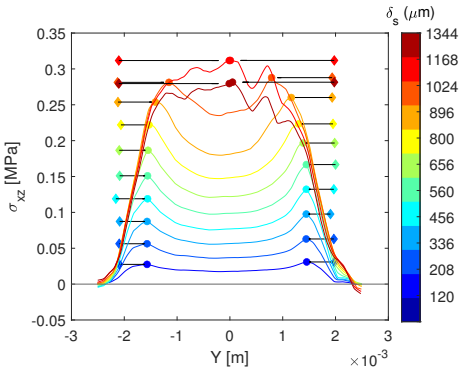

Figure 4.10: Profiles of the shear stress component σ_{xz} during a shear experiment at the PDMS surface and cropped normal to the direction of shear. The colored diamonds indicate the position of the contact border according to the *z-projection* method. The colored circles indicate the position of the profiles maxima. The horizontal segments linking the diamonds and circles show the slipping zone. Data refer to a simulation with the Arruda-Boyce hyper-elastic law based on the experimental data of specimen B-10-A. The color code is the same as for the markers in Fig. 4.2.

Verification of the elastic Young's modulus

Before starting the comparison with the theoretical models, we check if the fitted elastic modulus from the optical experiments (see Fig. 2.21) is representative of the actual material properties of our experiments. Thus, we integrate the shear stress σ_{xz} over the whole PDMS surface (the contribution of the non-contact zone is 0 in this integration) to calculate the

tangential force Q and compare the results with the experimental measurement. Figure 4.11 shows the results of this integration that was firstly done in two situations: one with a linear elastic behaviour with a Young's modulus equal to 1.55 MPa and one with the Arruda-Boyce model used in the simulations presented previously, i.e. with an initial Young's modulus E_0 of 1.55 MPa.

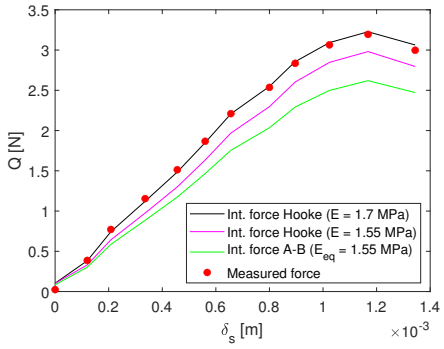

Figure 4.11: Measured tangential force compared with the integration on the PDMS surface obtained starting from the computed σ_{xz} stress field at surface. The integration is obtained in the case of FEM simulations with a linear elastic model (with E =1.55 MPa or E =1.7 MPa), and the hyper-elastic Arruda-Boyce model characterised by an equivalent Young's modulus of E =1.55 MPa.

The simulations with these models give an integrated force that underestimates the experimental measurement (the error is estimated between 7 and 17 %). To account for this, we chose to adjust the value of the Young's modulus in the linear elastic simulation in order to fit the experimental data and we found an optimum with E =1.7 MPa. The fact that the lower Young's modulus (obtained with fitting on the optical data) does not compare with the experimental measurements may have two different origins. The first one is related to the use of a linear elastic model to fit the experimental optical data, which is presumably non-representative of the actual behaviour of our specimen under high strains. The second one can come from our evaluation of the shear stress from DVC which is not exactly performed at the contact interface. The last point results again from the conjunction of two factors: first, the DVC region of interest is in fact located ~ 8 µm below the actual PDMS specimen surface obtained with image segmentation. Moreover, the strain and stress tensors are calculated at the integration points inside of an element. As it is expected that the maximum shear stress occurs at the contact interface, the calculation of shear stress in the last element below the surface is likely to present some mesh size sensitivity. Usual practice in standard FE modeling would suggest to refine the mesh in the vicinity of the contact interface to better capture the local gradients of stress and strain fields. This is unfortunately not possible in the present procedure where the FE mesh is constrained by the DVC setup (see section 2.4.2). A perspective in this context would then consist in separating the mesh used for DVC and the one used for FE simulations, while resorting to interpolation in order to define the DVC-based displacement for the boundary conditions of the simulations.

Comparison of the shear stress at surface with theoretical models

Now, we try to compare the experimental evolution of the σ_{xz} profiles with the theoretical predictions of the two models introduced in chapter 1: the model of Cattaneo-Mindlin and the

one of Savkoor. As those two models have been developed in a linear elastic framework, we present in the following the computation of the equilibrium shear stress using a FEM simulation obtained with linear elastic constitutive law (the parameter *NLGEOM* authorising large deformations is not activated).

Figure 4.12 shows the experimental profiles of σ_{xz} calculated with a linear elastic law (E =1.7 MPa) at the surface and along the direction of the applied shear displacement. For comparison, the same profiles evaluated respectively by the CM and Savkoor models are plotted in dot-dashed lines respectively in Fig. 4.12 (a) and (b). The profiles for the theoretical models are calculated from the experimental measurements of P, Q, a, E and δ_s with the equations provided in the sections 1.2.3 (Catteano-Mindlin) and 1.2.3 (Savkoor). First, we note that the experimental profiles are always larger than the theoretical ones, meaning that they always overestimate the contact area. Secondly, the experimental stress value at the contact center is more in agreement with the CM's predictions rather than the Savkoor's ones. However, this second model seems to better capture the final stress value during full sliding. Indeed, the experimental measurements seems to converge toward a constant value in the contact area at large shear displacement which is better described by Tresca's friction law, as in Savkoor model, than by a bell-shape proportional to the Hertzian normal pressure, as in CM model. In both cases, however, the global shape of the experimental profiles does not match perfectly the theoretical ones both in term of the position of the stress peaks and of the stick zone size.

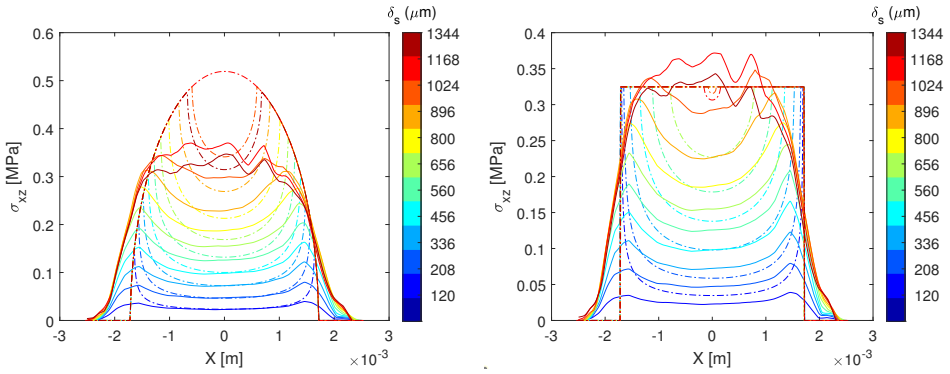

Figure 4.12: Comparison of the σ_{xz} profiles (continuous lines) with the theoretical models (dot-dashed lines): (a) Cattaneo-Mindlin model and (b) Savkoor model. The theoretical profiles are obtained starting from the measured experimental data (P, Q, a, E, δ_s) while the experimental one are for the simulation with a linear elastic law having E =1.7 MPa and based on the displacement field of the specimen B-10-A.

To understand these discrepancies between the models and the experiments, we should focus on the capability for a discrete grid of elements (as it is the case for the DVC mesh) to capture step changes in any physical quantities. Indeed, the measured strain/stress inside one element can be influenced by surrounding elements with the final results to have an average value that does not correspond properly to the real physical quantity. Furthermore, if we imagine that the measured quantity evolves significantly over a distance less than the typical size of an element, the final value measured on one element will correspond to the average value of this evolution. As the exact averaging behaviour inside an element is unknown, we propose to mimic it by filtering the theoretical profiles by means of a convolution with a Gaussian function having its

standard deviation equal to the element size. The results of the convolution with, for example, one of the Savkoor profiles is provided in Figure 4.13 at increasing standard deviation σ_G. The convolution with a Gaussian function introduces small tails at the base and at the top of the initial profile and also leads to the smoothing of the theoretical profiles closer to our experimental measurements.

In the case of the Gaussian function, the final shape of the convoluted profiles strongly depends on the standard deviation σ_G and the choice of this last value is complex as it depends on several parameters (like for example the fact that the measurement is done on points below the surface) and not only on the element size. The effect of an increasing σ_G is tested for values ranging from 1 to 4 times the element size (nearly 100 µm in the present case). Because the best value of σ_G describing our experimental results is twice the element size, we decided to adopt this value for the comparison between models and experiments. Indeed, it indicates that the stress value in a given spatial position may be smoothed and averaged over two neighbouring elements.

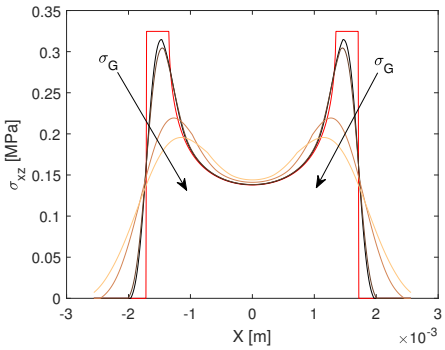

Figure 4.13: Convolution of the Savkoor shear stress profile. Evolution of the stress profile during partial slip convoluted with a Gaussian function at increasing σ_G from 1 to 4 times the element size.

Figure 4.14 shows the data of Figure 4.12 with the theoretical profiles convoluted with a Gaussian function with σ_G equal to two times the element size. The most evident effect of this convolution is to introduce a slope on the external boundary of the the theoretical profiles that allows a perfect match between the experiments and the Savkoor's model, at least for the stress decay at the contact boundary. This convolution method also allows to better reproduce the position of the stress maxima for both models. However, the agreement is again better with the convoluted Savkoor's profiles. Concerning the stress value in the stick zone, the smoothed CM model still presents a kind bell shape proportional to the normal pressure while the measured profiles shows a plateau. This plateau, which again could be linked to a friction behavior of the interface following a Tresca type law, is still better captured by the smoothed Savkoor profiles. Furthermore, this limit shear stress is also in agreement with other previous studies involving the contact of a PDMS sphere [4, 28] where the transition to full sliding is characterized by a constant shear strength.

Even though, from previous consideration, the Savkoor models seems to better describe our data compared to the CM model, the final choice of the best model to represent our measurement is not evident and requires further considerations. Indeed, contrary to models which predict a linear decay of the size of stick zone, the experimental reduction is very slow at low

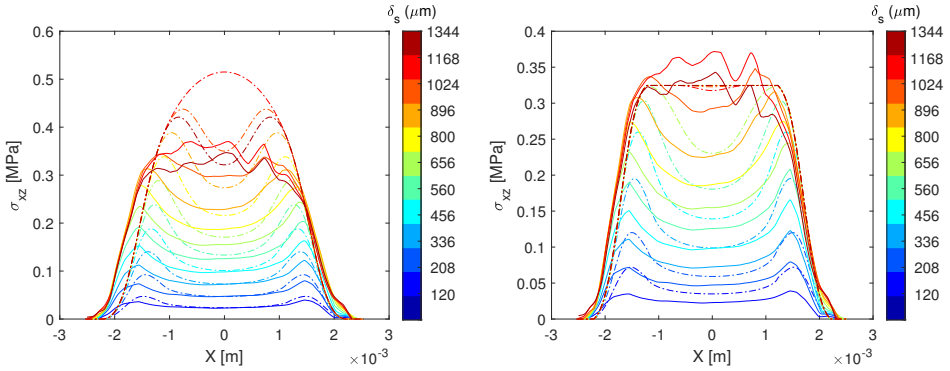

Figure 4.14: Comparison of the σ_{xz} profiles (continuous lines) with the theoretical models (dot-dashed lines): (a) Cattaneo-Mindlin model and (b) Savkoor model. The theoretical profiles are obtained starting from the measured experimental data (P, Q, a, E, δ_s) and convoluted with a Gaussian function having a standard deviation σ_G equal to 2 times the element size. The experimental one are for the simulation with a linear elastic law having E =1.7 MPa and based on the displacement field of the specimen B-10-A. The color code is the same as for the markers in Fig. 4.2.

shear displacement (the position of the stress peaks is almost constant all along the experiment) and accelerates only at very high shears, close to full sliding. The explanation for this difference can be both related to a real physical effect and to a measurement one. The first one can be linked to the quasi-static loading conditions used in the experiment where, between each shear step, there is a waiting time of almost 20 minutes to complete the scan. During this time, the PDMS could undergo a visco-elastic relaxation and/or re-stick of the previously slided zone. At the successive step, the amount of slip zone keeps constant. The fact that, after a given shear displacement, the slip zone suddenly increases can be related to the bending of the specimen and the fact that our sample is not properly respecting the semi-infinite assumption adopted in the theoretical models. The second explanation can be simply based on the measurement method, characterised by an estimation of shear stress with rather coarse finite elements (inherited from the DVC procedure), and the convolution of the theoretical profiles with the Gaussian function. Third, there could be additional assumptions that make the match between models and experiments not perfect. For example, we can mention the fact that the CM model considers a non-changing pressure profile and a constant contact area that, in the framework of our experiment, is not properly the case because of the changes of the contact area under the application of shear. Another assumption is that both models were developed with a linear elastic material behaviour in a contact on a semi-infinite space that it is not representing the actual experimental setup. Our qualitative comparison with the models shows then that an adaptation of the models is necessary to better describe our special situation and in general a problem still characterised by open questions [28, 22]. However, this first qualitative comparison can indicate that the Savkoor model could be more adapted to describe our experiments.

4.2.3 Bulk displacement field

Interfacial mechanisms such as contact area modifications, presence of stick and slip zones or contact lifting and laying can be better understood with the observation of the 3D displace-

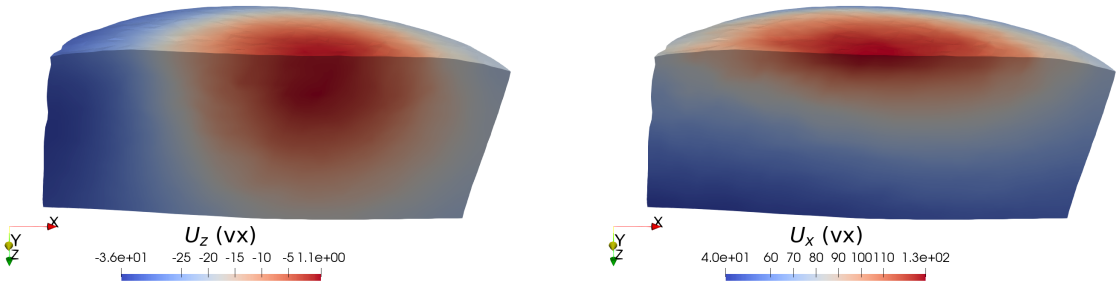

(a) (b)

Figure 4.15: (a) 3D observation of the displacement field at $\delta_c = 252$ µm and $\delta_s = 1168$ µm for the specimen B-10-A. (a) U_z in voxels and (b) U_x in voxels.

ment field beside a sheared contact interface as illustrated in 3D in Figure 4.15 at full sliding for the two components U_z and U_x. Figure 4.16, displays the global movement of the material all along the shear experiment thanks to oriented arrows which indicate the direction and amplitude of displacement in the material. Their length is proportional to the intensity of this movement (the scale of the arrows is 1:1 in the presented plot). By zooming in two regions on both side of the contact zone (see Figure 4.16 left and right) the details of the local movement inside the PDMS is emphasised. In the left part, beside the leading edge of the contact area, all the arrows are oriented towards the PMMA plane, contributing therefore to the laying mechanism. The opposite mechanism is observed on the right for the lifting mechanism. The increment/decrement of vertical component of the displacement field is, however, decreasing at increasing shear. This may indicate how the material's ascent and descent are more important in the first shearing phases and stabilize at the full sliding onset.

To perform a more quantitative analysis of the displacement orientation, Figure 4.17 presents the isovalues of the angle made locally by the arrows for a shear displacement $\delta_s = 896$ µm, determined as $atan(U_z/U_x)$ (the plots for all the steps are visible in Fig. 6.7 in Appendix 6). These isolines of displacement orientation highlight the presence of a neutral line (zero angle) passing through the contact center and indicating a zone where the displacement is oriented with the same direction as the applied shear. In addition, we can observe the existence of two extremes with opposite angles on each side of the contact zone corresponding respectively to movement towards (positive angles) and away from (negative angles) the PMMA plane. Interestingly, this maximum/minimum are located near the edge of the contact but beside the surface and not at the surface where the larger displacement is intuitively expected for the presence of surface laying/lifting.

Vertical displacement component U_z

Figure 4.18 shows the evolution of the vertical displacement field U_z under four increasing shear displacements δ_s (the plots for all the steps are visible in Fig. 6.9 in Appendix 6) when the U_z displacement field at the end of the compression step has been removed. In this way, we can focus exclusively on the vertical displacement generated by the shear step. The maximum/minimum of U_z are found below the surface and their depth does not evolve during the experiment. At the first shear step, no isoline between 0 and 2 micrometers are observable in the displacement field below the contact which means that the vertical displacement is negli-

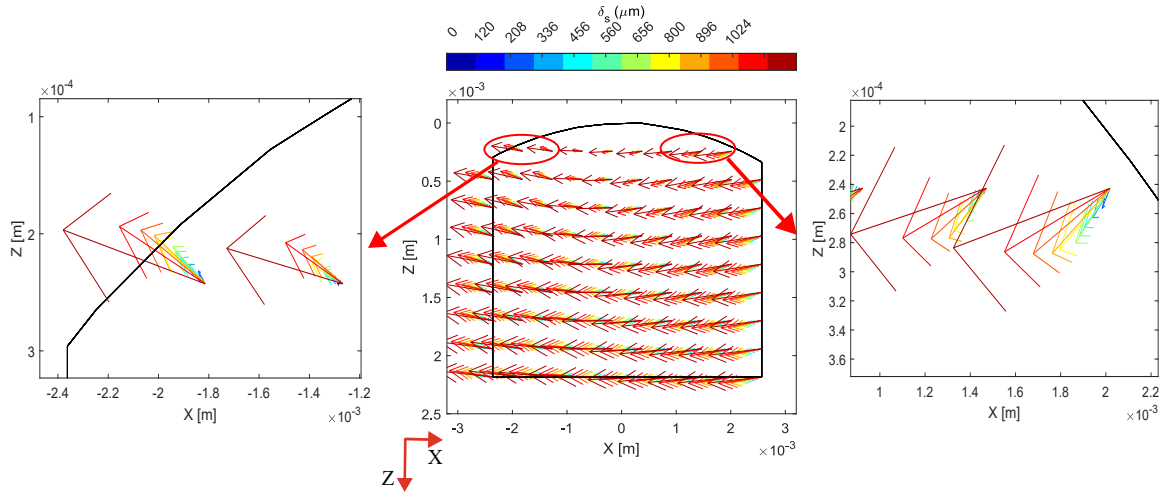

Figure 4.16: Displacement field in the central $X - Z$ plane of the PDMS specimen during a shear experiment and represented with oriented arrows. The image contains two zoomed parts takes symmetrically with respect to axis of symmetry and to underline the effects of lifting and laying happening beside the contact surface. Data for the specimen B-10-A. The color code is the same as for the markers in Fig. 4.2. The scale of the arrows is 1:1 in the present configuration. Data are in the reference system of the fixed PMMA plane.

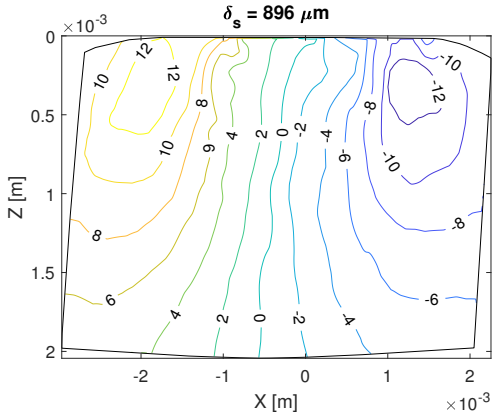

Figure 4.17: Isolines of the vectors' orientation ($atan(U_z/U_x)$) during shear at $\delta_s = 896$ μm. Data are in degrees. The ROI is deformed according to the displacement field. Data refers to the specimen B-10-A and are in the reference system of the fixed PMMA plane.

gible and close to 0. With the increasing δ_s, conversely, this zone is progressively invaded by a growing vertical movement and the zone characterised by a vanishing vertical displacement is now represented by a narrow vertical zone aligned with the contact center. In general, we can confirm here that the laying/lifting effects measured at surface originate from the bulk deformation of PDMS, even they only become visible at the contact surface in classical 2D optical experiments, where they affect the contact area. It is however still possible that other complex surface phenomena (e.g. related to adhesion) add another contribution to the contact surface evolution.

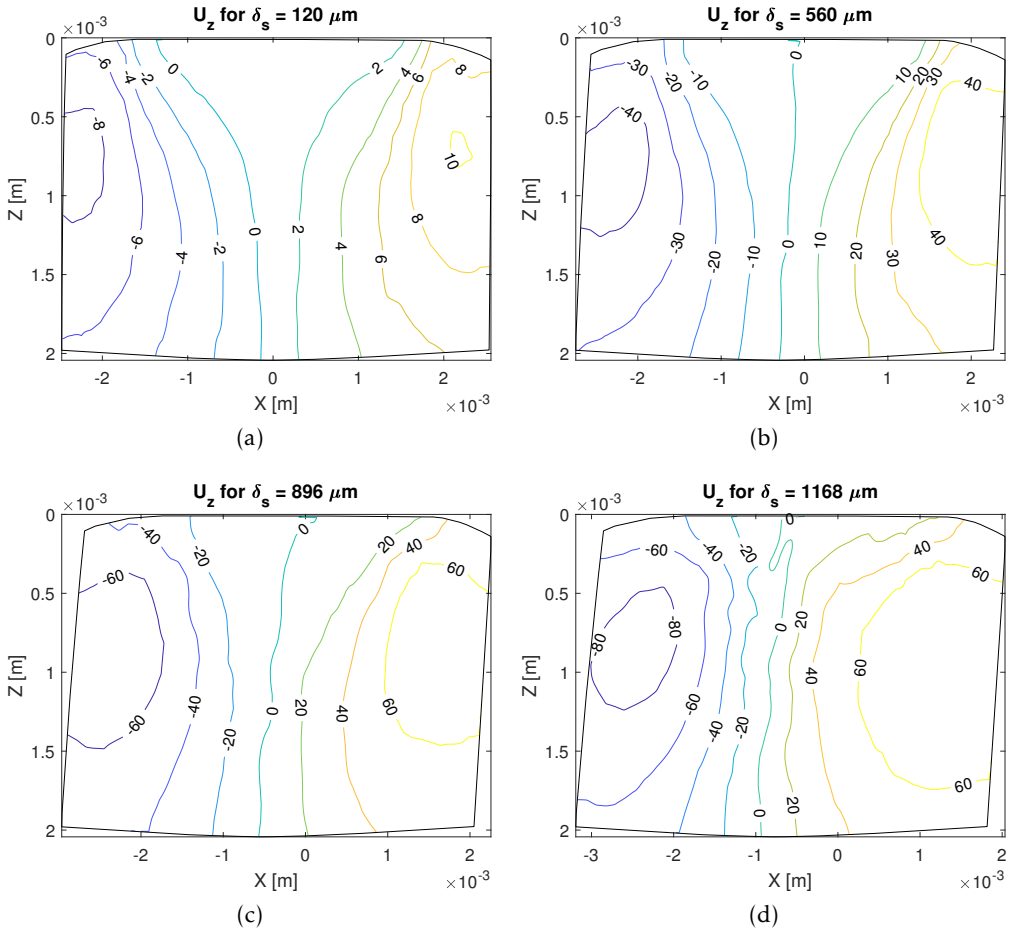

Figure 4.18: Isolines of the component U_z during shear (data are in micrometers) removed of the vertical displacement field at the end of normal compression. The ROI is deformed according to the displacement field. Data refers to the specimen B-10-A.

Figure 4.19 presents the evolution during shearing of the global U_z field, *i.e.* without any subtraction of the vertical displacement field at the end of the compression. The plots for all the steps are visible in Fig. 6.10 in Appendix 6. We make here the choice to plot the same isolines on each subfigure to better capture the shear effects. The global position of the isolines (and especially of their centroid) shifts with the position of the contact zone. As expected from previous observation, the left part of the PDMS experiences a larger absolute displacement towards PMMA, while on the right of the contact the opposite phenomena is observed. Furthermore, the inter-distance between each isoline is also changing. Indeed, on the left of the contact (leading edge), the isolines get closer to each other while, on the right (trailing edge),

they are moving apart. Despite these modifications, the vertical displacement field keeps the same global shape as at the end of compression. The variations on the vertical displacement field, brought by the applied shear displacement, can induce changes in the normal stress distribution and then in the normal pressure at the surface. This would confirm the loss of validity of the previously discussed models (CM, Savkoor) assuming the normal pressure distribution in the contact area to be independent of the shear force. Unfortunately, as already introduced in the previous chapter in section 3.3.3, the difficulty of computing σ_{zz} in the case of an elastomer makes the profiles of the normal stress very noisy and we were not able to extract physically relevant information that could confirm our hypothesis.

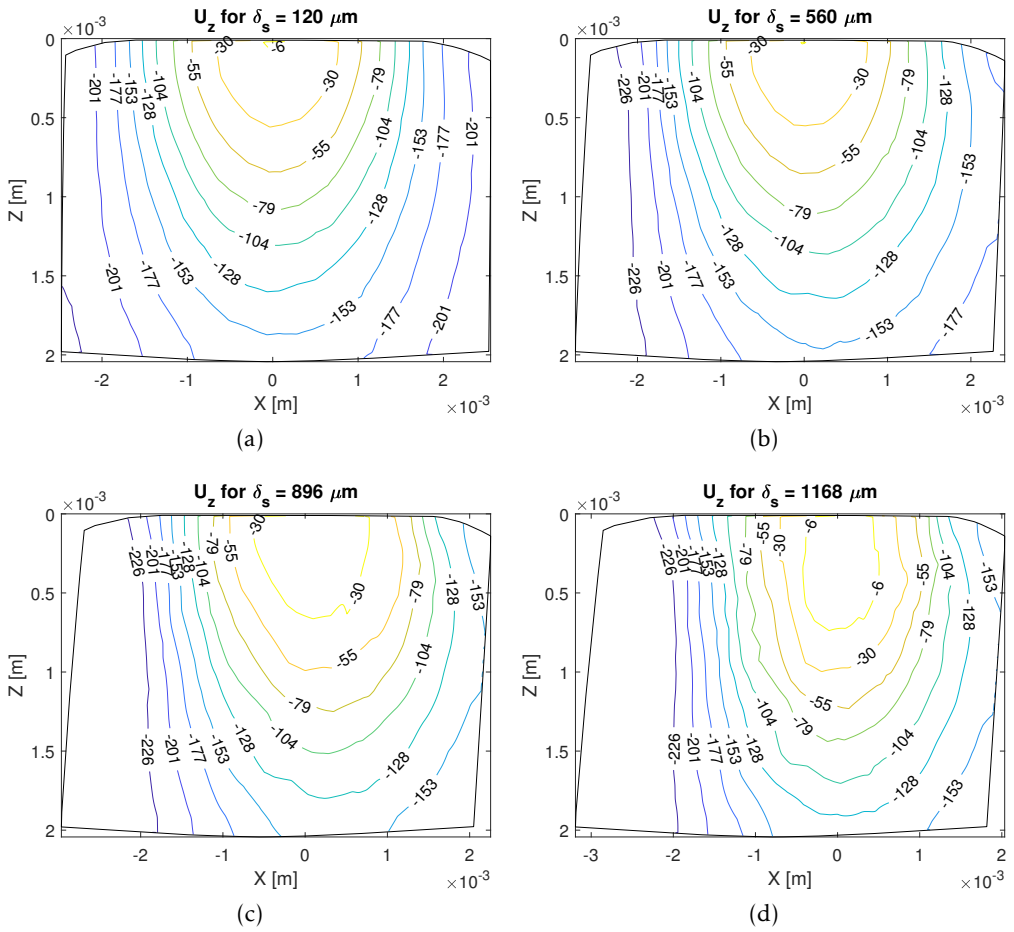

Figure 4.19: Isolines of the component U_z during shear (data are in micrometers) starting from the contour plot at the end of normal compression. The ROI is deformed according to the displacement field. Data refers to the specimen B-10-A. Data are in the reference system of the fixed PMMA plane and are in the reference system of the fixed PMMA plane.

Lateral displacement component U_x

To conclude the analysis of the displacement field, Figure 4.20 shows the evolution of the component U_x/δ_{s-PK} where δ_{s-PK} is the imposed shear displacement measured at the maximum of the shear force Q (force at peak) indicating the transition from static to dynamic friction. This normalization allows to better quantify how much the imposed displacement is partitioned inside the bulk and how far these values are from the displacement at peak. The

isovalues are separated by intervals of 5 % from 0 % to -100 % (the plots for all the steps are visible in Fig. 6.8 in Appendix 6). We remind that the displacement values represent only the shear contributions and that the U_x field related to the compression part of the experiment has been removed. To begin, we observe that the isolines starting from the edges of the contact zone shrink under the application of the shear displacement and that their value increases. In other words, we detect here an increasing displacement inside the contact area in agreement with the presence of an invading sliding zone over the stick zone as observed previously.

Successively, we can also note how all the isolines have a characteristic shape found all along the specimen. In the case of simple shear test, as in the present experiment, we expect the isolines of U_x to be horizontal and parallel to the direction of the imposed lateral displacement. The values for each isoline grow progressively from the contact plane towards the PDMS base. In Figure 4.20(d), the isolines at 100 % is not visible in the ROI but we expect to find it at the PDMS base. In the upper part of the sample, the presence of the contact area changes the shape of the isolines and makes them appear as parabolic with an apex aligned with the contact center. This parabolic shape results from the fact that the lateral movement is only impeded in the stick zone of the contact area, while it is free or partially free to move in the rest of the surface. Even if it is difficult to precisely evaluate the characteristic size over which the contact disrupts the displacement distribution compared to a simple shear test, we note that this characteristic size is of the order of magnitude of the size of the contact.

To illustrate the effect of the height of the specimen, Figure 4.21 shows the normalised lateral displacement δ_{s-PK} for the specimens B-10-A and A-10-A where the first one is the smallest. The isolines for the higher specimen (A-10-A) are more inclined which may indicate an higher contribution of rotation as expected for shear test on more elongated specimens. In particular, this phenomenon is especially true far from the contact area, showing how the influence of the contact area is felt and dominant up to a given depth. A complete analysis of the effects of the presence of a contact interface on the bulk behaviour will be detailed in the next section.

Partial slip effect on the bulk displacement field

Considering the shape of our samples, characterised by a cylinder mounted by a sphere, the rotation of the bulk should not be neglected as it can contribute to modify the mechanisms at play at the interface and in the bulk during shearing.

In order to quantify how the rotation of the bulk could have contributed to the measured displacement field, we performed the following test. A shear test was carried out on the sample B-10-A starting from an already compressed state corresponding to the maximum indentation showed in the previous chapter. Then 4 shear displacement steps were applied with the same order of magnitude of the displacement analysed here in this chapter. To analyse the effects on the overall bulk, data acquisition was conducted with a volume resolution of $10\ \mu\mathrm{m}$/voxel instead of the usual one at $4\ \mu\mathrm{m}$/voxel. Adopting the same mesh used for the DVC measurement with the current image resolution, we performed a FEM calculation (with the use of the Arruda-Boyce hyper-elastic law) imposing a constant displacement at the base (the average lateral displacement measured by DVC) and the PMMA displacement on the plateau of the mesh corresponding to the contact area. In this way the contact zone shifts laterally of the applied displacement, no partial slip mechanisms are possible at the contact interface that moves as if it would be perfectly adherent to the PMMA surface. In other words, we artificially remove all the interfacial phenomena assuming perfect adhesion in the contact zone. Then, thanks to

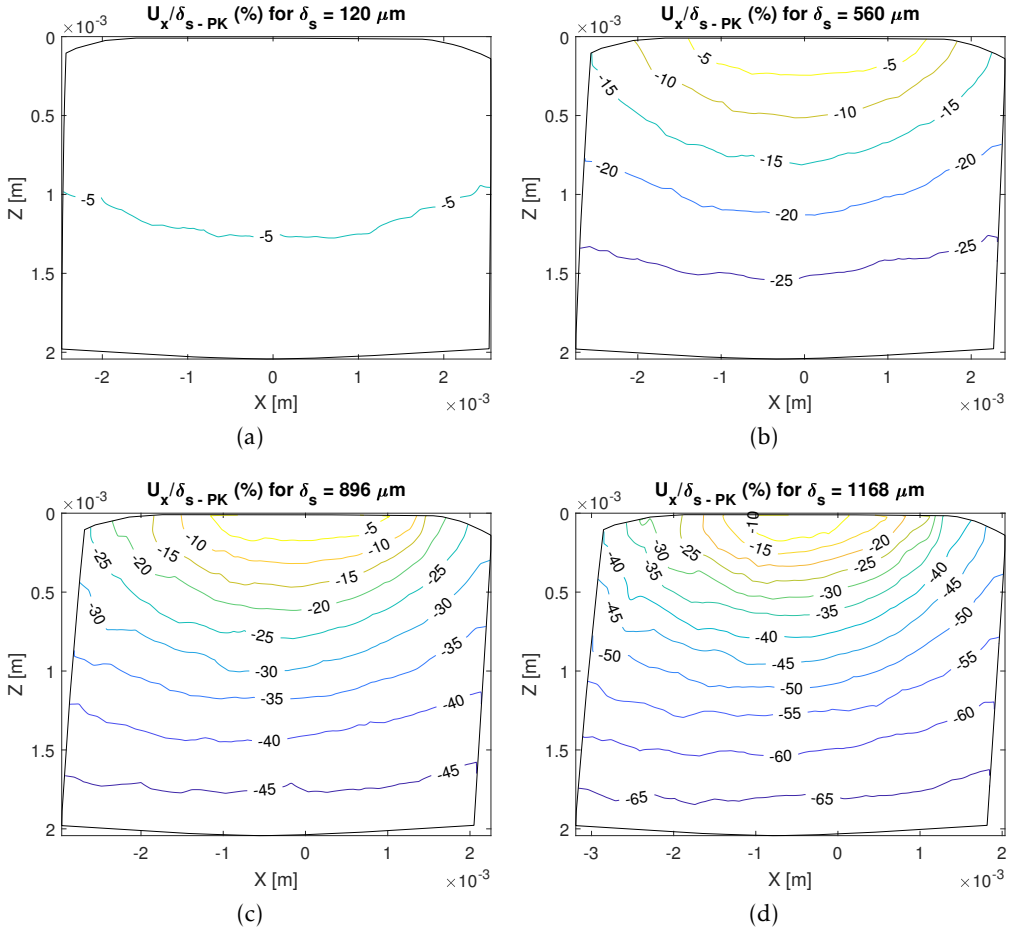

Figure 4.20: Isolines of the component U_x/δ_{s-PK} during shear in the case of the specimens B-10-A where δ_{s-PK} indicates the imposed displacement at peak of the tangential force. The displayed displacement here has been removed of the one measured at the end of the compression part. Data are in the reference system of the fixed PMMA plane.

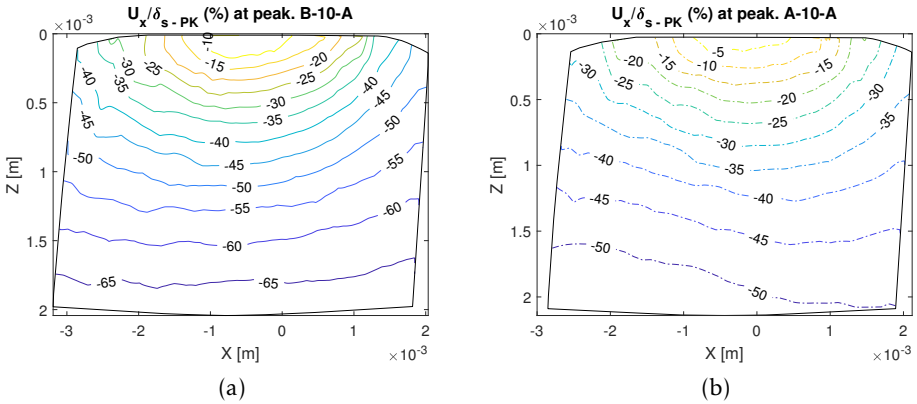

Figure 4.21: Isolines of the component U_x/δ_{s-PK} at tangential force peak in the case of the specimens B-10-A (a) and A-10-A (b) where δ_{s-PK} indicates the imposed displacement at peak of the tangential force. The displayed displacement here has been removed of the one measured at the end of the compression part. Data are in the reference system of the fixed PMMA plane.

the relation of equation 4.1, we can estimate the contribution of partial slip (U_{PS}), as if no rotations were included, by simply subtracting the field obtained with the previously described simulation (U_{FEM}) from the DVC displacement field (U_{DVC}).

$$U_{DVC} = U_{PS} + U_{FEM} \tag{4.1}$$

The results of this correction is illustrated in Fig. 4.22. For clarity for the reader, this difference is appreciable in form of vector field in the Fig. 4.22a where the DVC field is plot in red and the FEM one in blue. The lateral and vertical differences of these two vector field ($U_{DVC} - U_{FEM}$) are visible, respectively, in Fig. 4.22b and Fig. 4.22c. The coordinates of the sample have been normalised to the contact radius at the end of the normal indentation a_c (we assume here that the contact radius does not evolves significantly during the shear). Starting from U_x it is evident in Fig. 4.22b that the lateral difference increases from the base to the surface and the maximum is reached at the leading and trailing edge. The fact that this difference changes from bottom to top is an evidence that the mechanism at play in our PDMS sample is nearly represented by simple shear only on the lower part. In a zone of typical size one time the contact radius, the influence of a sheared contact interface, with all the related mechanisms such as partial slip, lifting and laying, change the behaviour of the sheared sample with respect to simple shear. Secondly, the vertical component too shows relevant differences. This is positive (*i.e.* moving far from the PMMA) on the left side of the specimen and at the trailing edge while it is negative (or moving towards the PMMA plane) on the right side of the specimen and at the leading edge. Clearly, this does not mean that the mechanism is inverted by a lifting at the leading edge and vice-versa, but only that the mechanism of lifting and laying inside the bulk would have been amplified if the interface mechanism (notably the presence of an evolving contact area) were not having a role during the experiment.

4.2.4 Bulk strain field

In analogy with the analysis made in the previous chapter about the evolution of the strain field under the application of a normal indentation, we show here the changes in the three components of the strain field ε_{xx}, ε_{xz} and ε_{zz} in 3D at full sliding (see Fig. 4.23) and in the central $X - Z$ plane, respectively in the figures 4.24, 4.25 and 4.26 (the plots for all the steps are visible, respectively, in Fig. 6.11, 6.12 and 6.13 in Appendix 6). Data refers to the shear experiment of a specimen B-10-A during the four steps analysed before in the case of the displacement field. The red and blue points in each figures correspond respectively to the position of the maximum and minimum and Figure 4.27 represents the evolution of those two values for each of the three strain components as function of the shear displacement. Differently from the case of a normal load experiments and because of higher deformations caused by the shear displacement, we plot here the values of the strain according to the Green-Lagrange formulation. The formulation of the Green-Lagrange strain tensor comes from the finite strain theory that is adopted when strains and rotations are not infinitesimal any more. The components of the strain in the Green-Lagrange formulation contain higher order terms as:

$$\overline{\overline{\varepsilon}} = \frac{1}{2}\left(\nabla\overline{U} + \nabla\overline{U}^T + \nabla\overline{U}\cdot\nabla\overline{U}^T\right) \tag{4.2}$$

where $\overline{U}$ is the local displacement vector.

On Figure 4.24, at the first step of shear, the in-plane lateral compression/dilation of the specimen (ε_{xx}) exhibits a maximum in the bulk beside the contact center and a minimum at the

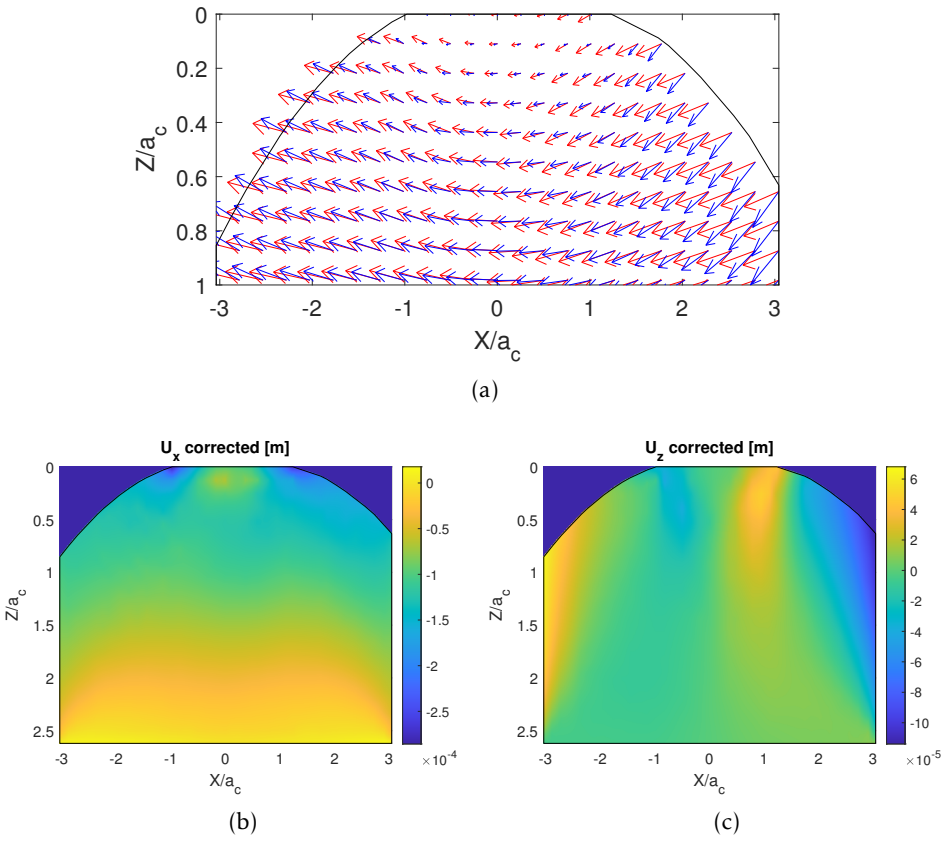

(a)

(b)

(c)

Figure 4.22: Contribution of the partial slip during a shear experiment. (a) Displacement field measured by DVC (red arrows) compared to the one obtained with FEM simulation assuming perfect adhesion in the contact. The arrows are magnified of a factor 2 for visualisation. (b) U_x displacement component corrected of the rotation part. (c) U_z displacement component corrected of the rotation part. The coordinates of the sample have been normalised to the contact radius at the end of the normal indentation a_c. Data for the specimen B-10-A.

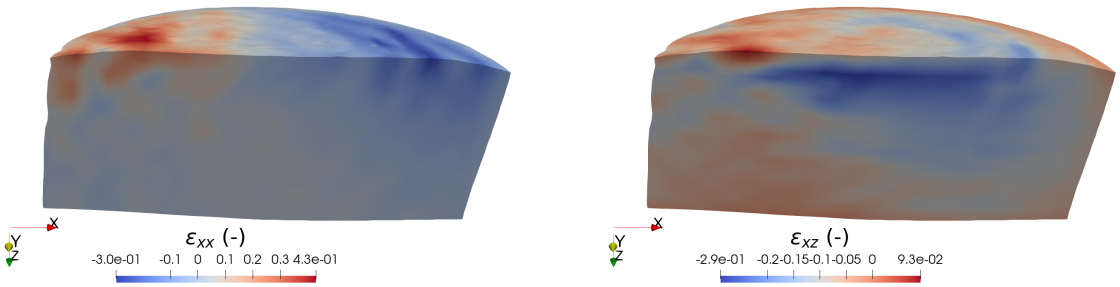

(a)

(b)

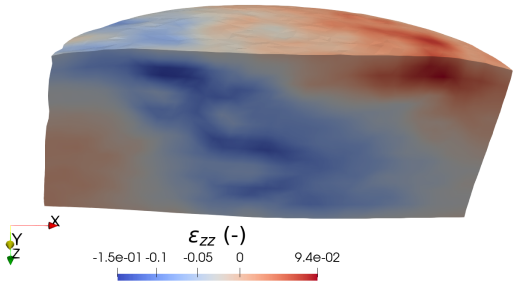

(c)

Figure 4.23: 3D observation of the components of strain ε_{xx}, ε_{xz} and ε_{zz} in the deformed configuration for a shear experiment with $\delta_c = 252$ µm and $\delta_s = 1168$ µm. Specimen B-10-A.

surface trailing edge. When comparing to the last compression stage (see Fig. 3.21), we see that the minimum at the trailing edge has already reached the PDMS surface under the application of a small shear displacement while, the maximum is still inside the bulk. In the second step of shear (see Figure 4.24(b)), conversely, the maximum has moved at the contact leading edge. Remembering that a positive value stands for dilation and a negative one for compression, we can observe the progressive intensification of a zone of dilation (respectively compression) in the bulk under the leading edge (respectively trailing edge). Those observations inside the bulk are in good agreement with the work of Lengiewicz *et al.* (and shown in Fig. 1.15) where they observed, in the contact interface, the presence of a dilation at the leading edge of the contact and one of compression at the trailing edge. On Figure 4.27, the minimum and maximum respectively decrease and increase in a quasi-symmetric way with a variation of the same order of magnitude.

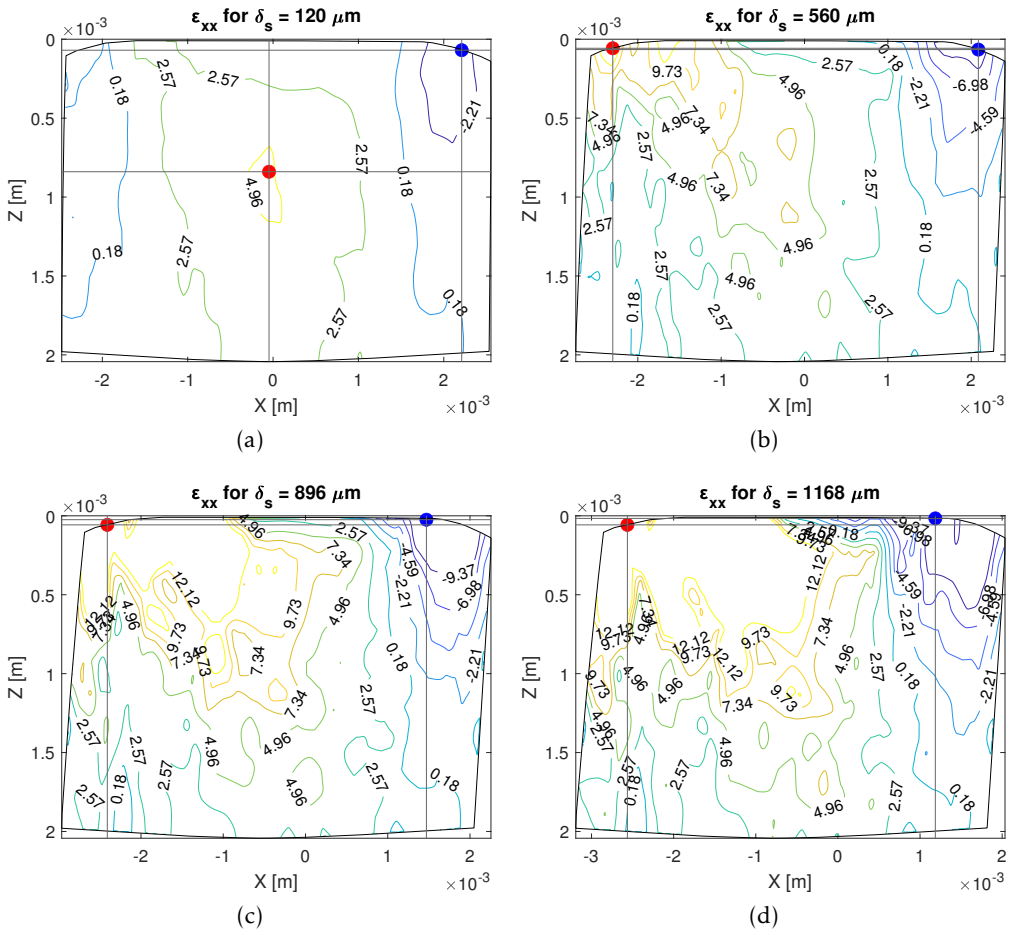

Figure 4.24: Contour plots of the strain component ε_{xx} (in %) on the central $X - Z$ plane obtained with the DVC measurement for the specimen B-10-A at four consecutive shear steps. The red and blue points stand, respectively, for the maximum and minimum values of the strain in the relative plot.

In Figure 4.25(a), the shear strain ε_{xz} still exhibits a minimum and a maximum at the contact edge with anti-symmetric values (*i.e.* two opposite shear directions) very similar to what was observed at the end of the compression stage (see Figure 3.21). As soon as the shear displacement increases (see Figure 4.25(b to d)), the maximum shear at the leading edge keeps its

position all along the experiment while the minimum value (the blue point) moves from the surface to a deeper position in the bulk under the contact. While the depth of this point does not further change for increasing shear, the lateral position evolves so that the point get closer to the contact center. This results in an high shear gradient at the leading edge of the contact, below the surface. In addition, the progressive development of an increasingly extensive area below the contact where the shear strain is nearly constant and minimum. Concerning the evolution of these maximum and minimum values, Figure 4.27 illustrates how the changes in the maximum evolves more with respect to the minimum.

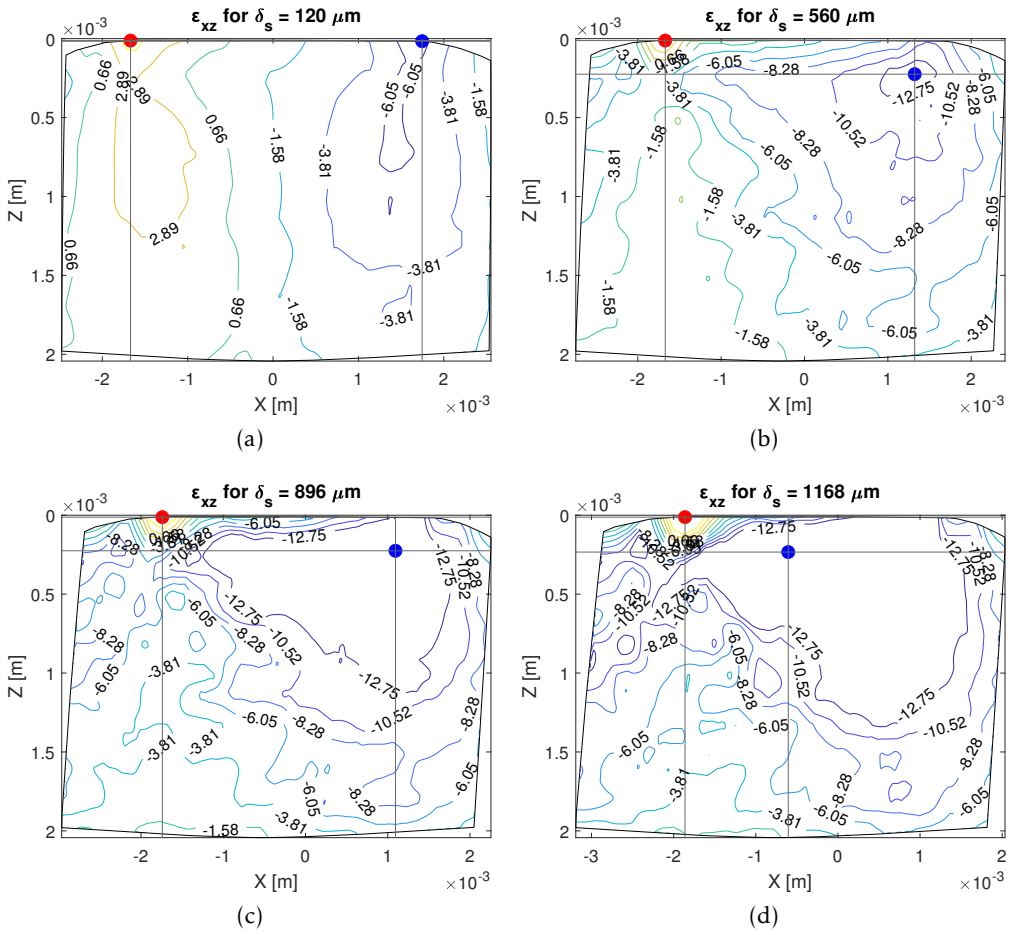

Figure 4.25: Contour plots of the strain component ε_{xz} (in %) on the central $X - Z$ plane obtained with the DVC measurement for the specimen B-10-A at four consecutive shear steps. The red and blue points stand, respectively, for the maximum and minimum values of the strain in the relative plot.

Finally, Figure 4.26 shows how the position of minimum ε_{zz} (blue point), starting from its position at the end of the compression test (below the center of contact), moves towards the leading edge of the contact as shear is increased. On the other hand, this change in position is not accompanied by any notable change in value (see Figure 4.27). The isolines, that were almost isotropic and centered around the minimum after the compression, gradually tighten during shearing and change orientation to ultimately be oriented at 45 degrees following the path of the minimum. Another interesting aspect is the appearance of two opposite dilation zones in term of position at the trailing edge and at the lower left corner of the analysed zone.

This first dilation zone can be related to adhesion effects: points that are lifting from the PMMA plane at the trailing edge can feel the presence of the adhesive forces and feel a resistance to lifting that is here measured as a dilation deformation. On the lower left corner, instead, we can appreciate more a bulk effect that is related to the bending of the specimen: this part of the specimen is both pulled towards the PMMA plane and towards the base of the sample where it is glued. However, we still need further analysis to confirm these hypotheses.

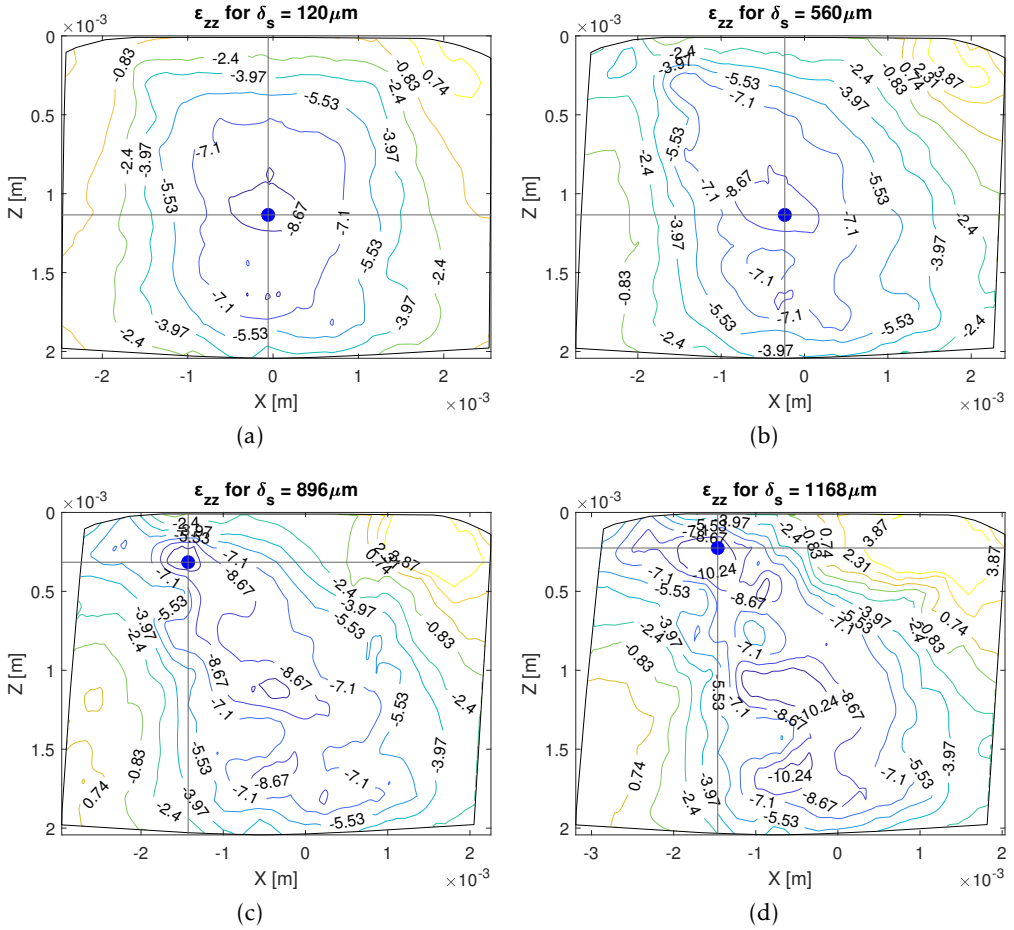

Figure 4.26: Contour plots of the strain component ε_{zz} (in %) on the central $X - Z$ plane obtained with the DVC measurement for the specimen B-10-A at four consecutive shear steps. The red and blue points stand, respectively, for the maximum and minimum values of the strain in the relative plot.

4.2.5 Bulk stress field

With the same procedure as in section 3.3.3, the displacement field measurements were used to carry out FEM simulations for the computation of the stress field with both a linear isotropic (*NLGEOM* deactivated) and hyper-elastic Arruda-Boyce (*NLGEOM* activated) constitutive laws (the used parameters implemented in the FEM code characterising the material are $\mu = 0.375$ MPa, $\lambda_m = 1.917$ and $D = 0.039$ MPa^{-1}). The components of the stress tensor were used to quantify the normalised Mises parameter of the stress tensor $\sqrt{J_2}/p_0$ (see eq. 1.18) in order to compare the results with the predictions from Hamilton's model [24].

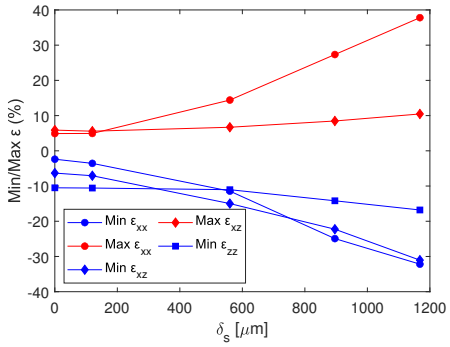

Figure 4.27: Evolution of the minima and maxima of the strain components ε_{xx}, ε_{xz} and ε_{zz} in the central $X-Z$ plane as a function of the shear displacement δ_s.

Comparison with Hamilton's model prediction

The contourlines of $\sqrt{J_2}/p_0$ in the central $X-Z$ plane are plotted in Figure 4.28 under the linear elastic constitutive assumption and compared with the resulting contours from the Hamilton's model at the four shear steps analysed all along this chapter. We remind that only the last step (see Figure 4.28 (d)) corresponds to full sliding condition. As the Hamilton's model supposes that the contact radius does not change under the application of the shear load (as in the Cattaneo-Mindlin model), the (X, Z) coordinates have been normalized to the contact radius a obtained from the Hertzian equations (see equation 1.2) with the normal load P measured during the experiment. To follow the position of the maxima of the stress, two circles are inserted in the images; respectively magenta for the FEM computation in linear elasticity, and black for the theoretical model.

At the first shear step (see Figure 4.28 (a)), a good qualitative and even quantitative agreement between our results and the models is observed. In both cases, we observe a deformation of the contour lines compared to their position at the end of compression (see Fig. 3.26 where the maximum position starts to shift towards the direction of the imposed displacement and closer to the surface. Already from the second step (see Figure 4.28 (b)), the maxima, for both the model and the experiment, are found at the contact surface and their values increase significantly. For the model, we pass from 0.31 in the case of purely normal load to 1.976 with the additional contribution of the tangential force Q. As expected, the applied tangential force increases the deviatoric component of the stress, which may favor the occurrence of yielding in another class of materials such as metals.

As far as the experiment gets closer to full sliding, the maximum moves to the surface and we loose the presence of concentric isolines. Conversely, according to the model, the expected effect of the tangential force is to position the maximum towards the direction of the imposed shear (keeping the presence of concentric isolines around this maximum below the surface) and to create a local maximum at the trailing edge. However, the experimental results found a maximum close to the trailing edge but it suddenly changes its position between panel (c) and (d). Note that, as the invariant is maximum and nearly constant in a large spread region under the contact, the exact position of the maxima is quite difficult to extract and may vary depending on the precision of our calculation. Concerning the isolines far from the surface, we found a good agreement qualitative and quantitative between model and experiment with an increasing difference at increasing shear. Some differences appear when approaching the

contact surface may be due to the influence of the interface mechanisms. Indeed, in our experiment many assumption of Hamilton's model are not respected. First, this model is based on a CM assumption to govern the behaviour of the interface (that we showed not to be the best model to describe our measured shear stress at the interface). Second, the friction coefficient assumed in the model is quite low (maximum 0.7) compared to the one in our experiment (approximately 2). Third, and more importantly, the model was derived for a full sliding interface which is only the case in the last step of our experiment. Nevertheless, as previously mentioned, it seems to better fit with our measurement a low shear maybe because, in such condition, even if full sliding is not achieved, the ratio between P and Q is lower.

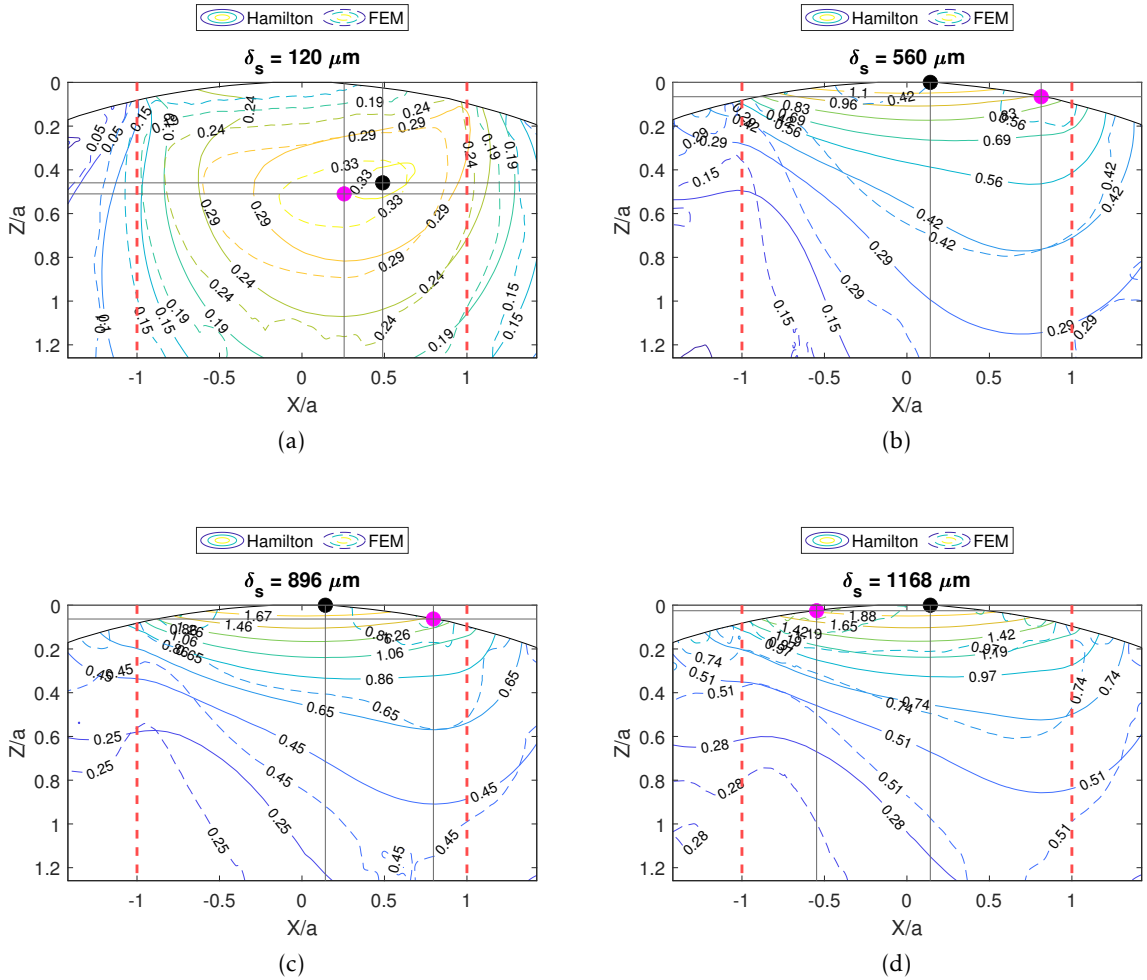

Figure 4.28: Contour plots of $\sqrt{J_2}/p_0$ (in MPa) on the central $X-Z$ plane for the specimen B-10-A indented of 252 µm and sheared on four consecutive steps up to conditions of full sliding: comparison between FEM simulations with a linear elastic model (dashed lines) and the predictions of the Hamilton's model [24] (continuous lines). The colored circles represent the position of the maximum from the FEM computation (magenta) and the theoretical model (black).

Effect of the bulk elasticity

To try to illustrate the effect of the constitutive law that described the bulk of the PDMS, the contourlines of $\sqrt{J_2}/p_0$ in the central $X-Z$ plane are plotted for a computation based on a linear elastic model and on the Arruda-Boyce hyper-elastic one in Figure 4.29. Here, the maximum for the linear elastic model is indicated by the magenta circle while the one for the Arruda-Boyce's is characterised by a blue circle. Qualitatively, the agreement between the two models is very good, especially considering the position of the maxima which shown to be always in the same position. Quantitatively, the dissimilarities are more evident at increasing shear as expected for the increase of the deformation which enhances the differences between a linear elastic and an hyper-elastic model. This is especially true in a zone below the trailing edge (right) while there is a better agreement at the left of the specimen and close to the contact. In fact, the zone where the difference is higher between the two constitutive models, reflects what has been observed in Fig. 4.25 for the ε_{xz} strain; apart from being the larger strain component in absolute values, the plots for the shear strain evidenced the presence of a large zone characterized by a constant high strain that may emphasise the difference between a linear and an hyper-elastic model. Unfortunately, in the absence of dedicated theoretical models, and passed the common sense indicating that the straining behavior of PDMS is rather hyper-elastic than linear elastic, these DVC-based simulations alone do not allow to determine which constitutive model is better to properly describe the physical mechanisms occurring during the sheared contact of such elastomer. We still need the development of new, more complete analytical models to both take into account the proper behavior laws of materials and the interface mechanisms (adhesion, friction, partial sliding, etc.).

4.3 Conclusions on shear experiments

In this last chapter, we investigated the effects of an imposed and increasing shear displacement on a contact interface. Thanks to the new experimental device developed during this study, we have demonstrated how it is possible to carry out *in situ* shear experiments and to follow in a three-dimensional way, thanks to the combination of tomography and DVC analysis, the evolution of the contact area and, for the first time, of the three different fields (displacement, strain and stress) inside the bulk of a sheared PDMS sphere.

First, we show that the extraction of the contact area was possible with the use of the $z-projection$ even with low contrast between the two part of a contact. Despite some minors errors, we were able to capture an evolution of the real contact area during shearing similar to what is observed in the literature for optical experiments [4, 7].
Second, the analysis of the displacement field, obtained from DVC, has confirmed the presence of laying and lifting effects at the contact interface which were recently identified as one of the main mechanism responsible for area reduction during shear of an elastomeric contact [7]. A parallel comparison between the gradient of the lateral displacement component U_x and the measured shear stress at surface obtained with FEM simulations based on experimental data, has demonstrated that this gradient can reveal the presence of slip and a stick zones inside the contact area. Differently from the continuous experiment (like in optics) or from the models, this stick zone is constant during the first shearing steps and suddenly decreases during the last steps close to the full sliding. We linked this phenomenon to the quasi-static characteristic of our experiments and we also compared the stress profiles with the Cattaneo-Mindlin and Savkoor models to see if they were able to capture our measurements. At a first glance, both models showed not to be appropriate to describe the shape of the shear stress

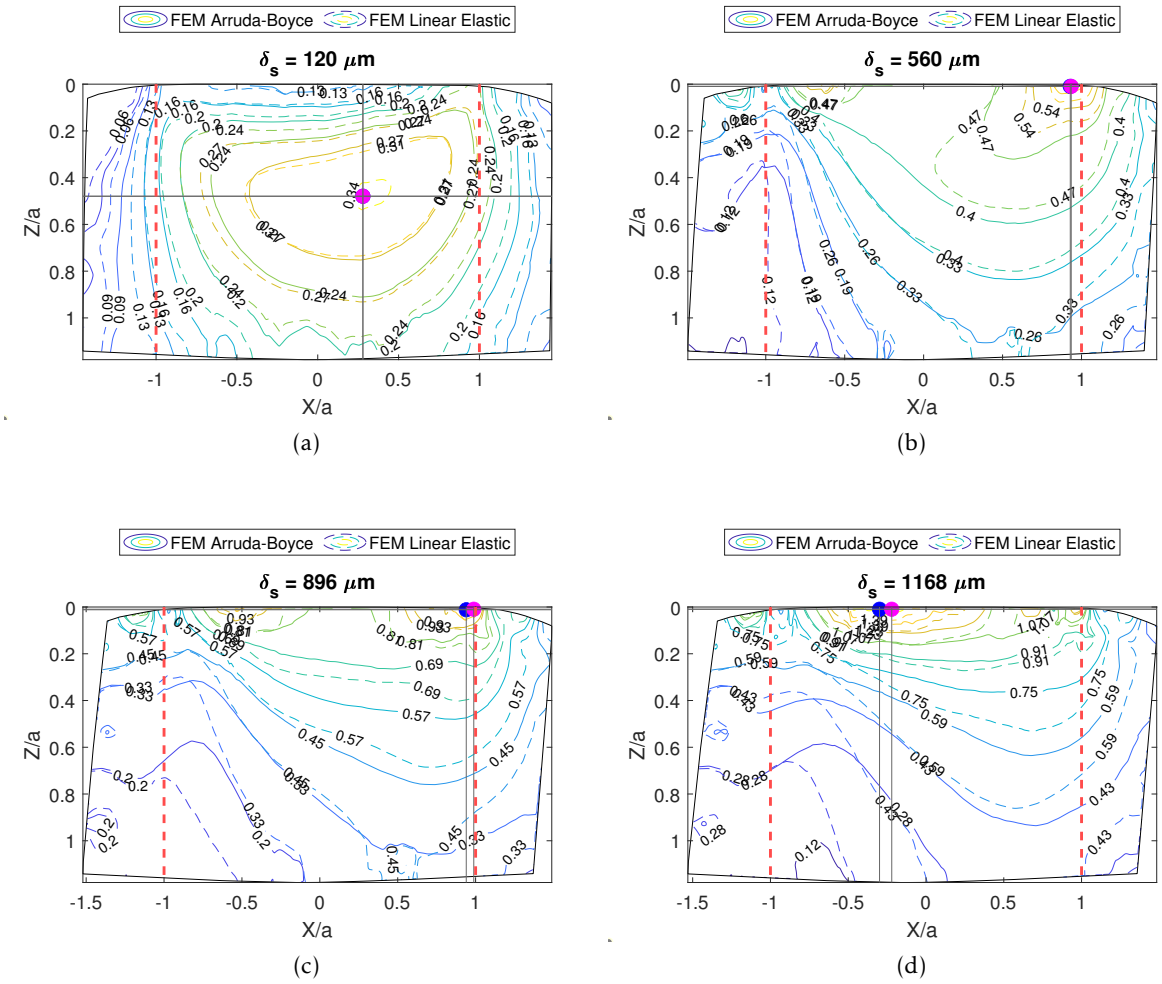

Figure 4.29: Contour plots of $\sqrt{J_2}/p_0$ (in MPa) on the central $X-Z$ plane for the specimen B-10-A indented of 252 μm and sheared on four consecutive steps up to conditions of full sliding: comparison between FEM simulations with a linear elastic model (dashed lines) and an hyper-elastic Arruda-Boyce model (continuous lines). The colored circles represent the position of the maximum from the FEM computation with linear elasticity (magenta) and the Arruda-Boyce model (blue).

profiles. It is only after convoluting the model prediction with a Gaussian function that the match between our data and the models becomes better. This convolution evidenced how our stress measurements are affected by the presence of a finite element mesh used to perform DVC analysis and that our result only corresponds to the average of the real values inside the typical size of one element. In any case, the Savkoor model showed to be more adapted to follow our measurements, confirming the presence of a Tresca's slide criterion rather than the Coulomb's one; the shear stress is nearly constant in the contact area during full sliding. The quantitative differences between measurements and models could be related to different theoretical hypotheses that were not applicable in the present study as, for example, the use of a constant normal pressure to derive the equations. Finally, we demonstrated how additional models, able to describe the contact mechanics of elastomers still need to be completed to capture, for example, visco-elastic and/or non-linear phenomena.

Third, the investigation of the displacement field inside the bulk has revealed important mechanisms able to explain the observed phenomena at the interface. For instance, other than a global lateral movement caused by the shear displacement, the vertical displacement generated during shear has shown that the lifting/laying effects (already observed with optical experiments [7]) explaining the changes in the contact area are originated by bulk heterogeneities in the displacement field. To further understand the effect of partial slip in the observed bulk mechanisms, a simulation assuming a perfect adhesion between PDMS and PMMA was conducted and remarked that the presence of a contact interface (and all the effects related to partial slip, lifting, laying etc...) is felt up to a characteristic depth of one time the contact radius while, after it, the behaviour of the sample is more likely described by simple shear. Furthermore, the presence of a contact interface has the effects of reducing of the vertical movement of the PDMS, both towards and downwards the PMMA plane.

Fourth, we have analysed the strain fields. For the xx component, under the effect of shear, a dilation state at the leading edge and a compression one at the trailing with the maximum values reached at the surface was observed. This in-plane compression/dilation was already observed experimentally with optical experiments [7] and, thanks to our experiments, we can observe how this surface deformation originates from bulk strain. For the xz component, we observed a vast zone, below the contact area, characterised by a constant (and maximum) shear. The maximum and the minimum, representative of shear in opposite directions, get closer due to the effects of the imposed shear and generate an high gradient below the contact leading edge. Finally, for the component zz, the minimum, which indicates vertical compression, moves to the contact leading edge together with the apparition of a dilation zone at the trailing edge.

Last, the analysis of the stress field, obtained with FEM simulations with linear elastic and hyper-elastic Arruda-Boyce behaviours, were compared with the Hamilton's prediction. The maximum of the normalised Mises parameter moves at the surface as expected and increases its values. The global shapes of the isolines qualitatively follow the model inside the bulk but there are more important differences close to the contact area. This was predicted by Hamilton when, in its paper, he evidenced how the equations were not valid for a coefficient of friction higher than 0.7 (like in the present case). The highest differences remarkable close to the contact, probably originates from the interface mechanisms that could not be described by the Hamilton's model which is based on CM hypothesis. All those results evidence how additional model are still necessary to describe the stress beneath the contact area in the presence of

contact interfaces characterised by very high friction coefficient and by high strains or hyper-elastic phenomena.

5 Conclusions and perspectives

5.1 General Conclusions

In this chapter a complete summary of the main conclusions exposed all along the present study will be done with a focus on the advantages and disadvantages related to the use of XRCT to contact mechanics experiments. Finally, we will propose some experimental perspective that can be helpful to start new types of experiments and to overcome some of the limits that were presented along this document.

We have seen how, from an introduction on the main results found in literature, surfaces are actually rough on different scales and that the real contact area A_R created when two bodies are put into contact is much smaller than what we can observe thanks to an external observation. Furthermore, we also showed how it is this real contact area which controls the friction force when two bodies are forced to slide. Starting from this assumption, experimental works during the last few years developed optical devices able to access the contact area *in situ* and *in operando* thanks to the use of high-resolution and fast-speed cameras. Despite the fact that these techniques allow easy access and measure of A_R in a wide range of experimental situations, they are mainly limited by the need to have at least one of the two materials optically transparent. It means that contact pairs like a tire-road one can not be analysed and a different technique is then necessary.

This big and fundamental limit was the first motivation of the present study and X-ray Computed Tomography was selected as an appealing candidate to get rid of the optical transparency limit (however, a good contrast to X-rays comes into play with this technique). With its three-dimensional access to important information both at the contact interface and inside the bodies, XRCT showed to be an ideal technique to both overcome the transparency limit and also observe the contact phenomena with a three-dimensional observation. In order to account for the limits of XRCT and its precision in the detection of the contact area, a simple model contact interface was adopted. The use of a sphere-on-plane contact enabled to compare our results with existing theoretical models while the employment of a soft polymer contact gave us the possibility to have a sufficiently large contact area with respect to the image resolution of our 3D XRCT scans. Furthermore, the use of a silicone permitted to easily disperse particles inside the bulk and have some visible markers inside the reconstructed scans that were used to perform Digital Volume Correlation. Even though the contact could have been completely composed of two non-transparent materials, we made use of a transparent PMMA

plane to have the possibility of comparing the XRCT results with those coming from a classical optical device for which we already mastered the tribological results. Before carrying the tests, the PDMS mixture (filled with particles) was tested on a unidirectional tensile test and we confirmed its non-linear elastic behaviour which was well described by the Arruda-Boyce model. To reproduce contact experiments, an already existing compressing machine for materials characterisation was slightly adapted to perform normal indentation experiments. Conversely, shear experiments required a new device that was designed, validated and used during this study.

Forced by the time required for the acquisition of a single 3D scan (nearly 20 minutes) experiments had to be done in a quasi-static way. Namely, after the application of a given normal and/or tangential displacement, the loading had to be interrupted to maintain the samples in position during the acquisition of the scan and avoid image blurring. This clearly limited the types of tribological experiments accessible and, in particular, the dynamic part of a sliding experiment is out of scope. As a consequence, we focused only on the part before the transition to full sliding. Given the 3D volumes for each step, we had to find a way to properly segment the images and extract the contact area. The Random Walker algorithm was found as the best for the image contrast available and allowed to segment, at the same time, three different types of materials (PDMS, PMMA and air). Then, the contact area was found and extracted with a finite element surface reconstruction based on the Marching Cube algorithm and the contact area was identified being the patch sharing the same element nodes position on the PMMA and the PDMS surfaces. In addition, the image segmentation gave also access to the coordinates of the external skin of the deformed PDMS sample, useful for the 3D measurement of the superficial displacement field. Other than the measurement of external quantities, we detailed an adaptation of an already existing DVC code to be used on the configuration of our experiments and, in general, to extract the 3D displacement field of a compressed and sheared sample.

In terms of results, the first part of the manuscript (chapter 3) was focused on purely normal loading experiments performed on a sphere-on-plane contact. The extraction of the contact area with the methods introduced before returned the expected circular contact area with also the attended $A_R(P)$ behaviour with an hysteresis between loading and unloading; a confirmation of the presence of adhesion. We showed that we were able to extract the contact area without the limits of optical transparency (the procedure could be applied to all types of materials characterised by a good contrast in terms of X-rays absorption). However, the shape of the contact boundary evidenced the presence of some irregularities that were linked to the presence of image artefacts at the interface. These artefacts were reduced thanks to experimental modifications during the image acquisition but they were not completely eliminated. The comparison of the $A_R(\delta_c)$ curve from tomography and optics evidenced the appearance of an offset which origin was found in the methods used for the measurement of the contact area. While the surface mesh reconstruction returned a negligible error not justifying the found gap, a first important contribution was found in the image resolution used for the scan acquisition: reducing the voxel size to half its previous value resulted in a halving of the measured shift. The error related to the image resolution was connected to the "partial volume effect" for which the gray-value of a given voxel, ideally representing a single material, was actually an average of the surrounding materials in a given spatial position (which is critical at the contact boundary with a triple air-PDMS-PMMA point). This effect affected our segmentation causing an overestimation of the contact area. Due to the limited image resolution (limited to $4\ \mu\mathrm{m}$/voxel for geometrical reasons), we proposed an alternative and *a posteriori* correction of the XRCT measurement based on the Hertzian contact law. We have then demonstrated how a correction

based on contact mechanics law could finally result in a very good superposition of the XRCT and optical data. The trend of XRCT in overestimating the contact area is something to be kept in mind and considered for future contact experiments involving tomography: the voxel size should be reduced to a minimum and some additional theoretical considerations should still be considered to get the true value of the contact area.

Having access to the coordinates of the external shape of the PDMS during its deformation allowed us to measure the superficial displacement field in 3D. In this case too, we proved the presence of adhesion and found a good average agreement with the theoretical models. These ones were calculated based on the material parameters obtained fitting the $A_R(P)$ data coming from an optical experiment. The good agreement with the models through optically measured parameters confirmed, again, the validity of the experimental results coming from XRCT and that we were able to accurately measure the displacement field by just knowing the shape of the deformed PDMS obtained with image segmentation. Because of the limited resolution, however, the incertitude related to the estimation of the PDMS profile did not consent to capture the tiny local differences between each theoretical models appearing near the contact edges.

Thanks to the use of dispersed particles and Digital Volume Correlation we also had access to the 3D displacement field inside of the bulk along the experiments. The measurement, based on a finite element mesh discretization, was able, at a first glance, to follow the evolution of the PDMS external skin and to reproduce the presence of a plateau representing the contact area. Starting from this, we proposed an alternative method for the measurement of the contact radius. The method was simply based on the superficial displacement field measured by DVC and the radius was obtained with considerations on the gradient of this field. The measurement showed to completely reproduce the benchmark optical measurement without uncertainties related to the image resolution or the image segmentation.

Concerning the behaviour inside the bulk, we focused on two displacement components on the central $X - Z$ plane of the sample. We have shown that U_z evolves linearly with the contact radius but that it does not evolve linearly inside the bulk, from the surface to the base of the PDMS. For U_x, instead, the displacement showed one maximum and one minimum related to the lateral movement of the PDMS linked to the presence of the contact area and to the incompressibility of the material. Observations on the displacement field were confirmed by considerations on the measured strain field.

Our analysis related to DVC measurements ended with finite element simulations based on the evaluated displacement field from DVC and adding a linear elastic or hyper-elastic constitutive law for the comparison of the results with the Hamilton's model, which equations were developed only for the stress field. For the comparison with the model, we adopted a linear elastic law, accordingly to the assumptions made to extract the theoretical equations. While the σ_{xz} showed a good agreement, it was not the case for σ_{zz} where problems associated to simulation of an incompressible materials emerged. It is for this reason that we believe that it is necessary in the future to develop analytical models expressed in displacement or deformation rather than in stress. Thus, their predictions can be directly compared to the results of the DVC without having to use FEM simulations. We also showed the evolution of the normalised Mises parameter evidencing a good agreement between simulation and Hamilton's equation; an agreement less valid at increasing indentation. This difference surely originates in the Hamilton model hypothesis which are not completely adapted to describe the contact of an elastomer for which an hyper-elastic model is necessary. In any case, we pointed out how it is

possible to obtain stress measurements inside the bulk of a deformed body in contact without assumptions on the contact mechanics laws on the surface and only relying on real measured quantities coming from an *in situ* experiment (in this case an assumption on the constitutive law is still necessary).

The last chapter was mainly focused on shear experiments obtained with our new experimental device. Experiments were conducted both on XRCT and on an optical tribometer to validate the first measurements and ensure that our tribological test reproduces all the main characteristics of this type of test in terms of friction force, evolution of contact area, etc.

Limited by the absence of a good contrast between PDMS and PMMA (due to choice of inserting aluminium particles in the bulk to promote image contrast), the contact area was qualitatively estimated by means of the $z - projection$, which showed to be able to capture the changes in the shape on the contact boundary caused by a shear load. The analysis of the superficial displacement field confirmed the presence of laying and lifting mechanisms as the origin of area reduction. For the component U_x at the surface, the analysis demonstrated that its gradient could be a preliminary indication of the zones of stick and slip inside the contact area. This was possible thanks to a parallel analysis of the stress component σ_{xz} at the surface for which we also noticed how the growth of the slip zone invading the stick area was not linear but strongly decreased at the end of the experiment, close to full sliding. This was related to the quasi-static conditions of our experiments that probably caused a "re-stick" of the precedent slipped area during the scan time. The profiles for the shear stress were compared with theoretical models and showed a good qualitative agreement only in the case where the theoretical profiles were convoluted by a Gaussian function. This evidenced how the presence of finite elements describing the stress field introduced uncertainties which size was linked to the size of the mesh used for DVC. Anyway, this first comparison with convoluted profiles confirmed how the Savkoor model and the Tresca's sliding criterion were more adapted to describe our experimental results. The remaining differences were more related to the fact that these models were developed assuming a constant normal pressure during the shear test and a linear elastic behaviour: both did not completely represent our conditions and shows again the necessity of additional models.

Inside the bulk, the analysis of the displacement field evidenced the presence of heterogeneities in the orientation of the displacement vectors. In terms of global behaviour of a pillar-like specimen as the one adopted, a FEM simulation showed how the behaviour was represented by a simple shear only beside a depth $Z = a$ while, the presence of a contact interface characterised by a stick and a slip zone, was felt up to this depth. Concerning the related strain field, represented in the Green-Lagrange formulation because of the high strains involved in a shear test, some interesting trends were observed: ε_{xx} showed a maximum and a minimum respectively at the leading and trailing edge, ε_{xz} was characterised by a minimum inside the bulk moving closer to the leading edge and a maximum at surface fixed at the leading edge and, finally, ε_{zz} evidenced how the minimum aligned on the axis of the specimen was moving towards the leading edge following the trajectory connecting its initial position and the leading edge.

Adopting FEM simulations, the comparison of the Von Mises equivalent stress with the Hamilton's model displayed a qualitative good agreement inside the bulk but an higher discrepancy close to the contact. This was probably due to the fact that the CM model, at the base of the Hamilton's equations, was not adapted to describe our interface mechanisms as introduced before. In addition, our friction coefficient was quite larger than the one for which the Hamil-

ton's equations were valid and we also showed how the presence of hyper-elastic phenomena, again, requires the development of additional models for the description of bulk and surface phenomena of a sheared contact involving elastomers.

To conclude, with XRCT we were able to study the case of a model sphere-on-plane contact between a deformable smooth PDMS sample indented and sheared over a rigid smooth PMMA plane. Our fist objectives have been achieved showing how this new method can be adapted to extract the real contact area of non transparent materials in contact, providing also justifications on the limits of the experimental technique. One of the main advantages of XRCT has been shown with the use of DVC, thanks to which the three-dimensional displacement field is obtained. This last one represents an exclusive advantage of this technique with respect of all the previous experimental investigations, found in literature, based on optical observations. The results brought by DVC has evidenced how the majority of the available analytical models are not sufficient to describe our experimental case. Consequently, XRCT shows to be a reliable experimental method for the development of new models. In this sense, our experimental data will be available to validate more complex models taking into account, for example, the hyper-elasticity or the adhesion at the interface.

5.2 Perspectives

In addition to the results and analyses presented in this document, our investigation on the use of XRCT in contact mechanics opens numerous perspectives both for the study of more complex or realistic surfaces and for theoretical developments.

5.2.1 Contact experiments with model multi-asperity surfaces

As we have already introduced in the first chapter of this manuscript, surfaces are actually rough on different scales and the topography of bodies in contact is of relevant interest for the determination of A_R. Based on a previous thesis aiming to tune the topography of a modeled multi-asperity interface to obtain a given friction response [57], we prepared more complex multi-asperities samples adapted to XRCT *in situ* experiments and try to apply the same analysis (segmentation, surface reconstruction, DVC etc...). The picture of one multi-asperity samples is shown in fig.5.1. This specimen is composed of 5 spherical asperities (each with a radius of curvature $R = 1$ mm) where 4 out of 5 are spaced of ± 2.5 mm from the central one. The central one shows a height of 350 µm while the 4 external ones are 280 µm in height. The mould for this specimen was obtained by micro-milling on an aluminium base (details are specified in [57]) while the preparation of the PDMS mixture (with aluminium and glass particles) and reticulation was the same as specified in section 2.2.2. Note that, the PDMS curing-base ratio was of 1:10, no spin-coating was applied and the PDMS was directly cast into the aluminium mould.

The specimen was installed inside the experimental device for XRCT to carry out normal and shear experiments. Figure 5.2 shows the crop (along the longitudinal plane passing from two of the four external asperities) of a reconstructed XRCT volume during a normal compression and shear experiment on a PMMA plane. The experiments started from a non-contact configuration, then the normal displacement (image (b)) and the shear one (image (c)) were applied successively. In between each image there were intermediate steps that are not represented here and, as usual, experiments were carried out step-by-step in a quasi-static manner.

Figure 5.1: Picture of a multi-asperity specimen used for XRCT experiments. The specimen in the photo is composed of a PDMS bulk filled with aluminium particles.

Starting from these volumes, the coordinates of the external skin of the deformed PDMS and the internal displacement field could be measured.

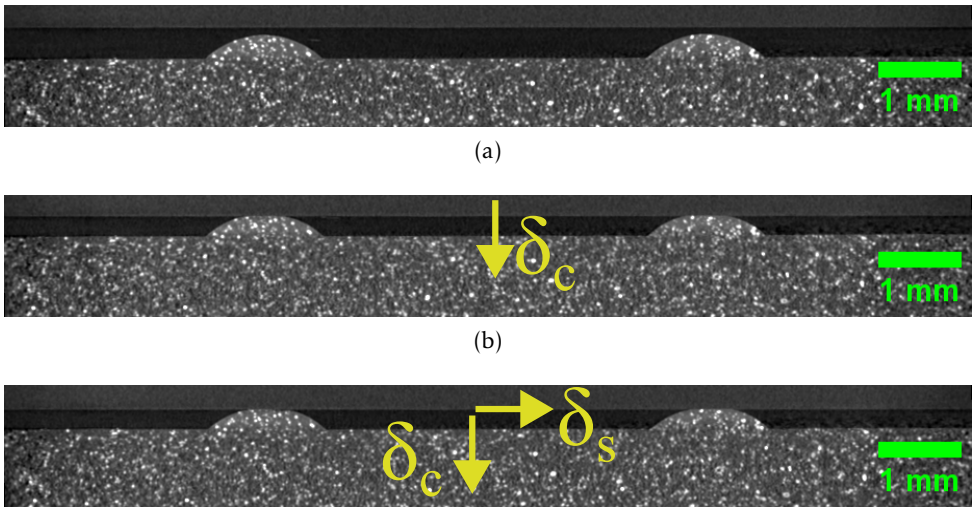

Figure 5.2: Crop of a 3D reconstructed volume from XRCT during a compression and shear experiment made with the sample in fig.5.1. The crop is taken on a longitudinal plane passing from two of the four external asperities. (a) Specimen not in contact, (b) Normal indentation of $\delta_c = 140$ µm and (c) Application of a shear displacement $\delta_s = 140$ µm keeping the same normal indentation of the image (b).

Figure 5.3a shows the results of the image segmentation (with the Random Walker algorithm) and the surface reconstruction (with the Marching Cube algorithm) applied on a multi-asperities specimen filled of glass particles. With the available resolution (4 µm/voxel), it is possible to visualize and measure the contact area with accuracy even for this more complex surfaces. The coordinates of the external surface of the PDMS are also used to create a mesh for DVC calculation (see fig.5.3b) and to analyse the evolution of the PDMS surface.

Figure 5.4 displays the evolution of the PDMS surface during a normal indentation test. The plot shows the coordinates along a longitudinal plane passing from the central asperity and two external ones. Precedent studies [79, 80] have shown that the behaviour of a single asperity is not independent from the presence of other asperities and the deformation of one of them

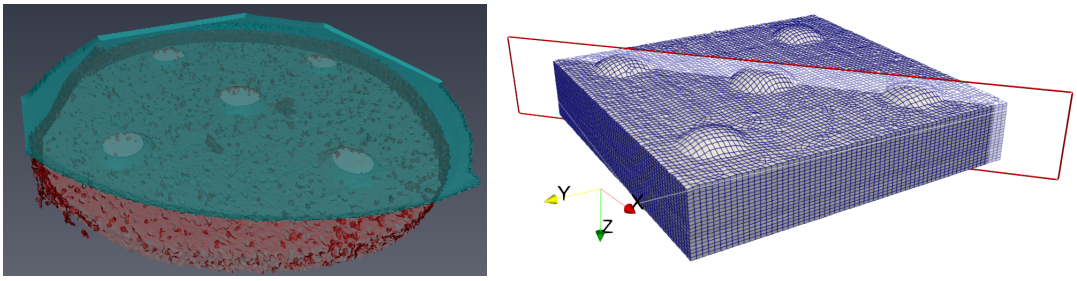

(a) (b)

Figure 5.3: (a) Results of image segmentation and surface reconstruction of a normally indented multi-asperities specimen (the same as in fig.5.1 filled with glass particles) with $\delta_c = 200\ \mu\mathrm{m}$. (b) Finite element mesh used for DVC. The red plane represent the plane where the 3D volume is cropped for DVC results in fig.5.5.

is influencing the others by deforming the bulk beside the asperities, lowering the base plane of the asperities and basically reducing the normal indentation that is exerted on the other contacts. The objective of our experiments is then to follow the evolution of the PDMS bulk and capture the phenomena (namely the interaction between asperities) that are otherwise impossible to observe with optical analysis. As soon as the normal indentation is increased, we observe the apparition of a contact area on each asperity. Because the central asperity is higher, the first contact on the lower asperities is expected to appear for higher indentations. More specifically, this should happen at $\delta_c = 70\ \mu\mathrm{m}$, corresponding to the difference in heights of the asperities. However, because of the PDMS deformation at the base the asperities, the first contact on the lowest asperities is delayed to $\delta_c \simeq 100\ \mu\mathrm{m}$. Indeed, the initial positions of the lateral asperities has changed due to the deformation at the base of the central one. This phenomenon, together with the fact that the deformation at the specimens base is extended up to the order of magnitude of the distance between the asperities, confirms the presence of the interactions between each contact.

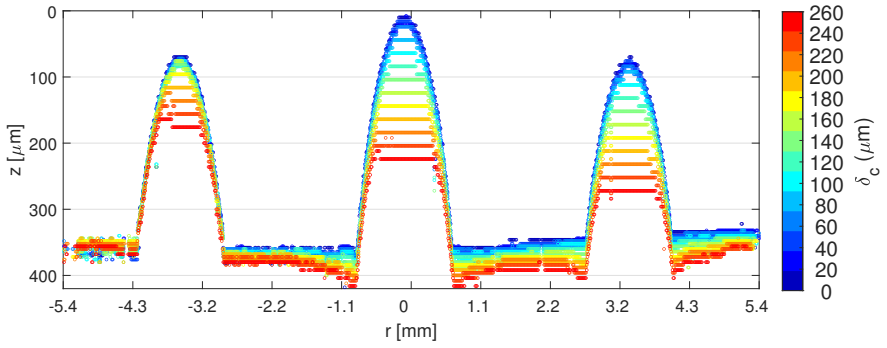

Figure 5.4: Evolution of the PDMS surface of a 5-asperity specimen during a normal indentation test. The plot represent a crop along a longitudinal plane passing from two external asperities and the central one.

Figure 5.5 shows the measured displacement field for the experiment in fig.5.2. For simplicity, we show here only the components U_z (direction of normal indentation) at the end of the compression and of the shear test. The volume has been cropped according to the plane shown

in fig.5.3b. We find here a displacement field distribution, in each asperity, similar to what it has been shown for the mono-contact case. There is, however, a remarkable difference between the central asperity and the lateral ones because of the higher indentation applied on the first. Unfortuntately, the small normal indentation applied, and the image resolution adopted, does not allow to capture any clear, visible interaction between the asperity neither under the pure normal case nor after the application of the shear displacement.

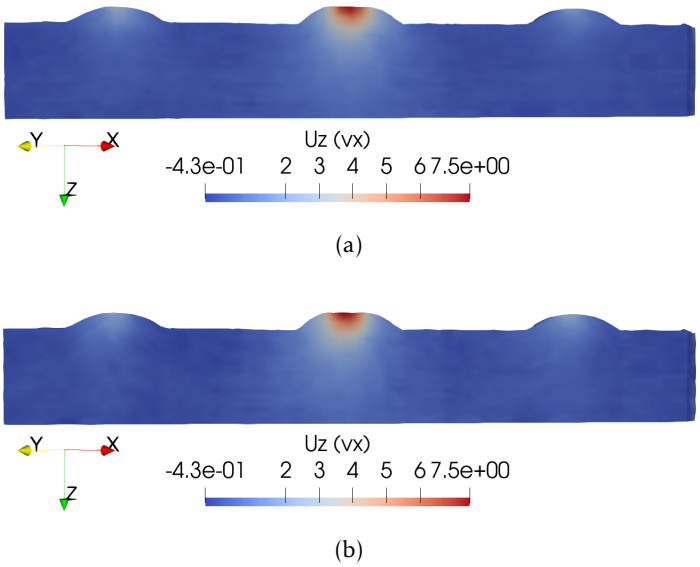

Figure 5.5: Results of DVC on the 5-asperity PDMS specimen during normal and shear experiment. The 3D volume has been cropped according to the red plane in fig.5.3b. The direction of normal indentation is Z while that of shear is Y. (a) U_z when $\delta_c = 140$ µm. (b) U_z when $\delta_s = 140$ µm keeping the normal indentation constant.

After these preliminary results, some questions are still open. For example, the comparison of the PDMS deformation with theoretical models [79, 80] should still be done. It is also probable that a better resolution of the experiments would help capturing the expected interaction phenomenon. Since the image resolution available with laboratory XRCT is limited, a perspective would consist in performing similar experiments using synchrotron XRCT, potentially using multi-mapping (also called "stitching") tomography techniques to still acquire a sufficient size of ROI, yet at a high resolution.

5.2.2 Improvement of DVC-driven simulations

In chapters 3 and 4, we have introduced the DVC-driven simulations adopted to compute the stress field and compare the results with models. Due to the incompressibility of the elastomer, simulations with $\nu = 0.5$ can lead to singularities especially for the diagonal stress components of the tensor σ_{xx}, σ_{yy} and σ_{zz}. Figure 5.6 shows, in 3D, the computed σ_{zz} field at full sliding for the specimen B-10-A. Here we adopt an hyper-elastic Arruda-Boyce constitutive law. We can observe a zone in compression (blue) in the center of the contact zone and a tensile zone outside it. As we expect a vanishing vertical stress out of contact due to the free surface, the presence of a significant tensile stress region seems problematic. However, it was not possible to state if this was effectively due to incompressibility, to non-linear effects related to the finite-strain shear between the constrained position of the top and bottom parts of the contact sample, or

also to a combination of both. A more detailed analysis is necessary to understand the origin of this tensile state and will have to be done in the next future.
Another perspective would consist in separating the mesh used for DVC, where the element size is constrained by the fine dispersion of 3D markers achieved during the elaboration of the specimens, from the mesh used for the finite element analysis. The latter would in fact benefit from selective mesh refinement in the regions of the sample where high gradients of stress or strain are expected, *e.g.* close to the contact surface. There is therefore a compromise to investigate between the mesh size achievable for DVC and the proper mesh refinement for FEM, with reasonable interpolation of the DVC displacement results to define the boundary conditions in the simulations.

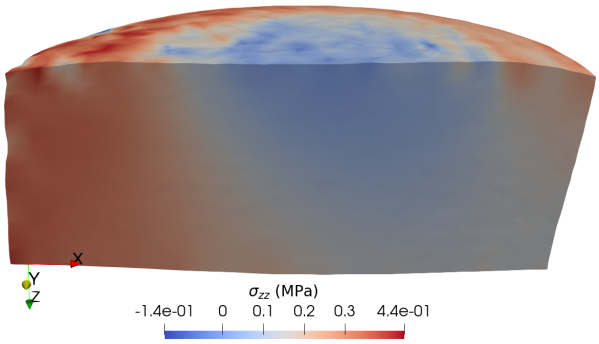

Figure 5.6: σ_{zz} (MPa) during full sliding for the specimen B-10-A. The DVC-driven simulation was obtained with the Arruda-Boyce hyper-elastic law.

5.2.3 Other perspectives

We have listed, all along this document, some of the experimental limits that prevented the observation of some physical quantities useful to understand observed phenomena and to better compare the results with models. We summarize here some actions that could be started in the near future to overcome those limits:

- We have observed the presence of adhesion during the experiment, that is especially marked during unloading. Unfortunately, the experiments including a loading and one unloading step were done with specimens filled with glass particles. As we have demonstrated that aluminium particles are better for DVC measurements, a loading/unloading experiment should be done with aluminium filled specimens to have a more accurate measurement of the displacement field and capture adhesive phenomena;
- In Chapter 4 it was not possible to properly segment the XRCT volumes because of the low PDMS/PMMA contrast. For this, the contact area was only estimated with the $z-projection$ method. It could be worth to repeat the experiment with a PDMS specimen empty of particles in order to focus the analysis on the evolution of the contact area under shear;
- Because our image resolution was limited and did not allow to capture the differences between the theoretical model (JKR, DMT, Maugis) and it caused an overestimation of the contact area, a way to reduce the voxel size can be reached obtaining XRCT scans on a synchrotron beamline. Furthermore, the use of such facility would allow also open the way to dynamic experiments because of the higher image acquisition rate [81];

- Our protocols and methods can also be tested on more complex and non-transparent rough surfaces within the limits of our image resolution;
- As the determination of the first point of contact is not simple with a lateral observation but it is easier with a top view access, the installation of a micro-camera and the modification of the aluminium rod necessary to consent the passage of light, can be useful for both accessing this information and carry out XRCT and optical experiments at the same time;

Beyond such short-term technical improvements that could return immediate results, the developed technique detailed in this study can open the way to completely new experiments. For instance, experiments adopting more complex surface topographies and materials can be planned. Another perspective would consist in testing another class of materials such as metals and perform experiments on all types of non optically transparent materials. Finally, and adaptation of the experimental device to apply more complex and realistic loading modes can be considered.

6 Appendixes

6.1 Appendix 1: Evaluation of the error on Maugis profiles calculation by using a Monte Carlo method

As the error on the real position of a profile during indentation is multi-factorial and very complex to estimate, we proposed to use a evaluation method based on a Monte-Carlo approaches. Starting from the average values of the Maugis fit parameters presented in Table 2.3, $N = 10000$ random values for each parameters E, ω_0 and λ are drawn at random following a Gaussian distribution. Then, we computed the 10000 deformed profiles of an elastic substrate indented by a rigid parabola using the method proposed by Maugis [18] and described hereafter. Finally, we evaluated the mean position of the profiles by averaging all the profiles.The error thus corresponds simply to the standard deviation of this averaging process.

For each computed profile we take one random values of E, ω_0 and λ. First, we compute the normalised indentation according to equation (6.9) from Maugis's paper as :

$$\Delta = \frac{\delta_c}{\left(\frac{\pi^2\omega_0^2 R}{K^2}\right)^{1/3}} \tag{6.1}$$

where δ_c is the imposed normal displacement, K is the bulk modulus defined as $K = (4/3)E/(1-\nu^2)$ and R the radius of curvature of the parabolic indenter.

The resolution of the problem is obtained solving the equation (6.17) of the paper:

$$y = \frac{\lambda A^2}{2}\left[\sqrt{m^2-1}+(m^2-2)tg^{-1}(\sqrt{m^2-1})\right]+\frac{4\lambda^2 A}{3}[\sqrt{m^2-1}tg^{-1}(\sqrt{m^2-1})-m+1]-1=0 \tag{6.2}$$

where m is a parameter defined in equation (6.19) of the paper and defined as:

$$m = \left\{\left[\frac{3}{4}\frac{(A^2-\Delta)}{A\lambda}\right]^2+1\right\}^{1/2} \tag{6.3}$$

and A is the normalised contact radius defined as (equation (6.7) in the paper):

$$A = \frac{a}{\left(\frac{\pi\omega_0 R}{K}\right)^{1/3}}. \tag{6.4}$$

which corresponds to the only unknown of the problem as m is written as a function of A.

Knowing A, we can determine the contact radius a from eq. 6.4 and the value of m from eq. 6.3. This value is, in fact, useful to determine c ($c = m \cdot a$) characterising the limit of the cohesive zone ($a < r \leq c$) and then the use of two different equations for the air gap (the gap from the parabolic indenter and the deformed surface).

if $a \leq r \leq c$

$$\bar{u_g} = \frac{A^2}{\pi}\left[\sqrt{\rho^2-1} + (\rho^2-3)cos^{-1}\frac{1}{\rho}\right] + \frac{8\lambda A}{3\pi}\left[\frac{\sqrt{\rho^2-1}}{\sqrt{m^2-1}} + \sqrt{m^2-1}cos^{-1}\frac{1}{\rho} - mE(\phi,k)\right] \quad (6.5)$$

with

$$\phi = sin^{-1}\left(\frac{m}{\sqrt{m^2-1}}\frac{\sqrt{\rho^2-1}}{\rho}\right) \quad (6.6)$$

$$k = \frac{\rho}{m}, \quad (6.7)$$

while for $r > c$

$$\bar{u_g} = \frac{A^2}{\pi}\left[\sqrt{\rho^2-1} + (\rho^2-3)cos^{-1}\frac{1}{\rho}\right]$$
$$+\frac{8\lambda A}{3\pi}\left[\left(1-\frac{m^2}{\rho^2}\right)\rho F(\phi,k) - \rho E(\phi,k) + \sqrt{m^2-1}\left(cos^{-1}\frac{1}{\rho} + \frac{1}{\sqrt{\rho^2-1}}\right)\right]$$

with

$$\phi = sin^{-1}\left(\frac{\sqrt{m^2-1}}{m}\frac{\rho}{\sqrt{\rho^2-1}}\right) \quad (6.8)$$

$$k = \frac{m}{\rho} \quad (6.9)$$

$$m = \frac{c}{a}, \quad \rho = \frac{r}{a}, \quad A = \frac{a}{\left(\frac{\pi\omega R^2}{K}\right)^{1/3}} \quad (6.10)$$

and $E(\phi,k)$, $F(\phi,k)$ are elliptic integrals.
The value of u_g is determined from the normalised gap $\bar{u_g}$ as

$$u_g(r) = \bar{u_g}\left(\frac{\pi^2\omega_0^2 R}{K^2}\right)^{1/3} \quad (6.11)$$

In addition, we obviously consider that $u_g(r) = 0$ when $r < a$ (no air gap in the real contact zone). Finally, the shape of the deformed profile $z_m(r)$ is determined as (see Fig. 6.1a):

$$z_m(r) = z_p(r) - u_g(r) \quad (6.12)$$

where $z_p(r)$ corresponds to the coordinates of a parabola.

Fig. 6.1b shows what it is obtained in the case of the present study considering all the parameters of the used elastomer (the adopted values are put in the caption). For 10 iterations we obtain 10 profiles that are used to determine the final profile as the average of them while the standard deviation is computed at each point along the radius. We remind that, for the profiles put in the manuscript, computations were made with 10000 iterations.

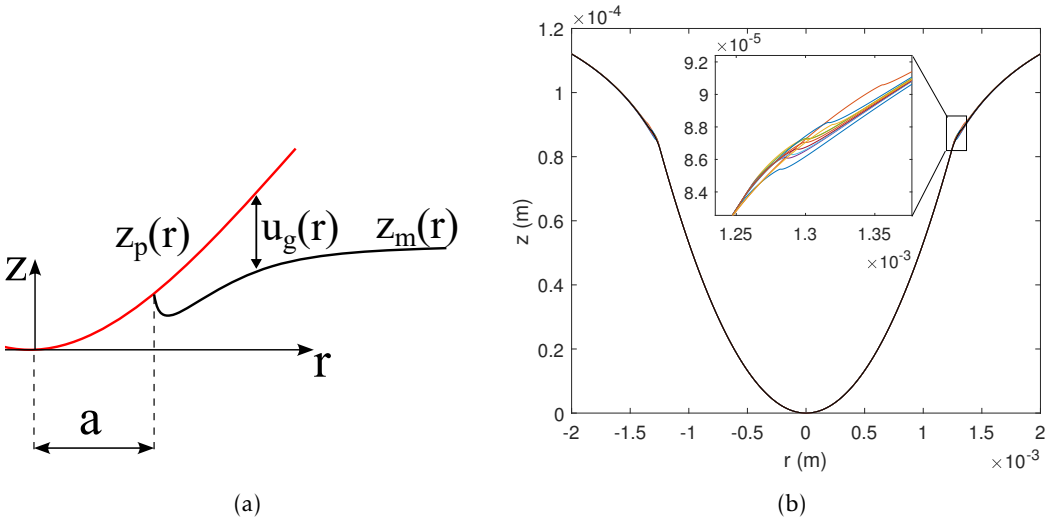

(a) (b)

Figure 6.1: Shape of the deformed surface of an elastic substrate indented by a rigid parabola: (a) illustration of the determination of the $z_m(r)$ coordinates, (b) obtained profiles according to the Maugis' equations over 10 random computations with $E = 0.75 \pm 0.016$ MPa, $\omega_0 = 0.059 \pm 0.008$ J/m^2, $\lambda = 1.22 \pm 0.51$, $R = 9.42$ mm, $\delta_c = 152$ µm and $\nu = 0.5$.

6.2 Appendix 2: Additional plots from Chapter 3

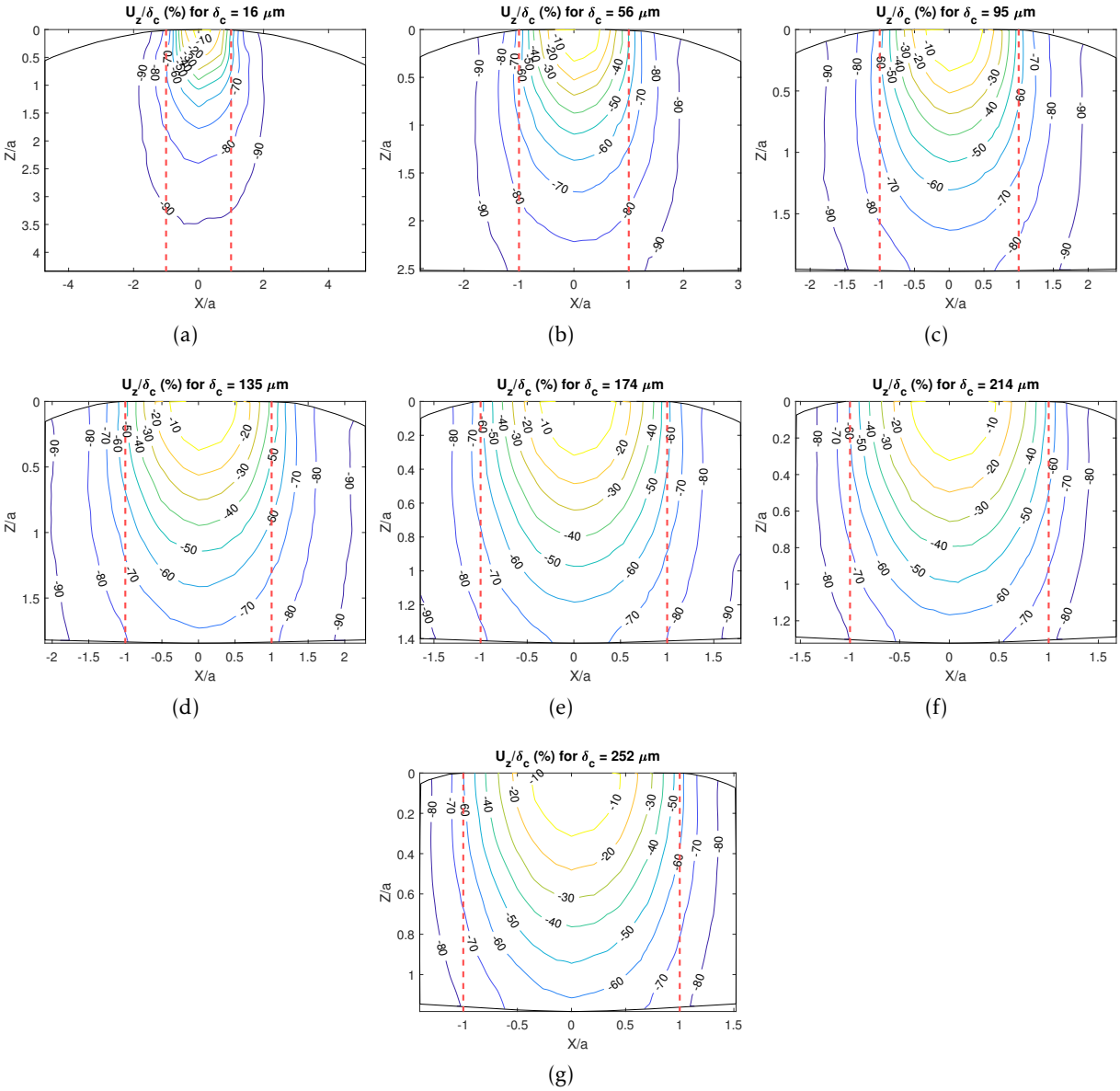

Figure 6.2: Contour plot of the displacement U_z normalised by the imposed displacement δ_c on the central $X - Z$ plane for the specimens B-10-A at all the indentations according to eq. 3.3. The vertical red dashed lines indicates the position of the contact boundary.

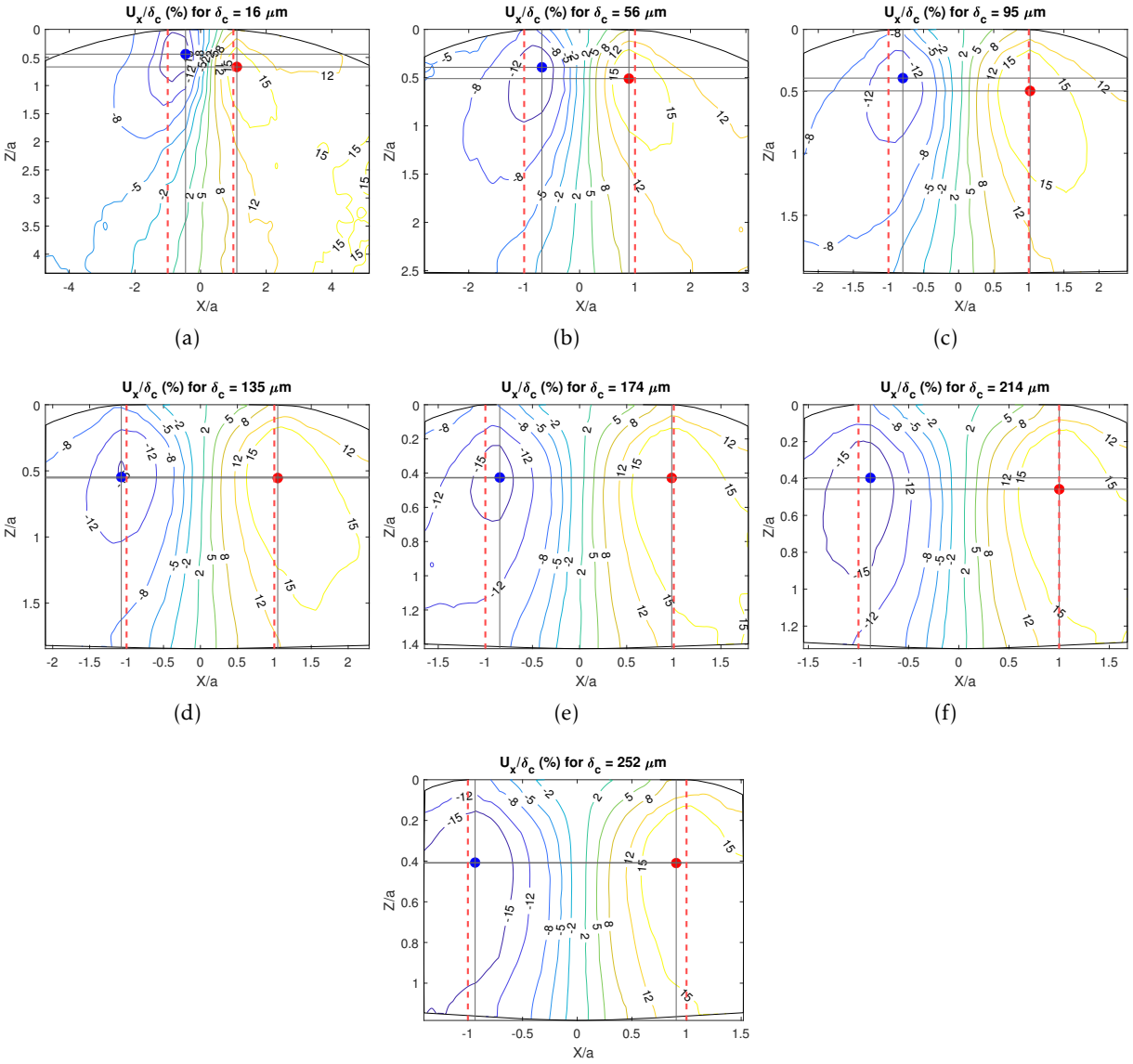

Figure 6.3: Contour plot of the displacement U_x normalised by the imposed displacement δ_c on the central $X - Z$ plane for the specimens B-10-A at all the indentations according to eq. 3.3. The vertical red dashed lines indicates the position of the contact boundary.

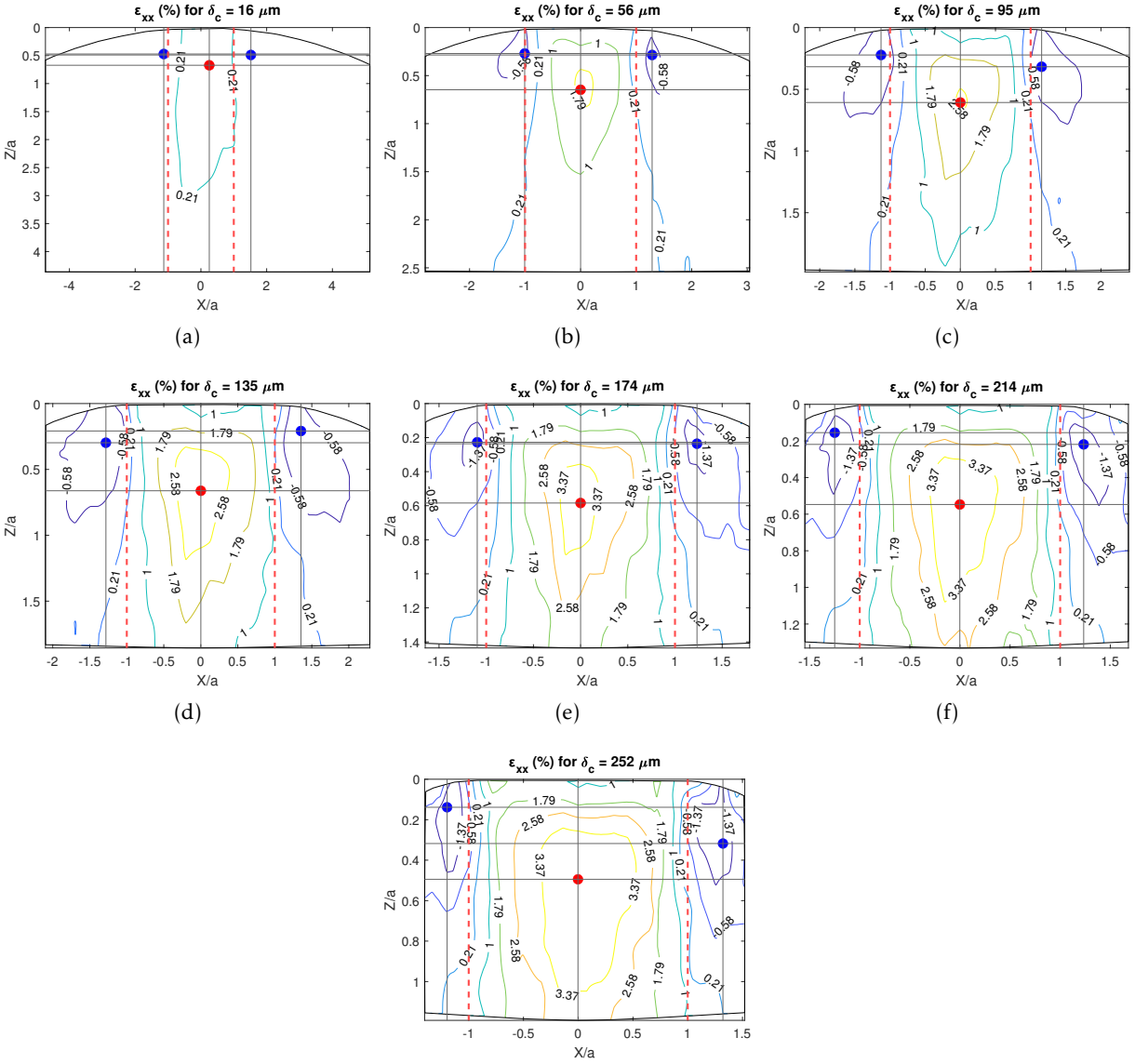

Figure 6.4: Contour plots of the strain field (in %) on the central $X - Z$ plane obtained with the DVC measurement for the specimen B-10-A at all the indentation steps specified in eq. 3.3. The plots represent the component ε_{xx}. The red and blue points stand, respectively, for the maximum and minimum values of the strain the relative plot. The vertical red dashed lines indicates the contact boundary.

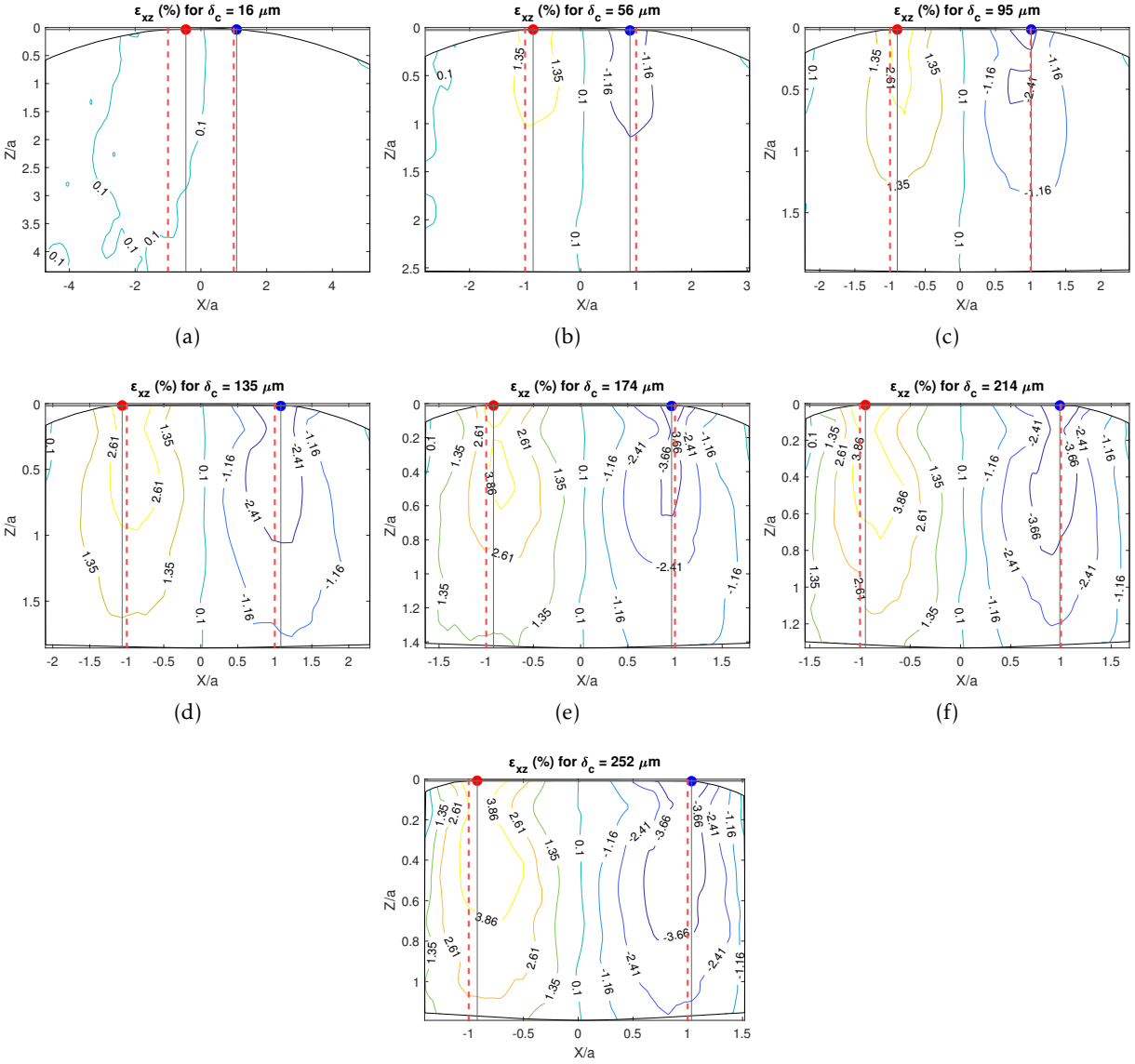

Figure 6.5: Contour plots of the strain field (in %) on the central $X - Z$ plane obtained with the DVC measurement for the specimen B-10-A at all the indentation steps specified in eq. 3.3. The plots represent the component ε_{xz}. The red and blue points stand, respectively, for the maximum and minimum values of the strain the relative plot. The vertical red dashed lines indicates the contact boundary.

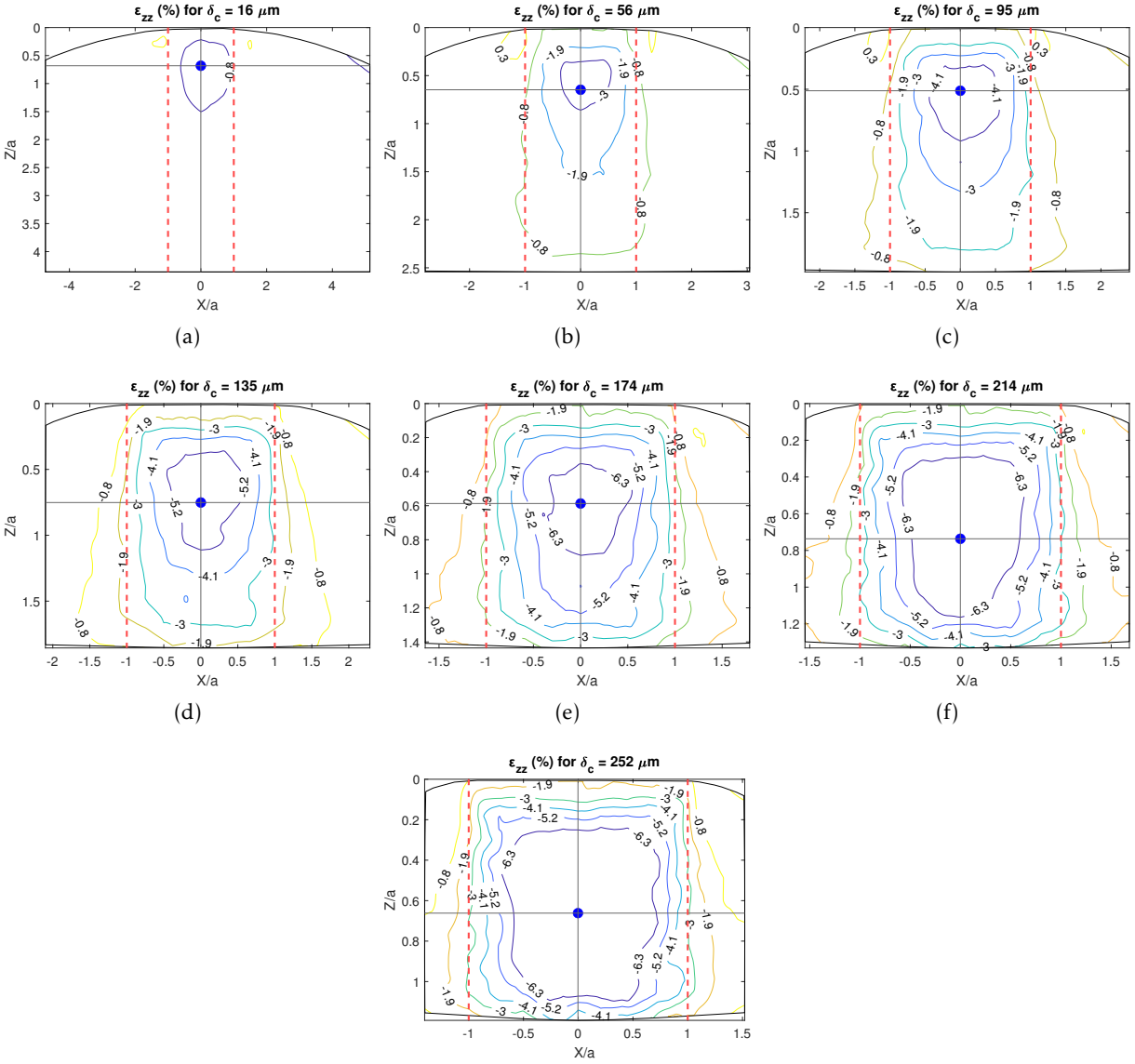

Figure 6.6: Contour plots of the strain field (in %) on the central $X - Z$ plane obtained with the DVC measurement for the specimen B-10-A at all the indentation steps specified in eq. 3.3. The plots represent the component ε_{zz}. The red and blue points stand, respectively, for the maximum and minimum values of the strain the relative plot. The vertical red dashed lines indicates the contact boundary.

6.3 Appendix 3: Additional plots from Chapter 4

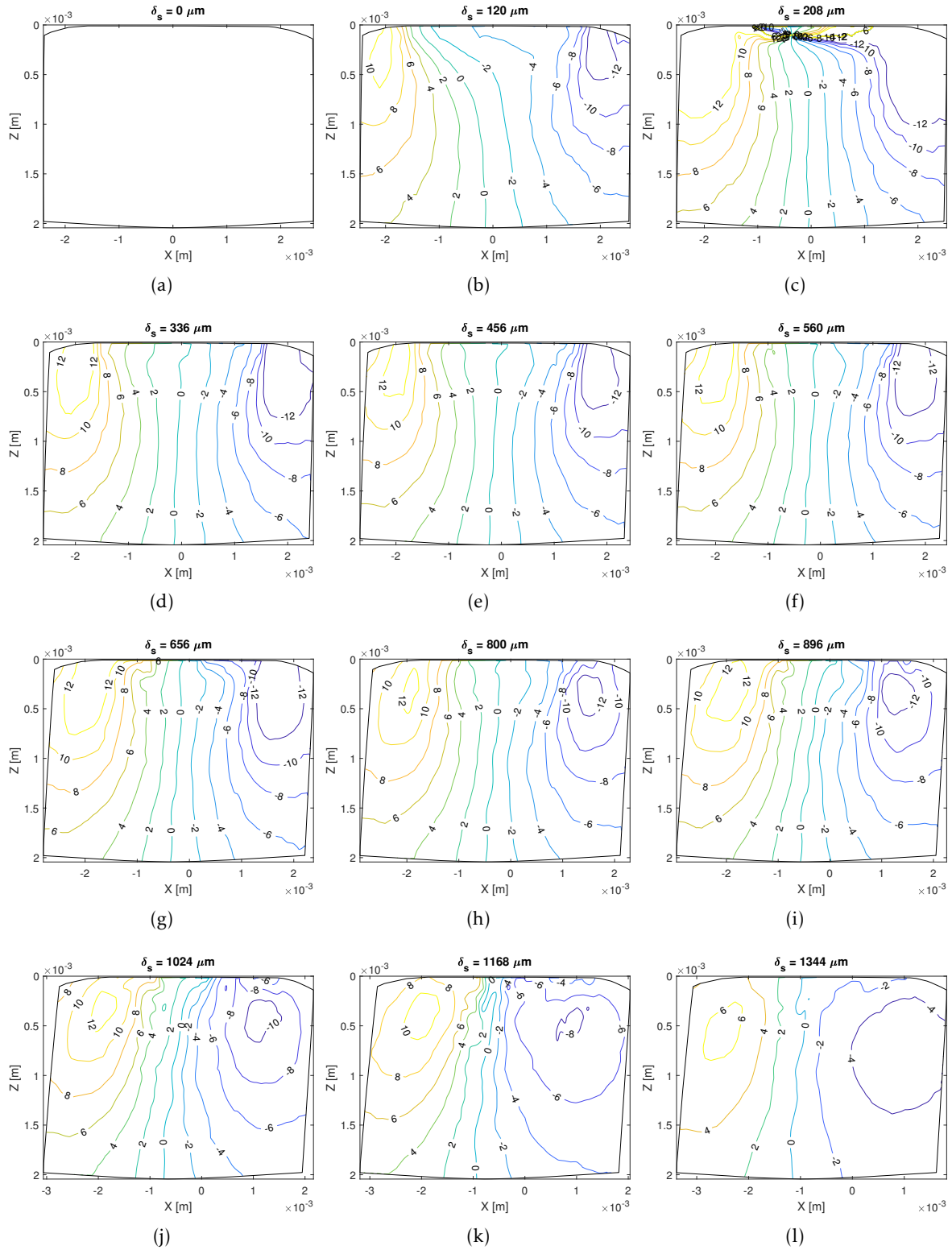

Figure 6.7: Isolines of the vectors' orientation during shear (data are in degrees). The ROI is deformed according to the displacement field. Specimen B-10-A.

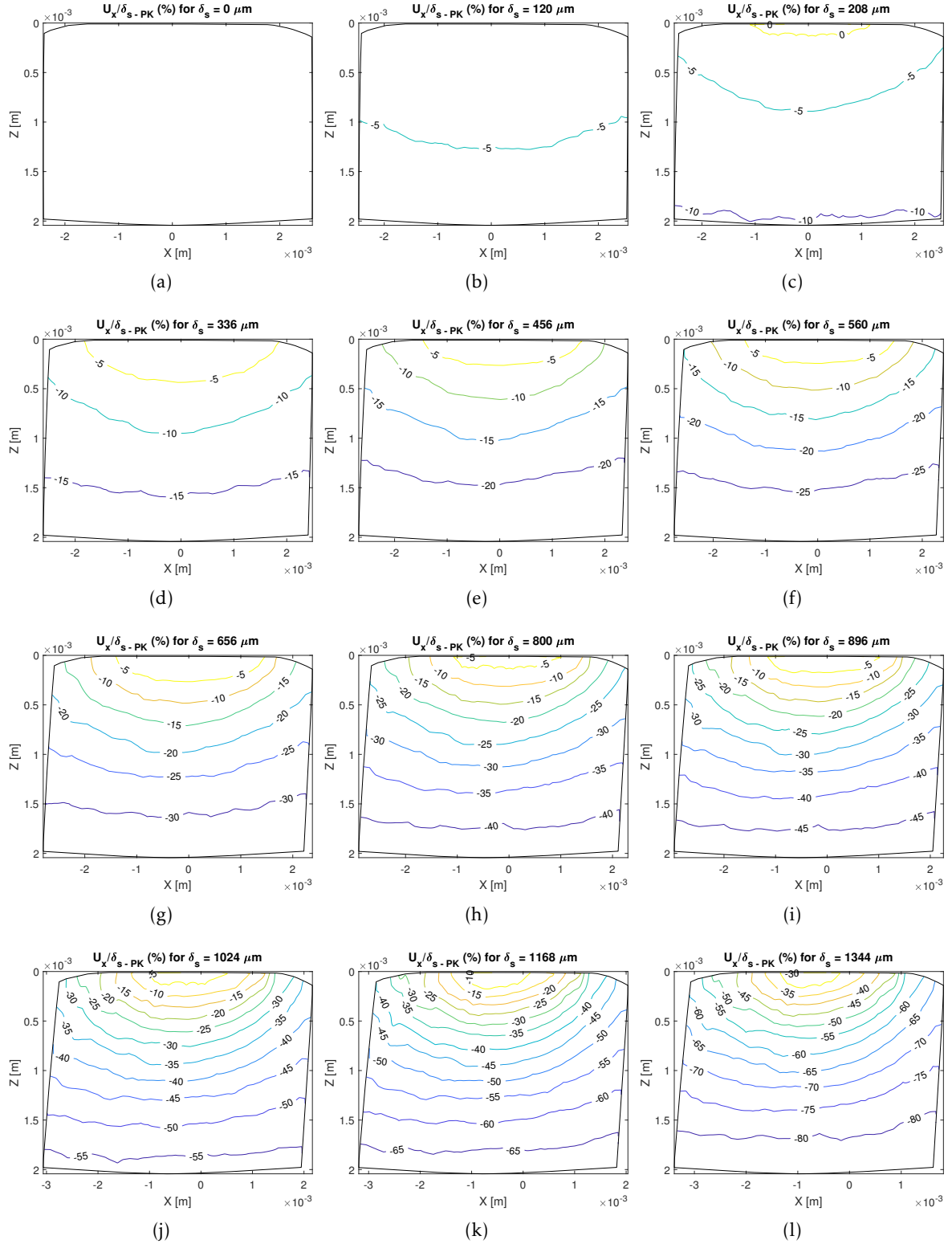

Figure 6.8: Isolines of the component U_x/δ_{s-PK} during shear in the case of the specimens B-10-A where δ_{s-PK} indicates the imposed displacement at peak of the tangential force. The ROI is deformed according to the displacement field of the specimen B-10-A.

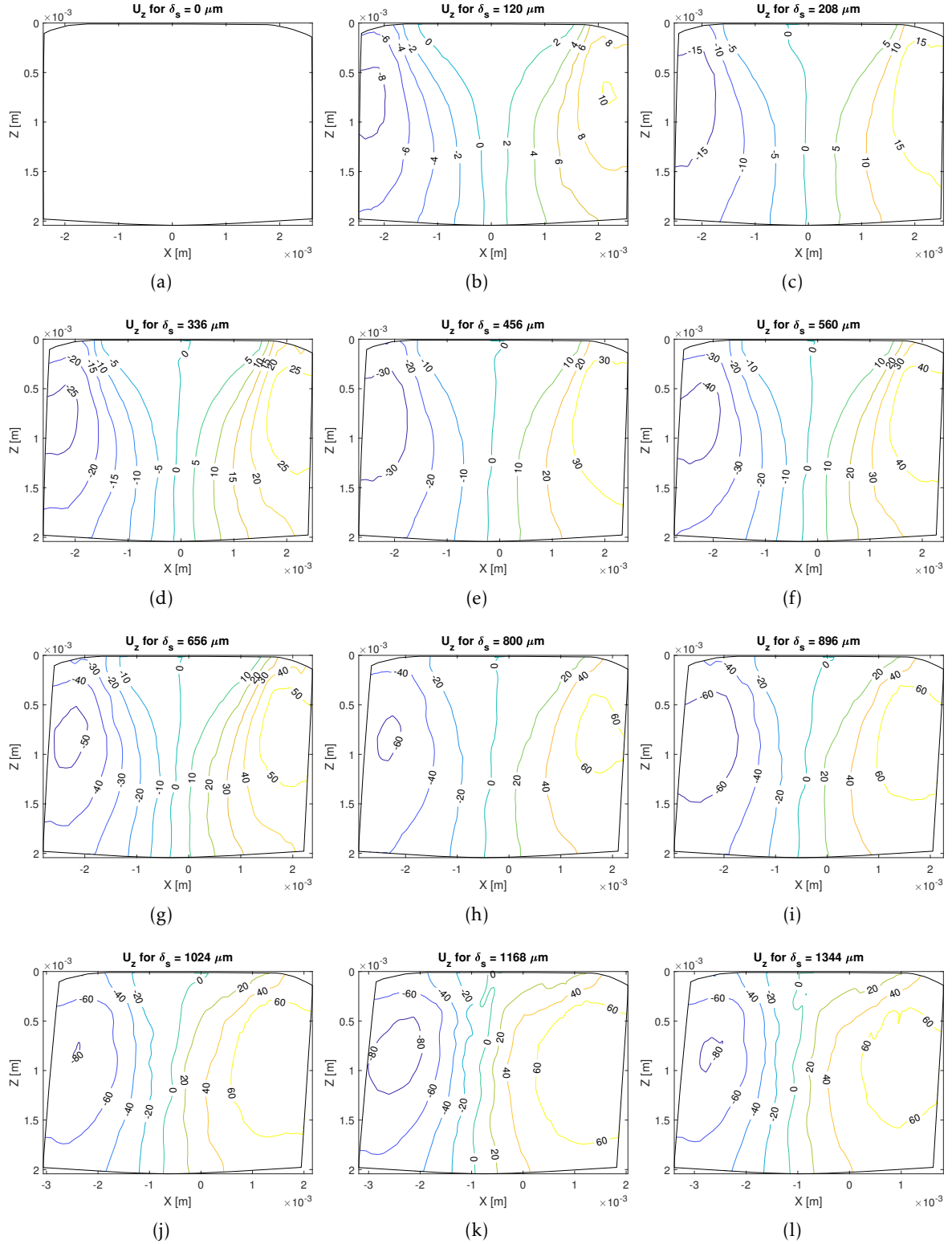

Figure 6.9: Isolines of the component U_z during shear (data are in micrometers) without the vertical contribution measured at the end of the compression part of the experiment. The ROI is deformed according to the displacement field. Specimen B-10-A.

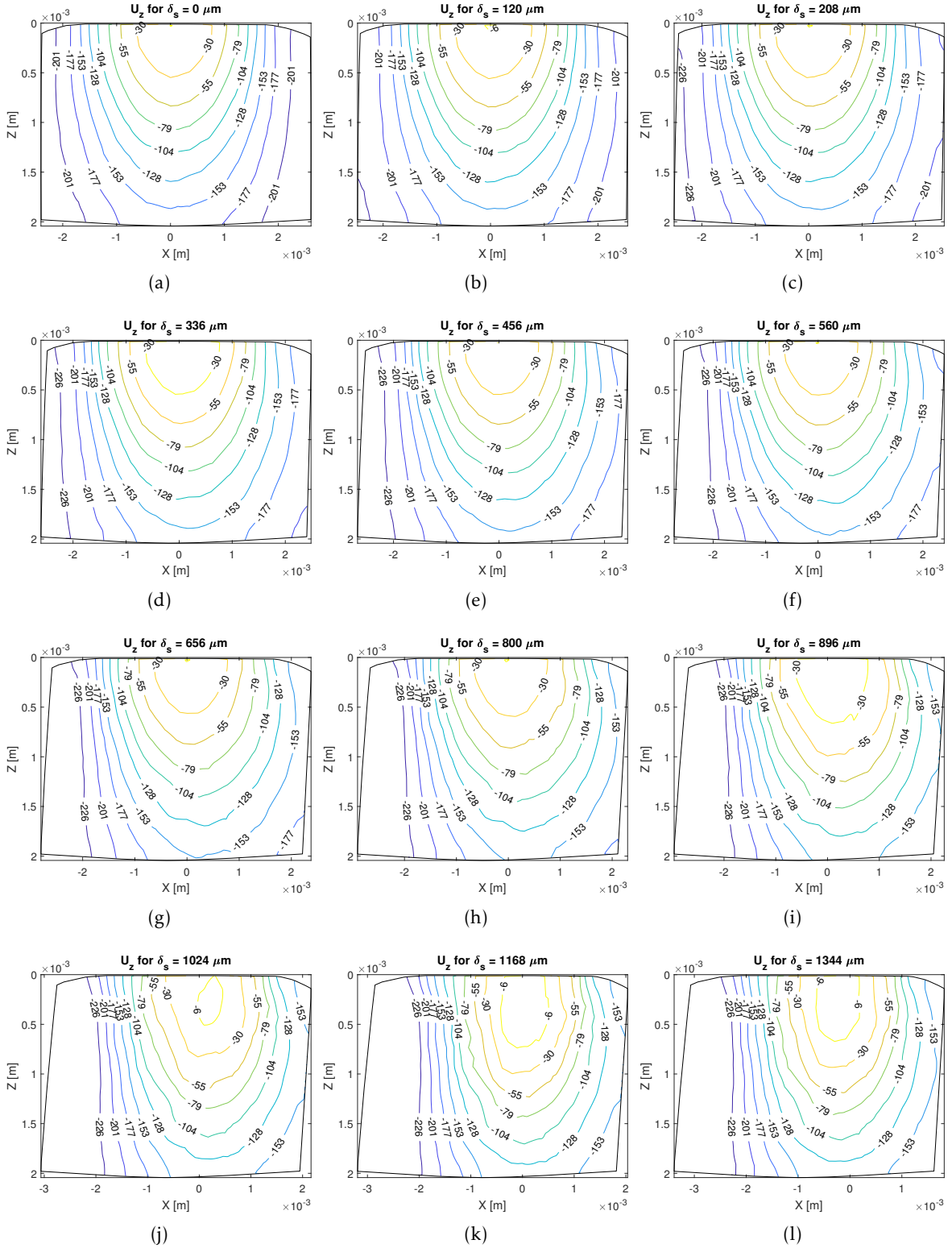

Figure 6.10: Isolines of the component U_z during shear (data are in micrometers) starting from the contour plot at the end of normal compression. The ROI is deformed according to the displacement field. Specimen B-10-A.

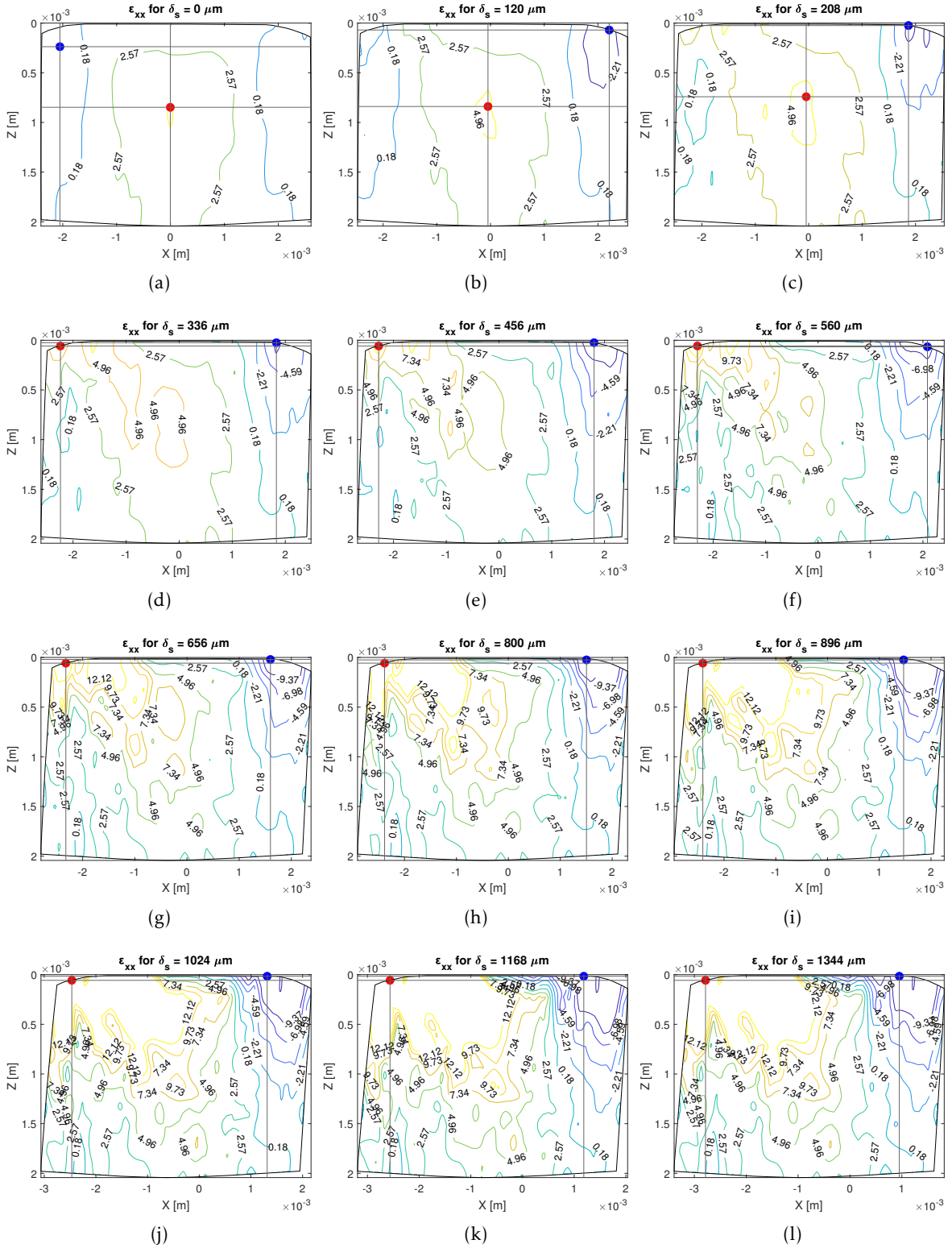

Figure 6.11: Contour plots of the strain component ε_{xx} (in %) on the central $X - Z$ plane obtained with the DVC measurement for the specimen B-10-A during all the shear steps. The red and blue points stand, respectively, for the maximum and minimum values of the strain in the relative plot. Specimen B-10-A.

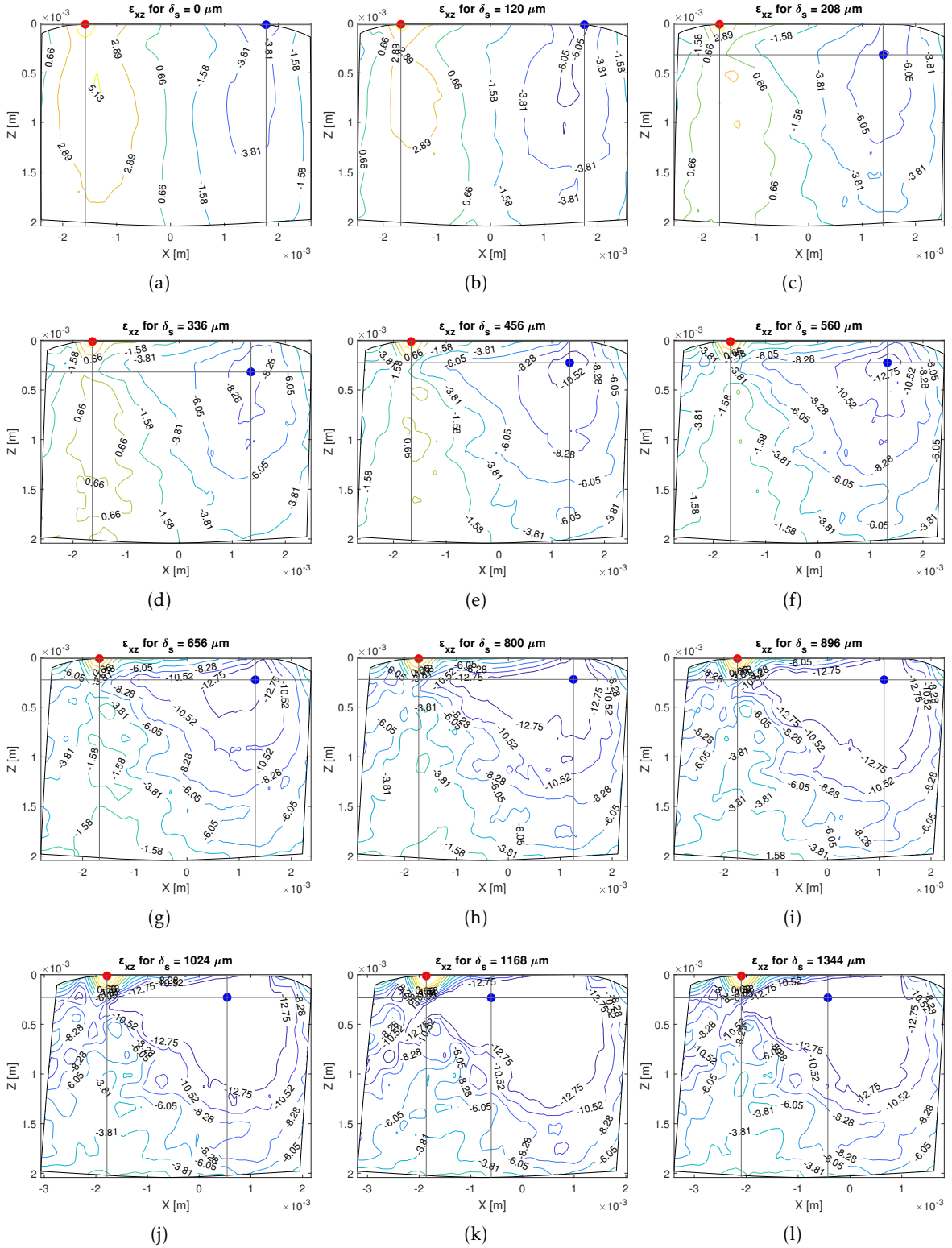

Figure 6.12: Contour plots of the strain component ε_{xz} (in %) on the central $X - Z$ plane obtained with the DVC measurement for the specimen B-10-A during all the shear steps. The red and blue points stand, respectively, for the maximum and minimum values of the strain in the relative plot. Specimen B-10-A.

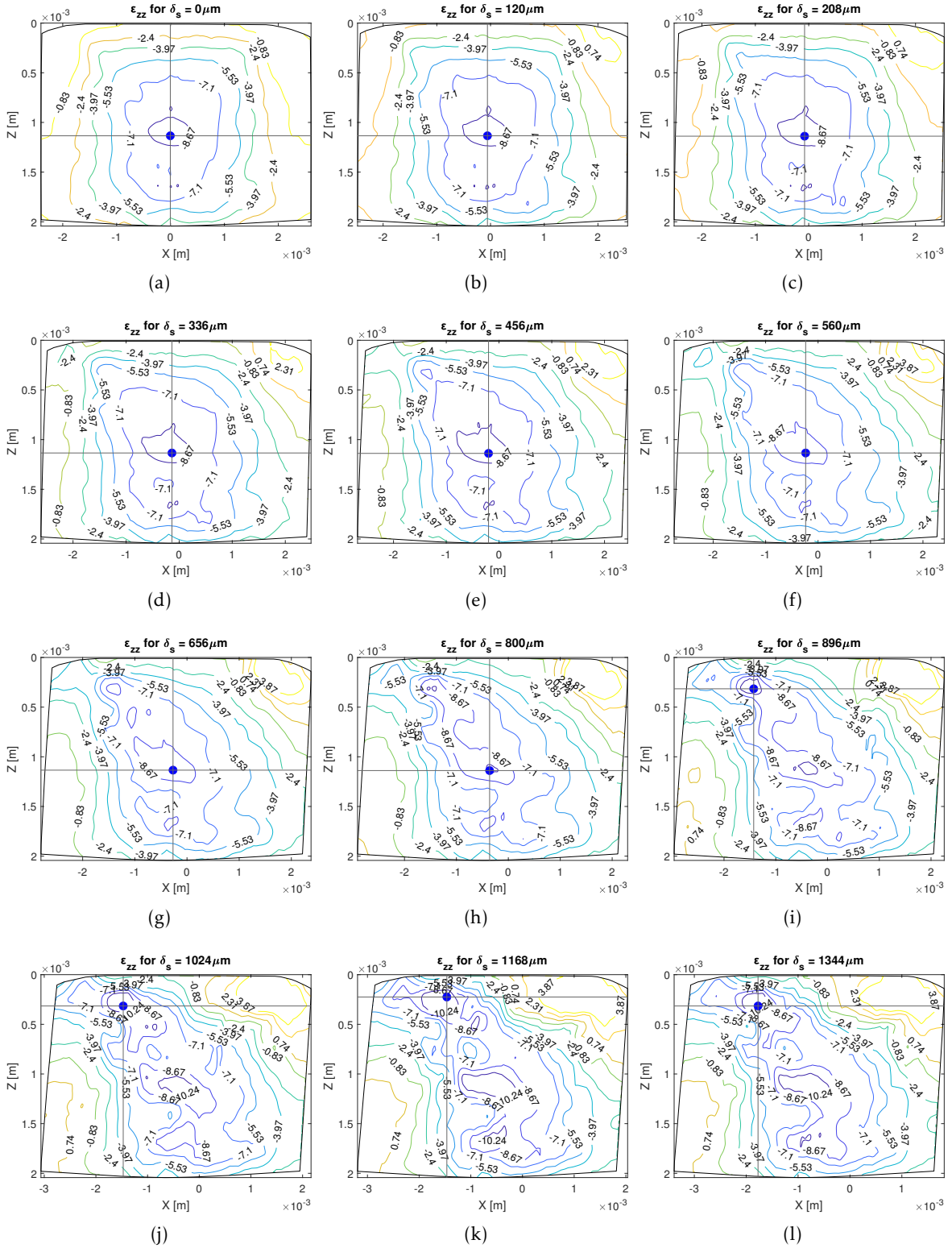

Figure 6.13: Contour plots of the strain component ε_{zz} (in %) on the central $X - Z$ plane obtained with the DVC measurement for the specimen B-10-A during all the shear steps. The red and blue points stand, respectively, for the maximum and minimum values of the strain in the relative plot. Specimen B-10-A.

Bibliography

[1] Ian M. Hutchings. "Leonardo da Vinci studies of friction". en. In: *Wear* 360-361 (2016), pp. 51–66.

[2] Charles Augustin Coulomb. *Théorie des machines simples en ayant égard au frottement de leurs parties et à la roideur des cordages*. fr. Bachelier, 1821.

[3] F. P. Bowden and D. Tabor. "Mechanism of Metallic Friction". en. In: *Nature* 150.3798 (1942). Number: 3798 Publisher: Nature Publishing Group, pp. 197–199.

[4] Mariana De Souza. "Onset of sliding of elastomer interfaces : fundamental insights from model sphere/plane contact experiments". These de doctorat. Lyon, 2021.

[5] James H. Dieterich and Brian D. Kilgore. "Direct observation of frictional contacts: New insights for state-dependent properties". en. In: *pure and applied geophysics* 143.1 (1994), pp. 283–302.

[6] R. Sahli et al. "Evolution of real contact area under shear and the value of static friction of soft materials". en. In: *Proceedings of the National Academy of Sciences* 115.3 (2018), pp. 471–476.

[7] J. Lengiewicz et al. "Finite deformations govern the anisotropic shear-induced area reduction of soft elastic contacts". en. In: *Journal of the Mechanics and Physics of Solids* 143 (2020), p. 104056.

[8] Julie F. Waters and Pradeep R. Guduru. "Mode-mixity-dependent adhesive contact of a sphere on a plane surface". en. In: *Proceedings of the Royal Society A: Mathematical, Physical and Engineering Sciences* 466.2117 (2010), pp. 1303–1325.

[9] Elise Degrandi-Contraires et al. "Sliding friction at soft micropatterned elastomer interfaces". en. In: *Faraday Discussions* 156.0 (2012). Publisher: The Royal Society of Chemistry, pp. 255–265.

[10] H. Hertz. "Über die Berührung fester elastischer Körper". In: *Journal für die reine und angewandte Mathematik* 92 (1881), pp. 156–171.

[11] K. L. Johnson. *Contact Mechanics*. en. Cambridge University Press, 1987.

[12] Valentin L. Popov. *Contact Mechanics and Friction*. en. Berlin, Heidelberg: Springer, 2017.

[13] Valentin L. Popov, Markus Heß, and Emanuel Willert. *Handbook of Contact Mechanics: Exact Solutions of Axisymmetric Contact Problems*. en. Berlin, Heidelberg: Springer Berlin Heidelberg, 2019.

[14] K. L. Johnson, K. Kendall, and A. D. Roberts. "Surface energy and the contact of elastic solids". In: *Proceedings of the Royal Society of London. A. Mathematical and Physical Sciences* 324.1558 (1971). Publisher: Royal Society, pp. 301–313.

[15] B. V Derjaguin, V. M Muller, and Yu. P Toporov. "Effect of contact deformations on the adhesion of particles". en. In: *Journal of Colloid and Interface Science* 53.2 (1975), pp. 314–326.

[16] D. Tabor. "Surface Forces and Surface Interactions". en. In: *Plenary and Invited Lectures*. Ed. by Milton Kerker, Albert C. Zettlemoyer, and Robert L. Rowell. Academic Press, 1977, pp. 3–14.

[17] E Barthel. "Adhesive elastic contacts: JKR and more". en. In: *Journal of Physics D: Applied Physics* 41.16 (2008), p. 163001.

[18] Daniel Maugis. "Adhesion of spheres: The JKR-DMT transition using a dugdale model". en. In: *Journal of Colloid and Interface Science* 150.1 (1992), pp. 243–269.

[19] M. Barquins. "Sliding friction of rubber and Schallamach waves — A review". en. In: *Materials Science and Engineering* 73 (1985), pp. 45–63.

[20] C. Cattaneo. "Sul contatto di due corpi elastici. Accademia dei Lincei". In: *Sul contatto di due corpi elastici. Accademia dei Lincei* 27 (1938), pp. 342–348.

[21] R. D. Mindlin. "Compliance of Elastic Bodies in Contact". In: *Journal of Applied Mechanics* 16.3 (), pp. 259–268.

[22] A. Prevost, J. Scheibert, and G. Debrégeas. "Probing the micromechanics of a multi-contact interface at the onset of frictional sliding". en. In: *The European Physical Journal E* 36.2 (2013), p. 17.

[23] A.R. Savkoor. "Dry Adhesive Friction of Elastomers". PhD thesis. TU Delft, 1987.

[24] Hamilton. "Explicit equations for the stresses beneath a sliding spherical contact". In: *Proc Instn Mech Engrs* (1983), pp. 53–59.

[25] A. I. Vakis et al. "Modeling and simulation in tribology across scales: An overview". en. In: *Tribology International* 125 (2018), pp. 169–199.

[26] Martin H. Müser et al. "Meeting the Contact-Mechanics Challenge". en. In: *Tribology Letters* 65.4 (2017), p. 118.

[27] Shmuel M. Rubinstein et al. "Crack-like processes governing the onset of frictional slip". en. In: *International Journal of Fracture* 140.1 (2006), pp. 201–212.

[28] Antoine Chateauminois, Christian Fretigny, and Ludovic Olanier. "Friction and shear fracture of an adhesive contact under torsion". In: *Physical Review E* 81.2 (2010). Publisher: American Physical Society, p. 026106.

[29] Brandon A. Krick et al. "Optical In Situ Micro Tribometer for Analysis of Real Contact Area for Contact Mechanics, Adhesion, and Sliding Experiments". en. In: *Tribology Letters* 45.1 (2012), pp. 185–194.

[30] F. Dalzin et al. “Tribological origin of squeal noise in lubricated elastomer–glass contact”. en. In: *Journal of Sound and Vibration* 372 (2016), pp. 211–222.

[31] Vito Acito et al. “Adhesive Contact of Model Randomly Rough Rubber Surfaces”. en. In: *Tribology Letters* 67.2 (2019), p. 54.

[32] Philip J. Withers et al. “X-ray computed tomography”. en. In: *Nature Reviews Methods Primers* 1.1 (2021). Number: 1 Publisher: Nature Publishing Group, pp. 1–21.

[33] Alexander Katsevich. “Theoretically Exact Filtered Backprojection-Type Inversion Algorithm for Spiral CT”. In: *SIAM Journal on Applied Mathematics* 62.6 (2002). Publisher: Society for Industrial and Applied Mathematics, pp. 2012–2026.

[34] J. Y. Buffiere et al. “In Situ Experiments with X ray Tomography: an Attractive Tool for Experimental Mechanics”. en. In: *Experimental Mechanics* 50.3 (2010), pp. 289–305.

[35] Michael A. Sutton, Jean Jose Orteu, and Hubert Schreier. *Image Correlation for Shape, Motion and Deformation Measurements: Basic Concepts,Theory and Applications*. en. Springer Science & Business Media, 2009.

[36] Bing Pan et al. “Two-dimensional digital image correlation for in-plane displacement and strain measurement: a review”. en. In: *Measurement Science and Technology* 20.6 (2009), p. 062001.

[37] G. Besnard, F. Hild, and S. Roux. ““Finite-Element” Displacement Fields Analysis from Digital Images: Application to Portevin–Le Châtelier Bands”. en. In: *Experimental Mechanics* 46.6 (2006), pp. 789–803.

[38] José Bolivar Vina. “Experimental study of the behavior of colonies of environmentally-assisted short cracks by digital image correlation, acoustic emission and electrochemical noise”. en. PhD thesis. Université de Lyon, 2017.

[39] B. K. Bay et al. “Digital volume correlation: Three-dimensional strain mapping using X-ray tomography”. en. In: *Experimental Mechanics* 39.3 (1999), pp. 217–226.

[40] Stéphane Roux et al. “Three-dimensional image correlation from X-ray computed tomography of solid foam”. en. In: *Composites Part A: Applied Science and Manufacturing*. Full-field Measurements in Composites Testing and Analysis 39.8 (2008), pp. 1253–1265.

[41] E. Maire and P. J. Withers. “Quantitative X-ray tomography”. en. In: *International Materials Reviews* 59.1 (2014), pp. 1–43.

[42] François Hild et al. “Multiscale displacement field measurements of compressed mineral-wool samples by digital image correlation”. EN. In: *Applied Optics* 41.32 (2002). Publisher: Optica Publishing Group, pp. 6815–6828.

[43] Bing Pan, Wu Dafang, and Xia Yong. “Incremental calculation for large deformation measurement using reliability-guided digital image correlation”. en. In: *Optics and Lasers in Engineering*. Computational Optical Measurement 50.4 (2012), pp. 586–592.

[44] Bo Wang and Bing Pan. "Incremental digital volume correlation method with nearest subvolume offset: An accurate and simple approach for large deformation measurement". en. In: *Advances in Engineering Software* 116 (2018), pp. 80–88.

[45] Feikai Zhang et al. "Experimental and finite element analyses of contact behaviors between non-transparent rough surfaces". en. In: *Journal of the Mechanics and Physics of Solids* 126 (2019), pp. 87–100.

[46] Feikai Zhang et al. "A discussion on the capability of X-ray computed tomography for contact mechanics investigations". en. In: *Tribology International* 145 (2020), p. 106167.

[47] András Kriston et al. "A novel method for contact analysis of rubber and various surfaces using micro-computerized-tomography". en. In: *Polymer Testing* 53 (2016), pp. 132–142.

[48] Nobuyuki Otsu. "A Threshold Selection Method from Gray-Level Histograms". In: *IEEE Transactions on Systems, Man, and Cybernetics* 9.1 (1979). Conference Name: IEEE Transactions on Systems, Man, and Cybernetics, pp. 62–66.

[49] Jure Aleksejev et al. "In-situ X-ray tomography of wear – A feasibility study". en. In: *Tribology International* 150 (2020), p. 106355.

[50] A. Perriot and E. Barthel. "Elastic contact to a coated half-space: Effective elastic modulus and real penetration". en. In: *Journal of Materials Research* 19.2 (2004). Publisher: Cambridge University Press, pp. 600–608.

[51] Emilie Delplanque et al. "Solving curing-protocol-dependent shape errors in PDMS replication". en. In: *Journal of Micromechanics and Microengineering* 32.4 (2022). Publisher: IOP Publishing, p. 045006.

[52] R. W. Ogden. *Non-linear Elastic Deformations*. en. Courier Corporation, 1997.

[53] M. Mooney. "A Theory of Large Elastic Deformation". In: *Journal of Applied Physics* 11.9 (2004), pp. 582–592.

[54] R. S. Rivlin and Eric Keightley Rideal. "Large elastic deformations of isotropic materials IV. further developments of the general theory". In: *Philosophical Transactions of the Royal Society of London. Series A, Mathematical and Physical Sciences* 241.835 (1997). Publisher: Royal Society, pp. 379–397.

[55] Mary C. Boyce and Ellen M. Arruda. "Constitutive Models of Rubber Elasticity: A Review". In: *Rubber Chemistry and Technology* 73.3 (2000), pp. 504–523.

[56] L. Mullins. "Softening of Rubber by Deformation". In: *Rubber Chemistry and Technology* 42.1 (1969), pp. 339–362.

[57] Antoine Aymard. "Design et réalisation d'interfaces texturées élastomériques à loi de frottement pilotée". These de doctorat. Ecully, Ecole centrale de Lyon, 2023.

[58] M. Guibert et al. "A versatile flexure-based six-axis force/torque sensor and its application to tribology". In: *Review of Scientific Instruments* 92.8 (2021). Publisher: American Institute of Physics, p. 085002.

[59] Manoj K. Chaudhury et al. “Adhesive contact of cylindrical lens and a flat sheet”. In: *Journal of Applied Physics* 80.1 (1996). Publisher: American Institute of Physics, pp. 30–37.

[60] Antoine Sanner and Lars Pastewka. “Crack-front model for adhesion of soft elastic spheres with chemical heterogeneity”. en. In: *Journal of the Mechanics and Physics of Solids* 160 (2022), p. 104781.

[61] Guido Violano, Antoine Chateauminois, and Luciano Afferrante. “A JKR-Like Solution for Viscoelastic Adhesive Contacts”. In: *Frontiers in Mechanical Engineering* 7 (2021).

[62] Francesc Pérez-Ràfols and Lucia Nicola. “Incipient sliding of adhesive contacts”. en. In: *Friction* 10.6 (2022), pp. 963–976.

[63] “Practical cone-beam algorithm”. EN. In: 1.6 ().

[64] L. Grady. “Random Walks for Image Segmentation”. In: *IEEE Transactions on Pattern Analysis and Machine Intelligence* 28.11 (2006). Conference Name: IEEE Transactions on Pattern Analysis and Machine Intelligence, pp. 1768–1783.

[65] Stéfan van der Walt et al. “scikit-image: image processing in Python”. en. In: *PeerJ* 2 (2014). Publisher: PeerJ Inc., e453.

[66] William E. Lorensen and Harvey E. Cline. “Marching cubes: A high resolution 3D surface construction algorithm”. In: *ACM SIGGRAPH Computer Graphics* 21.4 (1987), pp. 163–169.

[67] Ziji Wu and John M. Sullivan Jr. “Multiple material marching cubes algorithm”. en. In: *International Journal for Numerical Methods in Engineering* 58.2 (2003), pp. 189–207.

[68] Joël Lachambre. “Développement d’une méthode de caractérisation 3D des fissures de fatigue à l’aide de la corrélation d’images numériques obtenues par tomographie X”. These de doctorat. Lyon, INSA, 2014.

[69] Bertil Stora. “Hertz contact at finite friction and arbitrary profiles”. en. In: *J. Mech. Phys. Solids* (2005), p. 26.

[70] P. Cloetens et al. “Observation of microstructure and damage in materials by phase sensitive radiography and tomography”. In: *Journal of Applied Physics* 81.9 (1997). Publisher: American Institute of Physics, pp. 5878–5886.

[71] Julia F. Barrett and Nicholas Keat. “Artifacts in CT: Recognition and Avoidance”. en. In: *RadioGraphics* 24.6 (2004), pp. 1679–1691.

[72] Anton S. Kornilov and Ilia V. Safonov. “An Overview of Watershed Algorithm Implementations in Open Source Libraries”. en. In: *Journal of Imaging* 4.10 (2018). Number: 10 Publisher: Multidisciplinary Digital Publishing Institute, p. 123.

[73] R. Nock and F. Nielsen. “Statistical region merging”. In: *IEEE Transactions on Pattern Analysis and Machine Intelligence* 26.11 (2004). Conference Name: IEEE Transactions on Pattern Analysis and Machine Intelligence, pp. 1452–1458.

[74] D. Maugis. *Contact, Adhesion and Rupture of Elastic Solids*. en. Springer Science & Business Media, 2000.

[75] Janine C. Mergel et al. "Continuum contact models for coupled adhesion and friction". en. In: *The Journal of Adhesion* 95.12 (2019). arXiv: 1803.00046, pp. 1101–1133.

[76] C. Jacq et al. "Development of a Three-Dimensional Semi-Analytical Elastic-Plastic Contact Code". In: *Journal of Tribology* 124.4 (2002), pp. 653–667.

[77] Thibaut Chaise and Daniel Nélias. "Contact Pressure and Residual Strain in 3D Elasto-Plastic Rolling Contact for a Circular or Elliptical Point Contact". In: *Journal of Tribology* 133.041402 (2011).

[78] Koffi Espoir Koumi et al. "Modeling of the contact between a rigid indenter and a heterogeneous viscoelastic material". In: *Mechanics of Materials* 77 (2014), pp. 28–42.

[79] M Ciavarella, V Delfine, and G Demelio. "A "re-vitalized" Greenwood and Williamson model of elastic contact between fractal surfaces". en. In: *J. Mech. Phys. Solids* (2006), p. 23.

[80] L. Afferrante, G. Carbone, and G. Demelio. "Interacting and coalescing Hertzian asperities: A new multiasperity contact model". en. In: *Wear* 278-279 (2012), pp. 28–33.

[81] Eric Maire et al. "20 Hz X-ray tomography during an in situ tensile test". en. In: *International Journal of Fracture* 200.1 (2016), pp. 3–12.

List of author's publications

Vito Acito, Sylvain Dancette, Julien Scheibert, Cristobal Oliver, Jérome Adrien, Eric Maire, Davy Dalmas, *On the use of in situ X-ray computed tomography for soft contact mechanics*, European Journal of Mechanics - A/Solids, 101, 2023, 105057.

Remerciements

Bien que le travail de thèse soit, en théorie, quelque chose d'individuel et de personnel, il ne faut pas oublier que cette réalisation aurait été impossible sans le soutien de tant d'autres personnes. Je voudrais donc remercier tous ceux que j'ai rencontrées sur ce chemin, celles que je connaissais déjà et qui m'ont soutenu ou celles qui m'ont soutenu et se sont éloignées. Bref, je voudrais dire ici quelques mots pour ceux qui ont rendu ces trois années moins difficiles et surtout pleines de joie et d'énergie.

Tout d'abord, et cela semble presque évident, je remercie ma famille. Une mère, un père et un frère, suffisant pour former des piliers sur lesquels je pouvais m'appuyer et viser aussi haut qu'on un gratte-ciel. Je ne pourrai jamais oublier votre soutien inconditionnel, votre joie d'entendre parler de mes moindres réussites même si, souvent, ce que je faisais à cette époque n'était pas toujours clair. J'ai toujours tendance à me sous-estimer, mais vous voir vous vanter de mes réussites auprès de vos amis a pu sembler embarrassant au début, mais en fin de compte, cela m'a vraiment motivé. Même si j'étais loin, il vous suffisait de savoir que j'étais heureux, que j'étais fièr de moi et que je savais me relever à chaque chute. Sans vous, non seulement ma vie n'existerait pas mais elle aurait un goût bien plus amer.

Je voudrais continuer en remerciant ces amis d'une vie ou ceux qui m'ont rejoint sur le chemin, ceux qui se comptent sur les doigts d'une main. Gianluca, Marco, Paolo, Sandro et Chiara, je vous ai déjà remerciés trop souvent et j'espère ne jamais devoir m'arrêter. Nos passions, nos rêves nous ont conduit à être physiquement dispersés en Europe et à ne pas profiter chaque jour de la présence de l'autre. Pourtant, chaque fois que je vous revois, chaque fois que je vous serre dans mes bras, j'ai l'impression que le temps s'est arrêté entre deux rencontres. C'est parce qu'avec vous, je peux être certain que notre lien reste et restera indissoluble et que je peux compter sur vous, où que je sois, quelle que soit la difficulté dans laquelle je peux tomber. Vous serez toujours là pour me rappeler combien je vaux et combien il est bon de vivre dans la joie et la bonne humeur. Mais surtout, vous me montrerez toujours les différents aspects de la vie et vous me ferez grandir chaque jour.

Comment ne pas mentionner tous mes collègues et compagnons de route. Notre âge, nos craintes concernant la thèse, le partage de la joie d'un résultat obtenu ou d'un article publié, et le désir de s'épancher sur les problèmes avec nos superviseurs nous ont amené, au début, à simplement partager un bureau ou un déjeuner ensemble et à finir par créer une famille. Merci donc à cette grande famille de chercheurs en herbe, liés par un désir commun d'accroître la connaissance humaine et de viser plus haut. En particulier, permettez-moi de dire quelques mots à Cloé, ma "co-bureau", à qui je dois le sourire qu'elle arborait chaque jour en franchissant la porte du bureau et qui m'a rappelé que chaque petit résultat n'était pas acquis d'avance et que je devais croire davantage en mes propres capacités ; à Amaury, pour m'avoir donné de la force dans tant de moments difficiles et pour m'avoir appris la valeur de la simplicité ; à

Marina, ma psychologue gratuite qui a toujours su me donner les meilleurs conseils et qui m'a rappelé dans les moments les plus difficiles pourquoi j'avais décidé de commencer mon doctorat ; à Timothée, pour sa gentillesse rassurante et son calme indispensable pour dissiper le brouillard et la confusion et faire place à la sérénité ; à Théo pour avoir toujours été une source d'inspiration et m'avoir poussé à faire toujours mieux (ainsi que pour m'avoir montré combien de façons dégoûtantes on peut manger des pâtes) ; à Lucas sur qui on pouvait toujours compter et qui était toujours là pour nous donner un coup de main, ta gentillesse et ton calme resteront toujours une source d'inspiration ; à Mathilde pour nos échanges sur la musique, la culture, la politique, te retrouver et te parler a toujours été un plaisir et un réconfort. Je tiens à remercier tout le monde et j'espère n'oublier personne de tous ceux qui m'ont accompagné tout au long de ma thèse ou d'une partie de celle-ci. Merci Antoine, Cristobal, Emilie, Ianis, Guillaume, Jolan, Louise, Rexhina, Gabrielle, Youness, Adrien, Victor, Alexandre, Kaiser, Maxime, Louis, Théotime et Florian. Merci pour tous ces moments passés ensemble, pour votre sourire, votre soutien, votre ténacité, votre inspiration, votre passion pour la science et la recherche. Je vous souhaite le meilleur et j'espère que nos vies pourront encore se croiser, professionnellement et autrement.

Je voudrais continuer en remerciant mes amis italiens trouvés ici à Lyon. Grâce à vous, ma culture et mes racines ont été beaucoup moins éloignées et le temps s'est écoulé de manière plus agréable et plus douce. J'apprécie votre courage d'avoir quitté vos familles et vos amis pour suivre vos rêves et vos aspirations, et vous m'avez fait sentir moins seul dans ce choix difficile, qui oblige beaucoup d'entre nous à partir pour ce très long voyage. Vous avez été fondamentaux dans les moments de solitude et de nostalgie et ce fut merveilleux de passer tant de moments avec vous. Je voudrais remercier en particulier Stefano et Claudia pour leur incommensurable gentillesse, pour leur désir de vivre pleinement la vie à chaque instant. Nous, dans le sud, nous nous vantons souvent d'être plus chauds que ceux du nord de l'Italie, mais après vous avoir rencontrés, je dois revoir un peu mes stéréotypes. Je ne sais pas quoi ou qui je dois remercier pour vous avoir rencontrés et j'espère que la joie de se revoir à chaque fois ne s'estompera pas et restera toujours présente tout au long de notre vie.

Merci à mes amis d'Adoma, en particulier Yaz, Francesco et Giovanni. Je n'oublierai jamais à quel point il était réconfortant de trouver immédiatement des amis comme vous au moment les plus difficiles, notamment lorsque on arrive dans une nouvelle ville et que on ne connait rien ni personne. Vous avez été un phare dans l'obscurité.

Merci à Elena. Bien que tu m'aies soutenu pendant la première moitié de ce voyage, je ne peux pas oublier ton soutien indéfectible et ton acceptation initiale de ce voyage loin de la maison, en croyant en mes capacités et en respectant mes aspirations. Tu m'as accompagné main dans la main pendant la première période, la plus difficile, et maintenant je sens que je peux marcher seul grâce à tes enseignements.

Merci à mes deux encadrants Davy et Sylvain pour m'avoir guidé pendant ces trois années. Merci de m'avoir fait grandir, de m'avoir appris à croire en moi et à être heureux de mes résultats alors que je ne l'étais pas du tout. Merci de m'avoir appris à apprécier les petits pas et le plaisir de la découverte. Merci de m'avoir appris à être un vrai chercheur, à toujours analyser les choses avec la bonne critique, à faire les choses de la manière la plus précise et la plus détaillée possible, à toujours regarder autour de moi, à m'apprendre à penser avec jugement et logique. Je n'oublierai jamais l'énorme travail que vous avez accompli au cours de ces trois années et le temps que vous m'avez consacré (même le week-end ou la nuit, en particulier pen-

dant la correction de ce manuscrit). Lorsqu'on postule à un poste de doctorant, on ne connait pas nos encadrants et on fait un acte de foi. Je suis tombé du bon côté et j'ai eu beaucoup de chance de vous rencontrer. Je souhaite à beaucoup de gens comme moi de continuer à avoir des guides comme vous.

Merci à tous les chercheurs et ingénieurs des deux laboratoires où j'ai eu l'honneur de travailler. Sans vous, votre aide, vos discussions, vos critiques, vos conseils, votre soutien, rien de tout cela n'aurait été possible. Du côté du laboratoire LTDS, je citerais tout particulièrement Julien, Nasario, Emilie et Manuel, tandis que du côté du laboratoire Mateis, je remercierais en particulier Eric, Jerome, Joel, José, Erwan et Renaud. Pour une raison ou une autre, j'ai frappé à votre porte et j'ai eu la chance de toujours retrouver des personnes compétentes et serviables, qui parmi mille choses à faire ont toujours trouvé du temps à me consacrer même si ce n'était pas dû. Les deux labo ont vraiment de la chance de vous avoir.

Enfin, je voudrais remercier les membres du jury pour m'avoir consacré du temps et pour leurs précieux conseils. J'espère vraiment que mon travail a répondu à vos attentes et que je peux aspirer à vos futurs travaux de recherche.

Il n'a pas été facile d'arriver jusqu'ici et, parfois, la frustration de ne pas voir de résultats immédiats m'a dévasté et m'a donné envie d'abandonner. Si j'en suis arrivé là, c'est uniquement grâce à vous, à vos mots, à vos gestes, à vos sourires, à vos étreintes, à vos regards. J'ai été comme un brin d'herbe, vous avez été le vent qui m'a soulevé, soutenu et m'a permis de regarder vers le haut, de viser haut et d'atteindre mes objectifs. J'espère pouvoir vous apporter la même chose dans vos vies.

dernière page de la thèse

AUTORISATION DE SOUTENANCE

Vu les dispositions de l'arrêté du 25 mai 2016 modifié par l'arrêté du 26 août 2022,

Vu la demande du directeur de thèse

Monsieur D. DALMAS

et les rapports de

M. J. RETHORE
Directeur de Recherche CNRS - Institut de Recherche en Génie Civil et Mécanique (GeM)
Ecole Centrale de Nantes

et de

M. C. GAUTHIER
Professeur - Institut Charles Sadron - Strasbourg

Monsieur ACITO Vito

est autorisé à soutenir une thèse pour l'obtention du grade de **DOCTEUR**

Ecole doctorale Mécanique, Energétique, Génie Civil, Acoustique

Fait à Ecully, le 11 décembre 2023

Pour le directeur de l'École Centrale de Lyon
Le directeur de la recherche

Christophe CORRE

Titre : Tomographie à rayons X *in-situ* pour la mécanique des contacts mous

Mots-clés : Surface de contact ; élastomère ; segmentation d'image ; déformation de surface ; tomographie à rayons X ; mesure plein champ ; mécanique de contact ; tribologie

L'aire de contact réelle A_R entre deux solides en contact est une quantité fondamentale qui contrôle le comportement de frottement d'une interface de contact. Bien que la plupart des techniques expérimentales visant à mesurer cette quantité soient basées sur le contraste optique entre les régions en contact et hors contact, ces méthodes sont limitées par la transparence optique requise par au moins l'un des deux corps en contact. En outre, ces techniques ne permettent d'accéder qu'à l'interface de contact sans fournir d'informations sur d'autres quantités physiques importantes telles que la déformation globale ou les phénomènes hors contact à la surface. À partir de quelques travaux pionniers, nous proposons la tomographie à rayons X *in-situ* (XRCT) comme méthode alternative pour surmonter ces limites et accéder à la morphologie complète du contact en 3D avec des paires de contacts potentiellement non transparentes. Dans toutes les études précédentes, les analyses ont été effectuées sur des surfaces complexes sans se concentrer sur des examens préliminaires des limites de la XRCT (comme l'estimation des erreurs dans la mesure de A_R). Dans ce cadre, nous avons proposé l'utilisation d'un système modèle composé d'une sphère lisse en élastomère (PDMS) et d'une plaque rigide lisse (en PMMA) pour simplifier le problème et souligner les avantages et les inconvénients de cette méthode expérimentale. Nous nous sommes d'abord concentré sur la mesure *in-situ* de l'évolution de A_R au cours d'un essai de compression et de cisaillement réalisé sur notre système modèle. Les résultats ont été comparés à ceux d'un dispositif opto-mécanique 2D déjà maîtrisé. Enfin, à partir de la reconstruction en 3D in-operando du contact modéle indenté cisaillé, nous avons pu extraire les champ de déplacement, déformation et contraintes dans le contact par corrélation numérique des volumes (DVC) en utilisant comme marqueurs des particules préalablement dispersés dans le PDMS. Tous ces résultats ont été mis en regard des prédictions théoriques de modèles de la littérature.

Title: *In-situ* X-ray computed tomography for soft contact mechanics

Keywords: Contact Area; Elastomer; Image Segmentation; Surface Deformation; X-ray Computed Tomography; Full Field Measurement; Contact Mechanics; Tribology

The real contact area A_R between two solids in contact is a fundamental quantity that controls the frictional behavior of a contact interface. Although most experimental techniques aimed at measuring this quantity are based on the optical contrast between in-contact and out-of-contact regions, these methods are limited by the optical transparency required for least one of the two contacting bodies. Furthermore, these techniques only provide access to the contact interface without providing information on other important physical quantities such as the global deformation or the out-of-contact phenomena at the surface. Building on some pioneering work, we propose *in-situ* X-ray tomography (XRCT) as an alternative method to overcome these limitations and access the full 3D contact morphology with potentially non-transparent contact pairs. In all previous studies, analyzes were performed on complex surfaces without focusing on preliminary examinations of the limitations of XRCT (such as estimating errors in measuring A_R). In this context, we proposed the use of a model system composed of a smooth elastomer sphere (PDMS) and a smooth rigid plate (PMMA) to simplify the problem and highlight the advantages and disadvantages of this experimental method. We first focused on measuring *in-situ* the evolution of A_R during a compression and shear test carried out on our model system. The results were compared to those of a 2D opto-mechanical device already mastered. Finally, from the in-operando 3D reconstruction of the indented and sheared contact , we were able to extract the displacement, deformation and stress fields in the contact by digital correlation of volumes (DVC) using as markers particles previously dispersed in PDMS. All these results were compared to theoretical predictions from models in the literature.